RUHR-UNIVERSITÄT BOCHUM

Long Nguyen-Tuan

Coupled Thermo-Hydro-Mechanical Analysis:
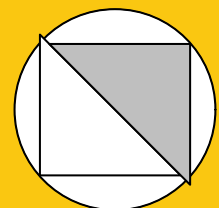Experiment and Back Analysis

Bochum 2014 Heft 49

Ruhr-Universität Bochum

Schriftenreihe Grundbau, Boden- und Felsmechanik

Heft 49

Coupled Thermo-Hydro-Mechanical Analysis: Experiment and Back Analysis

Dissertation

as a requirement of the degree of
Doktor-Ingenieur (Dr.-Ing.)

at the Faculty of
Civil and Environmental Engineering
Ruhr-Universität Bochum

submitted by
Long Nguyen-Tuan

Reviewers
Prof. Dr.-Ing. habil. Tom Schanz
Prof. Dr. Maria Datcheva
Prof. Dr. Yu-Jun Cui
Prof. DSc. Ivan Dimov

Bochum, July 2014

Vorwort des Herausgebers

Die Promotionsarbeit von Herrn Nguyen-Tuan ist auf dem Gebiet der Forschung zur Endlagerung von hochgefährlichen chemischen und radioaktiven Abfällen angesiedelt. Im Speziellen geht es um eine Verbesserung der bei Endlagerbauwerken verwendeten Baustoffe, des mechanischen Verständnisses der bei der Endlagerung verwendeten Baustoffe. Die hochgiftigen Abfälle werden im deutschen Konzept in Tiefen bis zu 800 m in geeigneten geologischen Formationen gelagert. Zum Abschluss der Grubengebäude werden sogenannte Verschlussbauwerke verwendet. In ihnen kommen hochverdichtete Bentonite als Mischungen mit Sand zum Einsatz. Auch in der unmittelbaren Nähe der radioaktiven Abfälle, die in der Regel in Kanistern gelagert werden, werden zur Lagerstabilisierung diese Mischungen von Bentonit und Sand eingesetzt.

Die Arbeit beschäftigt sich mit experimentellen und numerischen Analysen zum Verständnis des Materialverhaltens eben dieser Mischungen. Resultierend aus den spezifischen Gegebenheiten der Endlagersituation, wird die verdichtete Bentonit Sandmischung sowohl thermischen, als auch hydraulischen, als auch mechanischen Beanspruchungen ausgesetzt. Die mechanischen Beanspruchungen resultieren aus dem Gebirgsdruck. Die hydraulischen Beanspruchung, welche zu einem Quellen der expansiven Bentonite führt, resultieren aus dem unvermeidlichen Zutritt von Grundwasser aus der Umgebung des Grubengebäudes. Die thermischen Beanspruchungen resultieren zum einen aus den radioaktiven Abfällen, welche wegen dem radioaktiven Zerfall Hitze erzeugen, zum anderen werden die Baustoffe durch den Zutritt des im Vergleich zu den Abfällen kühlen Grundwassers beansprucht. Von entscheidender Bedeutung für eine realistische Materialbeschreibung ist deshalb das Verständnis des gekoppelten thermo-hydraulisch mechanischen Prozesses im Baustoff.

An dieser Stelle setzt die Arbeit von Herrn Ngyen-Tuan an. In einem weltweit einmaligen Technikumsversuch gelingt es ihm, die beschriebenen Mehrfeldprozesse in einem Endlager experimentell nachzuvollziehen. Es ist verständlich, dass derartige sehr aufwendigen Experimente nur in einer geringen Anzahl durchgeführt werden können. Aus diesem Grund besteht der zweite Hauptteil der folgenden Promotion von Herrn Ngyen-Tuan darin, ein adäquates numerisches Modell zu implementieren, welches an den Versuchsdaten kalibriert wird. Diese Kalibrierung erfolgt mittels eines inversen Verfahrens. Mit dem derartig kalibrierten, numerischen Modell ist es danach möglich, eine Vielzahl von sogenannten numerischen Experimenten effizient durchzuführen und dadurch die Endlagerbauwerke optimal zu gestalten.

Bochum, im Sommer 2014   Tom Schanz

Acknowledgements

This PhD thesis is a result of five years of my research work carried out at Laboratory of Foundation Engineering, Soil and Rock Mechanics, Ruhr-Universität Bochum. Therefore, first and foremost I hereby express my special thanks to my first supervisor Prof. Dr.-Ing. habil. Tom Schanz who gave me the opportunity to start my PhD research and has provided his continuing support over all these years. His encouragement and supervision all the way are highly appreciated.

My sincere gratitude goes to Prof. Dr. Maria Datcheva from Bulgarian Academy of Sciences - my second supervisor, who helped me during my research and thanks for her comments and suggestions throughout these years.

Many thanks go to Prof. Cui and Prof. Dimov for their agreement to be reviewers of this Dissertation. I appreciate very much their advices to improve my dissertation.

I would like also to acknowledge the financial support provided by Bundesministerium für Bildung und Forschung (BMBF) through research grant 02C1104 and the Research School in Ruhr-Universität Bochum.

I would like to thank my colleague Dr.-Ing. Wiebke Baille for her assistance during the laboratory work and useful discussions when we wrote together the paper. In particular, I wish to thank Dr.-Ing. Diethard König for his assistance whenever I needed. I would like to pass my gratefulness to all colleagues who assisted me during my period in Bochum.

I would like to express my thanks to my dearest wife. She always stays by my side, encourage me and the motivation for me to overcome all obstacles during the time studying in Germany. Thanks to my family in Vietnam, my parents and my sister, who are a spirit background for me to do my PhD.

<div align="right">Long Nguyen-Tuan</div>

<div align="right">Bochum July 2014</div>

Abstract

The research in this thesis considers the theoretical and experimental investigation of coupled thermo-hydro-mechanical (THM) phenomena as it applies to geotechnics.

The first aim was to enhance the existing equipment in order to better assess experimentally the processes that take place in unsaturated soil at non-isothermal conditions. In course of the study two devices have been modified: a soil column-type device for coupled THM testing and an oedometer cell. The main features of the column-type device are: hydraulic and thermal gradients are possible to be applied; transient water content, suction and temperature development can be measured continuously at three locations along the sample height; swelling pressure can be measured at top and the bottom of the sample. The high pressure oedometer cell was modified in order to perform tests under non-isothermal conditions for temperature range from 22°C to 80°C. The results of the tests performed using the new equipment are particularly presented and discussed. The collected experimental data permit derivation of some of the THM-model parameters.

Secondly, it is proposed a new model of hysteresis in the soil-water retention relationship that accounts for the air entrapment during soil drying and wetting cycles and the variation of the air entry value under cyclic hydraulic loading. The newly developed soil-water retention model was implemented in CODE_BRIGHT finite element software. The model was validated by the numerical simulation of two-phase flow and against data from sand column tests. The new model shows improved agreement between the experimental and the numerical simulation results when compared with other conventional models.

Thirdly, this study contributes to the identification of model parameters for coupled THM analysis by applying the back analysis approach to the performed herein experiments. The soil material parameters derived from the element test data obtained within this study and from literature were used as an initial set of parameters for the forward simulations. A novel strategy was proposed for identifying model parameters as well as for assessing the reliability and accuracy of the identified model parameters. The strategy consists of parameter sensitivity analysis, selection of the set of parameters to be identified and the setup of the parameter search space, selection of the optimisation algorithm and assessment of the reliability and accuracy of the identified model parameters. Both local and global sensitivity analyses are performed and the results are compared and critically discussed.

Zusammenfassung

Die Forschung in dieser Arbeit betrachtet die theoretische und experimentelle Untersuchung von gekoppelten thermo-hydro-mechanischen (THM) Phänomenen mit Anwendung in der Geotechnik.

Der erste Teil dieser Studie umfasst eine Modifizierung der bestehenden experimentellen Geräte, um dadurch die Prozesse, die in ungesättigten Böden bei nicht-isothermen Bedingungen stattfinden, besser nachzuvollziehen. Zwei Geräte wurden modifiziert: ein Säulengerät für gekoppelte THM-Untersuchungen sowie eine Ödometer-Zelle. Die Ausstattungsmerkmale des Säulengerätes sind: es können hydraulische sowie thermische Gradienten aufgebracht werden; Änderungen des Wassergehaltes, der Saugspannung und Temperatur können kontinuierlich an drei Stellen über die Probenhöhe erfasst werden; eine Messung des Quelldrucks ist sowohl am oberen als auch am unteren Ende der Probe möglich. Die Hochdruck-Ödometer-Zelle wurde so modifiziert, dass Experimente unter nicht-isothermen Bedingungen bei Temperaturen von 22°C bis 80°C durchgeführt werden können. Die experimentellen Ergebnisse werden im Einzelnen dargestellt und diskutiert. Zusätzlich konnten aus diesen Daten Parameter abgeleitet werden, die für das THM Modell verwendet wurden.

Im zweiten Teil wird ein neues Modell vorgeschlagen, welches die Hysterese innerhalb der Saugspannungs-Wassergehalts-Beziehung von Böden und damit Lufteinschlüsse während Trocknungs- und Bewässerungszyklen sowie die Variation des Lufteintrittspunktes unter zyklischer hydraulischer Belastung berücksichtigt. Dieses neu entwickelte Modell wurde in die Finite-Elemente-Software CODE_BRIGHT implementiert. Anschließend wurde das Modell anhand der experimentellen Daten aus den Säulenversuchen validiert, indem die Zweiphasen-Strömung numerisch simuliert wurde. Das neue Modell zeigt eine gegenüber den herkömmlichen Modellen verbesserte Übereinstimmung zwischen den gemessenen Ergebnissen und den Ergebnissen der numerischen Simulationen.

Im dritten Teil dieser Studie wird basierend auf inverser Analyseverfahren der durchgeführten Experimente ein Beitrag zur Parameter-Identifikation für eine gekoppelte THM Analyse geleistet. Die Parameter abgeleitet von den Elementversuchen aus dieser Studie sowie aus der Literatur wurden als Startwerte für die numerische Vorwärts-Simulation verwendet. Die Studie schlägt dabei eine neue Strategie für die Identifikation sowie die Bewertung von Zuverlässigkeit und Genauigkeit der identifizierten Modell-Parameter vor. Die Strategie besteht aus einer Sensitivitätsanalyse der Parameter, einer Auswahl an zu iden-

tifizierenden Parametern sowie der Einrichtung eines Parameter-Suchraums, der Auswahl des Optimierungs-Algorithmus und einer Bewertung von Zuverlässigkeit und Genauigkeit der identifizierten Modell-Parameter. Es wurden sowohl lokale als auch globale Sensitivitätsanalysen durchgeführt, deren Ergebnisse verglichen und kritisch diskutiert werden.

Contents

List of Figures

List of Tables

List of Symbols

α_{ss} Expansive index for TEP model

α_2 Parameter for elastic thermal strain

α_o Parameter for the elastic thermal strain

α_{sp} Expansive index for TEP model regarding pressure

β Parameter controlling the rate of increase in stiffness with suction

β_a The adjust significance of observation data and parameters information

χ Bishop's coefficient

δ_{ij} Kronecker's tensor

κ Compressibility coefficient for elastic

κ_i and κ_s Elastic slopes for TEP model

κ_{io} and α_i Thermo-elasto-plastic model parameters in TEP model

κ_{so} Elastic stiffness parameter when changing suction to zero net stress

λ_{dry} Parameter for soil thermal conductivity in the dry state

λ_{sat} Parameter for soil thermal conductivity in the saturated state

λ The shape parameter for retention curve

$\lambda(0)$ Stiffness parameter for saturated virgin compressibility

$\lambda(s)$ Stiffness parameter for unsaturated virgin compressibility

λ_T Parameter for soil thermal conductivity

μ_l Dynamic viscosity of the pore liquid

ω^v The mass fraction of the vapour

ω_k Weighting factor for each serial measurement

ω_{tm} Weighting factor for each measurement

ϕ_o Reference porosity

φ' Effective angle of internal friction

$\boldsymbol{x}$ Vector of model parameters

$\boldsymbol{y}$ Vector of model response

ψ Capillary pressure

ρ_s and ρ_l Solid and liquid densities

ρ_v Vapour density

$\boldsymbol{\sigma}$ Stress tensor

σ'_{ij} Effective stress tensor

σ_1 Total axial stress in conventional triaxial test

σ_3 Total confining stress in conventional triaxial test

σ^{sd} The standard deviation

σ_{ij} Total stress tensor

σ_T Surface tension of liquid

τ Tortuosity in molecular diffusion law

τ_f Shear stress on the failure plane at failure

θ_l^w and θ_g^w Volumetric mass of water and gas

θ Volumetric water content

$\boldsymbol{\varepsilon}^{T-e}$ Strain due to temperature change

$\boldsymbol{\varepsilon}^{\sigma-e}$ Strain induced by net stress

$\boldsymbol{\varepsilon}^{s-e}$ Strain induced by suction

ε^{e} Elastic strain

ε^{k} Error vector

ε^{p} Plastic strain

$\boldsymbol{i}_{c}$ Energy flux due to conduction

$\boldsymbol{b}$ Vector of body forces

c' Effective cohesion

CSS Composite scaled sensitivity

D_{m} Diffusion coefficient of vapour

e Void ratio

f^{Q} Internal/external energy supply

f^{w} External supply of water

$\boldsymbol{g}$ Gravity acceleration

g_{best}^{g} The global best of the objective function

$\boldsymbol{k}$ Tensor of intrinsic permeability

K_{a} Dielectric constant

k_{rl} Relative permeability

p Mean stress

p' Effective mean stress

p^{c} Reference stress

p^{net} Net mean stress

P_0 Model parameter for SWRC

p_0 Pre-consolidation stress

p_0^* Pre-consolidation stress for saturated condition

P_g and P_l Gas pressure and a liquid pressure

p_{at} Atmospheric pressure

q Deviatoric stress

r Compressibility coefficient for high values of suction

s Suction

S_r Degree of water saturation

S_e Effective degree of saturation

S_i The first order of sensitivity indices number i^{th}

S_{ls} Maximum degree of saturation

S_{rl} Residual degree of saturation

SS Scaled sensitivity

T_{ref} Reference temperature

v Specific volume

x^{norm} The normalisation of the parameter

1 Introduction and motivation

1.1 Background and motivation

With the rampant industrial development during the last century a large amount of dangerous and potentially detrimental to environment materials were produced and utilised. However, people often did not pay enough attention to treat such materials in a stable and safe manner while developing their new projects. One of the most dangerous waste products is the radioactive waste from nuclear power plants. Many procedures to solve the problem of long-term disposal of high-level radioactive waste (HLW) have been proposed over the past years. Some considered solutions are outer space disposal, ice sheet or beneath the seabed disposal, as well as deep geological repositories. The geological disposal is now undergoing intensive research. The common practice is to seal HLW inside stainless steel canisters. The canisters with HLW are proposed by some national nuclear agencies to be relocated in deep borehole repositories in a host rock surrounded by swelling buffer material. Nuclear waste repositories are embedded deep inside the rock stage for a long-term period.

In order to design and build a repository that operates properly providing safe permanent storage of HLW, the engineers must be able to assess and predict the phenomena that may affect adversely the repository facility and the environment. Assessing the performance of geological deep repositories involves detailed examinations of different processes that influence or may provoke the transport of radionuclides from the canisters to the biosphere. Many of those processes relate significantly to geotechnical problems. According to Gens (2003), the geotechnical assessment of the performance of a deep geological HLW storage facility requires some specific knowledge relate to:

- For the understanding of the behaviour of multi-phase geotechnical materials, it is necessary to incorporate new variables such as suction, temperature and accounting for geochemical environment.

- The phenomena relevant to nuclear waste repositories are frequently coupled with each other, and they should not be studied separately. Although the degree of interaction depends on the problem being examined, normally the adoption of generalised coupled approaches will be essential.

- Predicting material performance is required for an extensive period and the phenomena could be beyond any possible human experience.

- The interaction between human structures and natural soil or rock occurring before, during and after the excavation process should be examined. The range of geotechnical scales affecting repository performance is required to consider from micro-structural to geological macroscale features (e.g. the fracture pattern on a regional scale).

- The sensitivity and uncertainty of the geotechnical inputs which depend on the selected models, boundary value problems and experimental techniques must be understood and assessed quantitatively.

When analysing the geotechnical problems, the breadth of our knowledge on the physical phenomena plays a crucial role. Phenomena such as heat transfer, water flow, and stress distribution in the engineered clay barrier are of main importance for the behaviour of the buffer zone. Therefore, evaluating the influences of such phenomena on the barrier properties is vital while assessing the efficiency of the nuclear waste repositories. For this reason, coupled THM analysis has recently attracted the attention of the researchers and engineers involved in the conceptual design of engineered barriers for storing spent nuclear fuel and nuclear waste.

An important issue in interpreting the processes associated with waste repository functioning is the understanding of the coupled effects when both water and temperature vary within the engineered barrier. Experiments studying stress-strain behaviour while varying both water content and temperature have been conducted mostly using element tests in steady states such as tests in isochoric cells or oedometer cells (Villar, 2002; Tang and Cui, 2005; Romero et al., 2005; Cui et al., 2011). The effect of temperature on hydraulic conductivity in saturated conditions was addressed in (Cho et al., 1999; Delage et al., 2009) and the effect of temperature on unsaturated soil behaviour in a transient state was studied by e.g. (Ye et al., 2012). These element tests are one of the tools for studying the candidate materials for engineered barrier systems.

There are experimental tools that allow to gain more rich data as compared to the element tests by enabling to study the coupled THM behaviour of soils in transient state, making

possible to measure temperature, water content, suction, and swelling pressure to be measured during the tests. There are two approaches generally to be distinguished: full-scale field tests and laboratory tests, such as mock-up tests or benchmark tests. The full-scale field test is applied to investigate soil behaviour in a transient state accounting for without scale effect the interaction between soil material and other structures, such as host rocks or human activity. Such tests have been carried out within several research projects and results were reported in Alonso and Alcoverro (2005); Martín et al. (2006); Bossart and Nussbaum (2007); Geet et al. (2009). However, obtaining experimental data from in-situ/field tests is expensive and time consuming. In addition, controlling the boundary and initial conditions in situ is difficult, uncertainty prone, and sometimes even impossible. For these reasons, and for the purpose to observe more reliably the coupled THM behaviour of the buffer it has been proposed a column type test set-up. The column tests can be considered as an examination of a radial slice of the buffer cross section to reveal the coupled phenomena in the buffer material. Finally, the experimental setup aims to monitor the time history of temperature, T, pore water pressure, P_l, and mechanical displacement, u.

In terms of laboratory study, column-type devices used to study the vapour and heat transfer applying hydraulic or thermal gradients are reported in Mohamed et al. (1992); Cuevas et al. (1997); Gatabin and Billaud (2005); Villar et al. (2006); Bag (2011); Ye et al. (2012). The transient water content was determined indirectly by data on soil suction collected by relative humidity sensor or tensiometer in previous studies. The independently obtained relation between water content and suction was used to determine water content. However, the relation between water content and suction is time-dependent and density-dependent (Schanz et al., 2010a). Nowadays new technology such as the time domain reflectometry method (TDR) allows water content to be measured directly with high accuracy. All these devices so far have allowed the temperature to be controlled only at the heated head; the temperature of the supplied water head have not been controlled. The thermal conductivity of the sample changes according to the change in the water content during the heating test and the hydration test. Consequently, the temperature of the supplied water head varies during the test. This complicates prescribing the correct thermal boundary conditions in numerical simulations and determining correctly the thermal conductivity of the soil.

In terms of mathematical modelling, quantifying the stress-strain behaviour of unsaturated soils is a complicated problem. Several constitutive models have been suggested with a great number of constitutive parameters. For instance, Alonso et al. (1990) pro-

posed the Barcelona Basic Model (BBM) for unsaturated soil, employing the concept of two stress variables. Gens and Alonso (1992); Alonso et al. (1999) further extended their model and introduced the Barcelona Expansive Mode (BExM) for high-active soils, in which the micro-macro structure approach is employed to represent soil swelling and collapsing behaviour during drying-wetting cycles. Furthermore, a coupled model for unsaturated soil which takes temperature into account must be used to simulate properly the behaviour of the buffer materials. Such models have been proposed by several scientists, such as Hueckel and Borsetto (1990); Gens (1995); Cui et al. (2000); François and Laloui (2007); Wu et al. (2004). The appropriate model for representing the behaviour of unsaturated buffer material need to be discussed and the strategy for selecting the best model are the subject of the discussion in this study.

Beside modelling stress-strain behaviour, the hydraulic flow in unsaturated soil and in low permeability clayey soil is considered in this thesis. It is well accepted that the functional relationship between water content and water potential (i.e. suction or capillary pressure) called hereafter soil water retention curve (SWRC). The SWRC plays an important role in characterising the flow of the liquid and the gas phases in porous media. The hysteresis in SWRC has been studied extensively, but hysteretic unsaturated flow including air entrapment under hydraulic cyclic loads has usually been neglected or ignored in terms of modelling and numerical simulation. Therefore, it has been considered important for this study to discuss the phenomena related to air entrapment and its effect on SWRC hysteresis. Consequently, a new model for the hysteresis in SWRC has been proposed in order to reproduce, and a new model for the hysteretic SWRC is also developed to reproduce the experimental results of two-phase flow in unsaturated soil more adequately.

After constitutive models were built based on phenomenological or thermodynamical assumptions, the question was raised how to determine parameters for the current models. Several experiments were performed to identify targeted model parameters directly by controlling the other model parameters. Although experiments play an important role in studying the soil behaviour, they are time-consuming and costly. Furthermore, due to device and sensor restrictions it may not be always possible to directly measure and provide sufficient and reliable laboratory test data to determine material model parameters. In most cases the available experimental data requires back analysis to identify model parameters by minimising the error function between measurements and the model predictions (e.g. results of the numerical simulation of the experimental procedure). Moreover, back analysis can show improper features in the models, which might be appropriate for other types of soil or other boundary value problems. It has to be admitted that back analysis

to identify parameters for the constitutive model based on measurement data is necessary for quantifying precisely the behaviour of the buffer material.

In summary, firstly, there is a need to develop new or modify existing experimental equipment in order to better understand the behaviour of unsaturated soil in the buffer system. Secondly, there is a need to consider the coupled thermo-hydro-mechanical behavior in the modelling of buffer materials and a new soil water retention model should be developed. Thirdly, back analysis for identifying constitutive model parameters appears to be without alternative for quantifying precisely the performance of the HLW buffer material. Beside that, assessing the reliability of the identified parameters was necessary before using them to solve the boundary value problems and make predictions based on numerical simulations.

1.2 Objectives and methodologies

Based on the presented here-before state of the art, the three issues to be addressed as main objectives of this thesis are: improvement of the experimental methods and setup; extension of the soil water retention modelling concept to better account for the experimental observation and elaboration of methodology for identification of coupled THM model parameters via back analysis of enhanced experiments. Firstly, this study aims to introduce and to elaborate new experimental equipment to study the coupled THM behaviour of unsaturated soil. A column-type device is designed based on the idealisation of the cross section of proposed nuclear waste repository. The schematics is presented in Fig. 5.8. The setup of the column was first introduced in (Manju et al., 2008). However, further improvement is required to ensure the accuracy of the TDR measurement and to control better boundary conditions. The main features of the new device are the ability to: (*i*) measure the swelling pressure at sample top and bottom; (*ii*) apply suction and temperature gradients; (*iii*) and measure water content, suction and temperature at three sections along the sample, while minimally disturbing the sample. A new solution is utilised to measure the relative humidity (RH) providing temperature-controlled environment for the RH-sensors. This method guaranteed equal temperature in the RH-sensor chamber and in the sample at the same height level, thus avoiding vapour condensation. The advantages of the new column device are: (*i*) it allows the soil water retention profile to be obtained directly by measuring water content and suction at the same high levels; (ii) and it allows the temperature to be controlled at the boundary, where water is supplied, by means of a hydraulic cooling system. The column-type device

is used to investigate the coupled THM behaviour of a 50/50 per cent sand-bentonite mixture.

In addition a modified high pressure oedometer device is employed to conduct tests at different temperatures. Several tests are performed at 20°C or 80°C on the sand-bentonite mixture. In order to understand the soil water retention behaviour in unconfined conditions, two methods are used: axis translation technique (ATT) and vapour equilibrium technique (VET). The axis translation technique is used to determine soil water content at low suction (less than 1500 kPa). Vapour equilibrium technique is used to determine soil water content at higher suction.

Numerical simulations for column-type tests are carried out based on the coupled THM analysis in the CODE_BRIGHT finite element program (Olivella et al., 1996b). The thermo-elasto-plastic model (Hueckel and Borsetto, 1990; Gens, 1995) is used to represent the stress-strain behaviour under the effect of temperature. For hydraulic flow, generalised Darcy's law is used with porosity dependent intrinsic permeability and employed two parameters Van Genuchten model (van Genuchten, 1980) for the relationship between suction and the degree of saturation.

In this thesis, a new model for the SWRC with hysteresis is proposed. The model reproduces hysteresis and air entrapment phenomena under a cyclic hydraulic load. The newly proposed SWRC model is implemented in the CODE_BRIGHT finite element program. Afterwards, the SWRC model is validated by numerical simulations of two-phase flow against the experimental data from sand column tests reported in Lins (2009).

Finally, the current study contributes to the development of procedures to identify the constitutive model parameters for coupled THM models of unsaturated sand-bentonite mixtures using the back analysis approach. The parameter identification strategy consists of the following: (i) sensitivity analysis, (ii) selection of optimisation algorithms, (iii) selection of a set of parameters to be optimised and the setup of the parameter constraints, and (iv) assessing the reliability and accuracy of the material parameters as well as of the employed model. The current study aims to compare and discuss local sensitivity analysis with global sensitivity analysis. The relation between the confidence in the identified parameters and their sensitivity is also discussed.

1.3 Organisation and scope

The thesis goes through state of the art, experimental programmes, numerical simulations and finally back analyses. Some of the results that were obtained within this investigation have been published or submitted for publication (Schanz et al., 2011a, 2013; Nguyen-Tuan et al., 2013). The thesis consists of ten chapters, and this section provides a short summary of each chapter.

Chapter 1 introduces the general background and motivation for this study, where the demand and the need for researching this topic is made apparent. Next, the objectives and methodologies section provides a brief summary of the research methods and highlights various points in the thesis. The organisation and scope summarises the basic content.

Chapter 2 presents a review on the hydro-mechanical behaviour of expansive soil in non-isothermal conditions. The review summarises current views on the constitutive modelling of unsaturated soil behaviour. A critical discussion on different concepts on stress-state variables, volume change theory, shear strength, yield function, and expansive soil behaviour are included in this part. The review also focuses on the soil water retention curve and its role in characterising unsaturated soil behaviour. The effects of temperature on stress-strain behaviour and hydraulic behaviour are also discussed. The review concentrates on analysing the origin of a thermo-elasto-plastic model and its development, which is subsequently used in numerical simulations and back analyses.

Chapter 3 presents a review of the application of back analysis in geotechnical problems. It provides a general concept of back analysis including uncertainty and sensitivity analyses, optimisation methods, and reliability analysis. This chapter summarises the methods of defining objective functions and optimisation algorithms. Finally, the concept of reliability analysis of input parameters and a general overview of the methods of analysis applied in geotechnical problems are classified and summarised.

Chapter 4 presents the basic physical properties of the materials used. The basic investigated material used in this thesis is a 50/50 per cent sand-bentonite mixture. Other materials are also addressed for comparison and validation purposes, such as sandy loam, Hostun sand, and yellow sand.

Chapter 5 provides the description of the devices and experimental techniques employed in the research. It includes the description of element tests (using i.e. the oedometer device and the device for SWRC unconfined conditional tests), the column-type device, and the calibration tests (especially for temperature). In this chapter, the author focuses

on carefully presenting and discussing the calibration tests for the devices with varied temperature.

Chapter 6 presents the calibration for TDR under the change of temperature. Beside that, the physical phenomena behind the effect of temperature on TDR measurement are interpreted in the view points of soil-water relation. The data presented in this chapter can be used to quantify the water content during measurement at non-constant temperature in the range between 20 and 80 °C. The results obtained show that temperature affects significantly the dielectric constant measured for sand-bentonite mixture by TDR method.

Chapter 7 presents and discusses the experimental results. The most important aspects include the effect of temperature in the constrained swelling test, the effect of the thermal gradient on saturated hydraulic conductivity, the transient water content and suction in the column-type device, and the effect of temperature on swelling pressure. The results of element tests are used to derive several material parameters for the numerical simulation of coupled THM problems.

Chapter 8 presents the theoretical framework for THM analysis. It includes constitutive equations for the thermo-elasto-plastic model, for hydraulic model and the basic constitutive relation for thermal conductivity. A new model is introduced to reproduce hysteretic unsaturated flow, including the air entrapment phenomenon. The model is validated by numerically simulating two-phase flow in sand columns under a cyclic hydraulic load. Next, the numerical simulation for column-type test is also performed to validate the capacity of the constitutive models.

Chapter 9 presents the procedure to identify the model parameters using back analysis approach. The chapter focuses on local and global sensitivity analyses. The advantages of global analysis is discussed, and it is argued that global sensitivity analysis is preferred in THM analysis. A sensitivity analysis algorithm has been established which can automatically work with CODE_BRIGHT output and input files to analyse data in the output and generate the input files. After validating developed software, it is used analyse model parameter sensitivity for different boundary value problems. The criteria to select the objective function and the optimisation algorithm are discussed in this chapter. The discussion also focuses on the relationship between parameter sensitivity and confidence in the identified parameters.

Chapter 10 provides conclusions and outlook for this thesis. The main discussions is summarised in this chapter. Besides several promising works is proposed for the future research in the outlook subsection.

2 Thermo-hydro-mechanical modelling of soil behaviour: literature review

2.1 Constitutive modelling of unsaturated soil

There have been a significant number of papers reviewing on the constitutive modelling of unsaturated soils. Several high quality papers can be referred such as Gens (1996); Wheeler and Karube (1996); Jommi (2000); Khalili et al. (2004); Gens et al. (2006), and Sheng and Fredlund (2008). In this review, the author summarises and discusses the recent theories on the constitutive modelling of unsaturated soil behaviour.

2.1.1 Stress state variables

The choice of appropriate stress state variables for unsaturated soils is an intensively debated issue, often in connection with the possibility of defining a single effective stress by analogy with the effective stress in saturated soil case. Numerous attempts have been made to develop a similar concept of effective stress as that proposed for saturated soils by Terzaghi (1923). However, the use of a single effective stress for unsaturated soils has encountered many difficulties. In fact, "no single stress variable has ever been found which, substituted for effective stress, allows for a description of all the aspects of the mechanical behaviour of a given soil in the unsaturated range" - Jommi (2000).

Bishop (1959) and Bishop and Blight (1963) have attempted to incorporate the suction, s, explicitly into the effective stress definition. Eq. 2.1 presents Bishop's concept in terms of stress tensor.

$$\sigma'_{ij} = \sigma_{ij} - u_a \delta_{ij} + \chi \left(u_a - u_w \right) \delta_{ij} = \sigma_{ij}^{net} + \chi s \delta_{ij} \tag{2.1}$$

where σ'_{ij} is the effective stress tensor, σ_{ij} is the total stress tensor, χ is the Bishop's coefficient which may be assumed as a function of the degree of saturation S_r, δ_{ij} is the

Kronecker's tensor ($\delta_{ij} = 1$ if $i = j$ and $\delta_{ij} = 0$ if $i \neq j$). σ_{ij}^{net} is the net stress and $s = u_a - u_w$ is the suction. The pore air pressure, u_a, is always considered positive, while pore water pressure, u_w, is considered negative in an unsaturated state and positive in a saturated state. When pore water pressure is a negative value in a partially saturated state, the effective stress is a sum of net stress and matric suction multiplied with factor χ. When pore water pressure is positive, χ is equal to one, and the effective stress is defined the same as definition of effective stress in saturated soil. With this definition of u_w the effective stress can be used continuously for a relatively wide range of saturated states, from fully saturated to very dry states.

Richards (1966) incorporated the osmotic suction into the effective stress equation:

$$\sigma'_{ij} = \sigma_{ij} - u_a \delta_{ij} + \chi_m \left(h_m + u_a \right) \delta_{ij} + \chi_s \left(h_s + u_a \right) \delta_{ij} \qquad (2.2)$$

where χ_m and χ_s are effective stress parameters for matric suction and osmotic suction, respectively. h_m and h_s are matric suction and solute suction. The osmotic suction is defined to be "a negative gauge pressure to which a pool of water must be subjected in order to be in equilibrium through a semipermeable membrane with a pool containing a solution identical in composition with the soil water, respectively" (Fredlund and Rahardjo, 1993).

The concept of effective stress has some advantages:

- It is easy to implement into a finite element code, Charlier and Radu (1997).

- It provides qualitatively accurate predictions for problems involving mainly shear stresses.

But its application to modelling of mechanical behaviour of unsaturated soils has some disadvantages due to the following main reasons:

- Generally, the volumetric behaviour cannot be properly modelled within the concept of effective stress. There is no unique relationship between void ratio and effective stress as defined in Eq. 2.1 for most partially saturated soils below a critical degree of saturation.

- In particular, it is not possible to properly represent the collapse behaviour, which is a typical phenomenon of unsaturated soils during the wetting phase under certain external charges.

- Bishop's coefficient, χ, is a complicated function. Many experiments have shown that it may depend on the water saturation S_l but there is a non-unique relation

between χ and S_l for a given soil sample with different void ratio, Collin et al. (2002).

- And the experimental tests for determination of χ values, which are unapparent, was pointed out in Bishop and Blight (1963).

The above considerations lead to the use of two independent stress state variables to model the mechanical behaviour of unsaturated soils. Net stress and suction are mostly used as independent stress variables. Coleman (1962) proposed the use of net axial or radial stresses, and net pore water pressure to represent triaxial stress states. Matyas and Radhakrishna (1968) used the concept of "state parameters": $\sigma - u_a$ and $\sigma - u_w$ to describe the volumetric behaviour of unsaturated soil. The theoretical and experimental arguments of using two independent stress variables were further strengthened by Fredlund and Morgenstern (1977). In the paper Fredlund and Morgenstern (1977), it is concluded that any pair of the tree stress variables $\sigma - u_a$, $\sigma - u_w$ and $u_a - u_w$ can be used to describe the mechanical behaviour of unsaturated soils. The combination of the net stress and the matric suction has proved to be easy for description of stress-strain relation, Burland (1965b). But according to Khalili et al. (2004), using two stress state variables lead to complex constitutive equations for stress-strain relationships, which is a disadvantage. Nuth and Laloui (2008) criticised that considering suction as a variable in the stress-strain relation may lead to numerical difficulties when switching from partially to fully water saturated conditions and vice-versa. Although the two-independent-stress variables concept was criticised, it is widely used starting from the last nineties because the models and the parameters based on this concept are simply determined via conventional experiments.

Recently the problem with the effective stress in unsaturated soil mechanics has been discussed again. Khalili et al. (2004); Lu (2008) attempted to address two fundamental questions regarding the appropriate use of matric suction in unsaturated soil mechanics. There is an interdependency or coupling between matric suction and the net normal stress if both of them are concurrently used to describe the state of stress in unsaturated soils. Nuth and Laloui (2008) and Laloui and Nuth (2009) stated that suction is shown not to be a hardening variable but rather a shape parameter for the yield surface. They proposed to use generalised effective stress instead of Bishop's effective stress. The generalised effective stress concept is similar to the idea of Bolzon et al. (1996); Puzrin and Houlsby (2001). According to the authors (Laloui and Nuth (2009)), the advantage of generalised effective stress is that it makes the hydro-mechanical coupling straightforward, featuring

a direct modification in effective stress upon suction change and accounting the influence of the capillary hysteresis on the mechanical behaviour.

In summary, in attempt to reproduce the stress-strain behaviour of unsaturated soils, several authors have developed models based on different concepts of stress state variables. Some authors used two independent stress variables (e.g. net stress and suction), the other tried to insert unsaturated soil mechanics into the mainstream of current and past developments in saturated soil mechanics by using effective stress or generalised effective stress. The choice of appropriate stress variables for unsaturated soils is an intensively debated issue, often in connection with the possibility of defining a single effective stress measure.

2.1.2 Volume change theory and isotropic stress-strain models

Selection of stress state variables determines how the volumetric strain and stress relationship can be represented. Several authors prefer using effective stress to formulate the volume change theory in unsaturated soils, while the others select two stress state variables. This part of the thesis will review the two approaches for representing the volume change of soil behaviour.

Representatives of the authors who formerly follow the approach of the conventional effective stress are Aitchison and Donald (1956); Bishop (1959); Aitchison (1960); Jennings and Burland (1962); Burland (1965b). These authors attempt to quantify the χ parameter as well as the experimental method for determining χ in the relationship with degree of saturation. The pioneer among authors who use effective stress for volume change description for unsaturated soil is Coleman (1962). The current overall volume of the soil element is V, the volume of water is V_w. Then the relative changes of the volume of water and the total volume are express via:

$$-\frac{\mathrm{d}V_w}{V} = -C_{11}(\mathrm{d}u_w - \mathrm{d}u_a) + C_{12}(\mathrm{d}\sigma_m - \mathrm{d}u_a) + C_{13}(\mathrm{d}\sigma_1 - \mathrm{d}\sigma_3) \tag{2.3}$$

$$-\frac{\mathrm{d}V}{V} = -C_{21}(\mathrm{d}u_w - \mathrm{d}u_a) + C_{22}(\mathrm{d}\sigma_m - \mathrm{d}u_a) + C_{23}(\mathrm{d}\sigma_1 - \mathrm{d}\sigma_3) \tag{2.4}$$

where σ_m is the mean stress, σ_1 is total axial stress, σ_3 is total confining stress in conventional triaxial test, C_{11}, C_{12}, C_{13} are soil parameters associated with the change in the volume of water in the soil element, C_{21}, C_{22}, C_{23} are soil parameters associated with soil skeleton volume change. The equations (Eq. 2.3 and 2.4) presumed that the change in deviatoric stress $\mathrm{d}\sigma_1 - \mathrm{d}\sigma_3$ also produces volume changes.

However, many researchers later discovered that the skeleton of compacted soils is not adequately represented by the theoretical model based on the effective stress introduced in Aitchison (1960); Bishop and Blight (1963). Also they questioned the validity of the effective stress principle (Eq. 2.1) in unsaturated soils and argued that it cannot explain the collapse phenomenon upon wetting (Jennings and Burland, 1962), stating also that it is incorrect to combine $(\sigma_{ij} - u_a\delta_{ij})$ and $(u_a - u_w)\delta_{ij}$ into a single equation.

Recently, based on different concepts of effective stress various constitutive models of volume change have been proposed (Loret and Khalili, 2002; Wheeler et al., 2003; François and Laloui, 2007). For instance, Loret and Khalili (2002) developed a model within the elasto-plastic framework by defining effective stress as follows:

$$\boldsymbol{\sigma}' = \boldsymbol{\sigma} + \chi u_w\mathbf{I} + (1 - \chi)u_a\mathbf{I} \equiv -p'\mathbf{I} + \boldsymbol{s} \quad \text{and} \quad p' = p^{net} + s\chi \tag{2.5}$$

where, $\boldsymbol{\sigma}$ is the total stress tensor, $p^{net} = 1/3\text{tr}\boldsymbol{\sigma}^{net}$ is the mean net stress, $\boldsymbol{s}$ is the deviatoric stress part. The elastic change of the soil specific volume is defined by Eq. 2.6, whereas the current specific volume (NCL) is given by Eq. 2.7:

$$\mathrm{d}v = -\kappa\left(\frac{dp'}{p'}\right) \tag{2.6}$$

$$v = N(s) - \lambda(s)\ln\left(\frac{p'}{p'^c}\right) \tag{2.7}$$

where, v is the specific volume, p' is the mean effective stress, p^c is the reference stress state for which $v = N(s)$.

Meanwhile other authors developed the expression for the volumetric deformation based on two stress variables; e.g. $(\sigma_{ij} - u_a\delta_{ij})$ and $(u_a - u_w)$. One of the first elasto-plastic models designed explicitly to describe the mechanical behaviour of unsaturated soils was presented in Alonso et al. (1990). On unloading and reloading (at constant s) the soil behaves as elastic, according to Eq. 2.8. The specific volume at active loading is given by Eq. 2.9.

$$\mathrm{d}v = -\kappa\left(\frac{\mathrm{d}p^{net}}{p^{net}}\right) \tag{2.8}$$

$$v = N(s) - \lambda(s)\ln\left(\frac{p^{net}}{p^c}\right) \tag{2.9}$$

Beside volumetric strain induced by net stress, Alonso et al. (1990) proposed that the volumetric strain may be induced by suction. The virgin state is written as in Eq. 2.10

and for drying and wetting reversals in Eq. 2.11

$$\mathrm{d}v_s = -\lambda_s \frac{\mathrm{d}s}{(s + p_{at})} \tag{2.10}$$

$$\mathrm{d}v_s = -\kappa_s \frac{\mathrm{d}s}{(s + p_{at})} \tag{2.11}$$

where, λ_s is the stiffness parameters for changes in suction in virgin state, κ_s is the elastic stiffness parameters for changes in suction, p_{at} is the atmosphere pressure.

A large number of other elasto-plastic models using two stress variables were recently introduced in for example Kohgo et al. (1993); Wheeler and Sivakumar (1995); Cui and Delage (1996); Datcheva and Schanz (2003); Chiu and Ng (2003).

2.1.3 Shear strength of unsaturated soil

The shear strength is related to many geotechnical problems such as bearing capacity, lateral earth pressure, and slope stability. The early shear strength theory originates from unsaturated soil by the Mohr-Coulomb failure criterion. The criterion is based on the effective stress as follows:

$$\tau_f = c' + (\boldsymbol{\sigma}_n - u_w)_f \tan \varphi' \tag{2.12}$$

where τ_f is the shear stress on the failure plane, c' is the effective cohesion, $(\boldsymbol{\sigma}_n - u_w)_f$ is the effective normal stress on the failure plane, φ' is the effective angle of internal friction.

Eq. 2.12 defines a line as illustrated in Fig. 2.1(a). The line is commonly referred to as a failure envelope. The use of effective stress with the Mohr-Coulomb failure criterion has proved to be satisfactory in practical engineering associated with saturated soils. The following researchers developed the models based on the Mohr-Column criterion for unsaturated soil. Bishop et al. (1960) introduced the Bishop's effective stress in Mohr-Column failure criterion. Fredlund et al. (1978) incorporated matric suction into the shear failure criterion:

$$\tau_f = c' + (\boldsymbol{\sigma}_n - u_w)_f \tan \varphi' + (u_a - u_w)_f \tan \varphi^b \tag{2.13}$$

where $(u_a - u_w)_f$ is the matric suction at the failure state, φ^b is an angle indicating the rate of increase in shear strength relative to matric suction, Fig. 2.1(b).

Another approach for modelling of shear strength in clay soil is the method based on critical state soil models, e.g. Cam Clay Model for saturated clay (Roscoe et al., 1958,
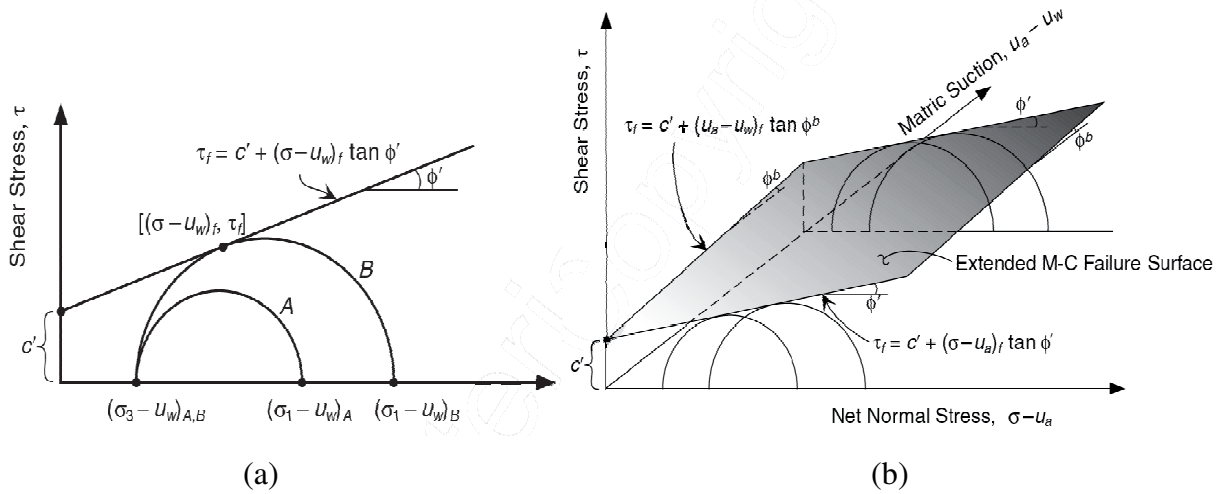
Figure 2.1: (a) Mohr-Coulomb failure envelope for saturated soil. (b) Extension of Mohr-Coulomb failure model for unsaturated soil, Lu and Likos (2004).

1963), see also for details in section 2.1.4. Later Cam Clay model was enhanced with dilatancy and the shear distortion model to the Modified Cam Clay (MCC) model, Burland (1965a); Roscoe and Burland (1968). The model presented the shear strength cooperated with hardening and dilatancy behaviour for plastic soil. The MCC model analysed the stability of the soil prior to failure and after failure where strain is presumed to be very large and unpredictable. Such critical state conditions were presented on the $p' - q'$ plane by Eq. 2.14. See section 2.5 for more details.

$$q = Mp' \tag{2.14}$$

where $p' = \frac{1}{3}(\sigma'_I + \sigma'_{II} + \sigma'_{III})$ is mean normal effective stress, $q = \sigma'_I - \sigma'_{III}$ is a deviatoric stress in conventional triaxial test, M is slope of the critical state line. Latter, Alonso et al. (1990) extended the MCC model to BBM model for unsaturated soil which have taken suction into account. They assumed that the slope of the critical state line (M) is defined in the saturated state and does not change with suction. This assumption does not correspond to the experiments of Geiser et al. (1997). The uniqueness of the critical state line with variation of suction is later discussed by Khalili et al. (2004); Nuth and Laloui (2008).

2.1.4 Yield function and hardening law

The harding laws and the yield functions have been so far developed based on the different stress state concepts. Many of the authors select Modified Cam Clay (MCC) model for

saturated soil (Roscoe and Burland, 1968) as a starting point. Alonso et al. (1990) proposed the hardening law as in equation Eq. 2.15 and Eq. 2.16 considering suction as a hardening variable. The volumetric deformation in elasto-plastic law is induced by both net mean stress and suction. The yield function is a function of net mean stress (p^{net}), deviatoric stress (q), and matric suction (s), Fig. 2.11. The yield function is presented in Eq. 2.17 in the (p, q, s) stress space. The load-collapse (LC) curve given by Eq. 2.18 represents the yield curve in $s - p$ plane.

$$\frac{\mathrm{d}p_0^*}{p_0^*} = \frac{v}{\lambda_0 - \kappa}\mathrm{d}\varepsilon_v^p \tag{2.15}$$

$$\frac{\mathrm{d}s_0}{s_0 + p_{at}} = \frac{v}{\lambda_s - \kappa_s}\mathrm{d}\varepsilon_v^p \tag{2.16}$$

$$f(p^{net}, q, s) = q^2 - M^2(p^{net} + p_s)(p_0 - p^{net}) = 0 \tag{2.17}$$

$$\left(\frac{p_0}{p^c}\right) = \left(\frac{p_0^*}{p^c}\right)^{\frac{\lambda(0)-\kappa}{\lambda(s)-\kappa}} \quad \text{with:} \quad \lambda(s) = \lambda(0)[(1-r)\exp(-\beta s) + r] \tag{2.18}$$

These hardening equations were criticised by Laloui and Nuth (2009). In their papers, they concluded that suction should not be a hardening parameter. Loret and Khalili (2002) modified the MCC as in equation Eq. 2.19. The yield curve was modified from the MCC to avoid overestimating the failure stress in dry cases according to the CSL conditions, Fig. 2.2.

$$f = \begin{cases} \dfrac{q^2}{M^2 p'} + p' - \dfrac{2}{r}p_0' & \text{if} \quad p' \leq \dfrac{p_0'}{r} \\ (r-1)^2\dfrac{q^2}{M^2 p'} + p' - \dfrac{2}{r}p_0' + \left(\dfrac{2}{r} - 1\right)\dfrac{p_0'^2}{p'} & \text{if} \quad p' \geq \dfrac{p_0'}{r} \end{cases} \tag{2.19}$$

Wheeler et al. (2003) introduced the term modified suction ($s^* = ns$) and stress ($p^* = p^{net} - sS_r$) and developed their model based effective stress concept, but the stress state variables used are p^*, q, s^*; thus the yield function is defined as a function of modified suction, where n denotes porosity.

2.1.5 Constitutive models for high expansive soil

In general, the BBM model (Alonso et al., 1990) or Khalili and Loret (2001); Laloui (2001) model and others can represent the behaviour of low activity soil. The BBM model is
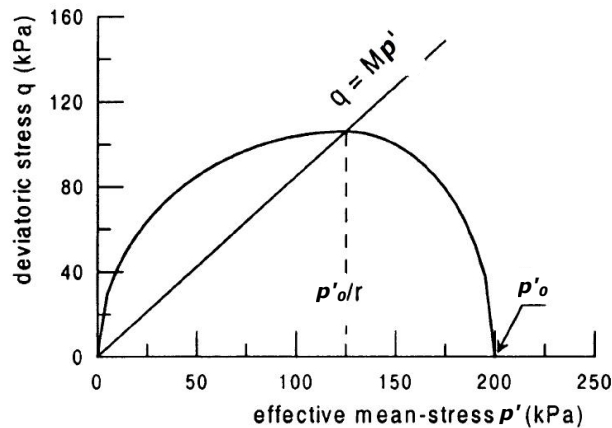
Figure 2.2: Loret and Khalili (2002) – The elliptical Cam-Clay yield function is modified to accommodate the ratio $r \neq 2$.

used popularly in numerical simulations, and it is presented in section 2.5. In the BBM the strain increment is a function of suction; therefore the soil model can swell or collapse due to variations in suction. However, there has been significant additional interest due to the fact that expansive clays are now widely used as the basic material for constructing waste-isolation barriers. It is generally acknowledged that most of the basic elasto-plastic models mentioned above cannot easily accommodate the behaviour of highly expansive soils and this was reported in many experimental papers (Gens and Alonso, 1992). The BBM cannot reproduce the dependency of swelling strains and swelling pressures on the initial state and on the stress path. In addition, the strain accumulation during the cycles of suction cannot be reproduced (Gens and Alonso, 1992). In order to develop a model consistent with present understanding of these basic phenomena, it appears necessary to explicitly incorporate the micro-structural effects in the model formulation.

In fact, it is likely that the key element in the model framework is to define satisfactorily the effects of particle-level phenomena on the overall behaviour of the material. To do this, it is necessary to take into account some fundamental aspects of the soil micro-structure, Fig. 2.3. Alonso et al. (1999) developed Barcelona Expansive Model (BExM) using the conceptual understanding of the unsaturated expansive soil (Gens and Alonso, 1992). It is based on the assumption that there are two scales in the soil structure named micro-structure and macro-structure. According to Gens and Alonso (1992), when the micro-structure expands its volume it affects the structural arrangement of the macrostructure, inducing an irreversible deformation. In order to describe the above-mentioned behavior, Alonso et al. (1999) defined two different levels; micro-structural level at which the swelling

of active minerals takes place and the macro-structural level, which incorporates major structural rearrangement.

Alonso et al. (1999) defined the strain of two separate structures: volumetric macro-structural strain (ε_{vM}) and volumetric micro-structural strain (ε_{vm}).

$$\mathrm{d}\varepsilon_{vM} = \frac{\mathrm{d}e_M}{(1 + e_M)} \quad \text{and} \quad \mathrm{d}\varepsilon_{vm} = \frac{\mathrm{d}e_m}{(1 + e_m)} \tag{2.20}$$

where e_M and e_m are the macro-structure and micro-structure void ratios, respectively.

Hardening law is governed by three yield loci: the suction increase (SI) line, the suction decrease (SD) line, and the load collapse (LC) curve, Fig. 2.4a. The total volumetric strain is the sum of elastic volumetric strain and plastic volumetric strain induced by three yield loci as follows.

$$\mathrm{d}\varepsilon_v = \mathrm{d}\varepsilon_v^e + \mathrm{d}\varepsilon_v^p = \mathrm{d}\varepsilon_{vM}^e + \mathrm{d}\varepsilon_{vm}^e + \mathrm{d}\varepsilon_{vSI}^p + \mathrm{d}\varepsilon_{vSD}^p + \mathrm{d}\varepsilon_{vLC}^p \tag{2.21}$$

The increment of the plastic volumetric strain depending on the microstructure strain (swelling/shrinkage) is defined as follows:

$$\mathrm{d}\varepsilon_{vM}^p = \begin{cases} f_D \mathrm{d}\varepsilon_{vm}^e & \text{when} \quad \text{SD is activated} \\ f_I \mathrm{d}\varepsilon_{vm}^e & \text{when} \quad \text{SI is activated} \end{cases} \tag{2.22}$$

where f_I and f_D are the two coupling functions which depend on the ratio of current pressure (p) and pre-consolidation pressure (p_0). The distinct micro-macro structure interaction mechanisms and their representation by the coupling functions f_I and f_D are summarised in Fig. 2.4b. The model using two alternative stress variables: the generalised mean effective stress ($\hat{p}$) was used to define elastic volumetric strain in the micro-structure, whereas a mean net stress and suction were used to express the elastic volumetric strain in macro-structure.

The BExM allows a good description of the accumulation of swelling strain during suction cycles at low confining stress, or the accumulation of compression strain during suction cycles at high confining stress. Later, several papers were published related to experiments on expansive soils confirming the applicability of the BExM double-structure concept, (Alonso et al., 2005b; Jacinto, 2010; Tang and Cui, 2009).

2.2 Characteristics of the soil-water retention

The soil-water retention curve (SWRC) is the curve describing the relationship between suction and volumetric/gravimetric water content or degree of saturation. The SWRC is
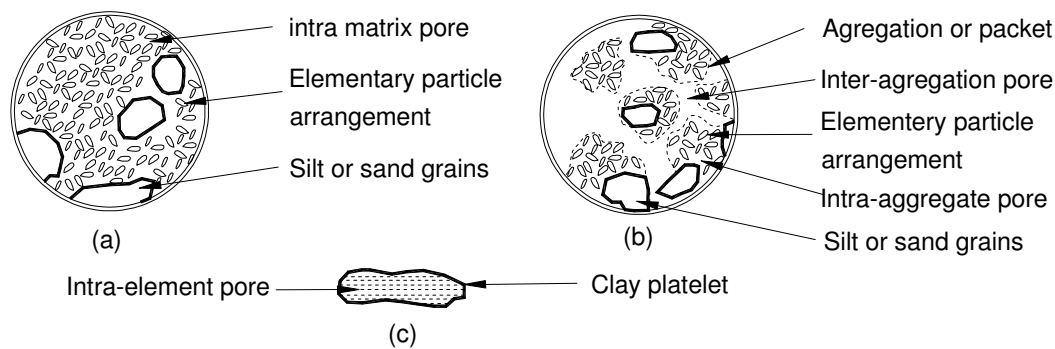
Figure 2.3: Fabric types. (a) Clay matrix predominantly constituted by elementary particle arrangements of clay platelets. (b) Micro-fabric of a clay predominantly made up of aggregations of elementary particle arrangements. (c) Elementary particle arrangement in a parallel configuration, according to Gens and Alonso (1992).

very important to estimate the hydro-mechanical behavior of unsaturated soils such as volume change, shear strength and hydraulic conductivity. Many papers contribute to the study of suction-water content in relation to effects of shear strength and volume change, including (Vanapalli et al., 1996; Lim et al., 1998; Fredlund, 2000). The correlation between SWRCs and the hydraulic conductivity has been studied by researchers such as (van Genuchten, 1980; Fredlund and Xing, 1994; Fujimaki and Inoue, 2003; Gerhard and Kueper, 2003). Therefore, it is necessary to utilise a proper model to predict the water/moisture or solute transport in unsaturated soils. Soil-water retention curves each other and depend on the structure or arrangement of the soil particles, the grain-size distribution, the pore-size distribution, and the soil density (Fredlund and Rahardjo, 1993).

A typical soil water retention curve is presented in Fig. 2.5a and 2.5b. According to Fredlund and Xing (1994), the SWRC includes three zones marked by the air-entry value, residual and maximum water contents. The following definitions are used hereafter:

Air-entry value is the matric suction at which air starts to enter the largest pore of the soil during the drainage process.

Residual water content is the water content at which an increase in matric suction does not produce a significant change in the water content.

The saturated zone is defined for suction from zero to the air-entry value (AEV). The residual zone is define the area where the suction value is smaller suction at residual water
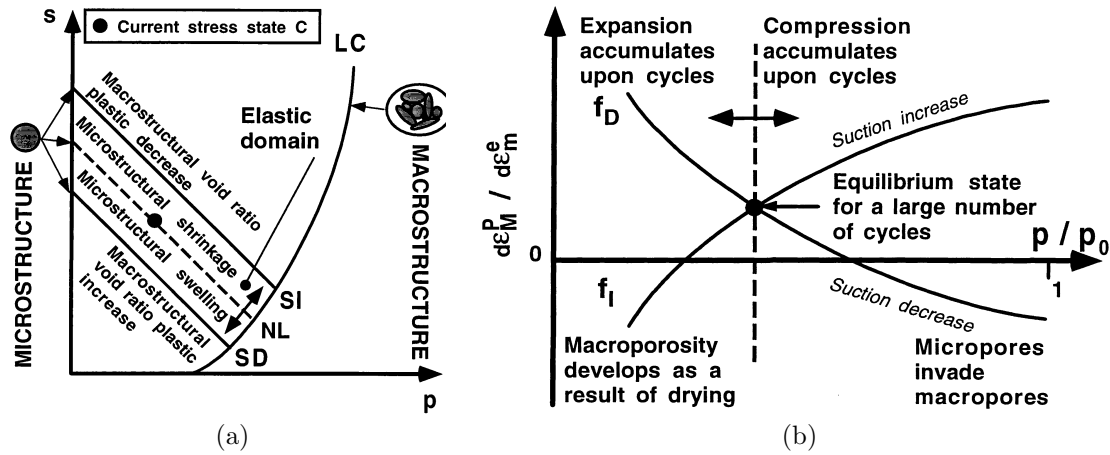
Figure 2.4: Schematic representation of Barcelona expansive model as double structure theory: (a) BExM yield loci in p-s plan, (b) summary of micro-macro pore interaction mechanisms, according to Alonso et al. (1999)

content. The transition zone is defined for suction in a range from the AEV to the residual water content Fig. 2.5a.

We consider hysteresis in the SWRC when the water content at a given suction for a wetting path is less than that for the preceding drying path. When the soil pore system starts drying from the fully saturated condition (θ_s), the relationship between the water content and suction during this drying path gives the initial initial drying curve. When the soil pore system starts to be wetted from its residual volumetric water content (θ_{min}), the corresponding SWRC is called main wetting curve. When the soil pore system starts drying from the maximum water content after saturated process (θ_u), the corresponding SWRC is called main wetting curve. The hydration paths between θ_{min} and θ_u form the scanning curves. The difference between the maximum water content for the initial drying and the main wetting paths most probably is caused by the entrapped air. The definition of hysteresis in the SWRC is illustrated in Fig. 2.5b. The difference in water content between the wetting and drying processes at the same suction level has been studied by Klausner (1991) and recently it was discussed in the excellent work of Lins (2009). The hysteresis in SWRC may be explained as due to:

1. Irregularities in the cross-sections of the void passages or the "ink-bottle" effect,

2. The contact angle being greater in an advancing meniscus than in a receding meniscus,

3. Occluded air, which has a different volume when the soil suction increases or decreases,

4. Thixotropic regain or aging along the wetting and drying history of the soil.

In general, models used to predict hysteretic SWRCs can be classified into two categories (Pham et al., 2005): physically based models (domain models) and empirical models. The popular representatives for the physically based models are the models developed via domain approach. When the behavior of the domain is not a function of the adjacent domains, and the behavior of the particular pore depends only on a range of soil suctions, the domain is called an independent domain. This general basic approach was proposed in a series of works of Everett (Everett and Whitton, 1952; Everett and Smith, 1954; Everett, 1954). After that, the theory of the domain-independent model was employed by Mualem (1974) in his Model II.

The domain approach was latter extended by Topp (1971a,b) to study of silty loam and clayey loam. In these papers, the independent domain theory of hysteresis was modified to takes into account the effect of the surrounding pore blockages against the entry of water or air into the pore, called a dependent domain. Later it was employed by (Mualem and Dagan, 1975) in the Model III, where the domain-dependent approach was simplified and shown to require fewer data for calibration, but at the same time owning better performance, Mualem (1984); Mualem and Beriozkin (2009).

Beside domain models, there are several empirical models for hysteretic SWRCs, such the proposed in Scott et al. (1983); Kool and Parker (1987); Feng and Fredlund (1999); Kawai et al. (2000); Li (2005). For instance, Scott et al. (1983) introduced a simple empirical hysteresis model and showed that this model predicts scanning curves and hysteretic flow processes for different soil types quite well. Kool and Parker (1987) adopted the empirical model of Scott et al. (1983) and the SWRC closed form of van Genuchten (1980) to produce parametric model of relative permeability - water content - capillary pressure relation taking air entrapment into account. The hysteretic SWRC model and the coupled SWRC with the flow law in both experiment and numerical simulations are reviewed in detail in section 8.2.

Recently, several authors attempted to incorporate soil-water hysteresis in the stress-strain behaviour using linear simplified SWRC model Wheeler et al. (2003); François and Laloui (2008). Wheeler et al. (2003) proposed a new elasto-plastic framework for unsaturated soils, suggesting that the degree of saturation has a significant influence on the stress-strain behaviour of an unsaturated soil. According to the authors, the model can
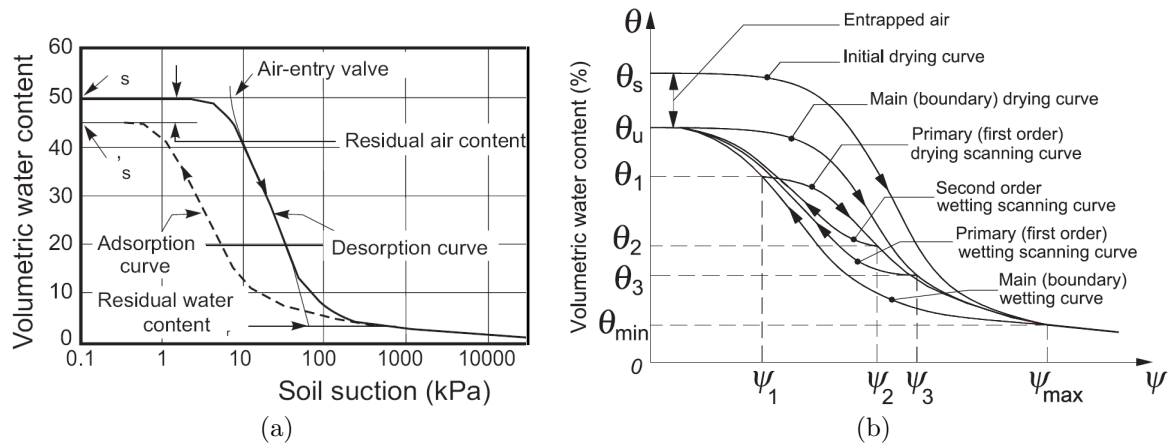
Figure 2.5: (a) Typical SWRC for silty soil, according to Fredlund and Xing (1994), (b) commonly used definitions for hysteretic soil-water hysteresis curves, Pham et al. (2005)

represent properly the transition between saturated and unsaturated types of response, and the irreversible volumetric strain during the drying stages of wetting-drying cycles. Based on the ideas similar to that of Wheeler et al. (2003), François and Laloui (2008) incorporated the simplified SWRC model taking the effects of temperature into account in their thermo-elasto-plastic model for unsaturated soil.

2.3 Modelling the effects of temperature on soil behaviour

Since the 1960s, it was believed that the thermo-mechanical behavior of the skeleton mey be affected by the presence and performance of the adsorbed water (Rosenquist, 1959; Murajama and Shibata, 1966). However, experimental data were insufficient for developing a micro-mechanical, quantitative model of the thermo-deformational behavior of clays or soils in general at that time. The first conceptual model for clay strain responses to heating was created by Campanella and Mitchell (1968). Thermal consolidation has been studied by Derski and Kowalski (1979); Bear and Corapcioglu (1981); Demars and Charles (1982). For instance, Bear and Corapcioglu (1981) proposed a mathematical model to represent the relation of fluid pressure, temperature, ground displacements due to hot water injection into thermo-elastic confined and leaky aquifers. However, no irreversible strains were considered explicitly in these studies. Later, numerical analyses of the thermal con-

solidation around spherical and cylindrical sources (e.g. hot water well) were performed by Booker and Savvidou (1985); Baldi (1987); Baldi et al. (1988); Savvidou and Booker (1989) in an elastic medium. The themo-mechanical model with irreversible strain considered for saturated clay was also proposed by Hueckel et al. (1987); Baldi et al. (1988); Hueckel and Borsetto (1990); Hueckel and Pellegrini (1992), known as elasto-thermo-plastic models. Hueckel's model extended the MCC for thermal effects; the current yield surface is assumed to be a function not only of stress and plastic volumetric strain, but also of temperature difference $\Delta T = T - T_0$ (referred to an environment temperature T_0) as in Fig. 2.6. The yield surface is defined in Eq. 2.23. The elastic volumetric strain is defined in Eq. 2.24 taking non-linear thermal strain into account. This thermal effect is incorporated on two levels: (i) reversible dilation is added to the elastic component of the strain tensor and (ii) a state variable is introduced in order to follow the evaluation of the yield surface with temperature. The model reproduced over-consolidated conditions with thermo-elasticity, while thermoplasticity is used for normally consolidated conditions.

$$f = f\left(p', q, \varepsilon_v^{tp}, \Delta T\right) \tag{2.23}$$

$$\varepsilon_v^e = \frac{\kappa}{1 + e_0} \ln \frac{p'}{p_{ref}} + \alpha\left(\Delta T, p'\right) \Delta T$$

$$\text{where} \quad \alpha\left(\Delta T, p'\right) = \alpha_0 + \alpha_2 \Delta T + \left(\alpha_1 + \alpha_3 \Delta T\right) \Delta T \ln \frac{p'}{p'_{ref}} \tag{2.24}$$

where α_0, α_1, α_2, α_3 are parameters for elastic thermal expansion. ε_v^{tp} is the plastic volumetric strain.

Based on previous studies on clay (Roscoe and Burland, 1968; Alonso et al., 1990) and on thermo-mechanical behaviour (Baldi, 1987; Hueckel and Borsetto, 1990) other researchers proposed a closed form model for over-consolidated soil (Robinet et al., 1996; Cui et al., 2000). Cui et al. (2000) proposed a fully coupled thermo-mechanical model for saturated fined grain soil based on experimental evidence. The typical features of the fine grain soil was discussed, such as: the effect of the high over-consolidation ratio on the volume change of a soil (expansion-contraction) subjected to heating, the slope of compressibility curves independent of temperature, the decrease of pre-consolidation pressure with an increase of temperature and the irreversible thermal volume changes in the normal consolidated sample. Cui et al. (2000) proposed the volumetric plastic mechanisms in the temperature-effective stress plane based on introducing the two yield loci, and one heat-contract curve. A loading yield (LY) locus was similar to Hueckel and Borsetto (1990), adopting the idea of loading collapse curve in Alonso et al. (1990); the curve is defined in Eq. 2.25. A
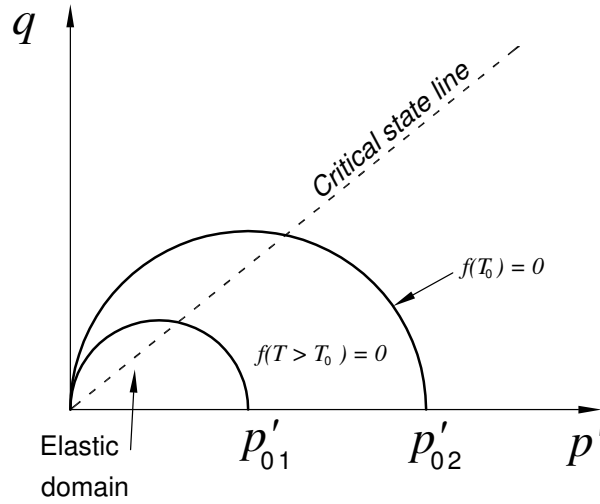
Figure 2.6: Yield surface shrinking due to temperature at elastic state, according to Hueckel and Borsetto (1990).

second locus, a thermal yield (TY) locus, was newly proposed based on experimental results about the reduction of pre-consolidation pressure with an increase in temperature, Eq. 2.26. The expanding-contracting behaviour due to heating was also defined by the (HC) curve, Eq. 2.27. The yield loci in the temperature-effective stress plane is presented in Fig. 2.7.

$$p'_{cT} = p'_{c0} \exp\left(-\alpha_0 \Delta T\right) \tag{2.25}$$

$$T_{cT} = (T_c - T_0) \exp\left(-\beta p'\right) + T_0 \tag{2.26}$$

$$p' = c_1 p'_{c0} \exp\left(c_2 \Delta T\right) \tag{2.27}$$

where β is a model parameter ranging from 0.4 to 800, T_0 is a reference temperature, p'_{c0} is effective pre-consolidation pressure, α_0, c_1 and c_2 are model parameters.

The nuclear waste repository projects have prompted scholars to study the thermal effects on unsaturated soil model in (multi-national) projects, such as FEBEX (Spain), ANDRA (France), SKB (Sweden), NAGRA (Switzerland) and DECOVALEX. Many coupled thermo-mechanical models have been developed from these projects, and several elasto-thermo-plastic models for soil can be listed, such as (Gens, 1995; Cui et al., 2000; Collin et al., 2002; Sánchez et al., 2004; François and Laloui, 2008; Tang and Cui, 2009). For instance, François and Laloui (2008) developed their model based on the generalised effective stress that allows suction to be taken into account in the yield surface as it relates
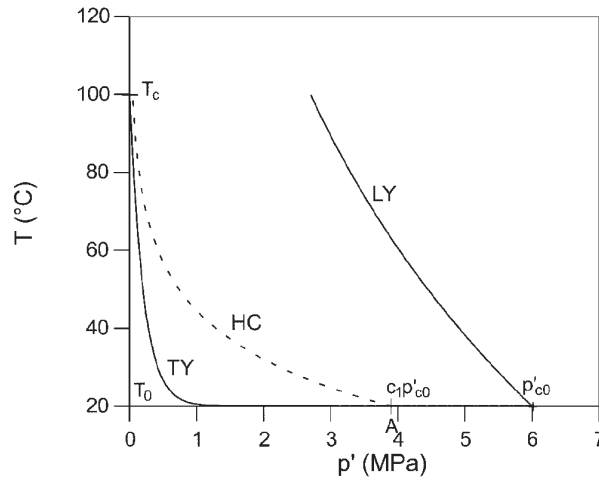
Figure 2.7: Yield loci in the $T - p$ plane. LY is the loading yield; TY is the thermal yield; HC is a contraction due to heating, (Cui et al., 2000).

to temperature, Eq. 2.28 and Fig. 2.8. The pre-consolidation pressure is defined as a function of temperature and suction as in Eq. 2.29.

$$f = f(\boldsymbol{\sigma}'_{ij}, \varepsilon_v^{tp}, T, s) \tag{2.28}$$

$$p'_c = \begin{cases} p'_{c0} \exp\left(\beta\varepsilon_v^p\right)[1 - \gamma_T \log(T/T_0)] & \text{if} \quad s \le s_e \\ p'_{c0} \exp\left(\beta\varepsilon_v^p\right)[1 - \gamma_T \log(T/T_0)](1 + \gamma_s \log s/s_e) & \text{if} \quad s > s_e \end{cases} \tag{2.29}$$

where β, γ_s, and γ_T are model parameters, p'_{c0} is generalised effective pressure at reference temperature T_0 and air-entry value suction s_e.

On the other hand, Gens (1995) proposed his model using net stress and suction as independent stress variables in unsaturated conditions. The thermo-elasto-plastic model adopted the model in Alonso et al. (1990) for unsaturated soil and the thermo-plastic model in Hueckel and Borsetto (1990) as a basis for development. The use of high active clay as a host for radwaste motivated researchers to study the characteristics of such an expansive model. Inheriting the model of Gens (1995), Sánchez et al. (2004) introduced the thermo-elasto-plastic model based on a double structure formulation for expansive clay developed by Alonso et al. (1999). The model can reproduce the behaviour of high expansive soil under non-isothermal conditions. However, Tang and Cui (2009) proposed a new constitutive model to describe thermo-mechanical volume change behaviour of compacted expansive clays. Their model was based on the model proposed by Alonso et al. (1999) for the hydromechanical behaviour of compacted unsaturated expansive
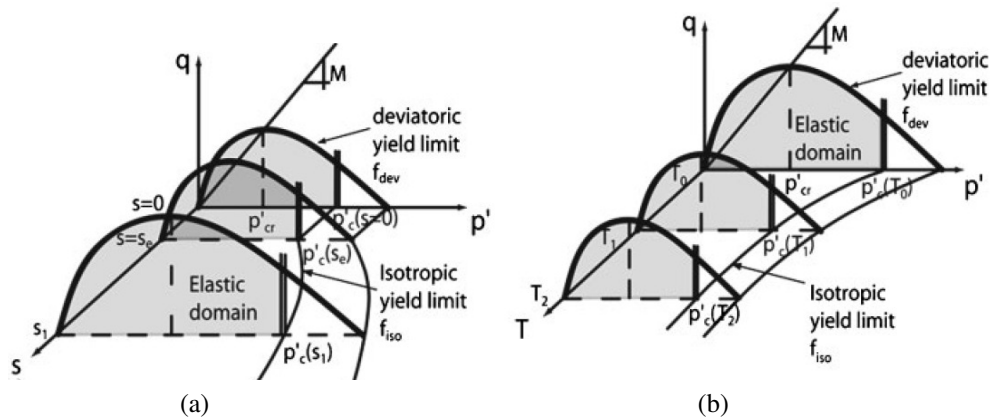
Figure 2.8: Effect of (a) suction and (b) temperature on the shape of coupled mechanical yield limits, (François and Laloui, 2008).

clays, and the model proposed by Cui et al. (2000) for the thermo-mechanical behaviour of saturated clays. The model performed the main volume change behaviour observed in experiments: swelling under wetting at low stress and non-isothermal conditions, elastic thermal expansion and plastic thermal contraction under various suctions and stresses.

Paralleling with the research groups in Barcelona, Spain; Lausanne, Switzerland; and Paris, France the group in Liège, Belgium has developed a model using their own code. Based on the previous study of Charlier and Radu (1997), Collin et al. (2002) proposed a thermo-hydro-mechanical model for unsaturated soil considering Alonso-Gens' model (Alonso et al., 1990) as a basis for development. The model used two independent stress variables to model the mechanical behaviour of unsaturated soils. The temperature effects in stress-strain relations was introduced simply as elastic thermal dilatation in this model. Subsequently Wu et al. (2004) enhanced their code by replacing fully coupled THM behaviour for mechanical behaviour. The model considered thermal softening in the load collapse curve and the thermal yield curve for over-consolidation pressure in the stress-strain relation. The interesting point in this model as compared with Cui et al. (2000) was that the slope of compressibility in normal consolidation state was temperature-dependent.

It is necessary to mention to the work conducted in Cardiff, UK for the attempt to enhance the constitutive mechanical model based on the previous works of the effects of temperature on unsaturated soil. Thomas and He (1995) extended the previous works for thermal stress-strain behaviour of unsaturated soil in their numerical simulation. The model was enhanced in their later works (Thomas et al., 2003, 2009).

When considering the effect of temperature on the unsaturated soil mechanics, one must

take the effect of temperature on SWRC into account because most of the current unsat-urated models are coupled hydro-mechanical models. Temperature effects on the suction in both categories include osmotic suction and matric suction. Capillary pressure is sur-face tension dependent on water purity, the change of temperature influences the surface tension, thus effects on the matric suction. The effect of temperature on the SWRC is characterised in terms of matric suction by Hopmans and Dane (1986); Nimmo and Miller (1986). In terms of osmotic suction, the increase in temperature of bentonite decreases the hydration force due to a reduction in the number of hydrates in the smectite surface within bentonite and increases the osmotic pressure in the molecular system (Pusch and Yong, 2003; Arifin and Schanz, 2009). The SWRC model taking temperature into account was proposed by the authors such as Liu and Dane (1993); Bachmann et al. (2002); Grant and Salehzadeh (1996); Grant (2003). For instance, capillary pressure can be expressed as a function of surface tension (Grant and Salehzadeh, 1996):

$$\psi = \frac{2\sigma^{gl} \cos \gamma}{r} \tag{2.30}$$

where ψ (Pa) is capillary pressure, σ^{gl} (Nm^{-1}) is surface tension, γ (°) is the contact angle, and r is the average radius of the liquid-gas interface. σ^{gl} is temperature-dependent and empirically calculated as the linear function of temperature (Eq. 2.31) in a range of temperatures (-10 to 50°C). The dependence of capillary pressure on temperature can be a separation of variables and the integration of Eq. 2.30 leads to an expression in Eq. 2.32.

$$\sigma^{gl} = a + bT \tag{2.31}$$

$$\psi(\theta, T) = \psi(\theta) \frac{\beta_\theta + T}{\beta_\theta + T_0} \tag{2.32}$$

where $a = 0.11766 \pm 0.00045$ (Nm^{-1}) and $b = -1.535 10^4 \pm 1.5 10^6$ for water air surface, T_0 is the reference temperature, $\beta_\theta = a/b$, $\psi(\theta, T)$ is the capillary pressure function related to suction and temperature.

Soil water retention curves can be expressed as a function of temperature, e.g. by using the van Genuchten equation (van Genuchten, 1980), and the SWRC is expressed as follows:

$$\theta(\psi, T) = \theta_r + \frac{\theta_s - \theta_r}{(1 + [\alpha\psi(T)]^n)^m} \tag{2.33}$$

where θ_s θ_r are saturated volumetric water content and reference volumetric water content, m and n are empirical fitting model parameters. The effect of temperature on matric suction was subsequently adopted in a similar form by Wu et al. (2004) in numerical

simulations. In their paper the SWRC is expressed as based on the Fredlund and Xiang model (Fredlund et al., 1994b).

Total suction is introduced in two terms: matric suction and osmotic suction. The effect of temperature in the soil water retention curve is so far analysed in its effects on matric/capillary pressure addressed to the reduction of surface tension with the increase of temperature. The effect of temperature on osmotic suction has been observed in experiments conducted by Villar and Lloret (2004); Villar and Gómez-Espina (2007). The experiments showed the suction significantly attenuated between 20°C and 80°C at the same water content and the lower water content, the higher the difference in suction is. The physical model of the temperature effect on soil osmotic suction has not been discussed and analysed, it can be a motivation for future work.

Effects of temperature on soil permeability have also been considered in previous studies. Pusch (1980a) observed an increase in the coefficient of permeability of bentonite MX-80 and Ca-bentonite according to Darcy's law (Erbslöh) when the temperature changed from 20°C to 70°C at a low hydraulic gradient. The effect of temperature was modelled using statistical methods as in Eq. 7.2.

$$k \propto \frac{f(T)}{t + t_0} \tag{2.34}$$

where k is coefficient of permeability (e.g. m/s), $f(T)$ is temperature function, and it is assumed as $f(T) = T^n \, \forall \, n > 1$, t and t_0 are times corresponding to the creep phenomenon. However Delage et al. (2009) reported that intrinsic permeability changed insignificantly in the temperature range between 20 °C and 90 °C. The effect of temperature on the permeability of unsaturated soil was quantified in Romero Morales (1999) and adopted in Wu et al. (2004) as in

$$k(e, w, T) = k_0(1 + \mu_T(T - T_0))10^{ae} \left(\frac{w - w_0}{e/G_s - w_0} \right)^\lambda \tag{2.35}$$

where e/G_s is the saturated water content, w and w_0 refer to the water content, μ_T is the empirical coefficient fitting of relative viscosity, and a is the model parameters.

In summary, the effects of temperature soil behaviour have been characterised in their effect on stress-strain behaviour and their effect on soil water transport in both saturated and unsaturated soil. Many attempts have been made to develop a thermo-elasto-plastic model for stress-strain relation considering effects of temperature. Some studies only described temperature inducing non-linear elastic behaviour; others attempted to describe the irreversible stress-train behaviour induced by temperature. The effect on soil water

transport was described in terms of soil-water retention curve and soil permeability. These effects on both saturated and unsaturated soil have been discussed as well as modelled in previous research.

2.4 Numerical simulation of fully coupled thermo-hydro-mechanical behaviour

Geotechnical problems involved in variation of temperature are a great motivation for studying coupled THM behaviour: heat storage (Burger et al., 1985), hot water wells (Baldi, 1987), nuclear waste disposal (IAEA, 1992; Gens et al., 1998; Karnland et al., 2000) are only a few examples. For instance, Fig. 2.9 is an example for the in-situ test model of the buffer material in nuclear waste repositories (FEBEX project). The data collected from these tests need to be understood and analysed by mathematical models. Coupled THM models have been created and utilised for this purpose. The experimental data and numerical simulation results are mutually verified and validated against each other by simulating the experimental process. With the advances in new computer generations, experimental techniques, and elasto-thermo-plastic models for soil, the numerical simulations with coupled THM behaviour have been more interesting in recent years.

In order to numerically simulate the behaviour of soil in saturated and unsaturated conditions, the physical phenomena occurring in a geotechnical environment must be classified and characterised. The phenomena in coupled THM models are stress-strain behaviour, liquid and gas flow, vapour transport, and heat transfer. The key aspect, also the most complicated part of coupled THM simulation, is the mechanical stress-strain models (e.g. elasto-thermo-plastic model). These models are introduced in section 2.3. Liquid advective flow is modelled based mainly on two interacting continua: one stands for liquid flow and the other for gas flow. Darcy's law or generalised Darcy's law has been popularly utilised for flow law. For behaviour relating to temperature, heat transfer consists of thermal conductivity (e.g. Fourier's law) in each phase and soil component. Vapour transport model is based on two processes: diffusion due to the vapour density gradient and advective flow due to the bulk flow of gas. For instance, vapour diffusion due to heat is based on Fick's law. The mutual relation in coupled models may be that thermal induced vapor diffusion and the dependence of water viscosity on temperature also significantly affect the water transfer process. On the other hand, the changes in hydraulic conditions influence

the temperature field via variations in thermal conductivity and affect the stress-strain field due to pore water pressure and pore gas pressure changes. These above interactions has to be analysed in the fully coupled frameworks, when numerical simulating for the boundary value problems.

Based on the thermo-elastic models and thermo-elasto-plastic model reviewed in the previous section, researchers perform many numerical simulations in finite element code in order to numerically simulate the behaviour of unsaturated soil in-situ tests and mock-up tests. Several finite element programs have been developed for the numerical simulations of coupled THM behaviour in unsaturated soil: CODE_BRIGHT (Olivella et al., 1996b), ACMEG-TS (François and Laloui, 2008), UNSAT-H (Fayer, 2000), LAGAMINE (Charlier, 1987), COMPASS (Thomas and He, 1995), and RockFlow (Xie et al., 2006). A multi-national project has been setup to validate the mathematical models of coupled THM processes to safely analyse radioactive waste repositories, called DECOVALEX (Jing et al., 1995).

Many numerical simulations for the experiments and geotechnical phenomena have been carried out using these softwares, particularly for the buffer area in in-situ tests, for the laboratory mock-up tests, and for the radioactive waste site. Several milestone papers have been written on various applications of fully coupled THM simulation in case studies. For instance, Kanno et al. (1999) used a fully coupled THM analysis in finite element code to simulate full-scale coupled tests - a BIG-BEN experiment. An isotropic linear elastic material was adopted to reproduce the mechanical behaviour of the buffer area. Collin et al. (2002) presented numerical simulations with coupling heat, moisture (liquid water and water vapour) and air transfer in deformable unsaturated soil for a mock-up test in the laboratory. The elasto-plastic model of Alonso et al. (1990) was adopted for stress-strain behaviour. The temperature effect was characterised in terms of thermal-elastic behaviour. In addition Gens et al. (1998) presented a numerical simulation for an in-situ experiment in FEBEX project. The simulation adopted thermo-elasto-plastic model developed in Alonso et al. (1990); Gens (1995) as a mechanical behaviour for bentonite. The paper also discussed the interaction between buffer material and granite host rock. Wu et al. (2004) presented the numerical simulation for a benchmark cell test. The fully coupled THM analysis for unsaturated soil was developed based on the stress-strain relation of Alonso-Gens' model. The study took the temperature effect on SWRC and soil permeability into account.

The other researchers used their FE codes to validate experimental data and other codes. Xie et al. (2006) performed a numerical simulation for a benchmark experiment based on

Computer model of
the HLW concept
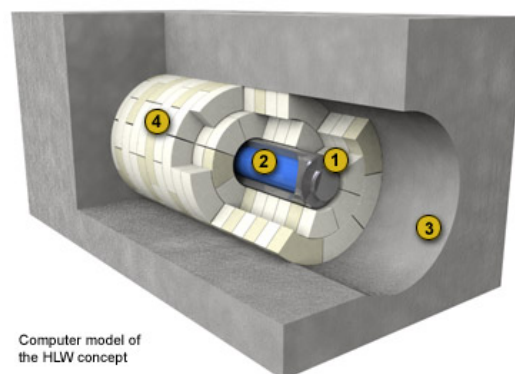
Figure 2.9: A typical High Level Waste (HLW) or Spent Fuel (SF) disposal concept in-
cludes steel canisters (1) containing waste (2) placed in horizontal drifts (3),
surrounded by a clay barrier made up of blocks (4) manufactured from high-
density compacted bentonite and situated deep within crystalline rock, Full-
scale Engineered Barriers Experiment (FEBEX) I.

their THM model and their code (GeoSys/RockFlow). The paper concentrated on the
mass transfer due to the effect of temperature. Rutqvist et al. (2001) used four computer
codes in the DECOVALEX project to predict coupled THM response in an in-situ heating
test, which simulates a nuclear waste deposition hole with a radwaste container and
bentonite buffer surrounded by fractured rock. Nguyen-Tuan et al. (2009) presented a
numerical simulation using coupled THM analysis for a column-type experiment. The
study adopted Gens (1995)'s constitutive model for numerical simulation (BBM-TEP
model). The THM parameters were also identified based on the back analysis approach
in this study.

In summary, many efforts have been made to adopt mathematical coupled models into
finite element numerical simulations of buffer problems. The models attempted to re-
produced the physical phenomena, such as the stress-strain behaviour, liquid and gas
flow, SWRC, vapour transport, and heat transfer. One key focus included integrating
the complicated stress-strain behaviour of unsaturated soils under temperature effects
into coupled THM analysis. However the attempts to understand the model parame-
ters as well as the reliability of the model and parameters should be studied further by
geotechnical engineers.

2.5 From Cam Clay model to BBM Thermo-elasto-plastic model

The thermo-elasto-platic (TEP) model is a selected model to numerically simulate the stress-strain relation in THM boundary value problems. The model is based on the BBM model; thus it is called BBM-TEP model. Therefore, this section will attempt to give a general view on how the primitive model evolved to the modern BBM-TEP model. Originally, an elasto-plastic constitutive model for soil was proposed by researchers at Cambridge University. The original Cam-Clay model was proposed by Roscoe et al. (1958, 1963) (CC) and the Modified Cam-Clay (MCC) model was proposed by Burland (1965a); Roscoe and Burland (1968). These models were derived from the energy concept, in which the total energy per unit volume of soil is assumed to consist of the internal energy (elastic energy) and the dissipated energy (plastic energy).

Roscoe et al. (1963) assumed that the work increment is a function of dissipated energy as in Eq. 2.36. It means the energy dissipated not only at the critical state, but also during the whole process of shearing, from the initial state to the critical state. The description of the dissipated energy appears not to take account of the plastic volume strain during the shearing process prior to the critical state. With this assumption the yield function is written as in Eq. 2.38. Burland (1965a) criticised this point. Roscoe and Burland (1968) proposed a new equation which includes the plastic volumetric strain directly in the dissipated energy (Eq. 2.37). Therefore the dissipated energy includes the plastic shearing strain and plastic volumetric strain during the shear process. Consequently the yield function is written as Eq. 2.39. The yield functions are illustrated in Fig. 2.10 in the $p - q$ plane and co-operated with the volume change.

$$dW = Mp'\mathrm{d}\varepsilon_s^p \tag{2.36}$$

$$dW = p'\sqrt{(\mathrm{d}\varepsilon_v^p)^2 + (M\mathrm{d}\varepsilon_s^p)^2} \tag{2.37}$$

$$f(p', q) = q + Mp'\ln\left(\frac{p'}{p_o'}\right) = 0 \tag{2.38}$$

$$f(p', q) = \frac{q^2}{p'^2} + M^2\left(1 - \frac{p_o'}{p'}\right) = 0 \tag{2.39}$$

The other new ingredient of the CC and MCC model is the plastic potential with hardening and softening rules. If yielding occurs to the right of the point at which the CSL intersects
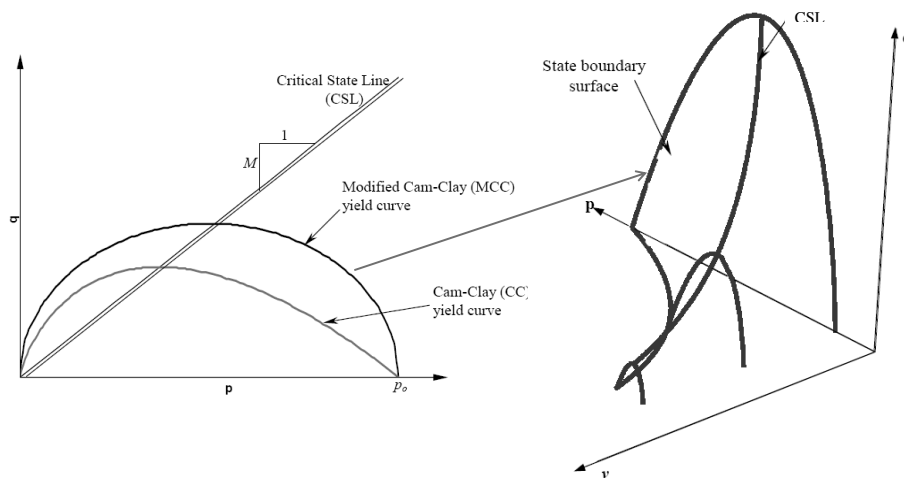
Figure 2.10: Yield function of Cam Clay and Modified Cam Clay

the yield surface, hardening behaviour is exhibited, accompanied by compression. It is also called the wet or subcritical side. If yielding occurs to the left of the intersection of the CSL and yield surface, the soil material exhibits softening behaviour, which is accompanied by dilatancy. It is also called the dry or supercritical side. CC and MCC models have some limitations, which were pointed out by other authors as follows:

- The critical state concept has been much less successful for modelling granular materials Nova and Wood (1979); Gens and Potts (1988).

- The critical state soil model assumed an associated flow rule and was unable to predict an important feature of behavior that observed in undrained test on loose sand and normal consolidated undisturbed clays. That peak in deviatoric stress occurred before the critical state (Bishop, 1972; Sladen et al., 1985).

- Yield surfaces adopted in many critical state models significantly overestimate failure stress on the dry side. To overcome this limitation the Hvorslev surface (Hvorslev, 1937) can be used. But the discontinuity in the yield surface may cause significant numerical difficulties Gens and Potts (1988).

In attempt to reach the integrated framework incorporating both volumetric and shear behaviour of unsaturated soil, Alonso et al. (1987) proposed an elasto-plastic model for unsaturated soil. This primary framework was initially presented in qualitative way rather than completely mathematically.

Alonso et al. (1990) proposed a fully developed mathematical formulation based on one modified from the MCC model taking the suction of yield surface into account. The model
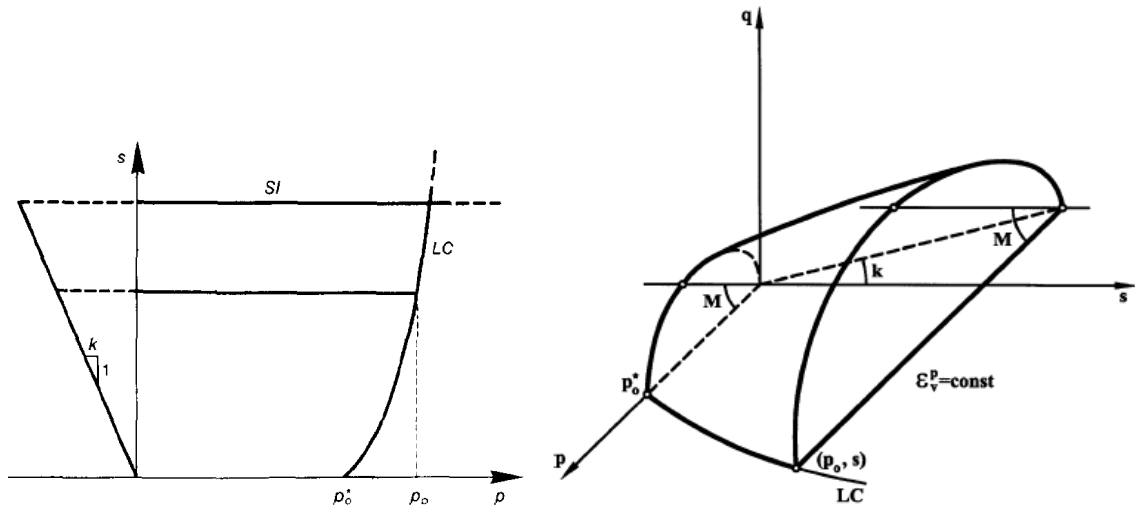
Figure 2.11: Alonso et al. (1990)– Three-dimensional view of yield surface in $(p - q - s)$
stress space

is one of the first elasto-plastic models designed explicitly for describing the mechanical behaviour of partially saturated soil. The model adopted net stress $(\sigma_{ij} - u_a \delta_{ij})$ and suction $(s = u_a - u_w)$ as fundamental variables. The model is known as the Barcelona Basic Model (BBM) and can be summarised in Fig. 2.11 where the three-dimensional yield surface in $p - q - s$ space is described. The surface is formulated by the equation 2.40. In saturated conditions $(s = 0)$, the yield surface corresponds to the MCC ellipse and the size of the elastic domain increases as the suction increases. The rate of increase, represented by the loading-collapse (LC) curve, is one of the fundamental characteristics of the model.

$$f(p^{net}, q, s) = q^2 - M^2(p^{net} + p_s)(p_0 - p^{net}) = 0 \tag{2.40}$$

where:

$$p_s = k\, s \tag{2.41}$$

$$p_0 = p^c \left(\frac{p_0^*}{p^c}\right)^{\frac{\lambda(0)-\kappa}{\lambda(s)-\kappa}} \quad \text{with:} \quad \lambda(s) = \lambda(0)[(1-r)\exp(-\beta s) + r] \tag{2.42}$$

where p_0 and p_0^* refer to the pre-consolidation pressure at suction s and in saturated conditions, respectively. p^{net} is a mean net stress. The BBM model has some limitations which have been pointed out by other authors:

- Alonso et al. (1990) assumed that $\lambda(s)$ decreases with an increase in suction so the parameter r must be smaller than one in Eq. 2.42. However, Wheeler and Karube (1996)'s experimental results with other soils showed the normal compression line where $\lambda(s)$ increases along with the increase in suction or $r > 1$

- Eq. 2.42 showed that the LC yielding curve is a vertically straight line on the $s - p$ plane when $p_c = p_0^*$ and the yielding curve becomes increasingly inclined as it expands, as assumed by Alonso et al. (1990). But when $p_c > p_0^*$, the yielding curves are illogical. Therefore, the values selected for soil parameter p_c should be smaller than pre-consolidation consolidation stress.

- A non-convexity may cause problems in mathematical convergence (e.g. when using the Newton Raphson method). In the BBM model, the non-convexity of the lower path of LC yielding curve for particular combination of r and p_0^* is of concern. One key step involves checking the range of values of $\frac{p_0^*}{p^c}$ to guarantee that non-convexity does not occur (Wheeler et al., 2002).

- Alonso et al. (1990) stated that critical state line slope (M) is suction independent. But the experiment results showed that the M might vary with suction, (Wheeler and Sivakumar, 1995; Geiser et al., 1997).

- The assumption that the change of specific volume with suction at pre-consolidation pressure (p_0^*) is equal to the change in specific volume at the reference pressure (p^c) has no experimental evidence.

In brief, Alonso et al. (1990) proposed a non-associated flow rule which correlates to the K_0 value in saturated soil and tended to an associated flow rule at critical states. Nine model parameters required in the BBM are $\kappa, \kappa_s, G, \lambda(0), \beta, r, p_c, M, k$. The current soil state is determined by the values of p, q, s and v. The BBM is able to reproduce the response of unsaturated soil under simple loading-unloading and drying-wetting processes. These phenomena include: an increase of shearing strength and pre-consolidation pressure with changing suction; the development of reversible swelling strains when suction decreases at low confining stress; the phenomenon of irreversible collapse strains when the suction decreases at high confining stress; and irreversible shrinkage when the suction exceeds the virgin state.

Based on the research of Baldi et al. (1988); Hueckel and Borsetto (1990); Hueckel and Pellegrini (1992), which pioneered research on saturated soil with temperature effect and Alonso et al. (1990) and on unsaturated soil, Gens (1995) drew the constitutive model under the thermo-elasto-plastic theory for unsaturated soil (BBM-TEP). Using the BBM

model for isothermal conditions, Gens (1995) enhanced the BBM-TEP model to reproduce stress-strain behaviour under non-isothermal conditions based on the basis of thermo-plastic model for saturated soil. In the new version the yield surface considered net mean stress, suction and temperature difference in its formula, Eq. 2.43. The elastic volumetric strain was described similarly to Eq. 2.24 in Hueckel and Pellegrini (1992), plus volumetric elastic strain induced by suction.

$$f = f\left(p^{net}, q, \varepsilon_v^{tp}, s, \Delta T\right) \tag{2.43}$$

$$\varepsilon_v^e = \frac{\kappa}{1+e} \ln \frac{p^{net}}{p_{ref}} + \frac{\kappa_s}{1+e} \ln \left(\frac{s + p_{at}}{s_{ref} + p_{at}}\right) + \alpha\left(\Delta T, p'\right) \Delta T \tag{2.44}$$

where p^{net} is mean net stress, ε_v^{tp} is the volumetric plastic strain considering temperature, s_{ref} is the suction in reference to pressure.

The yield surface was described similar to Eq. 2.40 and 2.42 Alonso et al. (1990), in which p_0^* and p^s are assumed as a function of temperature as in Eq. 2.45.

$$p_0^*(T) = p_0^* + 2(a_1 \Delta T + a_2 \Delta T |\Delta T|)$$
$$p_s(T) = k(1 - f_s(\Delta T))s \tag{2.45}$$

where $f_s(\Delta T)$ is a function which takes into account the variation of strength due to temperature changes.

As the other elasto-plastic models, the hardening depends on only plastic volumetric strain. In Gens (1995) the hardening equation considered elastic volumetric strain to be a function of temperature as follows:

$$\mathrm{d}p_o^* = \frac{1+e}{\lambda(0) - \kappa_T} p_o^* \, \mathrm{d}\varepsilon_v^p \tag{2.46}$$

where

$$\kappa_T = \left[\frac{\kappa_i}{1+e} + (\alpha_1 + \alpha_3 \Delta T)\Delta T\right](1+e) \tag{2.47}$$

where κ_i is a slope of elastic volumetric strain at the initial state of reference void ratio (e_0).

The model proposed by Gens (1995) can reproduce two separate effects: (1) an increase in temperature induces a reduction in the yield surface by reducing the p_c value, (2) in contrast, an increase in suction induces an increase in the yield surface. The BBM-TEP model has been applied in the finite element code (CODE_BRIGHT) to analyse multi-physical phenomena as the coupled thermo-hydro-mechanical behaviour of unsaturated

soil (Gens et al., 1998; Gens and Olivella, 2001). Latter, Sánchez et al. (2004) enhanced the BBM-TEP model using double structure theory of Alonso et al. (1999) for expansive soil to analyse THM behaviour in radwaste buffer materials.

In summary, the BBM-TEP constitutive model for unsaturated soil under the temperature effects has undergone a long developmental process. Starting from the elasto-plastic model for saturated soil behaviour, it was enhanced for unsaturated soil behaviour by Alonso and his colleagues and later became the well-known BBM model. Later it took into account temperature effects and was called the BBM-TEP model. The model was adopted by many researchers in numerical simulations of multi-physical coupled THM behaviour for radwaste buffer materials. The model demonstrated its capacity to reproduce many aspects of unsaturated soil mechanics under non-isothermal conditions. However because of its capabilities, the model is complicated and includes many parameters. It is necessary to validate its feasibility and effectivity with experiments and to identify the model parameters.

3 Back analysis for geotechnical problems: literature review

3.1 General remarks on back analysis

In the geotechnical engineering, observation and measurement data are treated differently, and measurement data may be used as evidence for mathematical models. The developing models are validated/evalueated by qualitative and quantitative corroboration with other observations or measurements at other conditions. The evaluated models are applied for simulating and comparing the observed data from different boundary value problems, and the results may be retroactively used to calibrate these models, see Fig. 3.1. The figure illustrates the process of modelling from model development, model evaluation to model application using independent data sets. Back analysis denotes this chain of modelling as a link between observations and measurements on the one hand and mathematical modelling on the other. Back analysis estimates model parameters based on observation data and on other information. It has become increasingly popular in geotechnical engineering research in recent years. Few literature review works discuss inverse analysis in geotechnical problems. There are several aspects of back analysis: uncertainty and sensitivity analysis, optimisation algorithms, and reliability analysis. Since the 1980s, back analysis has been applied to estimate model parameters based on the data from in-situ measurements (Gioda and Maier, 1980; Cividini et al., 1981, 1983; Gioda and Sakurai, 1987).

Back analysis can be classified in several ways. Generally accepted opinion, Cividini et al. (1981) adopted Gioda and Sakurai (1987)'s classification using the concept of inverse and direct approaches. In the inverse method the equation governing geotechnical problems were rewritten in such way that some of the quantities of data regarding known reality (i.e. model parameters) appeared as sets of unknowns. On the contrary, the model response quantities which are derived from measurements appeared as input components in the equations. On the other hand, the direct approach uses the forward numerical model for
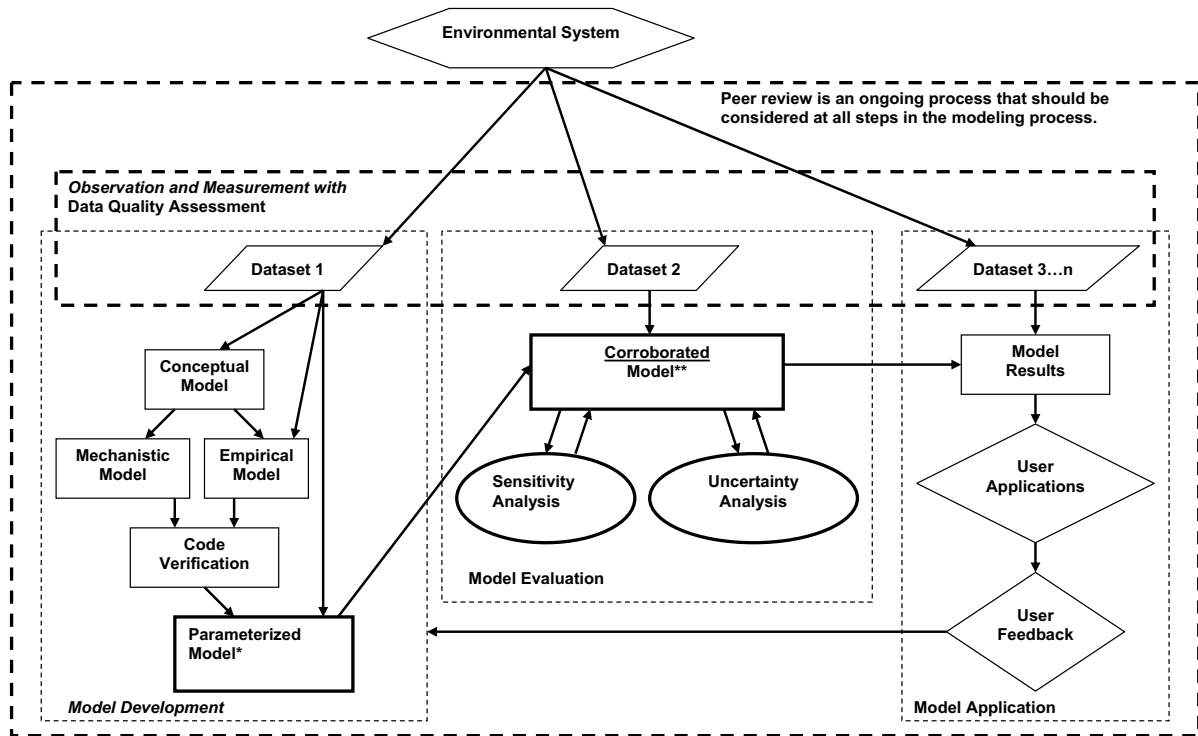
Figure 3.1: The modeling process, Gaber et al. (2009).

computing iteratively in a prescribed procedure. This procedure enables trial values of model parameters to be designed and establishes an estimation of the difference between measured results and corresponding numerical results by a "norm" defining objective function. Minimising the objective function is known as optimisation.

The back analysis methods were classified by Neuman (1973) as the direct methods and the indirect methods. This classification was employed afterwards by Honjo et al. (1994a). In the direct method, a unique relationship between field measured values (e.g. load distribution) and model parameter values (e.g. stiffness) may be initially derived preferably in the form of linear simultaneous equations. Then the model parameter values are estimated directly by inverting this relationship. For the indirect method, the criterion used in this approach is generally the minimisation of the "norm" of the difference between observed and calculated field values at specified observation points. The indirect approach is rather flexible to include more advanced statistical concepts into the inverse analysis. However, the process of minimising the objective function usually has to account for difficulties when dealing with non-monotonic and even non-convex problems. Based on the above-mentioned analysis, the terminologies in this study are adopted from Honjo et al. (1994a).

Regarding direct inverse approach, many was contributed by Japanese scholars. The works of Sakurai and Takeuchi (1983) can be considered as a standard numerical technique to estimate in-situ stress using convergence measurements in a tunnel. The method derives a linear relationship between the displacement at observation points and the normalised initial stress based on the finite element formulation of the stress analysis. Other direct inverse analysis was conducted by Asaoka (1978); Asaoka and Matsuo (1980, 1984) for a consolidation of soft clay. The essential idea of this method is to apply auto-regressive models to the consolidation problem. For this purpose, an ordinary differential equation is derived whose solution demonstrates the same settlement characteristics as typical one-dimensional consolidation, and prediction procedures are introduced based on the ideas of auto-regressive forecasting.

Regarding the indirect inverse approach, it has become more popular in recent years due to its advantage against direct approach. The advantage of this method is that there is no need to modify the physical model for inverse analysis; any model can be used as a subsystem in the inverse analysis procedure. The main in this approach is the formulation of the objective functions and the algorithm routines for optimisation. Several authors highlight this approach as a way to solve geotechnical problem of parameter identification, including (Neuman and Yakowitz, 1979; Maier and Gioda, 1981; Cividini et al., 1983; Tarantola, 1984; Honjo et al., 1994a; Ledesma et al., 1996a; Pichler et al., 2003; Schanz et al., 2011b). Subclassifying the method by conforming to objective functions and optimisation routines is presented in section 3.3.

Recently, back analysis for geotechnical problems is not only applied to identify the model parameters but also to assess the model parameters or capacities of the designed model, (Schanz et al., 2011b). Back analysis may involve a group of serial/parallel works such as sensitivity analysis, optimisation, reliability analysis. Sensitivity analysis (SA) is primarily the study of how the variation (or uncertainty) in the output of a model can be attributed to variation/uncertainty in the model input. It is a technique for systematically changing input factors in a model to determine the effects of such changes in the output responses. Several contributions towards the study of SA may be considered, such as (Helton, 1993; Sobol', 2001; Saltelli et al., 2004; Campolongo et al., 2000; Saltelli et al., 2008), among others. The review of SA will be discussed in section 3.2. One of the applications of back analysis is reliability analysis (RA) which involves measurement data as well as output of the numerical simulations. Research on reliability has been conducted by Meeker and Escobar (1998); Cawlfield (2000). According to Meeker and Escobar (1998), the general classes of reliability estimates are inter-rater reliability, test-retest reliability,
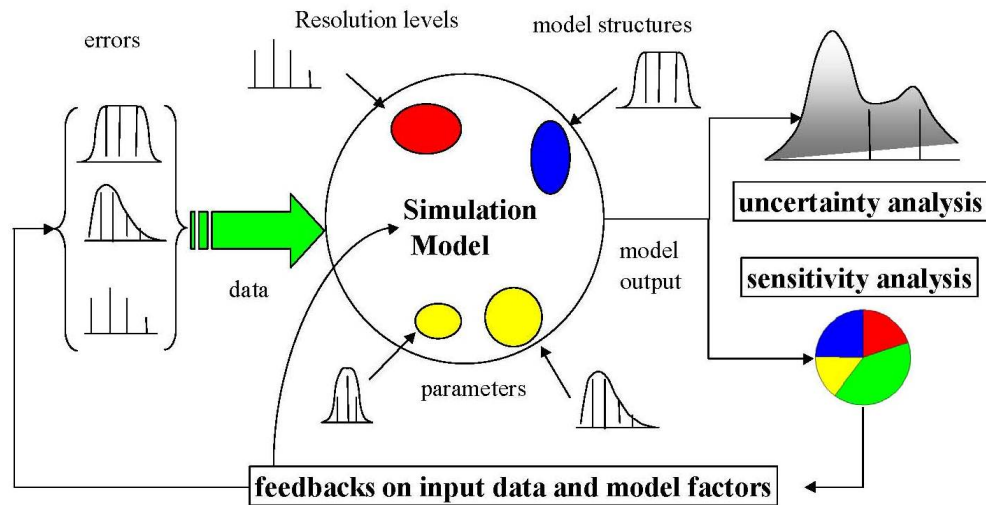
Figure 3.2: Ideal scheme of a possibly sampling-based sensitivity analysis, after Saltelli
          et al. (1999).

inter-method reliability, and internal consistency reliability. The review of RA is discussed
in section 3.4.

3.2 Uncertainty and sensitivity analyses

Sensitivity analysis according to Morgan and Henrion (1990) is a computation of the effect
of changes in input factors on the output. Input factor means any quantity that can be
changed in the model prior to its execution. This can be a model parameter, an input
variable or a model scenario. According to Saltelli et al. (2004) SA is a study of how the
uncertainty in the output of a model (numerical or otherwise) can be apportioned to dif-
ferent sources of uncertainty in the model input. Appropriate sensitivity analysis should
be done as follows: to conduct the analyses over the full range of plausible values of key
parameters and their interactions and to assess the impact of change in key parameters to
the changes in response (European-Commission, 2002). Sensitivity analysis has been ap-
plied for many fields of science (e.g. economics, social sciences and physics). Uncertainty
arising from different sources - errors in the data, parameter estimation procedure and
alternative model structures - is propagated through the model for uncertainty analysis
and their relative importance is quantified via sensitivity analysis, see Fig. 3.2. In this
section, the author reviews sensitivity and uncertainty analysis from the point of view of
geotechnical engineering.

There are several classifications of sensitivity analysis methods. The sensitivity analysis methods can be classified and named depending on the way for sampling of input factors and for analysing the model responses. According to Gaber et al. (2009), several methods may be considered: the screening method, Morris's one-at-a-time method, differential analysis, Monte Carlo analysis and the variance-based method. According to Saltelli et al. (2000), several possible procedures can be utilised to perform uncertainty and sensitivity analysis, such as local methods, sampling-based analyses, methods based on emulators (e.g. Bayesian's based), screening methods, variance based methods and methods based on Monte Carlo filtering. There are also other methods of sensitivity analysis mentioned in Hamby (1995); Frey and Patil (2002); Ascough II et al. (2005). In this section, some concepts of the applicable and popular methods of sensitivity analysis are summarised as follows:

- **Monte Carlo analysis**

  Monte Carlo (MC) analysis is based on performing multiple evaluations with randomly selected model input, and then using the results of these evaluations to determine both uncertainty in model predictions and apportion the input factors' contribution to this uncertainty. MC analysis involves selecting ranges and distributions for each input factor, generating a sample from the ranges and distributions specified in the first step, and evaluating the model for each element of the sample. In addition, uncertainty analysis and sensitivity analysis must be conducted.

  Various sampling procedures are used in MC studies, for example random sampling, stratified sampling (e.g. latin hypercube sampling and quasi-random sampling). The authors who apply MC in their research include (Hornberger and Spear, 1981; Helton and Davis, 2000; Sobol', 2001; Dimov and Georgieva, 2010), particularly in geotechnical applications (Helton, 1993).

- **Response surface methodology**

  This procedure is based on the development of a response surface approximation to the model under consideration. This approximation is then used as a surrogate model for the original model in uncertainty and sensitivity analysis.

  The analysis involves the selection of ranges and distributions for each input factor, the development of an experimental design defining the combinations of factor values on which to evaluate the model, evaluations of the model, the construction of a response surface approximation to the original model, uncertainty analysis and sensitivity analysis (Myers and Montgomery, 1995).

Sensitivity measures for the input factors are derived from the constructed response surface. This surface plays the same role in a response surface methodology as the Taylor series in differential analysis Sobol' (2001).

- **Screening designs**

  Factor screening may be useful initially when dealing with a model containing a large number of input factors (hundreds). Often, only a few of the input factors and groupings of factors have a significant effect on the model output. Screening experiments are used to identify the subset of factors that controls most of the output variability with a relatively low computational effort. As a drawback, these economical methods tend to provide qualitative sensitivity measures, i.e. they rank the input factors in order of importance, but do not quantify to what extent a given factor is more important than another. The authors developed and used this method include Welch et al. (1992); Campolongo et al. (2000, 2007) and (Saltelli and Tarantola, 2002) applied this method to geotechnical engineering.

  Typical screening designs include the one-at-a-time (OAT) experimental technique, in which the impact of changing the values of each of the chosen factors is evaluated in turn. Although simple, easy to implement, and computationally cheap, the OAT technique is limited insofar as interactions among factors cannot be estimated, and it usually provides a sensitivity measure that is local (around a given point of the input space). Morris (1991) proposed an extension of the OAT design technique, which does not depend on the choice of the specific point in the input space.

  Alternative approaches to the problem of screening are the Cotter design, the Iterated Fractional Factorial Designs (IFFDs) introduced by Andres and Hajas (1993), the "sequential bifurcation" method proposed by Bettonvil and Kleijnen (1997); and the method proposed by Morris, which covers the whole input factor space while still being an OAT experiment.

- **Variance based methods**

  These methods decompose the unconditional variance $V(Y)$ of output response Y into terms due to individual factors plus terms due to interaction among factors. Full variance decompositions are only meaningful when the input factors are independent of one another. Variance-based methods for sensitivity analysis were first employed by (Cukier et al., 1973). The method, known as FAST (Fourier Amplitude Sensitivity Test), was quite effective; however, it has limited success among practitioners because of the difficulty in encoding. The method did not allow the computation of higher-order sensitivity indices, although this was made possible

much later by extensions developed by other investigators, (Homma and , 1996; Saltelli et al., 2000; Saltelli and Tarantola, 2002). The other approaches for the variance-based method are Sobols' approaches Sobol' (1990) by decomposing the sensitivity indices to the index subsets and calculating the higher order of sensitivity indices. The approach usually involves the Monte Carlo experimental design of input factors.

- **Local derivative based methods**

  Local SA investigates the impact of the input factors on the model locally, i.e. at some fixed point in the space of the input factors Hamby (1995); JRC (2011). Local SA is usually carried out by computing partial derivatives of the output functions with respect to the input variables (differential analysis). In order to compute the derivative numerically, the input parameters are varied within a small interval around a nominal value. The interval is not related to the degree of knowledge of the variables and is usually the same for all of the variables. The derivative-based method relates to the linearisation of the model response.

  One shortcoming of the linear sensitivity approach is that it is not possible to assess the impact of possible differences in the scale of variation of the input variables effectively unless the model itself is linear. When significant uncertainty exists in the input parameters, the linear sensitivities alone are not likely to provide a reliable estimator of output uncertainty in the model. When the model is non-linear and various input variables are affected by uncertainties of different orders of magnitude, a global sensitivity method should be used.

  Derivative based analysis technique involve taking the partial derivative of the output with respect to an input factor. Derivative-based methods have been used extensively in a variety of applications, such as the solution of inverse problems, where they have proven their worth (Saltelli et al., 2008). Nevertheless, the use of global methods, possibly quantitative, should be preferred to derivative-based SA for all problem settings where finite parameter variations are involved, unless the model is known to be linear or the range of variation is small, Turanyi and Rabitz (2000).

Many approaches of sensitivity analysis have been introduced recently, and each method has advantages and disadvantages. A task of engineers was recently assembled to review various sensitivity analysis methods. The engineer had to explicitly recommend which method is the best; instead they developed a list of attributes for preferred sensitivity analysis methods. Recently, the scholars has developed the analysis so-called "global

sensitivity analysis" in which a neighborhood of alternative assumptions is selected and the corresponding interval of inferences is identified. The features of an ideal global sensitivity analysis method should be as follows (Saltelli et al., 2008; JRC, 2011):

- Coping with the influence of scale and shape. The influence of the input should incorporate the effect of the input variation range and the form of its probability density function (PDF). It matters whether the PDF of an input factor is uniform or normal, and what the distribution parameters are.

- Including multidimensional averaging. In a local approach to SA partial derivatives are computed, as discussed above. This is the effect of factor variation when all others are kept constant at the central (nominal) value. A global method should instead evaluate the effect of a factor while all others vary as well.

- Being model independent. The method should work regardless of the additivity or linearity of the model. A global sensitivity measurement must take into account the so-called interaction effect, which is particularly important for non-linear, non-additive models. These arise when the effect of changing two factors is different from the sum of their individual effects.

- Being able to treat grouped factors as if they were single factors. This property of synthesis is essential for the agility of the interpretation of the results. One would not want to be confronted with a sensitivity results made of dense tables of sensitivity measures.

3.3 Optimisation methods: definition of the objective function and the choice of optimisation algorithm

Formulating an optimisation problem involves making statements, defining the general goals and requirements of a given activity, and transcribing them into a series of well-defined mathematical statements. Comprehensively, the formulation of an optimisation problem involves: (*i*) selecting one or more optimisation variables, (*ii*) choosing an objective function, (*iii*) selecting optimisation routines, and (*iv*) identifying a set of constraints. The objective function and the constraints must all be functions of one or more optimisation variables.

3.3.1 Objective function

In the indirect method of back analysis, the model parameters are estimated by minimising a "norm" of the difference between observed and model calculated values at specified observation points. The norm is known as "objective function". Optimisation algorithms drives an objective function in a way to find the best values of the objective functions by changing the model input parameters. There are a single objective function and a multiple objective function.

In geotechnical problems, the objective function is commonly established within a statistical framework. According to Kalman (1960); Honjo et al. (1994a), the model involves establishing the relation between observation data and the numerical solution of the employed physical model under the given boundary conditions as follows:

$$y_o^k = y_c^k \left(Z|X \right) + \varepsilon^k \tag{3.1}$$

where y_o^k is measurement data vector at time k, y_c^k is calculated data vector by FEM at time k, Z is known input data vector (i.e. soil profiles, loading conditions, and boundary condition), X is the vector of model parameters to be estimated in domain $\mathbb{X}$ and ε^k is error vector.

Thereby the most comprehensive objective function to be minimised in the parameter value estimation procedure is written base on Honjo et al. (1994a):

$$\min_{X \in \mathbb{X}} J(X|\beta_a) = \min_{X \in \mathbb{X}} \left\{ J_o(X) + \beta_a J_p(X) \right\} \tag{3.2}$$

where J_o stands for the objective information, i.e. observation data (Eq. 3.3), J_p represents the subjective information data i.e. variance of parameters or prior parameters (Eq. 3.4), and β_a is proposed to adjust the significance between the observation data and parameters information. β_a is used to combine 2 types of essentially incommensurable information.

$$J_o(X) = \sum_{k=1}^{K} \left(y_o^k - y_c^k \right)^T R^{-1} \left(y_o^k - y_c^k \right) \tag{3.3}$$

$$J_p(X) = (X - \mu)^T S^{-1} (X - \mu) \tag{3.4}$$

where μ is a prior mean of the model parameter vector, X which is assumed to follow a multivariate normal distribution, R is the covariance matrix of the error vector. It is called covariance analysed error, S is the prior covariance error matrix of input parameters.

- **The least square method**

  If $\beta_a = 0$ in equation 3.2 and $R = I$, I is an unit matrix. Then the resulting objective function yields the least square method. No prior information is introduced, and all the observation values are equally weighted in this case. This was the most widely used method for formulating objective function in geotechnical inverse analysis in the past. Gioda and Maier (1980) applied this method to define objective function for the back analysis of pressure tunnel test in order to investigate mechanical properties of rock. Cividini et al. (1981) used this method to determine the geometry, material and load parameters on the basis of displacements obtained from a hypothetical in-situ load test. Arai et al. (1983); Shoji et al. (1989, 1990) describes the use of finite element back-analysis of two-dimensional elastic consolidation, enabling the execution of safety management utilising the observational procedure method. Schanz et al. (2008, 2011b) used this method to identify the parameters in coupled hydro-mechanical and thermo-hydro-mechanical processes in the engineered barrier of nuclear waste repositories. Many other papers utilised this method to formulate objective functions for analysing geotechnical problems (Mattsson et al., 2001; Mahnken and P., 2001; Pichler et al., 2003; Szeliga et al., 2004; Tang and Kung, 2009; Levasseur et al., 2009; Knabe et al., 2013)

- **The maximum likelihood method**

  If $\beta_a = 0$ in equation 3.2 and $R \neq I$. This implies that the observation values are weighted according to their significance. The resulting objective function yields the weighted Least Square method or the Maximum Likelihood method Ledesma et al. (1991, 1996a). Ledesma et al. (1991) studies a fictitious tunnel excavation in material whose stress-strain relationship is given by a hyperbolic function. The parameter estimation capability at different loading stages are discussed together with the estimation uncertainties. The other papers applying this method for geotechnical problems are Honjo and Darmawan (1991); Sah et al. (1994); Pintado et al. (2002); Carrera et al. (2004).

- **Conventional Bayesian method**

  If $\beta_a = 1$ in the equation, 3.2 gives the formulation for the Conventional Bayesian method Cividini et al. (1983). $\beta_a \neq 1$ is Extended Bayesian Method. This is a straightforward application of the Bayesian statistical method to the inverse analysis. Cividini et al. (1983) is a pioneer using Bayesian approach in geotechnical engineering, where the a priori information concerning the unknown parameters is optimally combined with the a posteriori knowledge supplied by the displacement

measurements. The estimation of parameters defining local elastic properties and/or geometrical aspects was studied in the paper. Following Cividini, other authors also applied this method for geotechnical problems, such as Cooley (1982); St George (1986) among others.

- **Extended Bayesian method**

  If the equation is exactly the same form as that of Eq. 3.2, the method is Extended Bayesian method. The extended Bayesian method introduces the adjusting positive scalar β_a multiplying by prior parameter information. This form was first proposed by Neuman and Yakowitz (1979); afterwards other researchers proposed extension papers for the method particularly for the interpretation of scalar β_a, such as (Carrera and Neuman, 1986; Honjo et al., 1994a; Lee and Kim, 1999; Zhou et al., 2007; Zhang et al., 2010). The challenge of utilising Extended Bayesian method is to define the scalar β_a. Honjo et al. (1994a) used the Bayesian theorem to maximise a new objective function relative to the sensitivity vector. Meanwhile Zhou et al. (2007) proposed a modified theorem by introducing an automatic adjustment of the Tikhonov regulator.

3.3.2 Optimisation algorithm

After setting up the objective functions, an algorithm must be found which minimises/maximises the objective function. When optimising a single criterion (g), an optimum is either its maximum or minimum depending on what is being observed (Fig. 3.3). The *local minimum* $\hat{X}_l \in \mathbb{X}$ of a function $g : \mathbb{X} \mapsto \mathbb{R}$ is an input element with $g(\hat{X}_l) \leq g(X)$ for all X neighboring $\hat{X}_l$. The local minimum of an objective function is defined by:

$$\min_{X \in \mathbb{X}} g(X) := \hat{X}_l \mid \exists \varepsilon > 0 : g(\hat{X}_l) \leq g(X) \, \forall X \in \mathbb{X}, |X - \hat{X}_l| < \varepsilon \tag{3.5}$$

For *global minimum* $\hat{X}^* \in \mathbb{X}$, an input element with $g(\hat{X}^*) \leq g(X) \, \forall X \in \mathbb{X}$. If $\mathbb{X} \subseteq \mathbb{R}^n$ then the global minimum can be written as:

$$\min_{X \in \mathbb{X}} g(X) := \hat{X}^* \mid g(\hat{X}^*) \leq g(X) \, \forall X \in \mathbb{X} \tag{3.6}$$

The above-mentioned equation is for a minimum of the single objective function. However by optimising a single function, one can obtain a partial view on the results, when in real problem more than one function may influence which option should be selected. Therefore the multi-object optimisation concept was also recently developed such as in (Donoso and
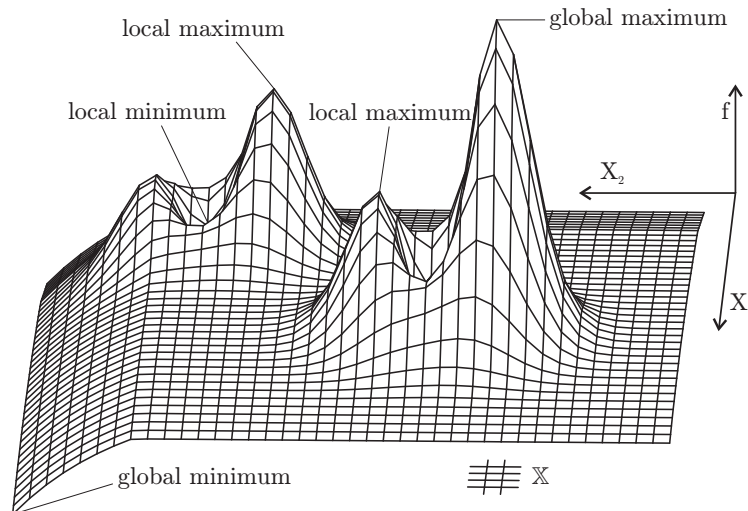
Figure 3.3: Example of global and local optima of a two-dimensional function (Weise,
        2009).

Fabregat, 2010). A typical feature of this type of problem is that these functions may
conflict with each other, when a function is optimised, other functions may worsen.

There are also several ways to classify the optimisation methods. Classifying according
to methods of operation, the optimisation can be divided into two basic classes (Weise,
2009): deterministic and probabilistic algorithms. A deterministic algorithm is an algo-
rithm which, in informal terms, behaves predictably. For a given particular input, it will
always produce the same output, and the underlying machine will always pass through
the same sequence of states. The method considers neither uncertainties in the observed
data and the forward model nor any prior information. When the relation between a
solution candidate and its "fitness" are not so obvious or too complicated, or there is
a high dimension of the searching space, it becomes difficult to solve a problem with a
deterministic algorithm. Then, probabilistic algorithms should be used. This method
has become one of most important research fields in optimisation in recent years. An
especially relevant family of probabilistic algorithms is the Monte Carlo-based approach.
Although the direct Monte Carlo-based method is a solution which is slightly inferior to
the best possible, it is preferable to one which takes considerable time to be found. To
improve the method, the heuristic search was developed (Vaessens et al., 1992; Rayward-
Smith et al., 1996; Michalewicz and Fogel, 2004). Heuristics is part of an optimisation
algorithm that utilises the information currently gathered by the algorithm to help to
decide which solution candidate should subsequently be tested or how the next can be
produced. Heuristics are usually problem-class dependent. The other extension of the

heuristics method is metaheuristics. An important class of probabilistic Monte Carlo metaheuristics is evolutionary computation (Bäck and Hammel, 1994; Bäck, 1996) and swarm intelligence (Kennedy and Eberhart, 1995).

When classifying according to properties of the algorithm, the optimisation methods are classified based on their algorithmic structure and underlying principles. The optimisation algorithms may be classified as follows: the sampling-based stochastic method, the gradient-based method, the derivative-free (or direct search) method, population-based method.

The sampling-based stochastic method is the method based on random samples, e.g. the Monte Carlo method (Metropolis and Ulam, 1949), using a Latin-Hypercube sampling to generate a parameter vector of random numbers McKay et al. (1979), and a grid/pattern-based method based on approximate points of variables under special constraints (Lewis and Torczon, 1996; Powell, 1998; Coope and Price, 2001). The advantage of this method is its robustness, which means the solutioncan always be obtained precisely with this method, and to a certain extent, so can a global search. One disadvantage of the method is that it is a very slow and crude search.

Gradient-based optimisation is a strategy which iteratively searches a minimum of a D dimensional of an objective function using gradient descendence. In order to find a minimum of a function using gradient descent, steps are taken relative to the negative of the gradient of the function at the current point x_0. The same method with the positive of the gradient is called gradient ascent; this method is used to find the local maximum of the object function. Related methods are the Levenberg Marquard Method (Levenberg, 1944) and the Newton and Quasi Newton Method (Davidon, 1991). These methods are fast because each step leads immediately to a better solution. However, the method is not sufficiently robust and is unstable in a low gradient spacefor the non-monotonic models, local search, and for the high dimensions of input factor. Some researchers have adopted this method in back analyses of geological problems: Ledesma et al. (1996b); Pintado et al. (2002) used the Gauss-Newton method, Tang and Kung (2009) utilised the Quasi-Newton method and Honjo et al. (1994a) applied the Quasi-Newton method according to the Davidon-Fletcher method.

The derivative-free method is a method which optimisation procedure does not base on using derivative value (e.g. Newton method) but using the other methods (e.g. simplex method). Instead of comparing two initial points, the simplex method compares among more than two initial points; the next point is predicted by operations of reflection, contraction, or expansion from the initial points. The review of this method can be found

in Conn et al. (1997). Related methods include the Downhill Simplex Method (Neldel and Mead, 1965) and Powell's method (Powell, 1964). On the one hand, this method is more robust than the gradient method. On the other hand, this method is also a local search. Some researchers have adopted this method in back analyses of geological problems such as the modified Nelder-Mead optimisation (Schanz et al., 2011b; Zhang et al., 2013).

Population-based optimisation algorithms apply biology-inspired mechanisms like mutation, crossover, natural selection, and survival of the fittest in order to refine a set of solution candidates iteratively. Many members of the population-based optimisation family can be listed: Particle Swarm Optimisation (PSO) (Kennedy and Eberhart, 1995), Ant Colony Optimisation (Guntsch and Middendorf, 2001), Tabu Search (Glover, 1986), Genetic Algorithms (Ronald, 1995) and Evolutionary Algorithms (Bäck and Hammel, 1994; Bosman and Thierens, 2002). The advantage of this method is that it is robust and fast, and it provides more range of search space. However, the disadvantage of the method is that it is relatively expensive due to slow convergence and the fact that it may reach to a local solution. Despite that shortcoming, the solutions achieved by this method do not depend on the initial guess. Therefore, some researchers have adopted this method in back analyses of geological problems such as (Nguyen-Tuan et al., 2011; Knabe et al., 2013) who used the PSO method, Zhang et al. (2013) who utilised a hybrid PSO and Nelder-Mead search method and (Pichler et al., 2003) who applied an artificial neural network.

Recently, the popular term "Global Optimisation Algorithms" has appeared, which is the branch of applied mathematics and numerical analysis that focuses on optimisation by combining several methods or new methods, for example (Hoang, 1998; Horst et al., 2000; Weise, 2009).

One way to overcome the limitations of optimisation methods is to propose a hybrid or combined method for the optimisation algorithm. For instance, an algorithm GOD-LIKE (Oldenhuis and Vandekerckhove, 2009) is an abbreviation of **G**lobal **O**ptimum **D**etermination by **L**inking and **I**nterchanging **K**indred **E**valuators. This algorithm is an attempt to generalise and improve the robustness of the four meta-heuristic optimisation algorithms: genetic algorithms, particle swarm optimisation, differential evolution and adaptive simulated annealing. Furthermore, it generalises the optimisation process by being capable to solve both single-objective and multi-objective optimisation problems. The algorithm SHERPA (Sherpa, 2006) is a method that always tests the minimum using a different method of optimisation. The program applies two main methods: single-shot techniques (e.g. Powell, Simplex, etc.) and scatter-shot techniques (e.g. Grid method,

Monte Carlo, Grid-Powell, etc.). The optimising process is the summary and automatic mutual reference among these techniques.

Although the authors have focused on improving the search algorithms, the cost of the optimisation cannot improve in general. This was indicated as a law "*No free lunch theorems for search*". According to Wolpert and Macready (1995, 1997) if the algorithm A outperforms algorithm B on some cost functions, there are always exactly as many functions where B outperforms A. The hybrid method may perform the solution more robustly, but in fact the more algorithm are used, the higher the user's costs will be.

3.4 Reliability analysis

There are many ways to define reliability analysis. According to Gaber et al. (2009) reliability is the confidence that potential users have in a model and in the information derived from the model such that they are willing to use the model and the derived information. Specifically, reliability is a function of the performance record of a model and its conformance to best available, practicable science. According to Todinov (2005), reliability is the ability of an "entity" to perform a required function under given conditions for a given time interval. The International Organisation for Standardisation (ISO, 1986) defined the reliability as "The ability of an item to perform a required function under given environmental and operating conditions and for a stated period of time."

According to Trochim (2006), there are four general classes of reliability estimates. (*i*) inter-rater or inter-observer reliability, (*ii*) test-retest reliability, (*iii*) parallel-forms reliability, and (*iv*) internal consistency reliability.

- Inter-rater or inter-observer reliability is used to assess the degree to which different raters/observers give consistent estimates of the same phenomenon. This method is one of the best ways to estimate reliability when the measure is an observation. However, it requires multiple raters or observers.

- Test-retest reliability is the variation in measurements taken by a single person or instrument on the same item under the same conditions. Test-retest approach might be used when there is only a single rater. In some studies it is reasonable to conduct both inter-rater and test-retest to help establish the reliability of the raters or observers.

- Parallel-forms reliability is used to assess the consistency of the results of two tests constructed in the same way from the same content domain. The parallel forms

estimator is typically only used in situations where you intend to use the two forms as alternate measures of the same thing. It is often used in the measurements of geotechnical problems.

- Internal consistency reliability is used to assess the consistency of results across items within a test. This method is applied to estimate the reliability of the instrument by observing how well the items that reflect the same construct yield similar results. The correlation of one item with other items is one of the values utilised to estimate the consistency of the internal items.

Reliability analysis is applied in many fields of industry and science (Meeker and Escobar, 1998; Todinov, 2005; Hamada et al., 2008). Reliability analysis is related to model analysis, system design, hardware design, software design, manufacturing, testing, transport, storage, operations research, technical documentation, and training. In this part, reliability analysis is considered in its application to geotechnical engineering (e.g. model reliability, parameters estimated, and geotechnical design).

In terms of numerical simulations of geotechnical problems, once the model has been formulated, it usually involves a number of parameters which requires to reproduce the material behaviour. The estimators is introduced to assess the reliability of the model and input parameters. The quality of the input parameters varies widely from unbiased and efficient, characterised by a small error, to biased and inefficient, characterised by a large error. With a view to Chatfield (1995) adopted by (Todinov, 2005), the mathematical model should satisfy the following conditions for a high reliability model:

- Physical insight: the model should provide insight into the underlying physical mechanism of the modelled random factor.

- Parsimonious: The model should be as simple as possible (and also contain as few parameters as possible) consistent with describing the important features of the data.

- Robust: small variations in the input data or in the estimates of the model parameters should lead to small variations in the model predictions.

- Capable of correct predictions outside the data range and provide a good fit within the data range.

According to (Todinov, 2005), constructing a model is not about getting the best fit to the observed data. It is about constructing a model which is consistent with the underlying physical mechanism. The ability of a model to adequately match a single

data set may indicate little because a good fit can be achieved simply by making the model more complicated by over-parameterising. As a rule, over-parameterised models have poor predictive capability.

Many authors attempted to look for an estimator based on probabilistic analysis for assessing the reliability of numerical models. Akaike's work used probabilistic analysis (e.g. the Bayesian estimator and Akaike infromation criterion (AIC)) as the estimators to assess the reliability of the mathematical models (Akaike, 1974, 1978, 1981). Beside that, the other papers applied reliability estimators to assess the capacity of the foundation and embankment. For instance, Oka and Wu (1990); Christian et al. (1994); Gilbert et al. (1998) assessed the risk of the embankment after it was built using probabilistic analysis. Cherubini (2000) developed reliability analysis to evaluate shallow foundation bearing capacity. Honjo et al. (2009) introduced the method for limit state design in geotechnical engineering. Honjo (2010) presented an overview of the procedures for geotechnical structure reliability-based design.

The reliability of the set of the identified via back analysis parameters was also an important issue in geotechnical engineering. Pintado et al. (2002) applied back analysis to thermo-hydraulic bentonite properties using data from laboratory tests. They used the maximum likelihood approach to introduce the objective function. The Gauss-Newton algorithm was used as a tool for minimising the objective function. The reliability of the identified set of parameters was estimated based on analysing its sensitivity matrix and the covariance matrix. Ledesma et al. (1996b); Knabe et al. (2013) assessed the reliability of the identified parameters of geotechnical boundary problems in cavern excavation and embankments, respectively, identified based on back analysis. The reliability of the identified parameters was estimated similarly based on sensitivity analysis Pintado et al. (2002). The confidence interval was introduced based on the sensitivity matrix. Recently Zhang et al. (2013) identified parameters via back analysis using PSO as an optimisation algorithm. However, they concluded that any attempts to identify substantial numbers of the parameters simultaneously can prove risky due to the non-uniqueness of the solution found by the algorithm.

In summary, back analysis in geotechnical problems is strategic work concerning uncertainty and sensitivity analysis, the optimisation method and reliability analysis. Many methods have been proposed to estimate local and global sensitivity. However, using global sensitivity has not received substantial focus for geotechnical problems. Reliability analysis based on local sensitivity analysis may not reflect the confidence of parameters in its entire searching space. Although many optimisation methods have been proposed

in order to minimise the objective function, the non-unique solution and trapped local minimum of the objective function in the non-monotonic and non convective functions are still open for future research.

4 Materials and experimental programmes

4.1 General remarks

This chapter characterises the properties of the materials used in the experiments performed herein. The experimental program utilised in this study was planned in order to account for several possible hydro-mechanical or thermo-hydro-mechanical mechanisms that are likely to occur in the nuclear waste disposal facilities. Depending on overall understanding of soil material behaviour, parameters of the soil can be estimated and selected according to the parameter of similar soils (e.g. FEBEX, Serrata bentonite). Since the aim of this project is to study the buffer and sealing elements in repositories of high level nuclear waste, the material for the buffer and sealing elements should be selected respectively the following criteria and requirements:

- Ensuring a low transport of harmful substances including radionuclides into and out of barrier system

- Having good predictability of barrier materials behaviour, which is related to the long-term safety assessment of the repository

- Providing good thermal performance in order to ensure temperature redistribution when a high temperature is generated in the repository so that no damage occurs due to thermal and thermo-mechanical loads

- Moderate activity in both mechanical (collapse or swelling) behaviour and chemical reaction

- Low cost expense: The buffer and sealing system use an enormous volume of materials; selecting suitable and local available materials will reduce expense.

In order to satisfy the above criteria, the material most commonly considered is compacted expansible clay, normally some kind of pure bentonite or mixed with other materials like

sand. However, cement-based materials (special concretes) and crushed salt (for repositories in salt rock) are also appropriate for some specific applications. Bentonite is often selected because of its suitable properties for barrier systems, such as low permeability and easy handling, which can be favorable when using this material as a buffer and sealing element for nuclear waste disposal. However, the swelling pressure develops excessively when bentonite is wetted during the operation stage of the repository, so it should be limited as it might cause damage to the repository material or the utilised structures. Moreover, bentonite has low thermal conductivity, which induces a high temperature in the nuclear waste canister. In attempt to improve these properties for bentonite, researchers used some mixture of bentonite and other materials. Sand-bentonite mixture is one of these choices which can be studied as the candidate material.

4.2 Properties of materials used

The main material investigated in this study was a mixture of a calcium-type bentonite, called Calcigel, which is mined from southern Germany, and yellow (quartz) sand. Beside that validating materials were also used to validate the device and as a point of comparison with the main material. Preliminary experiments were performed consisting of basic soil tests and physico-chemical characterisation for both the bentonite and the sand.

4.2.1 Basic properties

The basic soil tests were performed according to DIN standards (DIN:18121-1, 1998). The tests included the determination of Atterberg limits, specific gravity, and grain-size distribution. Two methods were used to determine the grain-size distribution of the bentonite used: the sieve method and the sedimentation method (DIN:18121-1, 1998), and soil materials were selected to contribute to two types of tests. Firstly, the materials used to validate and calibrate the new devices included Hostun sand, yellow sand, Calcigel bentonite (No: Cal.05.179) and sandy loam Schanz et al. (2011a). Secondly, the material utilised for the column-type test and the element test was Calcigel bentonite (No: Cal.05.179) mixed with yellow sand. The grain-size distribution curves determined for the bentonite for the sand are shown in Fig. 4.1 and Table 4.1 according to DIN 18 121.

Table 4.1: Characteristics of the soils used

Soil type	Sample N^o	Dry density (g/cm³)	w/c[1] before test %	w/c after test %	Grain size distribution (%)			Liquid Limit %	Plastic Limit %	Surface area m²/g
					Sand (mm) 2-0.074	Silt (mm) 0.074-0.005	Clay (mm) <0.005			
Sand-	SBM01	1.60	10.2	10.1	50.0	21.3	28.8	39.6	21.4	263
bentonite	SBM02		16.4	16.4						
mixture	SBM03		19.9	20.1						
	SBM04		25.1	25.0						
Sandy loam	SL01	1.53	13.0	13.2	65.4	34.6	15.4	23.3	17.3	37
	SL02		18.2	18.7						
	SL03		26.3	25.5						
Hostun sand	HS01	1.52	5.2	5.6	96.8	3.2	0.0	-	-	0.22
	HS02		10.4	10.4						
	HS03		15.5	15.5						
	HS04		24.3	23.8						

4.2.2 Physico-chemical characterisation

Adding sand to bentonite has been found to be advantageous regarding ease of handling, manufacturing, and economic factors. Moreover, the addition of sand improves the thermal conductivity for bentonite. For a given dry density the swelling pressure of a bentonite-sand mixture is expected to be higher than that of pure bentonite. The coefficient of the permeability of the compacted bentonite-sand mixture may also be lower compared to that of the compacted pure bentonite depending on the percentage of sand added and the dry density of the compacted mixture. Thus, the optimum percentage of sand added has been investigated (Agus, 2005). JNC (1999) proposed using a heavily compacted mixture of bentonite and silica sand as buffer material for the Japanese nuclear waste disposal construction concept. Similarly, AECL (1994) suggested utilising a high density mixture of 50% bentonite and 50% silica sand for Canadian repository construction. In column-type and element experiments, the ratio selected was 50/50% for sand-bentonite mixtures.

The sand and bentonite used for the column-type tests and oedometer tests have the same mineralogy with the material used in Agus (2005). The mineralogy composition and index properties of Calcigel bentonite and yellow sand are given in Table 4.2 and Table 4.3. Cation Exchange Capacity (CEC) data was collected from Agus (2005) because they used the same bentonite. The amount of basic exchangeable cations (i.e., Na^+, Ca^{2+}, Mg^{2+} and K^+) was determined using Inductively Coupled Plasma - Atomic Emission Spectroscopy (ICP-AES) according to the European Standard EN ISO 11885, (1985).
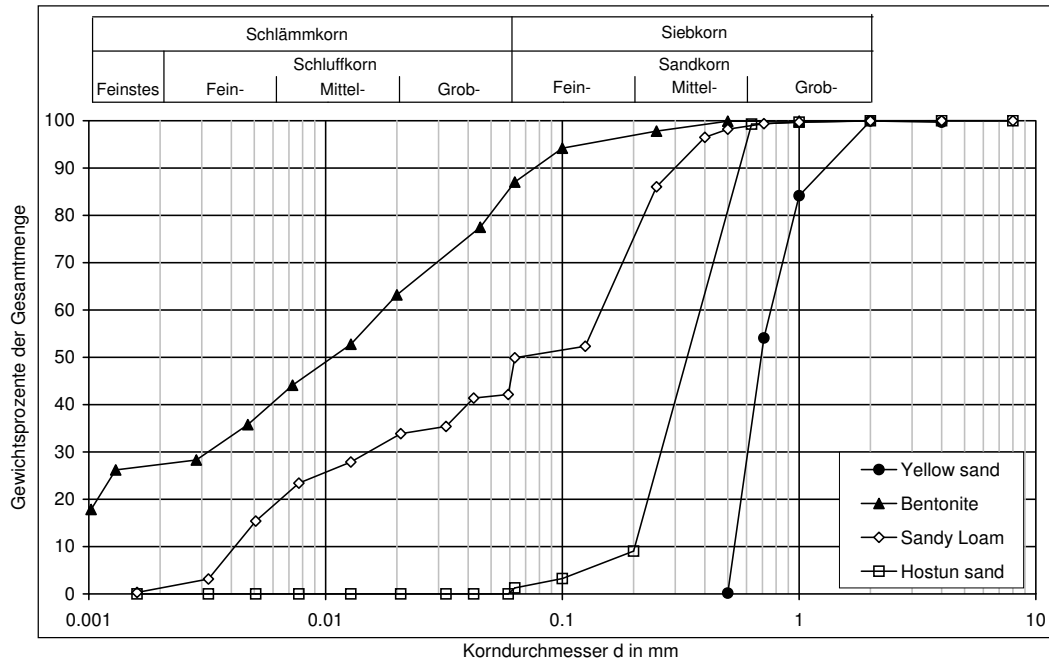
Figure 4.1: Grain-size distribution curves of the soils used

Table 4.2: Mineralogy composition of Calcigel, Agus (2005)

Mineral	Montmorillonite	Quartz	Feldspar	Calcite	Dolomite	Others
Weight ratio %	50-60	5-10	5-8	1-5	10-15	2-29

4.3 Preparation of samples and protocols

The element tests play an important role in determining parameters for the soil material models. The parameters are determined by controlling some variables and changing other ones (i.e. stress, temperature, pore water pressure). The as-prepared samples should have the initial conditions which are likely to occur in the field. The test was carried out based on the guiding documents in order to determine parameters for BBM-TEP model (Alonso et al., 1990; Gens, 1995; Geiser, 1999). Moreover the tests with changing temperatures not only determine parameters for the soil model but also investigate the behaviour of unsaturated clayey materials in non-isothermal conditions. A combination of element tests and column-type tests supplies reliable data to evaluate the THM behaviour of unsaturated SBM. The protocols of three types of the test presented in this section are the oedometer test, column-type test, and unconfined soil water retention tests.

Table 4.3: Properties of Calcigel bentonite, Agus (2005)

Properties	Value
Bentonite:	
Specific gravity	2.8
Liquid limit (%)	180
Plastic limit (%)	56
Plasticity index (%)	124
Cation exchange capacity (meq/100g)	74
Basic exchangeable cation	
Na^+, Ca^{2+}, Mg^{2+},K^+ (meq/100g)	22, 29, 17, 0
Monmorillonite content (%)	50-56
Sand:	
Specific gravity	2.65
D10	0.25
D60	0.4
D30	0.7

4.3.1 Oedometer tests

The mixture of sand and calcigel bentonite (SBM) was selected as a material for the oedometer tests. The pre-determine initial density of as-prepared samples was about 1.4 g/cm^3. The natural water content of Calcigel bentonite in laboratory environment is 7.8%. Water content of yellow sand was considered 0%. The initial water content of SBM in the factory container was 3.9%. Water was added into the soil in order to increase adherence during compaction. All soil specimens prepared for oedometer tests had the same initial water content and suction. The suction was controlled by the vapour equilibrium method while considering the change in temperature (Tang and Cui, 2005; Arifin, 2008). The initial condition of soil specimens are presented in Table 4.4. Specimens of diameter 50 mm and height 20 mm were prepared using the static compaction method by directly compacting bentonite-water mixtures in the specimen ring to overcome preferential flow along the soil-cell interface Fig. 4.2. The specimens in the compaction machine were compacted in 4 layers into the cell ring, and each layer was compressed under a hydro-static load. For high or saturated initial water content specimens, the predetermined amount of water was added to the specimens depending upon the dry density and mixed

daily for about one week to ensure there was a homogenous mixture and water distribution.

In order to control suction via VET, two types of salt solutions were selected, Sodium chloride (NaCl) and Calcium chloride (CaCl$_2$), since they are less poisonous and demonstrate more stable physico-chemical behaviour under high temperature. Sodium chloride was used to apply lower suction at about 20 MPa, Calcium chloride was used to apply higher suction at 40 and 58 MPa.

Table 4.4: Initial condition of soil samples for the oedometer test

No	Test name	mixture ratio (%)	Initial void ratio (-)	Initial dry density (g/cm^3)	Initial w/c (%)	Initial saturation (%)	Initial total suction (kPa)
1	OE-SBM-20-3	50B/50S	0.89	1.43	6.1	18.4	58300
2	OE-SBM-20-4	50B/50S	0.88	1.43	6.1	18.6	58300
3	OE-SBM-20-5	50B/50S	0.88	1.44	6.1	18.7	58300
4	OE-SBM-20-6	50B/50S	0.89	1.44	6.1	18.5	58300
5	OE-SBM-80-1	50B/50S	0.89	1.44	6.1	18.5	58300
6	OE-SBM-80-2	50B/50S	0.88	1.43	6.1	18.8	58300
7	OE-SBM-80-3	50B/50S	0.89	1.44	6.1	18.5	58300
8	OE-SBM-80-4	50B/50S	0.88	1.44	6.1	18.8	58300

4.3.2 Unconfined soil water retention tests

Soil water retention curves were investigated for the sand-bentonite mixture 50B/50S. Two methods were applied to determine the SWRC in unconfined conditions: the axis translation technique (ATT) and the vapour equilibrium technique (VET) (Fredlund and Rahardjo, 1993). Both methods require specimens to be prepared identically. The soil specimens were mixed with a pre-determined volume of water to become fully saturated when it was compacted into the as-prepared density of 1.4 g/cm^3. After soil had been mixed, it was kept in air-tight container for two weeks to reach equilibrium. Then the specimens were compacted by static compaction (Fig. 4.2). After the soil specimen had been compacted to a cylindrical shape, it was placed on saturated porous stone and placed into a humid chamber for a day to reach a fully saturated state and mechanical equilibrium.

Figure 4.2: Compact device using hydraulic pressure

In order to investigate the water content and suction relation at a high suction value ($s > 4000$ kPa), the VET was used. The soil samples were initially prepared in a fully saturated state. The procedure to prepare the sample in a fully saturated state resembled the oedometer test procedure. After the samples had been prepared in the saturated state, their suction were controlled utilising the VET procedure. To reduce the time required for the process, six desiccators were utilised, each of which had a prescribed suction value. The suction values in the desiccators were 2320, 4260, 4260, 9530, 21850, 58120, 249100 kPa, based on the different osmotic suction capacity of the salt solution. The prepared salt solutions were NaCl 38 g/l, NaCl 63 g/l, NaCl 125 g/l, KCl saturated, Na_2CO_3 saturated, LiCl saturated, corresponding to the increase of suction values respectively.

Firstly, two prepared samples were placed into one desiccator. Each desiccator represents one value of suction corresponding to a water content value. The testing process stopped when the suction between soil sample and solution attained equilibrium. Equilibrium is defined as the equal value in the weight of the specimens after being weighed twice. The difference between two weight measurements was about 10 days. After soil samples had obtained equilibrium, the water content of the soil sample was determined. A serial values of respectively suction and the water content were drawn, which is called the initial drying curve of the soil water retention curve.

Next, the wetting process was carried out so the main wetting curve could be drawn. The soil samples were placed into a drying oven for 48 hours to become fully dry. The test was conducted to obtain the wetting curve for the same soil specimens with the same desiccators. This time, when the soil samples were dried, the reverse process occurred. Soil samples sucked water in, which reduced its suction. Consequently the main wetting curve was drawn based on the obtained value of suction and water content for each sample. The properties of samples to determine the SWRC using the VET method are presented in Table 4.5.

The ATT method was used to investigate the specimens at a suction less than 1500 kPa. Two pressure plates were used, one for the drying process and the other for wetting process. Each pressure plate contained two specimens. The initial saturated condition of the specimens is presented in Table 4.6. The target suctions were obtained by applying air pressure on the pressure plate. To draw the drying curve the air pressure was reduced in increments. To draw the wetting curve the air pressure and suction was increased incrementally as well. The suction step was finished when the soil samples had attained the suction equilibrium.

Table 4.5: Initial condition of SWRC samples for the VET method

No	Test name (Drying) (Wetting)	Dimension		Dry density (g/cm^3)	Desiccator suction (kPa)
		h (mm)	d (mm)		
1	VET-D-11	21.60	51.20	1.41	2320
2	VET-D-12	21.20	51.00	1.42	2320
3	VET-D-21	20.80	50.90	1.41	4260
4	VET-D-22	21.40	50.40	1.40	4260
5	VET-D-31	11.10	51.20	1.41	9530
6	VET-D-32	11.20	51.10	1.40	9530
7	VET-D-41	11.40	51.00	1.41	21850
8	VET-D-42	11.00	51.20	1.40	21850
9	VET-D-51	11.40	51.10	1.40	58120
10	VET-D-52	11.80	50.90	1.41	58120
11	VET-D-61	10.80	51.20	1.40	249100
12	VET-D-62	11.00	51.20	1.41	249100

Table 4.6: Initial condition of SWCC samples for ATT method

No	Test name (Drying)	Dimension		Dry density
		h(mm)	d(mm)	(g/cm^3)
1	ATT-D-11	10.60	50.80	1.41
2	ATT-D-12	10.80	50.80	1.42
3	ATT-W-11	10.80	50.40	1.42
4	ATT-W-12	10.80	50.40	1.42

4.3.3 Tests in the column-type device

The SBM was selected as a material for investigation. Calcigel bentonite (No: Cal.05.179) was mixed yellow sand with a ratio of 50 % bentonite and 50% sand in dry weight. The pre-determined initial density of the as-prepared samples was 1.4 (Mg/cm^3), which was the same as in oedometer test. In addition, Hostun soil was used to validate the newly developed device. The soils were mixed and water was added to the sand-betonite specimens, and they were kept in an air-tight container for more than 2 weeks so that they could attain vapour equilibrium. The initial conditions for the soil specimens in this type of test are presented in Table 7.4. Specimens were compacted outside the column using the dynamic method. The dimensions of each sample were the diameter $\times$ height equal to 150×300 mm, respectively. It was compacted into 3 separate parts and encased into the column. After installing TDR probes and relative humidity chambers, the specimen was kept in the same condition for 6 days to attain mechanical and vapour equilibrium before the beginning the test. The initial water content was calculated based on the oven drying method, (DIN:18121-1, 1998). The initial soil suctions presented in Table 7.4 were measured and calculated by means of the chilled mirror device section 5.2.2.3.

Table 4.7: Initial conditions for the soil samples

Test name	mixture ratio (%)	Initial void ratio (-)	Initial dry density (g/cm^3)	Initial w/c (%)	Initial saturation (%)	Initial total suction (kPa)
THM-S	100S	0.71	1.55	26.5	98.9	0
HM-SBM	50B/50S	0.93	1.40	8.2	23.8	20200
THM-SBM	50B/50S	0.92	1.41	8.7	25.5	13930

5 Experimental equipment and methods

5.1 General remarks

The aim of the experiments in this study is to investigate stress-strain behaviour as well as the expansion of the sand-bentonite mixture with different loading steps and temperatures. In addition the test results were used to determine several parameters for the thermo-hydro-mechanical analysis. During the experiment two types of test were carried out. The element tests includes oedometer tests, and soil water characteristic curve tests. The oedometer tests were carried out in temperatures of 22°C and 80°C. The SWRC tests were performed at a temperature of 22°C. The other tests were THM column-type tests in a new THM column with a subjection of a hydraulic gradient and a thermal gradient. The aim of THM column test is to investigate the transient temperature, water content, relative humidity, and swelling pressure at the same sections under temperature and hydraulic gradients.

5.2 Element tests

5.2.1 Oedometer tests

5.2.1.1 Device

In this section, a modified high pressure oedometer device in Ruhr-Universität Bochum fabricated by Wille Company Germany is presented. The device had originally been used at laboratory temperature by Baille et al. (2010). The aim of modified device is to perform the test on unsaturated soil at different temperatures. The original description of the device is presented in Fig. 5.1. The cell has the capacity to increase the pressure

1 Top part	7 Bottom porous plate	13 Provision for vapour supply	19 Water chamber
2 Central part	8 Force transducer	14 Water or vapour supply	20 Electrical cables
3 Bottom part	9 Strain gauge	15 Vent	21 Fluid reservoir
4 Specimen ring	10 Loading piston	16 O-ring	22 Loading frame
5 Soil specimen	11 Adapter for 8	17 Heavy screw	23 Base plate
6 Pressure pad with top porous plate	12 Upper restraint	18 Thread	24 Adapter for 23

Figure 5.1: Original high pressure oedometer device with schematic of the cell (left), and the test setup (right), Baille et al. (2010).

up to 50 KN or 25 MPa. The cell includes thee parts. The bottom part is a thick steel plate consisting of porous stone (N°.7), from which water/vapour can interact with outside environment by two pipes (N°.14). The bottom part and the middle part (N°.2) are fastened to each other by 4 screws (N°.17). The middle part contains the specimen ring (N°.4). A loading pad containing the top porous stone is located on the top of the ring. From the porous stone the water/vapour can exchange with outer environment by the pipes (N°.13). The middle part and the top part are fastened to each other by thread (N°.18). The force transducer (load cell) (N°.8) had a maximum loading capacity of 50 kN with a precision of 0.001 kN. A strain gauge (N°.9) with a precision of 0.001 mm and a total run of 25 mm was connected directly to the loading piston to record the vertical deformation. The device can perform oedometer tests, swelling tests under controlled pressure, and isochoric tests.

The cell was modified to perform the test for the specimen at a temperature of up to 100°C, Fig. 5.2. The cell and the salt solution container were covered by the heating coats 1 and 2

Figure 5.2: Scheme of modified high pressure oedometer device.
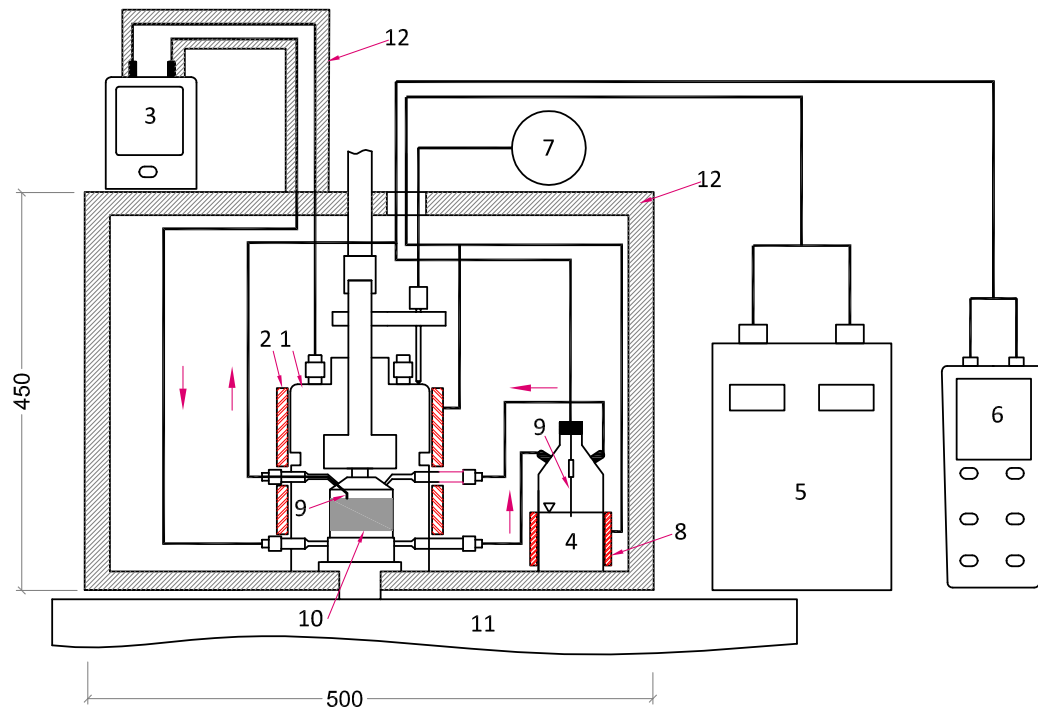
1	Oedometer cell	2	Heating coat 1	3	Circulation fan
4	Salt solution container	5	Temperature regulator	6	Thermocouple device
7	Strain gauge	8	Heating coat 2	9	Temperature sensors
10	Specimen	11	Base-plate of frame	12	Isolation box

(N°2 and N°8). The two heaters were controlled by a temperature regulator (N°5). These heaters were secured using double temperature sensors. The primary temperature sensor is a sensor for the temperature regulator. The secondary sensor is called fire insurance. The secondary sensor is used in case the primary sensors are out of order, the power will stop if the heating temperature exceeds the preset temperature. The effective temperature in the soil specimen and in the salt solution was monitored by two thermocouple sensors (N°9) and the monitor device (N°6).

The suction of soil was controlled utilising the VEP method, see section 4.3.1. The salt solution, a liquid container (N°4), was circulated by the fan (N°3). Two exchanging humidity interfaces were on the top and the bottom of soil specimen. The entire system was placed in a thermal isolation box in order to keep the temperature stable.

5.2.1.2 Experimental procedures

It has been known that material properties of the devices and the accuracy of the sensor may change with temperature. Therefore, the calibration was carried out for the stress-strain relation of the frame and the cell at 20°C and 80°C before the testing process. It was found that the change in temperature affects the accuracy of the load cell. The calibration tests are presented in section 5.4.

The specimens were prepared with the same initial water content (6.1%). The initial suction of the SBM was measured by the chilled mirror method (section 5.2.2.3), $s = 58,300$ kPa. Afterwards, the SBM mix was kept in the air-tight container for more than 2 weeks to attain hydraulic equilibrium. The SBM was compacted using a hydrostatic compactor to achieve the dry density 1.4 g/cm^3 in a steel ring After the cell was put into a loading frame, the suction was controlled at the target values as in Table 5.2. When the specimen reached hydraulic and stress-strain equilibrium, the loading steps began as in Table 5.1. The condition to change the load step is based on ASTM-D2435 (1996) for a one-dimensional consolidation test. The compression was increased incrementally between 0.3 kN and 8.0 kN corresponding to 140 kPa and 4000 kPa, respectively. The protocol of the controlled net stress and suction is presented in Fig. 5.3.

For tests in the saturated state, the soil specimens were prepared with the same initial water content (6.1%). The specimens were hydrated by supplied water from burette. The volume of water supplied before and after saturated state was recorded in order to calculate the water imbibition in the specimens and saturated hydraulic permeability.

In order to identify parameters in the soil skeleton expansion, α_0, the specimens were controlled at the same suction at 20°C then heated to 80°C. From expansion of the soil due to temperature we can determine thermal expansion coefficient.

The suction was controlled using the VET at different levels of target temperatures. Osmotic coefficients of salt solutions vary as the temperature changes (Pitzer et al., 1984; DOW, 2003). The equilibrium suction can be calculated from different coefficients of the osmotic solution at the given temperature. The relationship between suction and the concentration of a salt solution at 20°C and 80°C has been studied by Arifin and Schanz (2009). Two solutions were selected to control soil suction: sodium chloride and calcium chloride. This solution has been selected for its non-toxicity, its stability at various temperatures, and its stable osmotic pressure even at varying temperatures. The Fig. 5.4 shows the temperature effects on the salt solution. The suction values were controlled based on the suction curve in concentration of salt solutions at different temperatures.

Table 5.1: Load steps corresponding to temperatures

Temp. (°C)	Applied load (N)					
	P1	P2	P3	P4	P5	P6
20 & 80	153	306	509	1019	2037	4074

Table 5.2: Controlled suction of the tests at two temperature levels

Temp. (°C)	Applied suction (kPa)			
20 & 80	saturated	10000	32000	58300

Two levels of temperature were investigated. The temperature refers to normal room temperature at 20°C and at 80°C, which usually occurs in column tests. The controlled suction was the same at both 20°C and 80°C. It is presented in Table 5.2.

5.2.2 Devices and methods for SWRC in unconfined conditions

The soil water retention curve was drawn based on the relation between water content and suction at laboratory temperature (20°C). The wetting and drying tests were performed under unconfined conditions using several as-prepared specimens of 50/50 bentonite-sand mixture at a dry density of 1.4 g/cm^3. The ATT technique in the pressure plate apparatus was used to perform the test at the suction value smaller than 1500 kPa. For suction higher than 1500 kPa, the vapour equilibrium technique (VET) by means of desiccator tests was used (Fredlund and Rahardjo, 1993; Agus, 2005). The initial conditions of the soil specimens are described in section 4.3.2.
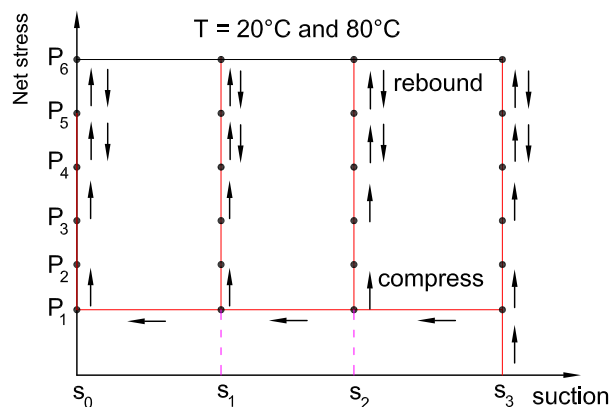
Figure 5.3: Stress and suction path planed for oedometer tests at 20°C and 80°C
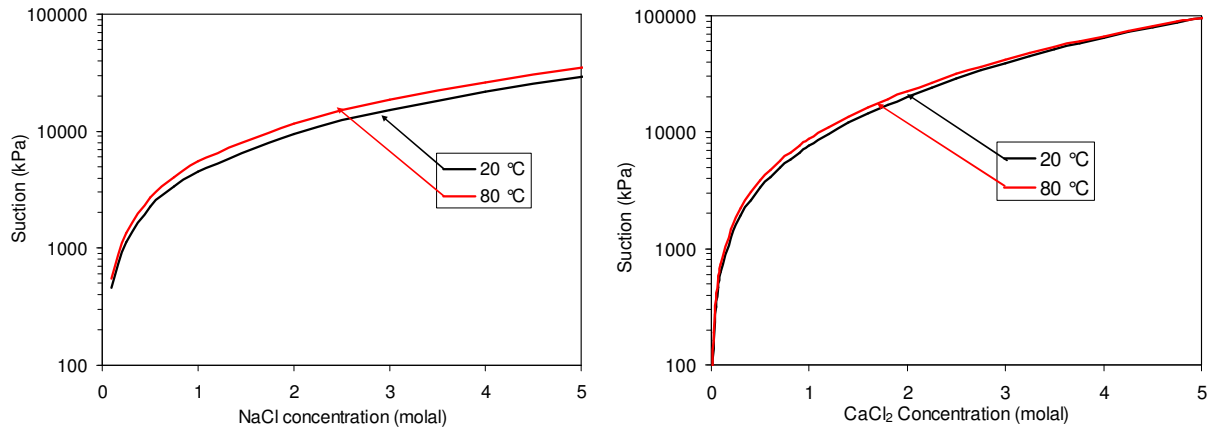
Figure 5.4: Temperature effects on suction of salt solution: (left) sodium chlroide, (right) calcium chloride

5.2.2.1 Vapour equilibrium technique

The vapour equilibrium technique was used to determine wetting and drying curves in the high total suction range (i.e., greater than 2000 kPa). Six large glass desiccators were used for different suction steps: 2320, 4260, 9530, 21850, 58120, 249100 kPa (Fig. 5.5). Several aqueous and molal salt solutions were used to induce total suction to the specimen by changing the relative humidity of the vapour space in the desiccator. The hydraulic equilibrium is defined as when the weight of the soil specimens do not change between two weight measurements. The initial state of the specimens at the beginning of the test is fully saturated. The soil dried due to the differential suction between the salt solution and the specimen. When the specimen had reached equilibrium, the dimensions were measured, and it was placed in a drying oven in order to get fully dry. Afterwards the specimen was returned to desiccator to undergo the test to determine the wetting curve.

The experiment was conducted in a temperature-controlled room that maintained a constant temperature of $20°C \pm 0.5°C$. The actual suction was calibrated in Agus (2005) by the filter paper. It was found that the actual total suctions were not different from the targeted values.

5.2.2.2 Axis-translation technique

Axis-translation technique was adopted to determine unconfined wetting and drying curves in the low suction range depending on an air entry value of the ceramic plate (i.e., less than 1500 kPa). In the technique, matric suction is indirectly applied. A pres-
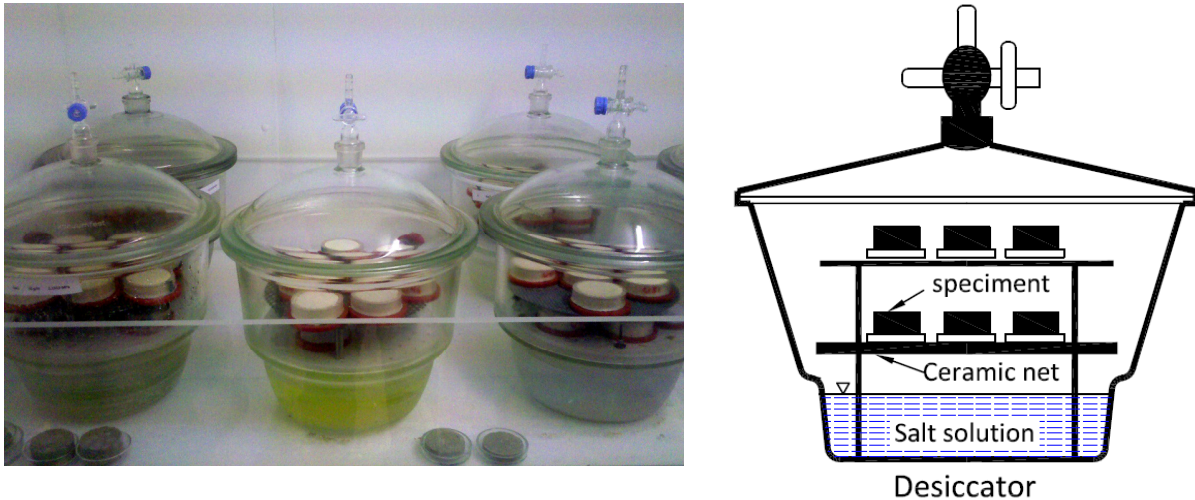
Figure 5.5: Setup of the desiccator test.

sure plate apparatus from the soil moisture was used in this experiment Fig. 5.6. The main part of the pressure plate apparatus is the high-air entry ceramic plate. Three ceramic plates with the air entry values of 1500 kPa were used for the investigation depending on the applied matric suction. The use of ceramic plate with a high air entry value is not necessary when much lower matric suction is to be applied. The water outlet in the pressure plate apparatus was connected to a burette in order to keep the ceramic plate saturated. The test started with saturating the ceramic plate with distilled de-aired water.

Flushing the water compartment occurred regularly to remove the diffused air bubbles collected beneath the ceramic disk. It is important to note that the existence of diffused air bubbles in the water compartment results in the discontinuity between the water phase in the specimen and the source of water. The water phase continuity has to be established throughout the experiment to warrant the liquid transfer of water into and out of the specimen.

The process of saturating the ceramic plate is called flushing process. The process was performed as follows: the soil specimens were moved out of the pressure chamber and replaced with de-aired water, see Fig. 5.6(right). Whole ceramic place was flooded with de-aired water. The pressure chamber was applied air pressure of about 500 kPa, and the water-air mixture flowed though the ceramic plate out to the burette. The flushing process was completed when there was no air bubble observed flowing out of the pressure plate. It took approximately two hours to complete this process. Next the de-aired water was moved out of the pressure chamber. The water left on the ceramic plate was wiped
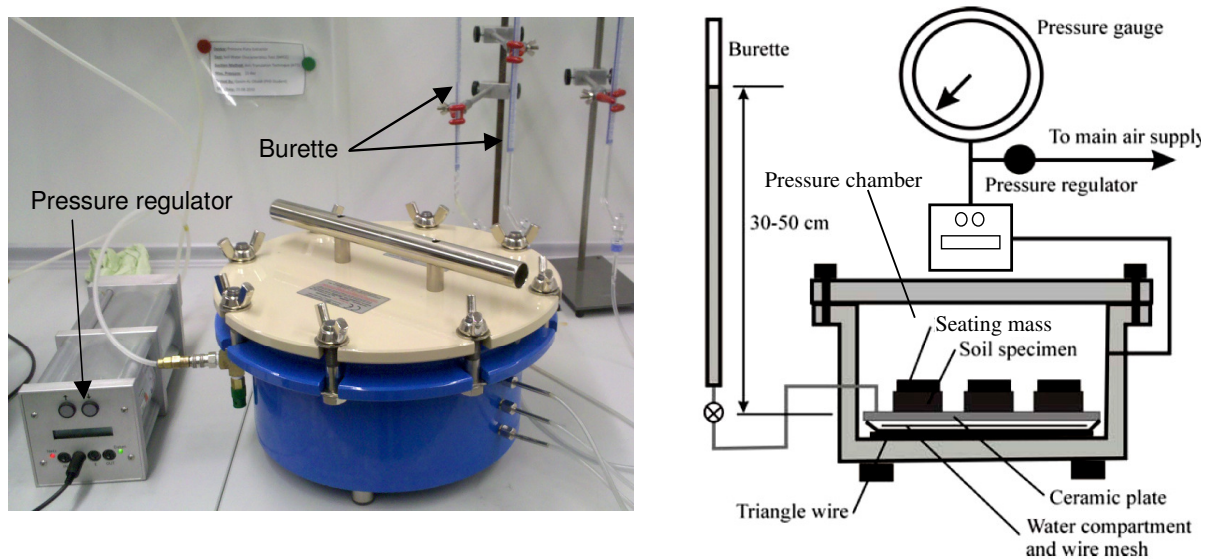
Figure 5.6: Setup of the pressure plate.

off. The specimens were placed on the ceramic plate. A seating mass of about 50 g was placed on the specimen to maintain good contact between the specimen and the ceramic plate (Fredlund and Rahardjo, 1993).

The pressure chamber was closed tightly. Firstly, the burette was opened and closed quickly so water in ceramic plate could reach the specimens. Air pressure was slowly and incrementally applied to reach the target matric suction. When the air pressure in the chamber was higher than the water pressure in compartment controlled by burette, the burette valve was opened to apply fixed water pressure under the pressure plate.

The change in the mass and dimensions (i.e., the diameter and height) of the specimen were monitored. A precision weighing balance with an accuracy of 0.001 g was used to weigh the specimen. The dimensions of the specimen were monitored using a ruler that could measure the specimens with accuracy of 0.02 mm. At low matric suction (i.e., below 50 kPa) measuring the soil specimen dimensions was performed only after the specimen had reached equilibrium based on the water content versus time plot. After each suction equilibration, the ceramic disk was re-saturated by the flushing process. Both water content and the void ratio of the specimen were used to judge the equilibrium conditions before applying the next matric suction step. The matric suction ψ is an air pressure in the chamber (u_a) subtracted from the water pressure (u_w) applied by the burette. The air pressure increased in each test step to draw the drying curve, and decreased to draw wetting curve. The step size of the pre-determined matrix suction are presented in Table 5.3.

Table 5.3: Axis-translation technique: target matric suction

	Target matric suction					
Step	1	2	3	4	5	6
ψ (kPa)	20	50	100	200	400	1000

5.2.2.3 Chilled-mirror method to measure total suction

The chilled-mirror hygrometer used in this study is a water activity meter type 3TE produced by Decagon Devices Inc. Fig. 5.7. The equipment has a special specimen closed chamber of about 12 cc in volume, where the soil specimen is contained. The results obtained from this measurement are used to calculate the total suction of the specimen. The total suction of the specimens pre- or post-oedometer tests and THM column test was measured utilising these methods.

Prior to use, the chilled-mirror hygrometer was verified for its performance in measuring total suction. The verification was carried out using standard salt solutions provided by the manufacturer. The readings obtained for the standard salt solutions were found to vary less than 0.2% RH with a response time of no longer than three minutes. The fast measurement time of the device enables many total suction measurements to be conducted quickly.

The sensor in the chilled-mirror apparatus measures the relative humidity of the air space over the soil specimen at a given temperature. Agus and Schanz (2005) stated that the technique can be used for suction measurements as low as 1500 kPa if the maximum measurement error is limited to 30%. The total suction in the chilled-mirror technique can be calculated using the Kelvin equation, which is the thermodynamic relationship between total suction and relative humidity of the vapor space in the soil (Sposito, 1981). The thermodynamic relationship between the total suction and the partial pressure of pore water vapour is written in Edlefsen and Anderson (1943) and was subsequently adopted by Leong et al. (2003); Tripathy et al. (2003) as follows:

$$s_t = \frac{RT}{\nu_{w0}\omega_v} \ln\left(\frac{u_v}{u_{v0}}\right) \tag{5.1}$$

Where s_t is the total suction (kPa), R is the universal (molal) gas constant (i.e. 8.31432 J/(mol K)), T is the temperature in Kelvin (K), ν_{w0} is the specific volume of water or the inverse of the water density (m^3/kg), ω_v is the molecular mass of water vapour (i.e. 18.016

kg/kmol), u_v is the partial pressure of pore water vapour (kPa), and u_{v0} is the saturation pressure of water vapour over the flat surface of pure water at the same temperature (kPa). The term $\left(\dfrac{u_v}{u_{v0}} \right)$ is called relative humidity (RH).

The mechanism of the chilled mirror device is described briefly as follows. As shown in Fig. 5.7(b), a soil sample in equilibrium with the surrounding air is placed in a chamber containing a mirror and a detector of condensation on the mirror. The temperature of the mirror is precisely controlled by a thermoelectric cooler. The condensation point is determined using a photoelectric cell, which detects the presence of condensed water on the mirror through a reduction in the mirror's reflection. A thermocouple attached to the mirror records the temperature at which condensation occurs. The relative humidity is computed from the difference between the dew-point temperature of the air and the temperature of the soil sample, which is measured with an infra-red thermometer. A fan is included in the sealed compartment to speed up the equalisation period between the sample and the surrounding air. An average equilibration time of approximately three minutes was taken for the total suction measurement of the materials used in this study.

The process of measurement using this technique was started by placing the chamber with the soil specimen or salt solution into the device. In the case of compacted specimens, small pieces of specimen were cut from the part of compacted specimens after the tests. Extra care was taken when cutting the compacted specimens with high sand content as the process might introduce structural disturbance to the specimens. There was concern that disturbance might affect the capillary component of suction. The soil in the specimen chamber in the device was able to reach isothermal equilibrium, which was defined as the difference between the temperature of the vapour space and the specimen. The device showed the difference in temperature between the headspace and the mirror. The temperature of the mirror should be set to a slightly higher value than the temperature of the vapour space, particularly when measuring high relative humidities (or low total suctions) as condensation may occur on the mirror (Agus and Schanz, 2005). The chamber was subsequently closed and after reaching equilibrium, and the relative humidity and the temperature of the vapour space were displayed.
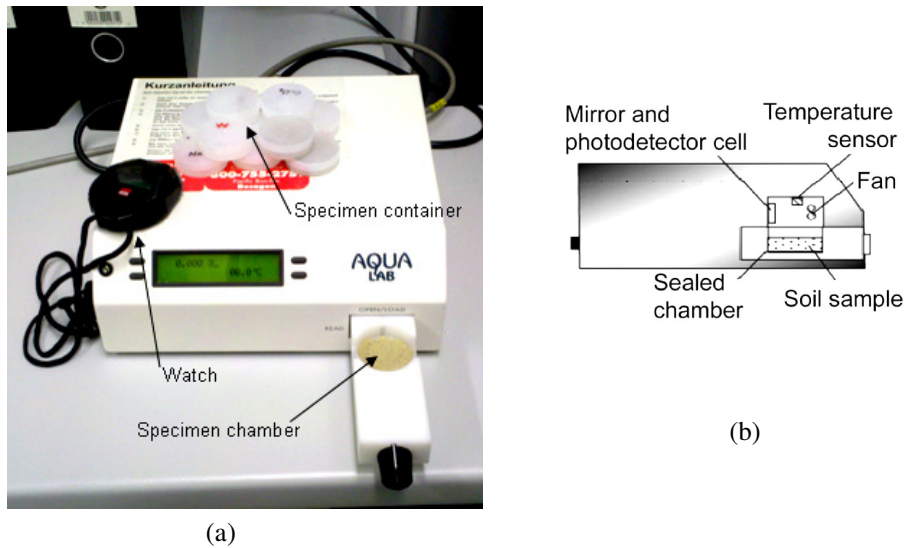
Figure 5.7: (a) The chilled-mirror hygrometer used in this study, (b) Scheme of chilled-mirror dew-point psychrometer (Cardoso et al., 2007).

5.3 THM column tests

5.3.1 Introduction

Experimental and theoretical study of the behaviour of buffer materials was performed mainly in terms of thermal, hydraulic and mechanical loading separately or coupling two of them. Investigating the effects of temperature on saturated soil behaviour has been a topic of discussion for a long time (Campanella and Mitchell, 1968; Baldi, 1987; Hueckel and Pellegrini, 1992), but has recently attracted intense attention once again (Delage et al., 2000; Abuel-Naga et al., 2007; Laloui and Cekerevac, 2008; Abuel-Naga et al., 2009; Liu and Xing, 2009; Delage et al., 2009). The effect of temperature on the behaviour of unsaturated soils has also drawn increasing interest from both experimental and numerical simulation performing research groups (Grifoll et al., 2005; Jia et al., 2007; Fernández et al., 2007), and this is due to the necessity of understanding engineered barrier system behaviour (i.e. the behaviour of buffer and sealing materials).

The mechanical behaviour of unsaturated soils due to the change of water content and temperature has been studied experimentally mainly based on element test data such as data obtained in isochoric or oedometer cells (Villar, 2002; Tang and Cui, 2005; Romero et al., 2005; Cui et al., 2011). The effect of temperature on soil hydraulic conductivity has been also studied for saturated cases (Cho et al., 1999; Delage et al., 2009) and unsaturated case, (Ye et al., 2012). For example, in Ye et al. (2012) the influence of

temperature on soil hydraulic conductivity in unsaturated soil was assessed based on measured relative humidity and employing independently obtained soil water retention curves derived by means of the equilibrium method (i.e. the axis translation technique and the vapour equilibrium technique). However, the relation between suction and soil water content varies with time (Schanz et al., 2010a); therefore applying the equilibrium method to determine the transient water content from the soil water retention curve may yield inaccuracy for long term experiments such as the case for expansive and low permeable materials.

To investigate the coupled THM behaviour of buffer material in transient state and track temperature, water content, suction, and swelling pressure development, two principal experimental approaches are performed, including the full-scale field test or laboratory tests such as mock-up test or prototype test. In terms of the full-scale field test approach, such tests have been carried out within several projects, such as Alonso et al. (2005a); Martín et al. (2006); Bossart and Nussbaum (2007); Geet et al. (2009). However, obtaining experimental data from in-situ/field tests is expensive and time consuming, and at the same time controlling the boundary and initial conditions in-situ is difficult, uncertainty prone, and even may be impossible, e.g. because of the large scale. For these reasons, a concept of a column test has been developed as a tool to study the THM-coupled behaviour of the buffer. The column testing device is modelling the processes that take place in a radial slice of the buffer cross section, to reveal the coupled phenomena in the buffer material (Fig. 5.8). As shown in Fig. 5.8, the canisters containing the radwaste are surrounded by a material which forms a buffer between the canister and the host rock. The buffer material, initially unsaturated, is subjected to relatively high temperature emitted by the radioactive waste and a hydraulic gradient induced by water intruding from the host rock. In addition, the material undergoes swelling or shrinking according to the variation of water content and temperature. Therefore, the experimental setup has to monitor the time history of temperature, pore water pressure, and mechanical displacement.

Column–type testing devices used for applying hydraulic or thermal gradients are reported in Mohamed et al. (1992); Cuevas et al. (1997); Gatabin and Billaud (2005); Villar et al. (2006); Bag (2011); Ye et al. (2012). In particular, Mohamed et al. (1992) designed an apparatus for imposing heat and water flow and for monitoring the temperature and swelling pressure as a function of time and space. The size of the sample is about 80 mm in diameter and 87 mm in length. Cuevas et al. (1997) developed a column device with larger dimensions (150 mm in diameter and 130 mm in height). This column device
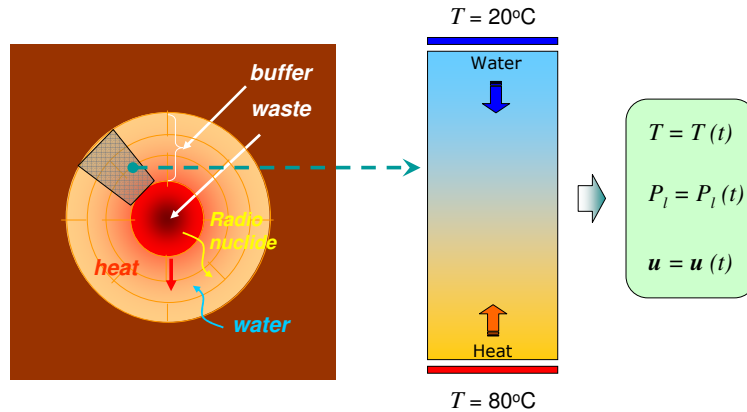
Figure 5.8: Schematic illustration of a cross section of the buffer system with a diagonal slice element with the boundary conditions for the inner and outer sides.

allows thermal and hydraulic gradients to be applied and provides measurements for the temperature distribution profile during the test. However, the water content is determined only after completing the test. Gatabin and Billaud (2005) carried out similar kind of column test on relatively large clay samples which were 200 mm in diameter and height. The equipment allows the temperature, relative humidity profiles and axial stress to be measured at the top during heating and hydration tests, but the water content is not measured simultaneously with temperature and relative humidity. All of the column test devices discussed here do not consider the possibility to control the temperature of the supplied water.

This section presents an original THM column setup with new features that are introduced based on the experience gained after performing a series of tests using a column device previously developed and described in Manju et al. (2008). The main features of the new column device are: (i) measurement of the swelling pressure at the top and bottom of the sample; (ii) ability to apply suction and temperature gradients; and (iii) measurement in three sections along the sample height of water content, suction and temperature with a minimal disturbance to the sample itself. In addition we utilized a new solution to measure the relative humidity (RH) providing a temperature-controlled environment for the RH-sensors, thereby guaranteeing equal temperature in the RH-sensor's chamber and in the sample near the location of the RH-sensor, thus avoiding vapour condensation. The advantages of the column device presented here are: (i) it allows the soil water retention profile to be determined directly by measuring water content and suction at the same sample cross-section perpendicular to the sample vertical axis of symmetry; (ii) it provides the possibility to control the temperature boundary condition in a more reliable

way by combining the water cooling system and the electrical heater.

5.3.2 Main features of the column test device

The cell is divided in three parts: the bottom plug, the cylindrical cell body and the top plug. The body of each part is made of stainless steel 316L. Three parts are attached each other and attached to the base plate by six 12 mm diametric screws for each part. The entire device is placed on a shelf. The shelf can change the slope of the column in order to manage the parts of specimen in or out of the column.

The Bottom plug consists of a base plate, a bottom load cell, electrical heating, hydraulic cooling and water supply systems. It is made up of stainless steel 316L. The base supports the cell body on its external collar and accommodates the bottom load cell, the hydration system and the heating plate internally. It is attached to the cylinder cell body by 3 12 mm diameter screws. Three other screws keep the bottom body attached to the base plate. The water tightness of the cell is guaranteed by means of O-rings capable of withstanding temperatures of up to 100°C.

Cell body including PTFE casing and metal body:

PTFE casing: The role of the casing is to limit heat transfer by conduction, either radially or longitudinally. In order to avoid the heat dissipation to the greatest possible extent, the internal part of the cell is made out of Teflon PTFE, and the thermal conductivity is 0.23 W/m.K. The thickness of the casing is 17 mm. Its internal diameter is 150 mm and height is 410 mm. The casing is pressed tightly in the cell body.

Metal body: The metal body ensures the rigidity of the cell and mechanical support of the PTFE casing against the swelling pressure of the clay. To provide the above reinforcement it is made out of stainless steel. The thickness of the cell is 25 mm. Its internal diameter is 167 mm and the height is same as the casing, 410 mm. The wall of the cell body is provided with drilling to install the instrumentation. The cylinder is therefore pre-equipped with calibrated holes to the diameters of the corresponding sensors.

Top Plug is equipped with a conduit through which a coolant flows to maintain a constant temperature limit at the top of the sample. The top part of the conduit is covered with a stainless steel plate to ensure water tightness and mechanical support. The top plug also has a hydration water distribution circuit via a porous and sintered 3 mm thick stainless steel disk. The conduit base of the coolant system is

in contact with the sintered stainless steel disk to ensure that the hydration water is distributed homogeneously to the sample. The cooling system along with the porous and sintered stainless steel disk is placed within the Teflon casing. A heating system similar to the one in bottom plug is also placed in top plug. This arrangement has been provided to study the effect of uniform temperature on the buffer and as well as to observe the effect of different temperature gradients on the sample. The top part of the conduit has the arrangement for placing the top load cell. To center and guide the load cell, the assembly is placed in the external collar which is covered with a stainless steel plate measuring 192 mm in diameter and 50 mm in height. The stainless steel plate secures the load cell in order to operate at a constant volume. Six-6 mm diameter screws are used to block both the external collar on the cell body and the top plate.

De-aired and de-ionized water is supplied by water supply system on both top and bottom faces of the specimen. The water is injected into the cell by means of burette placed over a precision scale and nozzle fitted with a stop valve through the upper hydration line. Sample will be saturated under the hydraulic head as the sample containing bentonite is able to be saturated by diffusion at low external pressure.

The outer arrangement of THM column in laboratory is presented in Fig. 5.10. The cell is placed on a shelf that can be inclined in order to place in or remove the specimen. Table 5.4 summarises the quantity and characteristics of the instruments in order to better understand the arrangement of THM column cell.

5.3.3 Description of the measuring equipment

5.3.3.1 Sensors for measuring the water content

The function of the TDR-sensors for measuring water content is based on obtaining the dielectric constant of the material along waveguides by observing reflected waveforms. An electric pulse is supplied to the sensor and the reflected wave is digitally recorded. The dielectric constant of the material is determined by locating the inflection point on the plot of the electric resistance versus time. An automated data interpretation routine is used to locate this inflection point from the sensor output. The dielectric constant may be related to the soil volumetric water content and usually for standard soils, and to maintain constant temperature the volumetric water content is calculated via Topp's relation (Topp et al., 1980). However, in this study, temperature was not always constant,
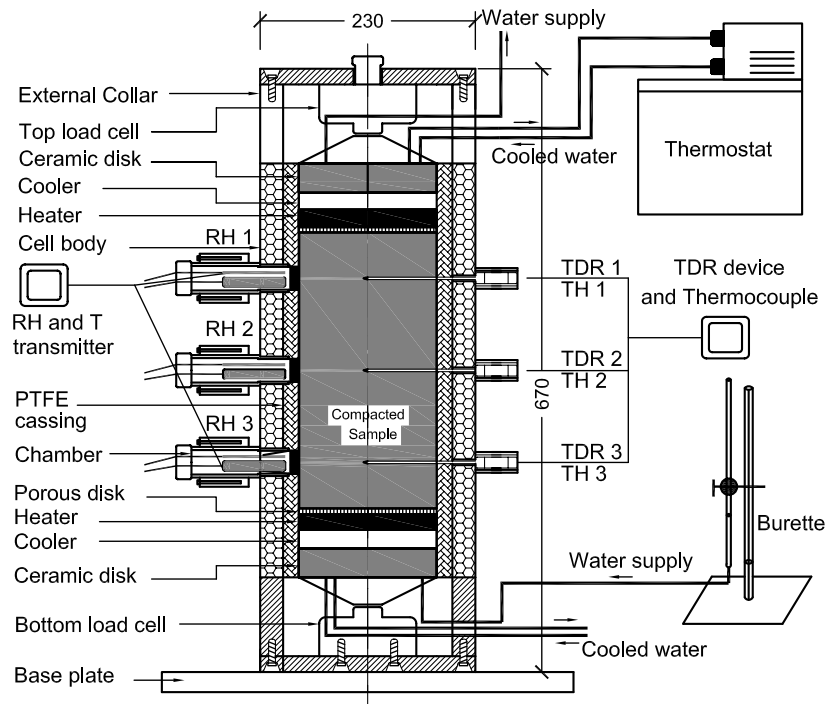
Figure 5.9: Scheme of the column setup.

and the material was an expansive clay containing soil; therefore the gravimetric water content was used as a function of the temperature. In addition the dielectric constant was obtained using an interpolation procedure to collect data using a set of laboratory calibration tests.

The column device discussed in this paper is equipped with mini-buriable waveguides Trase 6050X3K1 from Soil Moisture Equipment Corp., California. These mini-buriable waveguides are designed for use in making shallow, near surface measurements as well as for laboratory column testing. The waveguides are 80 mm long and 3 mm in diameter with 2.5 cm spacing between the outer waveguide. The advantage of using TDR-waveguides is that they measure the transient water content of the soil sample instantaneously and due to their small size, their presence induces minimal disturbance to the sample. In the case of high compacted specimens, it is difficult to place the waveguides into the specimen. For this reason, holes of a diameter the same as the diameter of the waveguides were drilled prior to TDR installation.
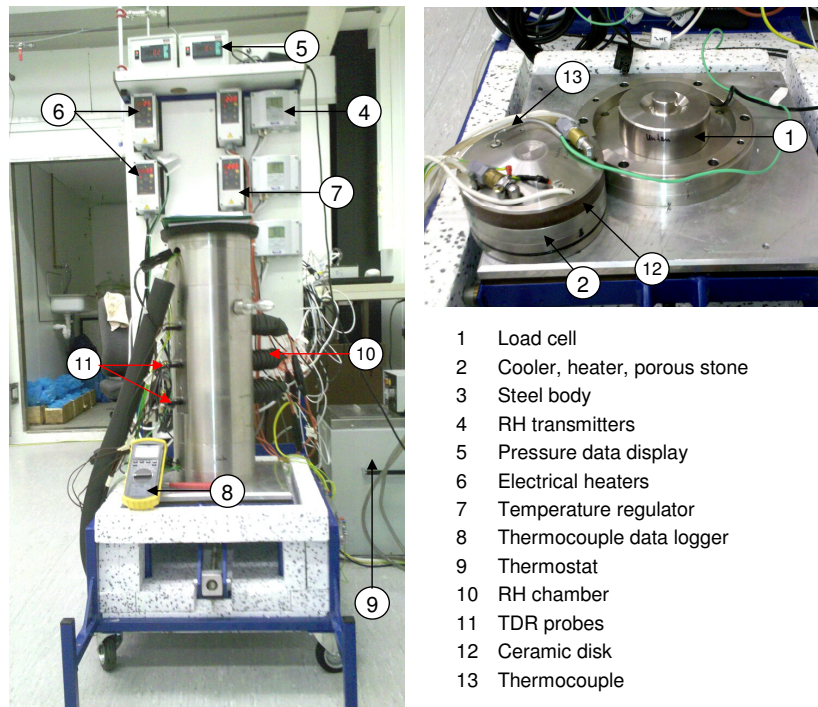
Figure 5.10: The column device for coupled thermo-hydro-mechanical testing.

5.3.3.2 Sensors for measuring suction

Temperature controlled chambers:

A separate temperature controlled chamber is designed where relative humidity (RH) sensors are placed Fig. 5.11. It is capable of calculating the total suction at the surface of the clay specimen by means of measured relative humidity. The temperature in the RH chamber needs to be regulated at the same temperature as that inside the soil specimen measured by a thermocouple at the same level. This balancing temperature is to avoid water condensation in chamber's wall in case of high relative humidity conditions. The temperature controlled chamber is made of bronze and is screwed to the steel wall of the cylindrical cell body. The inside diameter of the cylindrical chamber was 30 mm outside the steel body and 25 mm inside the steel body Fig. 5.11. The temperature inside the RH chamber was regulated by the embedded heater and temperature sensor of each chamber. To make the hole watertight, it was fitted with an O-ring and a porous stone disk was placed next to the O-ring. The purpose of placing the porous stone disk was to allow the exchange of vapor between the soil sample and the external chamber where the RH sensors were placed. Furthermore, it does not allow the specimen to extrude due to swelling into the chamber. The chamber hole can be closed by replacing the porous stone

Table 5.4: Measuring devices used in the column test

Instrument	N°	Function	Installation format	Declared precision
RH–sensor, VAISALA HMT337	3	RH–measurement	Near soil surface	±0.6% in RH = 0-40% and ±1% in RH = 40-97%
TDR probe	3	determination of water content	Inside soil mass	±2% in w = 0-30%
Load cell	2	measurement of axial force	On top and bottom faces of the column	±0.2%
Thermocouple	5	measurement of temperature	3 inside soil mass 2 inside the heater	T = ±1%
Electrical heater	2	Heater	On top and bottom faces of the column	T = ±0.25%
Thermostat	2	Cooler	On top and bottom faces of the column	T = ±0.1°C
Temp. controlled chamber	3	temperature regulation	Near soil surface	T = ±0.25%

with a rubber cap when conducting the tests with positive pore water pressure.

Temperature and relative humidity transmitter

These sensors are used to monitor the suction profile at the along surface of the cylinder sample. The sensors used are VAISALA HMP337, which include a humidity sensor that changes its dielectric characteristics with small variations in humidity (capacitive type relative humidity (RH) sensors), see Fig. 5.12. They also include temperature probes (Pt100) using a thermocouple type. The accuracy of the humidity sensors including non-linearity, hysteresis and repeatability is ±1.0% over the range of 0-90%RH and ±1.7% over the range of 90-100% RH theoretically for temperatures +15...+25%RH. In the range of -20...+40°C, the accuracy is ±(1.0+0.008×reading)%RH. In the range of -40...+180°C, the accuracy is ±(1.0 + 0.015×reading)%RH. The accuracy of a temperature sensor at a given temperature is presented in Fig. 5.13 by Vaisala-Oyj (2011). As in results of experiments with temperature changes, the range of temperature is from 20°C to 45°C. In this current range of temperature, the accuracy of the attached temperature sensor varies from ±0.2 to ±0.3°C. Each sensor is fitted with analogue 2-10 V output for 0-100% relative humidity and protected by cylindrical stainless steel filter. The HM sensors are 12 mm in diameter. In order to avoid deformation, corrosion and defection in the sensor's

Figure 5.11: (a) HT-MC temperature regulator. (b) Scheme of temperature controlled chamber.
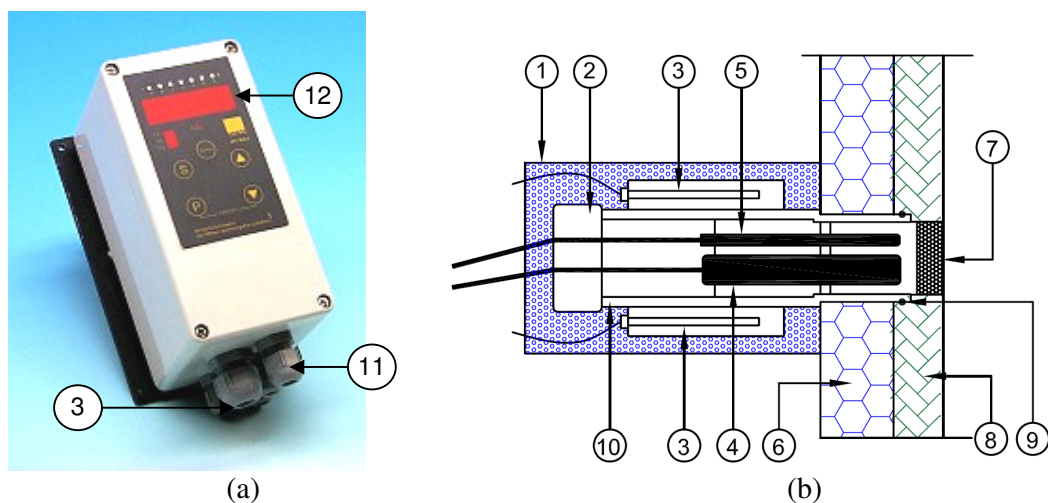
1	Temperature isolation coat	2	Rubber cap	3	Heater and sensor
4	RH probe	5	Temperature probe	6	Steel body
7	Porous stone	8	TPFE casing	9	O-ring
10	Bronze body	11	Temperature cable mount	12	Display with keypad

fully saturated state, they are designed not to be embedded in the sample.

5.3.3.3 Sensors to measure temperature

Thermocouples (T-type sensors) are used to measure temperature at three levels along the column height. The three T-type sensors are encased into the specimen using the openings along the column that had been formed prior to sample installation. The Omega HH147 data logger is used to read and convert the electrical signal to temperature value, (Fig. 5.10, N°8). The technical configuration states: "resolution 0.1°C/0.1°F, NIST Traceable certificate of calibration."

In order to restrict water leakage from the drilled holes for the temperature and TDR probes, the sensor probes were covered by a plastic tube ending with rubber O-rings. Validation tests had been performed, and the results indicated that the waterproof for the probe holes was functional.

1	Signal and power cable	2	Cable gland for PC connector	3	Cable gland for
4	Cover screw (4pcs)	5	Display with keypad		temperature sensor
7	Thermocouple probe	8	Relative humidity probe	6	Cover LED
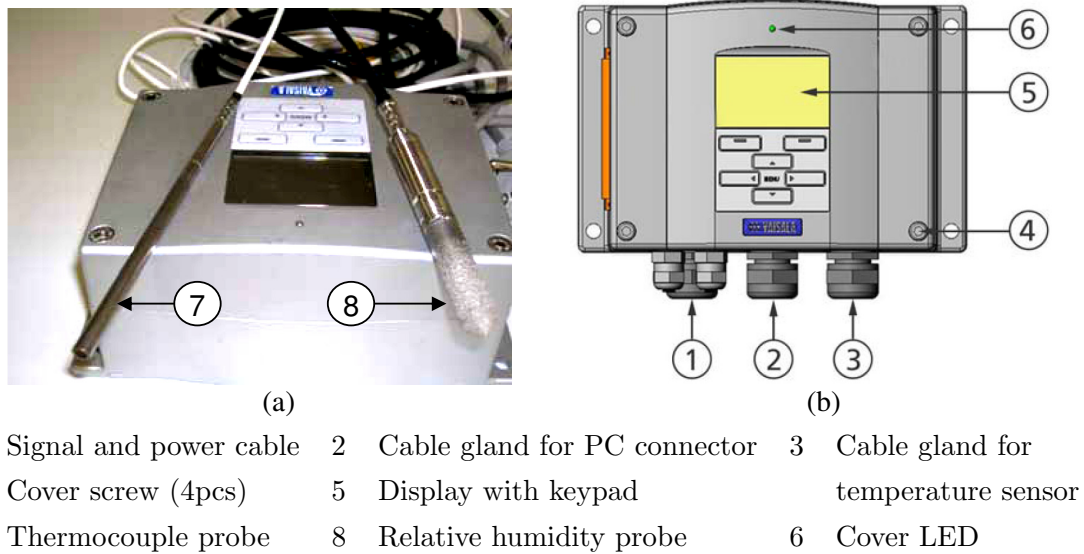
Figure 5.12: Temperature and relative humidity transmitter.
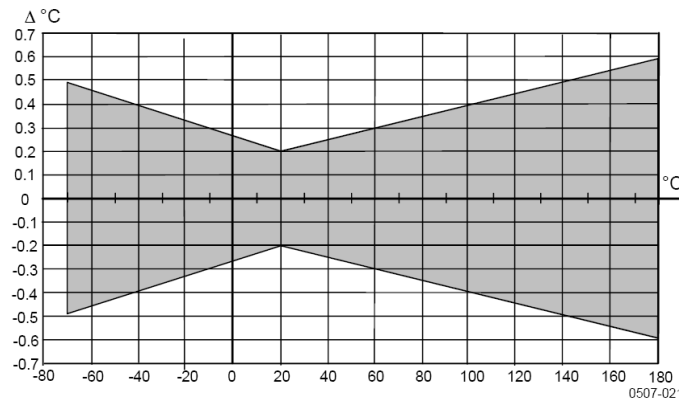
Figure 5.13: Accuracy over temperature range, Vaisala-Oyj (2011)

5.3.3.4 Load cells

The column was equipped with two load cells in order to measure the axial swelling pressure. The load cell included stainless steel pressure transducers (N°1) and the digital data display (N°5) Fig. 5.10. The load cell parameters have transducer type KAM-E, KI-0.2, measurement range 100kN, accuracy 0.2%, nominal temperature range -20 to +60°C. Cells are calibrated in compression by FGP and directly associated with a specific conditioning drawer. Hence, the 0-10V analogue output of the drawer has also been calibrated and ranges exactly between 0 and 100kN. However, the design does not allow the sensors to be used at high temperatures; they are temperature compensated up to 60°C. During the experiment, such conditions are not problematic since the load cell

has been insulated with the help of an isolating ceramic plate placed at the bottom end of the heating system.

5.3.3.5 Electrical heaters and hydraulic cooling system

Each electrical heater plate includes four heater sources embedded on the metal plate and one thermocouple sensor (Fig. 5.10, N°2). The electrical source provides electrical lines, all of which are temperature resistant up to 200°C and watertight. The temperature of electrical heaters are controlled by thermal regulators (N°6) using the thermocouple sensor. The HORST serial HT-MC1 has a heating power of up to 3450 Watts, and the degree of accuracy is 0.25%.

The hydraulic cooler plate is located next to the electrical heater. It has two water lines in/out from the cooler plate connected to a thermostat. The thermostat (N°9), a **mgw-Lauda** Regie can control the water temperature from -50 to 150°C at an accuracy of ±0.02°C theoretically. Before conducting the test, a dummy test was carried out to measure effective temperature on the surface of the specimen. The bottom part was plugged in the cell body; one thermocouple was embedded onto surface of the porous plate to measure the corrected temperature on the surface of the specimen. The dummy test demonstrated that if specimen surface needed to be cooled to 20°C, the water of thermostat was set at 16°C and heater was heated to 21°C simultaneously. To heat the surface of the specimen to 80°C the heater had to be heated to 82°C, and the cooler was turned off.

5.4 Calibration tests

5.4.1 Assessment of an expansion of the inner column volume with temperature

Many devices equipped with the THM column-type setup need to be calibrated at non-isothermal conditions. One issue is the extent to which the column will expand and whether the inner volume of the column is a substantial expansion or reduction. This factor will significantly effect on the swelling pressure measurement. The inner material of the column was made out of TPFE, which expands less at increasing temperatures. However, it is necessary to quantify the inner volume change during experimental process. A test was designed to verify the expansion of the column Fig. 5.14(a). The soil specimen
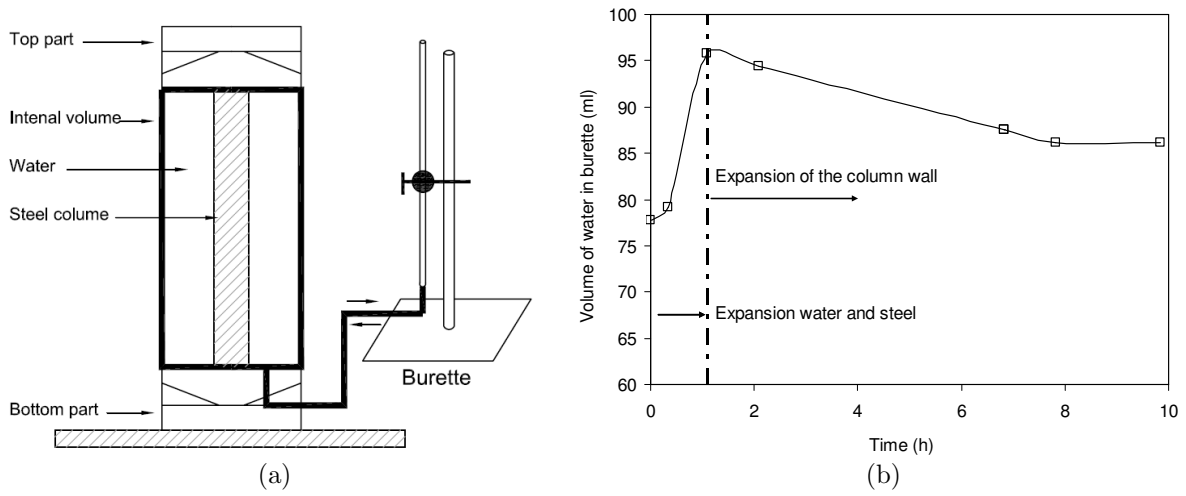
Figure 5.14: (a) Schematic plan of the verification test for internal volume expansion. (b) Volume water of the burette with time.

was substituted with water. The steel column L316 with rubber on both heads was placed inside the specimen to maintain the height of the column constant. The mean volumetric thermal expansion coefficient of the steel is 4.80E-5 (1/°C) within 0-100°C (Product data sheet stainless steel 316/316L, 2007). The burette was connected to the bottom water supply to measure water level of the column. The column was heated on both the bottom and top, and the water level of the burette was observed to calculate the expansion of the column.

When the column was heated on both sides, the volume of water in the burette increased in about one hour then decreased to the steady state as in Fig. 5.14(b).

- In about one hour, the water and steel inside the column were heated from 20°C to 80°C and expanded in the first state. The expansion of the material inside the column increased the water in the burette.

- In the second state, because the PTFE layer resisted the temperature conducting to the steel wall, the temperature of the steel wall increased slowly to 36°C. The increase in the PTFE casing and the steel body temperature of the PTFE casing and steel body induced an expansion in the internal volume of the column. The internal volume of the column increase made the water volume in the burette decrease (Fig. 5.14(b)).

$$\alpha_V = \frac{1}{V}\left(\frac{\Delta V}{\Delta T}\right) \tag{5.2}$$

Table 5.5: Calculation of the expansion for the internal volume of the column wall

	Steel	Water	Total column	Expansion (cm^3)	
				Material	Column
α_V (1/°C)	4.80E-05	2.14E-04			
ΔT	60	60	60		
ΔV (cm^3)	7.5	34.7	8.3	42.2	33.9
Volume expansion (%)					**0.64%**

The expansion of the L316 dummy steel and water are known as Eq. 5.2; therefore the expansion in the internal volume of the column wall can be calculated. Table 5.5 describes how the expansion of the column can be calculated in the steady state. The maximum materials expansion was 8.3 cm^3; the water volume in the burette only increased to 42.2 cm^3. Therefore 33.9 cm^3 is the volume expansion of the column. It can be seen that the volume of the internal space of the column increased by about 0.64%. When the soil was heated on both sides, the expansion of the column was observed at 0.64%; therefore when the soil was heated in only one head of the column, the expansion of the internal volume was smaller. In summary, the expansion of the inner volume of the column is *insignificant*.

5.4.2 Calibration of the load cell with temperature

Although the ceramic disk plays a thermal resistant role, the values measured by the load cell were also calibrated before the experiment to 20°C and at 37°C (the temperature at the load cell when the bottom heater was heated at 80°C)). The load cell on the top and the bottom were used to compare with each other at different temperatures. The top load cell was always kept at 20°C, while the bottom load cell changed temperature by heating the bottom heater. The wood dummy was 10 cm in diameter and 30 cm high, and it was placed in the column. The wood dummy played a pressure transfer role and did not allow heat to be transferred from bottom to the top. It was found that the values measured by the load cell are temperature dependent. The temperature calibration of the load cell is presented in Fig. 5.15.
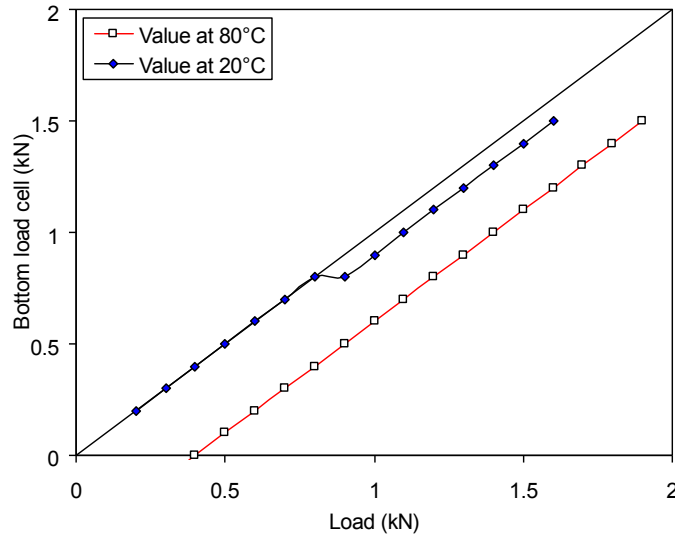
Figure 5.15: Calibration of the load cell with temperature at 20°C and 80°C

5.4.3 Calibration of RH sensors

The relative humidity sensors (RH 1, RH 2, RH 3) were calibrated based on the chilled-mirror method. The chilled mirror method is another method to determine relative humidity based on the dew-point technique. This method could achieve higher accuracy and more stability than a psychrometer method (a thin film which varied its dielectric constant according to moisture) (Agus and Schanz, 2005).

The RH transmitters were calibrated using six different salt solutions: NaCl 38 g/l, NaCl 63g/l, NaCl 125 g/l, KCl saturated, $NaCO_3$ saturated and LiCl saturated. The salt solutions were placed in six desiccators. The RH sensors and thermometer sensors were embedded in desiccators for at least three hours until the measurement reached a steady state, Fig. 5.16(a). Afterwards the salt solutions were measured utilising the chilled mirror method. Two results are compared in the Fig. 5.16(b). The relative humidity was converted to suction by Kelvin equation (Eq. 5.3) from Leong et al. (2003).

$$s_t = \frac{RT}{\nu_{w0}\omega_v} \ln\left(\frac{u_v}{u_{v0}}\right) \tag{5.3}$$

Where s_t is total suction (kPa), R is the universal (molal) gas constant (i.e. 8.31432 J/(mol K)), T is the temperature in Kelvin (K), ν_{w0} is the specific volume of water or inverse of density of water (m^3/kg), ω_v is the molecular mass of water vapour (i.e. 18.016 kg/kmol), u_v is the partial pressure of pore water vapour (kPa), and u_{v0} is the saturation

(a)   (b)
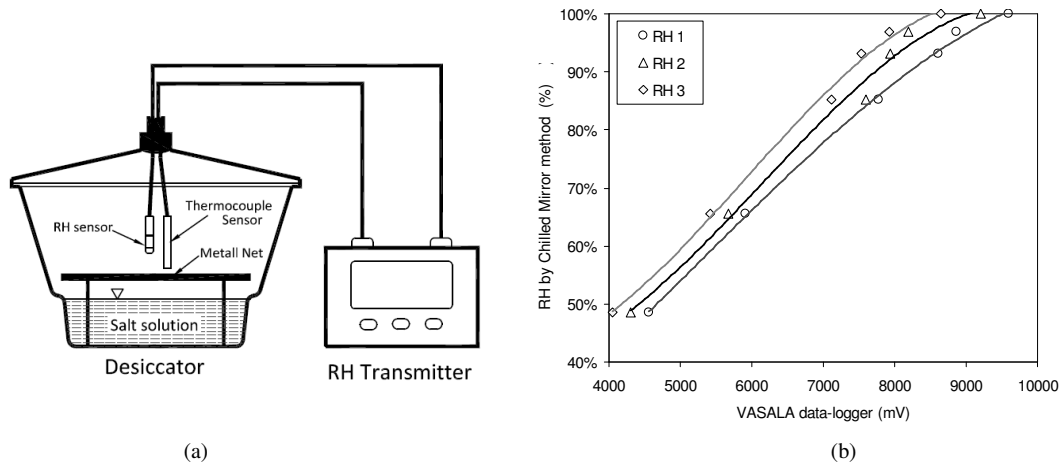
Figure 5.16: (a) Setup of the RH–sensor calibration test, (b) calibration from voltage signal of VAISALA RH-sensors datalogger to relative humidity measured by chilled-mirror method

pressure of water vapour over the flat surface of pure water at the same temperature (kPa). The term $\left(\dfrac{u_v}{u_{v0}}\right)$ is called relative humidity (RH).

5.4.4 Calibration of TDR–probes

Several investigations have been made in the past to study the effect of temperature on the soil physical characteristics. The effect of temperature on soil dielectric properties of the main soil ingredients have been separately characterised. It was found that the dielectric properties of solid phase and the air in the soil pore system show negligible dependence on temperature variation (Weast et al., 1986), whereas the dielectric constant of pore water is significantly temperature-dependent and decreases with increasing of temperature, (Weast et al., 1986; Roth et al., 1990). Weast et al. (1986) presented an empirical equation for the temperature dependence of the dielectric constant. Other researchers also attempted to explain the effect of temperature on TDR-probe readings for different soils, (Pepin et al., 1995; Wraith and Or, 1999; Skierucha, 2009). The detail discussion on this issue is presented in the next section.

Schanz et al. (2011a) carried out TDR–probe calibration study for sand-bentonite mixture (the same material as in the present paper) and proposed an explanation for the soil and soil water behaviour due to temperature changes. The calibration was performed by the use of an apparatus specially designed for this purpose. This part presents the results
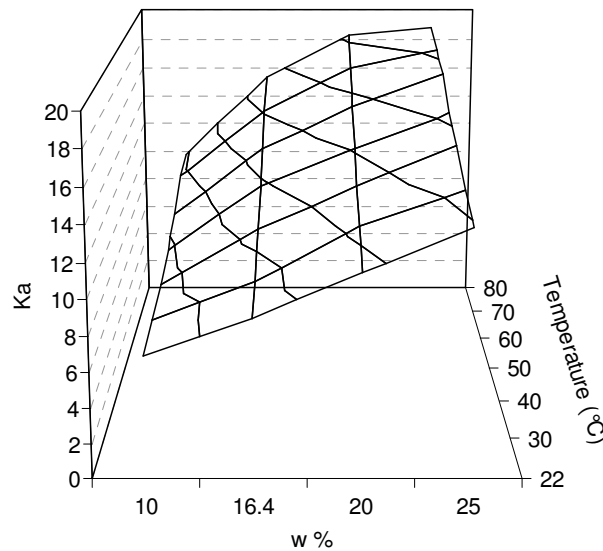
Figure 5.17: The approximation of the gravimetric water content, dielectric constant, and
             temperature relationship for the used sand-bentonite mixture.

of the TDR probe, which is partially inserted into the sample as it is in the column.
Figure 5.17 presents the relationship between the gravimetric water content, dielectric
constant and temperature. The gravimetric water content is determined via interpolation
of the results in Fig. 5.17.

5.4.5 Calibration of oedometer tests

5.4.5.1 Calibration of the load cell with temperature

The load cell was placed inside the oedometer device. The accuracy of the pressure
transducer changes with the increasing temperature up to 80 °C. Therefore, the calibration
test was carried out at 20°C and 80°C. For the load cell calibration, an independent
loading method is required. A loading frame with weight masses is used to calibrate the
test (Fig. 5.18). The loading step with weight masses in the loading frame was 0.1 kN
each loading step less than 1.0 kN and 1.0 kN and each loading step greater than 1.0 kN.
The calibration was carried out for both loading and unloading states.

The result of calibration is presented in Fig. 5.19. The result read in loading frame display
is called an apparent pressure. The pressure applied by mass level is called real pressure.
The apparent pressure illustrated by the load cell is linear and parallel with the real
pressure loaded by mass loading frame. There is a very little offset between real and
apparent pressure read by the load cell at 20°C. The error between loading and unloading

1	Load cell	2	Heating coat	3	Temperature isolation
4	Inner thermometer sensor	5	Outer thermometer sensor	6	Heater line
7	Thermostat	8	Thermocouple data logger	9	Weight mass
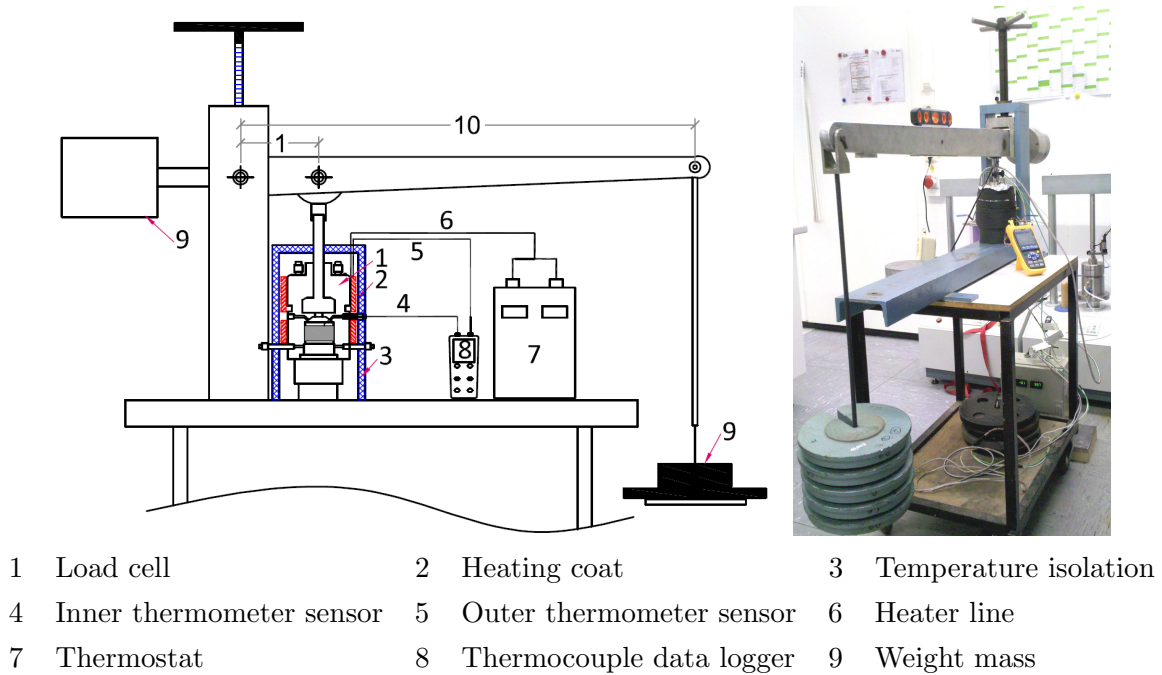
Figure 5.18: Scheme of load cell calibration with temperature of 20°C and 80°C

by read pressure is not the same. It shows that hysteresis occurs between the loading and unloading steps measured by the pressure transducer. There is a larger offset between the real and apparent pressure read by the transducer at 80°C. The relationship between the apparent pressure and the real pressure at 20°C and 80°C is parallel, Fig. 5.19(a); therefore the calibration pressure at higher pressure can be extrapolated from this calibration result. The calibration test indicates that a certain pressure value can be applied considering the difference between the apparent pressure and the real pressure by Fig. 5.19(b).

Fig. 5.20 presents the error of the load cell if there were no calibration. It indicates that at high loading pressure the error in percentage is small; however, the error increases significantly at low loading pressure.

5.4.5.2 Calibration of the temperature guage

The calibration was carried out for the specimen at 20°C and 80°C. The dummy was substituted for the soil specimen in the test. The dummy is steel stainless austenitic 316, and temperature expansion coefficient was $\alpha_o = 16.0 \times 10^{-6}$ m/m K, Young's modulus $E = 193$ GPa. The dummy has very high Young's modulus as compared with the soil Young's modulus (E $\approx$ 400 MPa); therefore it is considered absolutely stiff.
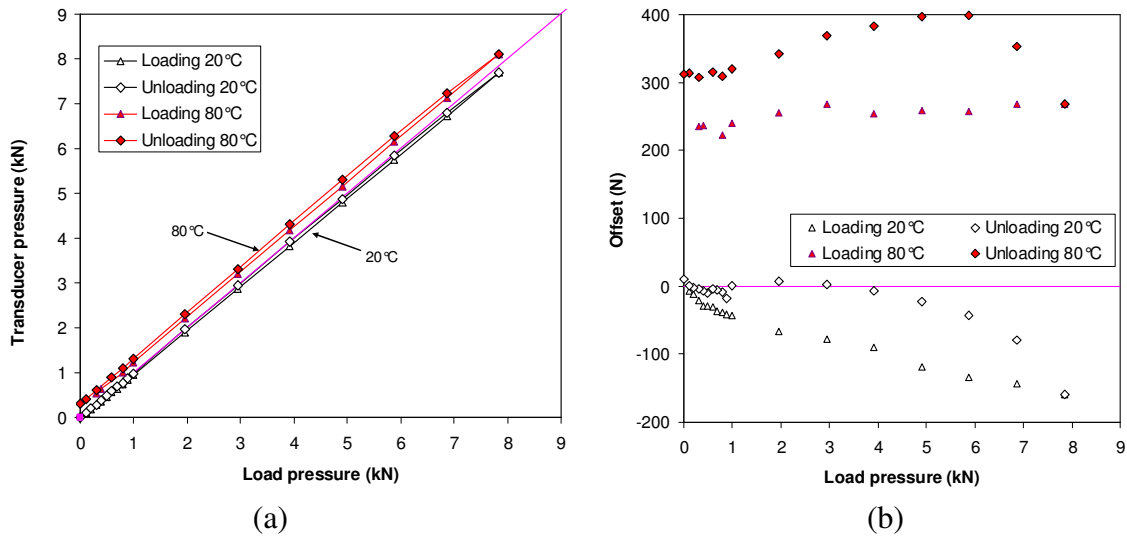
Figure 5.19: Calibration result: (a) Loading pressure vs. pressure transducer reading. (b) the offset between loading pressure and pressure transducer reading

By calibrating the gauge device, the applied load step was used from the calibrated load for the load cell as in the previous section. The result of calibration tests for the frame at 20°C and 80°C is presented in Fig. 5.21. The frame was loaded at 0.3 kN corresponding to 0.279 kN, and the load cell display indicated the temperature was 20°C. After that the cell was heated up to 80°C. The calibrated load for the load cell at 0.3 kN and at 80°C was 0.536 kN. The difference shown on the display between 20°C and 80°C at a 0.3 kN load is depicted by a black arrow in Fig. 5.21(a).

By applying load with the weight mass, it can be seen that the difference between the loading and unloading steps is very small at 20°C as well as at 80°C. By applying load in the load frame with a pressure controlled by the load cell, the difference between the loading and unloading in Al-Badran (May 2011) is relatively large as compared with the results at 20°C. It can be concluded that the difference between the loading and unloading in gauge calibration is induced by the difference in the pressure which was controlled by the load cell. If the pressure were controlled accurately during the loading-unloading process, the deformation would be the same. This also means that the materials of the frame and oedometer cell work in their elastic zone. The inaccuracy in the loading and unloading came from the load cell which controls the loading pressure upon the soil sample. However, the inaccuracy is insignificantly small (±0.005 mm).
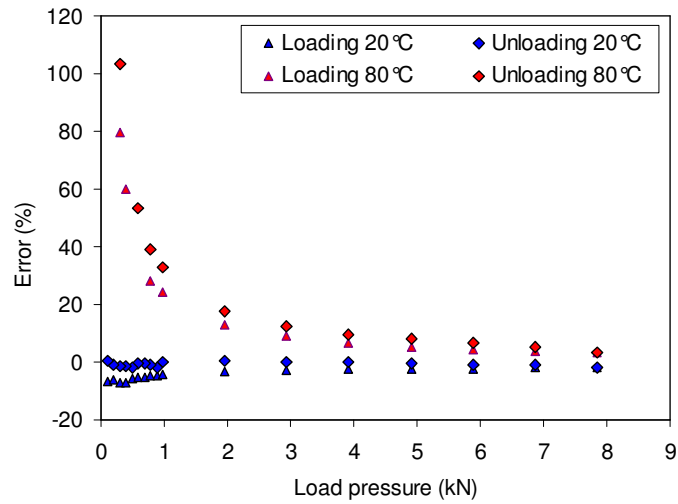
Figure 5.20: Error of load applied by load cell respective with the pressure prior to the calibration
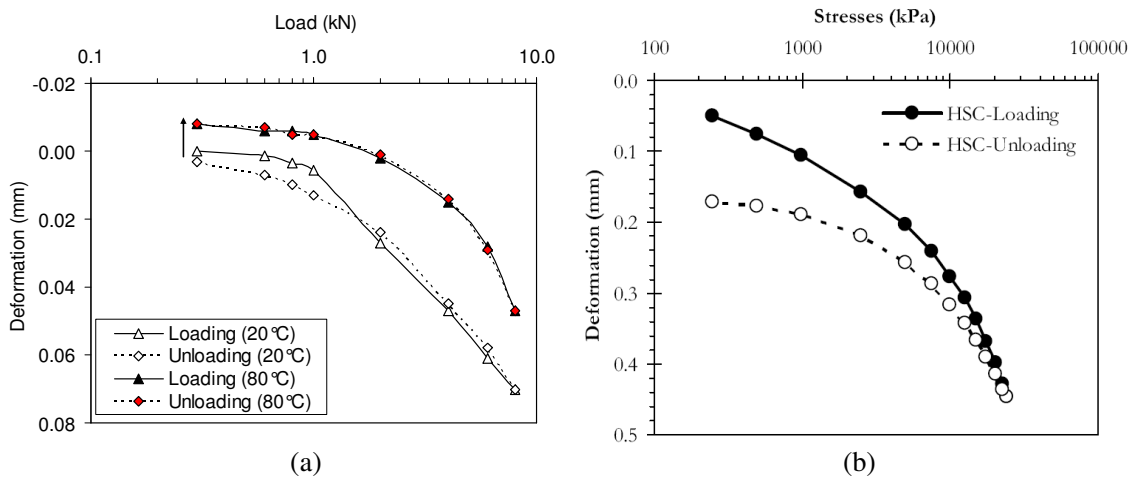
Figure 5.21: Calibration for gauge: (a) temperature of 20°C and 80°C this study. (b) temperature of 20°C (Al-Badran, May 2011)

6 Effects of temperature on soil water content measurements using TDR

6.1 Introduction

The time domain reflectometry (TDR) method for measuring the water content of materials is widely utilised nowadays (Siddiqui et al., 2000; Wright et al., 2001; Robinson et al., 2003). The method provides an indirect measurement of water content with satisfactory accuracy for engineering purposes. One of the main advantages is that measuring using TDR sensors is a non-destructive method. With these features, the TDR method for measuring water content is applied in many fields of engineering, especially for the in-situ monitoring of moisture distribution over an extended time period. For example, information about the water distribution in the subsoil is of importance in agriculture and environmental engineering; furthermore moisture content measurements, also in combination with other methods, can deliver valuable information about rainfall events, evaporation rates, and stream levels (Olivares et al., 2009; Lin and Tang, 2005). It was also used to investigate the long term effects of water intrusion into concrete leading to cement deterioration, which may cause settlements of the construction.

The motivation for the present study derives from laboratory column tests for the investigation of the thermo-hydro-mechanical (THM) behavior of sand-bentonite mixtures (SBM). The material was proposed as a buffer and sealing material in barrier systems for deep underground waste repositories. In those column experiments, a temperature gradient was imposed on the 30 cm long specimen (80 °C at the bottom and 20 °C at the top) and the water content of the specimen was monitored by means of TDR at three different positions along the specimen.

By means of time domain reflectometry, the soil bulk dielectric constant (K_a) is measured. The bulk dielectric constant is determined by the dielectric constant of the soil constituents: solid particles, water and air. At 20 °C, the dielectric constant of water is

80, as compared to the much lower dielectric constants of the solid and the air, which are 3 to 8, and 1, respectively. Therefore, water content changes are immediately reflected in the measured bulk dielectric constant of the soil. Topp et al. (1980) established an empirical relationship between the measured soil bulk dielectric constant and the volumetric water content using specimens of a sandy loam, a clayey loam, and a clay, but he has already mentioned that specialised applications or using unusual soils require calibration for the particular soil studied.

It is known that the dielectric constant of dipole materials such as water is temperature-dependent. Therefore, it is necessary to calibrate the measurement of soil bulk dielectric constant with respect to variation in temperature. Topp et al. (1980) reported that a variation of K_a in a temperature range from 10 to 36 °C is less than $\pm 1\%$ for clayey loam. Verstricht et al. (1994) measured $+2\%$ additional water content for each 10 K temperature increase in clayey soil. Pepin et al. (1992) observed that K_a decreases with an increase of temperature for sand, loam, and peat soils, in a temperature range from 5 to 50 °C. Ledieu et al. (1986) proposed a relationship between traveling time and volumetric water content taking temperature and bulk density into account but did not provide any experimental data to confirm this relation. Recently, Wraith and Or (1999); Skierucha (2009) stated that there are two competing phenomena for temperatures from 5 to 55 °C: K_a increases with temperature following the release of bound water from soil solid particles, and K_a decreases with an increase of temperature following the temperature effect of free water molecules. Skierucha (2009) proposed the concept of an equilibrium point of water content at which both competing phenomena compensate for each other.

In order to provide an appropriate relationship between the volumetric water content and the measured soil bulk dielectric constant for water content measurement in the THM column experiment, a temperature-dependent calibration was carried out in this study. Besides the sand-bentonite mixture, a fine sand and a sandy loam were used. For each soil type, the bulk dielectric constant of at least three specimens which had identical dry density but varying water content was measured in a temperature range from 20 to 80 °C.

6.2 Background

The determination of soil water content using TDR is based on the principle that the dielectric constant of water is much higher than that of the other soil constituents, soil solid and air. The dielectric constant of water, solid, and air are 80, 3 to 8, and 1, respectively.

Therefore, the change in the dielectric constants of the soil reflects predominantly the change in water content.

The waveform of the TDR probes and a section of the transmission line are presented in Fig. 6.1. The voltage step occurred just before the zero point. At 2.0 m from the instrument, a TDR probe was connected to the cable. The relative voltage levels V_I, V_R, V_{01}, V_{02}, V_{MIN}, V_F were used to calculate the bulk electrical conductivity of the medium in which the probe had been inserted. Inflections in the first derivative of the waveform were used in the software to determine the pulse travel times.

A step voltage was applied between the conductors at the pulse generator. The signal propagated down the line and was reflected from the end of the probe; the returning signal was sampled in the TDR device (Fig. 6.1(b)). The TDR instrument converted the time measurement to length units by using the relative propagation velocity factor setting. The propagation velocity factor, ν, of the signal in a dielectric medium is expressed as:

$$\nu = \frac{c_o}{\sqrt{K_a \mu}} \tag{6.1}$$

where c_o is the speed of light in vacuum, K_a is the real part of the dielectric constant, μ is the relative magnetic permeability (Topp et al., 1980). The latter is defined as:

$$\mu = \frac{1 + \sqrt{1 + \tan^2 \delta}}{2} \quad \text{with} \quad \tan \delta = \frac{K_a'}{K_a} \tag{6.2}$$

where $\tan \delta$ is the loss tangent, K_a' is the imaginary part of the dielectric constant or electric loss. For soil study, the electric loss is small ($\tan \delta << 1$), so it can be neglected and μ is equal to 1 (Topp et al., 1980; Pepin et al., 1995). On the other hand, the velocity of the signal traveling forth and back along the rod (ν) is:

$$\nu = \frac{2L}{t_t} \tag{6.3}$$

where $t_t = (t_2 - t_1)$ is traveling time, L is the length of the rod.

Substituting Eq. 6.3 to Eq. 6.2, and rearranging the equation means:

$$K_a = \left(\frac{c_o t_t}{2L}\right)^2 \times \frac{1}{\mu} \tag{6.4}$$

Since the electric loss is very small for soil, the relative magnetic permeability μ is equal to 1. Based on experiments on sandy loam, clayey loam and clay, Topp et al. (1980) proposed an empirical polynomial function describing the relationship between the volumetric water content(θ_v) and K_a (Eq. 6.5).

$$\theta_v = \left(-530 + 292K_a - 5.5K_a^2 + 0.043K_a^3\right) 10^{-4} \tag{6.5}$$
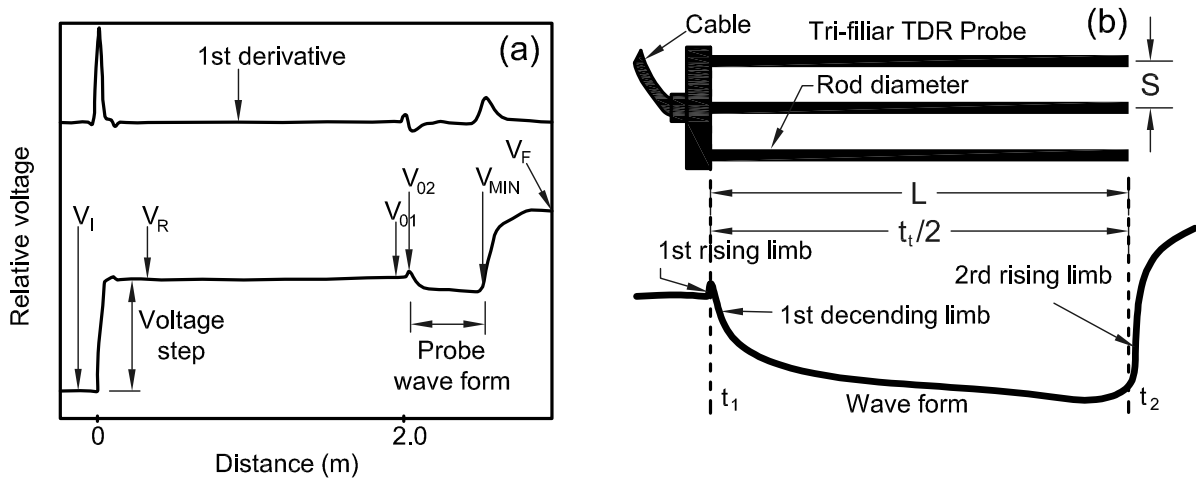
Figure 6.1: (a) Plot of the waveform, 1st derivative, (b) schematic of a typical TDR probe and the corresponding waveform, L is the probe rod length, S is the rod spacing, d is the rod diameter, modified after Schanz et al. (2011a).

Woersching et al. (2006) proposed the following relationship between the volumetric water content and the measured dielectric constant for loam (Eq. 6.6).

$$\theta_v = 23.039 K_a^{0.3321} - 30.472 \tag{6.6}$$

 Several attempts have been made to predict the K_a of soils from theoretical considerations using dielectric mixing models that consider the volumetric proportions of soil minerals; organic, water, and air constituents; as well as soil mineralogy and particle shape and packing considerations (Dirksen and Dasberg, 1993; Whalley, 1993; Friedman, 1997; Evett et al., 2005).

6.3 Effects of temperature - state of the art

Several investigations have been made in the past to study the effect of temperature on soils. For this, the effects of temperature on the dielectric properties of the major soil constituents have been characterized separately. It was found that the effects of temperature on soil solids and air are negligible (Weast et al., 1986), whereas the dielectric constant of water is significantly temperature-dependent and decreases with an increase in temperature (Weast et al., 1986; Roth et al., 1990). Weast et al. (1986) presented an empirical equation for the dielectric constant of water depending on temperature (Eq. 6.7),

where $\Delta T = T - 25°C$.

$$K_{water}(T) = 78.54(1 - 4579 \times 10^{-3}\Delta T + 1.19 \times 10^{-5}\Delta T^2 - 2.8 \times 10^{-5}\Delta T^3) \quad (6.7)$$

This relationship was later confirmed with the experimental study by Pepin et al. (1995); Persson (1997); Wraith and Or (1999).

Therefore, it was expected that the measured bulk dielectric constant (K_a) of a soil (including K_{water}, K_{solid}, and K_{air}) should decrease with an increase in temperature. But the studies of several soils demonstrated different results. The measurements of Pepin et al. (1995) and Persson (1997) for sand showed that K_a decreases with temperature for both low and high water content. Petersen et al. (1995); Wraith and Or (1999); Skierucha (2009) reported that in several soils with a specific surface area from 9 to 83 m^2/g, K_a decreases with an increase in temperature for wet soils but increases with temperature for dry soils. According to these authors, there are two competing phenomena related to two types of water: free water and bound water. Soil-free water is composed of the water molecules for which rotation in the electric field is not hindered, and soil-bound water is composed of water molecules which are so close to the solid phase, that their rotation in the electric field is hindered. In free water, a decrease in K_a occurs with an increase in temperature. The bound water adsorbed onto the solid surface is less mobile in the imposed electromagnetic field. Consequently, the more water molecules are bound on the solid surface, the higher the relaxation frequency is or the smaller the measured soil bulk dielectric constant at a given temperature. The increase of temperature induces the increase of kinematic energy, and the bound water molecules are released from solid surface into the free water, which is more mobile in the imposed electromagnetic field. Therefore the measured soil bulk dielectric constant increases. According to this hypothesis, Skierucha (2009) proposed the concept of the equilibrium point of water content, at which both competing phenomena compensate for each other. At that point the dielectric constant is independent of temperature in a certain range of temperatures.

Recently, Schanz et al. (2011a) stated in their research that in the sand-bentonite mixture, an increase in the measured K_a was observed as the temperature increased for the whole water content range tested. No equilibrium water content was found for the sand-bentonite mixture. The reason is that its high specific surface area of 263 m^2/g leads to a high amount of bound water as compared to free water. Thus, the effect of an increase in dielectric constant of water due to a release of bound water into free water with an increase in temperature dominates the measurement of K_a. In general, it can be concluded that for granular soils the effect of temperature on the measured K_a is significant only in the higher

range of water content (w>16%). For soils with clay content, the effect of temperature on the measured soil bulk dielectric constant depends on the ratio of bound water to free pore water and on the clay content. The higher the clay content, and thus the specific surface area, the more significant the amount of bound water in the total soil water is, leading to a dominating effect of the bound water in response to a temperature increase. The higher the specific surface area, the higher the tendency of soil bulk dielectric constant to increase is as the temperature increases, even at low water content.

In summary, the temperature dependent calibration of TDRs presented in this section is a pre-condition for interpreting the experiments, where TDRs are used at varying temperatures for water content measurements. The data presented in this paper can be used to quantify the water content during measurements at non-constant temperature in the range between 20 and 80 °C. For this purpose, the calibration data is plotted in a 3D-diagram determined by the three variables: water content, temperature, and the dielectric constant. By using the interpolation technique, a 3D surface is created from the experimental calibration points, and the water content for any measured dielectric constant and temperature can be calculated.

6.4 Experimental setup

A specially designed and fabricated experimental setup was used to perform the temperature dependent calibration (Fig. 6.2). The experimental setup consists of a water filled basin, where a water-tight specimen container was placed. The temperature of the water in the basin can be controlled within the range of 20 to 80 °C and an accuracy of ±1 K by means of a thermostat. In order to avoid the temperature fluctuations, the basin is thermally isolated from outside. The specimen was dynamically compacted directly in the specimen container to the desired dry density. Afterwards, the cover was screwed onto the container. The cover plate consists of a steel layer and a polytetrafluorethylene (PTFE) layer. Three holes in the cover plate were made in order to place two TDR sensors (probe 1 and probe 2) and one thermocouple. After closing the container with the cover plate, holes were drilled into the specimen to introduce the TDR probes without influencing the density and the texture of the surrounding soil. TDR probe 2, which was introduced from outside through the cover plate into the soil specimen, simulates the special geometrical conditions of the TDR probes placed into the THM column (Manju et al., 2008). Only half of the length of the steel rods of the TDR probe was embedded into the soil specimen. The results of calibration of the TDR probe 2 is not considered in this section, but in
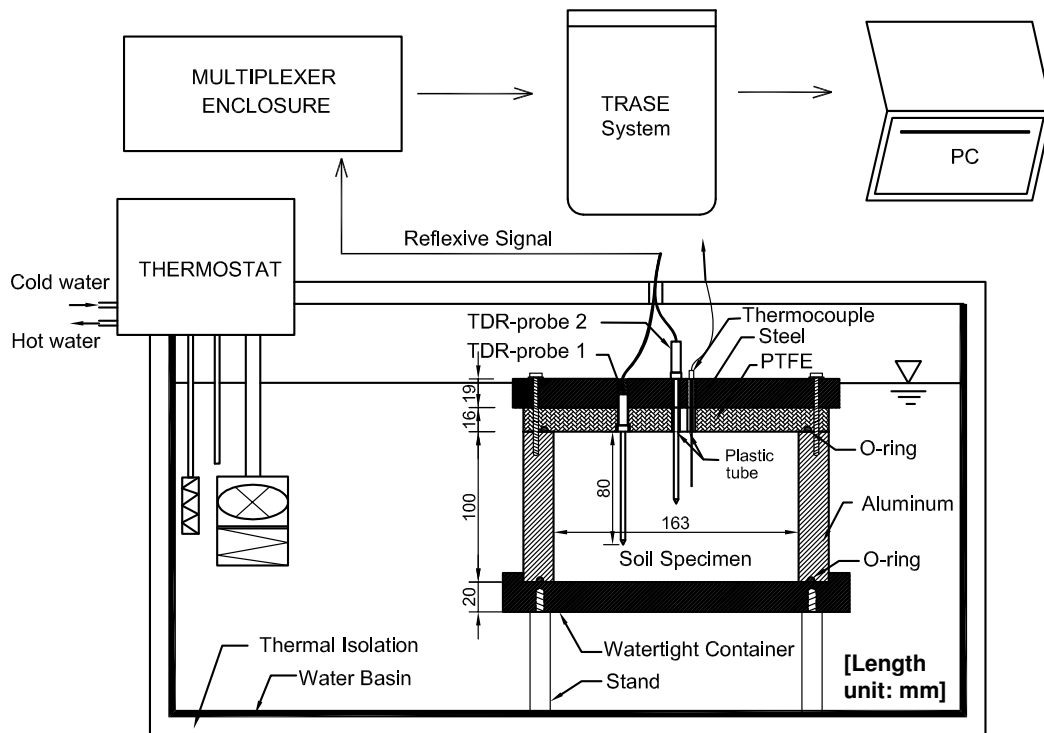
Figure 6.2: Schematic of the experimental setup.

the section 5.4. The TDRprobe 1 steel rods were fully surrounded by the soil specimen. The results of the temperature-dependent calibration of TDR-probe 1 will be discussed further in this paper.

Three-rod miniature TDR probes (Soilmoisture Equipment Corporation) 80 mm long and 3 mm in diameter were used. The sensors were connected to a Multiplexer and the transmit time of the signal was directly calculated using the Trase system and Eq. 6.4. The dielectric constant is calculated by the Trase system.

The data acquisition system was controlled by a PC. For each specimen with a given water content, the soil bulk dielectric constant was measured at 20, 30, 40, 50, 60, 70, and 80 °C. For this, the desired temperature was imposed on the soil sample by the surrounding water, the temperature of which was controlled by the thermostat. The temperature within the soil specimen was verified with the thermocouple inserted into the specimen. It took approximately 120 minutes to reach equilibrium in specimen temperature for each temperature increment.

Before performing the test on the soil specimens, the experimental setup was validated by measuring the K_a value for deionized water and for dry air. For the latter, silica gel was
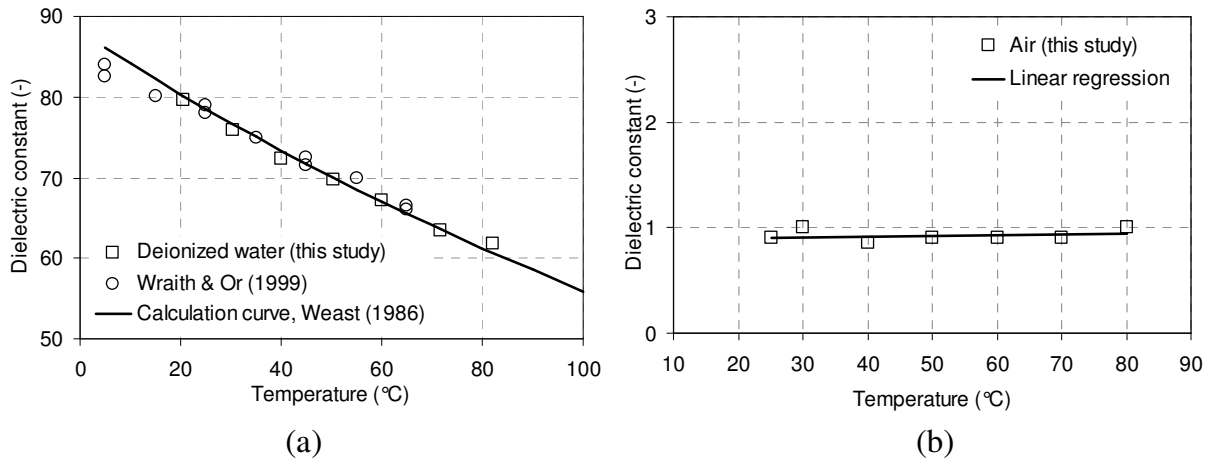
Figure 6.3: (a) Dielectric constant vs. temperature plot for water. (b) Dielectric constant vs. temperature plot for air.

placed at the bottom of the container to keep the air dry in the container. The measurement of K_a for deionized water and dry air was also performed at different temperatures ranging from 20 to 80 °C with increments of 10 K. The verification of the experimental setup with deionized water demonstrated more satisfying results as compared with the former results obtained by other authors (Weast et al., 1986; Pepin et al., 1995; Wraith and Or, 1999), see Fig. 6.3. The measurement of K_a for air is presented in Fig.6.3. No influence of temperature is observed and the measured average value of 0.95 is close to 1, which is indicated in the literature (Topp et al., 1980) as the K_a value of air.

6.5 Results and discussion

In the following section, the results of the temperature-dependent calibration are presented and are discussed in the context of results from the literature. In Fig. 6.4, the waveforms for fine sand at water contents of 10% and 24% are shown, in which the reflection coefficient (ρ) is determined from the measured waveform voltages, described as $\rho = (V_i - V_0)/V_0 - V_{ref}$, where V_i is the discrete data from the waveform, V_0 is the voltage in the cable before entering the probe and V_{ref} is the reference voltage in the cable test. At a water content of 10%, no considerable change in the waveform for varying temperatures was observed, whereas at a water content of 24% a change in the waveform was clearly visible, leading to a smaller value of t_2 and therefore a smaller K_a as the temperature increased. The sand-bentonite mixture has a higher electrical conductivity as compared with sand and sandy loam. It is known that a higher electrical conductivity of a soil
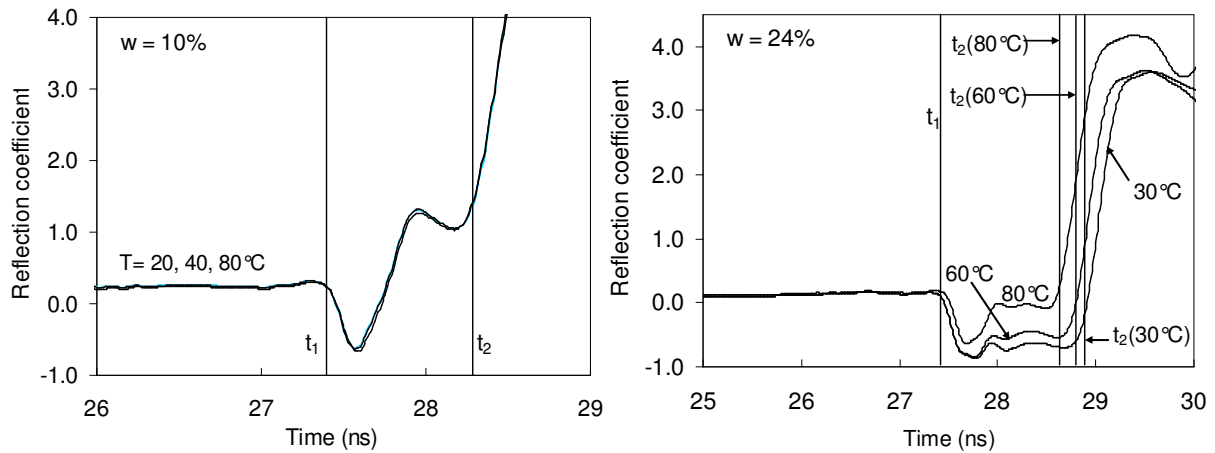
Figure 6.4: Waveform obtained for fine sand at different temperatures in the samples of 10% water content and 24% water content.

may induce signal attenuation (Mojid et al., 2003). In Fig. 6.5(a) and 6.5(b), examples of waveforms obtained during the calibration are given. Fig. 6.5(a) shows the waveform obtained for the sand-bentonite mixture at 20% water content at temperatures of 20, 40, and 80 °C. It can be seen that the reflection signal is clear enough to determine the point of reflection (and thus t_2). Fig. 6.5(b) compares the reflection signals obtained for the three soil types at 20 °C. The determination of the point of reflection is illustrated in this figure. In case of the sand-bentonite mixture, the signal attenuation observed is greater as compared with the signal of fine sand or sandy loam. However, the reflection signal is still pronounced enough to determine the point of reflection with sufficient accuracy. For each soil type, the results are presented in a dielectric constant versus temperature plot (Fig. 6.6(a), 6.7(a), and 6.8(a)) and in a volumetric water content as opposed to the dielectric constant plot (Fig. 6.6(b), 6.7(b), and 6.8(b)). In the latter, calibration curves reported in the literature were added for the sake of comparison with the experimental points obtained. For fine sand, four specimens which had water content of 5.4, 10.4, 15.5 and 24%, were tested. From Fig. 6.6(a) it is visible that for low water contents ($w = 5.4\%$ and $w = 10.4\%$), temperature has no influence on the dielectric constant, whereas at $w = 15.5\%$ a slight decrease occurred, and at $w = 24\%$ a significant decrease of K_a with increasing temperature occurred. This is because at low water content, there is less influence of the dielectric properties of the water on bulk dielectric constant of the soil. The dielectric constant of the air and of the soil solid are known not to be influenced by varying temperature. Therefore, no influence of a temperature increase was observed with regard to the soil bulk dielectric constant for low water content values. In Fig. 6.6(b), the volumetric water content is plotted against the measured bulk dielectric constant of
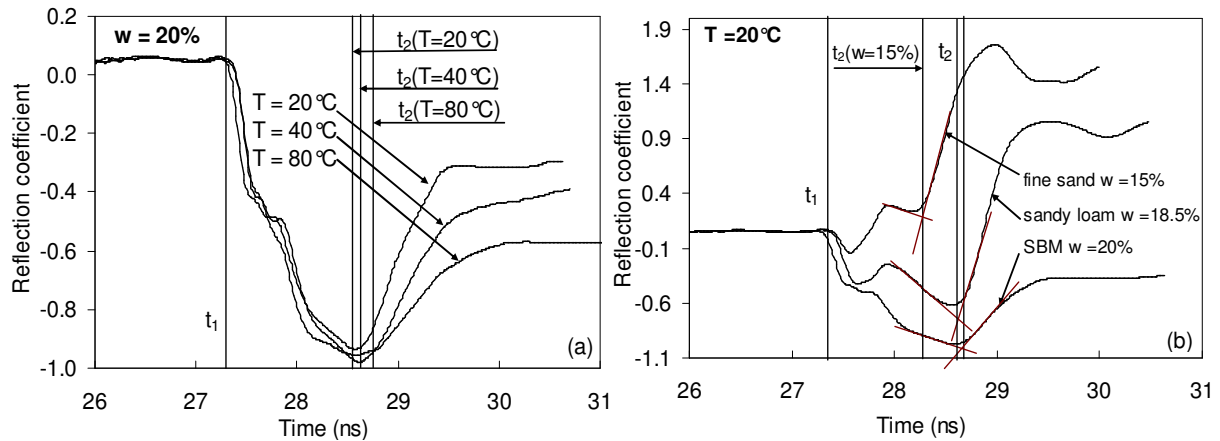
Figure 6.5: (a) Waveform of the 20% water content sand-bentonite mixture at different temperatures, (b) waveform at 20 °C of the different soils used.

the sand. The results of previous studies (Lins, 2009; Topp et al., 1980) are given in comparison with the obtained measurement. Again, it is clearly visible that the influence of increasing temperature on the soil bulk dielectric constant is only significant for higher water contents.

For sandy loam, three specimens were tested. The chosen water contents were 13, 18.5, and 26%, the latter corresponding to the saturated state. The results show that the dielectric constant slightly increases as the temperature increases at low and medium water contents ($w = 13\%$ and $w = 18.5\%$), and decreases as the temperature increases at high water content ($w = 26\%$), Fig. 6.7(a). Fig. 6.7(b) presents the relationship between the volumetric water content and the dielectric constant of the soil at different temperatures. The experimental points for the calibration for sandy loam at 20 °C were relatively close to the calibration curve determined for a loam by Woersching et al. (2006). Similar to the fine sand results, the influence of temperature on the measured bulk dielectric constant increased as the volumetric water content increased.

In fine-grained soils with considerable clay content, the soil water occurs as (1) free bulk water, and (2) bound water. Bound water has different dielectric properties as compared with the free water. The dielectric constant of free water is approximately 80 at room temperature, while that of bound water can be very small, approximately 3.2 for the first layer of water molecules adsorbed on the soil surface (Skierucha, 2009). The dielectric constant of bound water is so small because the rotation of the water molecules is hindered by the surface charge of the soil solid. The effects of a temperature increases on the dielectric constant of free water and are opposed on bound water. Whereas a temperature
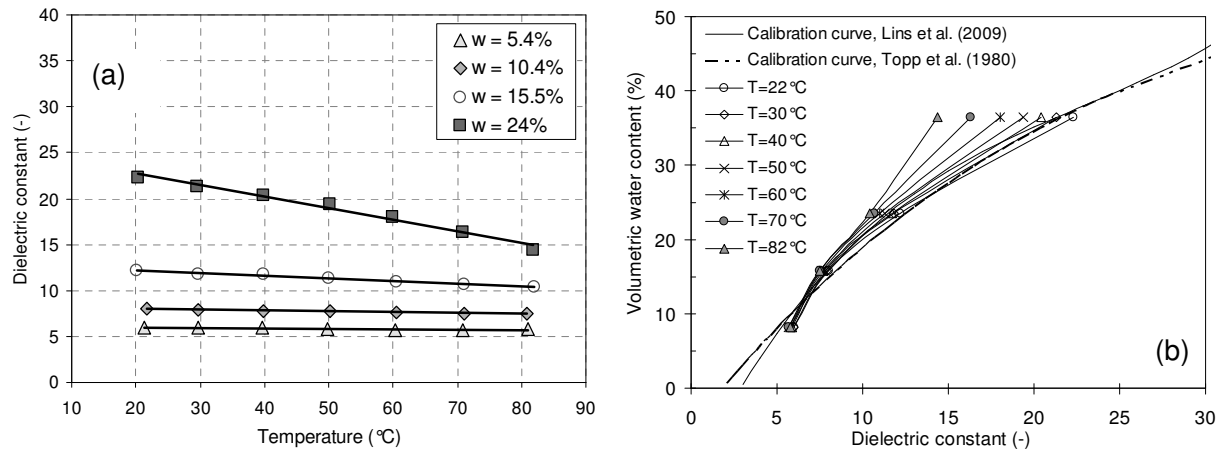
Figure 6.6: Test results obtained for fine sand, (a) dielectric constant vs. temperature at different water contents, (b) volumetric water content versus the dielectric constant at different temperatures.

increase leads to a decrease in the dielectric constant in free water, a temperature increase in bound water leads to an increase in the kinetic energy of the molecules, and thus, they can release from the soil solid surface and become free water. This process leads to a greater dielectric constant with increasing temperature due to an increasing amount of free water. Therefore, in fine-grained soils with clay content, the measured value of the bulk dielectric constant is determined by the relative proportions of free and bound water and their opposed effects on the dielectric properties in the presence of an imposed electrical field at varying temperature (Wraith and Or, 1999).

The results shown in Fig. 6.7(a) can be explained by the consideration given above. At low and medium water content, the amount of bound water as compared with free water is high enough so that the soil bulk dielectric constant increases slightly due to the effect of a release in bound water into free water accompanied by an increase in the dielectric constant of the water, and thus an increase in the soil bulk dielectric constant. For the specimens with a $w = 26\%$ water content the amount of bound water as compared with free water in the soil is insignificant. Therefore, the dielectric properties of free water dominate the measured soil bulk dielectric constant: K_a decreases with increasing temperature. Fig. 6.8(a) and Fig. 6.8(b) clearly indicate the dominating effect of the release of bound water with increasing temperature leading to an increase in the soil bulk dielectric constant. The ratio of bound water to free water at all the tested water contents was clearly sufficient enough so that the soil bulk dielectric constant increased with increasing temperature. Skierucha (2009) found a soil type characteristic water
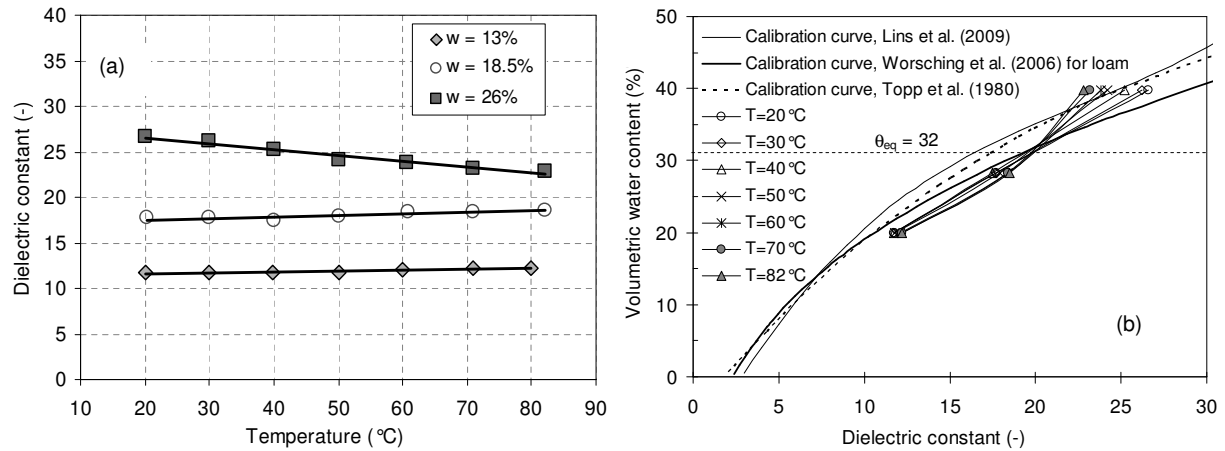
Figure 6.7: Test results obtained for sandy loam, (a) dielectric constant versus temperature at different water contents, (b) volumetric water content versus dielectric constant at different temperatures.

content value, called the "equilibrium water content", θ_{eq}, where the measured dielectric constant does not depend on temperature. At this water content, the ratio of free water and bound water in the soil water is such that the opposed effects of an increase in K_a with increasing temperature for bound water and of a decrease in K_a with increasing temperature for free water compensate each other. These findings were confirmed in the present study for the sandy loam. The equilibrium volumetric water content was found to be $\theta_{eq} = 32\%$, Fig. 6.7(b). For the sand used in this study, no equilibrium water content was found. Because sand as a granular material, contrary to clays, has no ability to adsorb water molecules as bound water, the compensating effect of two phenomena as described above is not expected to occur. In case of sand-bentonite mixture, the equilibrium water content was not found to occur in the water content range tested. The high clay content in the sand-bentonite mixture leads to a high amount of bound water as compared with free water and subsequently to an increase in the soil bulk dielectric constant with increasing temperature.

6.6 Conclusion

In the present study, the soil bulk dielectric constant was measured at different known water contents and at varying temperatures from 20 to 80 °C by means of time domain reflectometry. The effect of temperature on the measured bulk dielectric constant depending on soil type and water content was conducted.
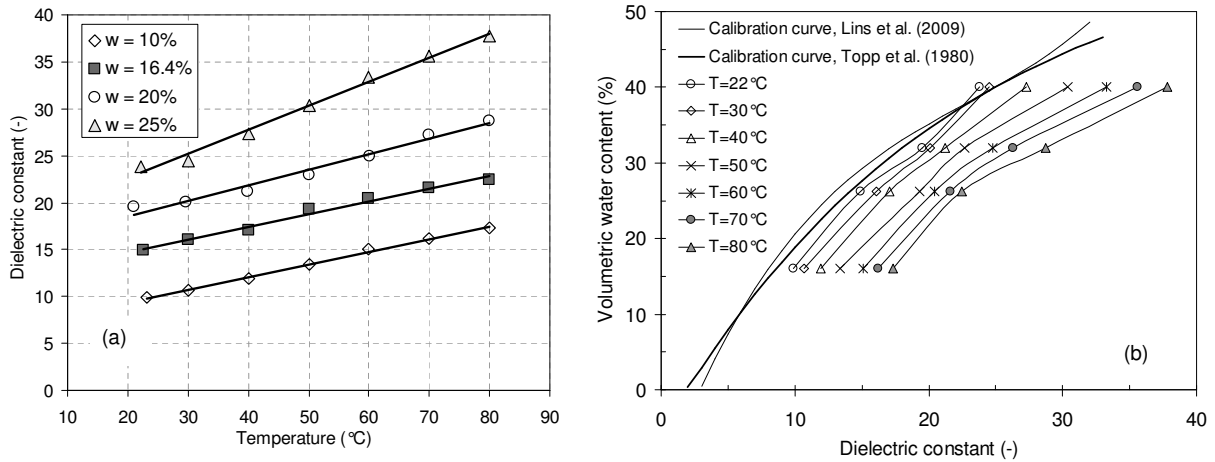
Figure 6.8: Test results obtained for the sand-bentonite mixture, (a) dielectric constant versus temperature at different water contents, (b) volumetric water content versus dielectric constant at different temperatures.

In case of sand, varying temperature affected the measured bulk dielectric constant for volumetric water content greater than 16%. The bulk dielectric constant decreased with an increase of temperature. At water contents smaller than 16%, the temperature had only an insignificant effect on the measured bulk dielectric constant of the sand.

The measurements on the sandy loam confirm results of Wraith & Or (1999) and Skierucha (2009), who found opposing effects of temperature increase for the measured K_a depending on water content. The opposing effects result from two competing phenomena: (1) K_a decreases with an increase of temperature for free pore water, and (2) K_a increases with an increase of temperature due to the release of bound water from the solid surface into free water. There is an equilibrium water content at which both phenomena compensate each other. The equilibrium water content of the sandy loam was found to be 32%.

For the sand-bentonite mixture, an increase in the measured K_a with increasing temperature was observed for the whole water content range tested. No equilibrium water content was found for the sand-bentonite mixture. The reason is that its high specific surface area of 263 m^2/g leads to a significant amount of bound water as compared with free water. Thus, the effect of an increase in the dielectric constant of water due to a release of bound water into free water dominates the measurement of K_a as the temperature increases. In general, it can be concluded that for granular soils the effect of temperature on the measured K_a is significant only in the higher range of water content (w>16%). For soils with clay content, the effect of temperature on the measured soil bulk dielectric constant

depends on the ratio of bound water to free pore water and on the clay content. The higher the clay content, and thus the specific surface area, the more significant the amount of bound water in the total soil water is, leading to a dominating effect of the bound water in response to a temperature increase. The higher the specific surface area, the higher the tendency of soil bulk dielectric constant to increase with increasing temperature is, also at low water contents.

The temperature-dependent calibration of TDRs presented in this paper is the precondition for the interpretation of the experiments, where TDRs are used under varying temperatures for water content measurements. The data presented in this paper can be used to quantify the water content during measurements at non-constant temperature between 20 and 80 °C. For this purpose, the calibration data is plotted in a 3D-diagram determined by the three variables: water content, temperature, and the dielectric constant. By using the interpolation technique, a 3D surface is generated from the experimental calibration points, and the water content for any measured dielectric constant and temperature can be calculated.

7 Experimental results and discussion

7.1 General remarks

This chapter provides the results and discussion of the results from the element tests and the column tests. The element tests include oedometer tests and unconfined SWRC tests. The oedometer tests aim to analyse the stress-strain behavior in non-isothermal and constant suction conditions. The column tests, on the other hand, observe soil behaviour in thermal and hydraulic gradients. The results are discussed based on the comparison between stationary conditions in element tests and transient conditions in column tests.

7.2 Results of the element tests

7.2.1 Results of oedometer test at $T = 20°$C and $T = 80°$C

The relation between stress and strain under non-isothermal conditions is presented in this section. The results of isothermal wetting tests under a constant applied load are also discussed. The tests were carried out at two different (constant) temperatures: $T = 20°$C and $T = 80°$C.

Fig. 7.1(a) and Fig. 7.1(b) show the compression curve of soil samples at $20°$C and $80°$C. The reported results were reasonable as compared with the results from similar tests in unsaturated over-consolidated soil, reported in Geiser (1999); Alonso et al. (2005b), in which two zones could be distinguished: the elastic zone and the plastic zone (normal consolidation path). The elastic and plastic zones were separated with regard to the applied vertical stress by the pre-consolidation pressure p_0 in a partially saturated state and p_0^* in a fully saturated state. Fig. 7.1(a) shows that the slopes of the normal consolidated line are quite the same at different controlled suctions. Reviewing the oedometer test for unsaturated soils, there were several reports and discussions on effect of the suction on the
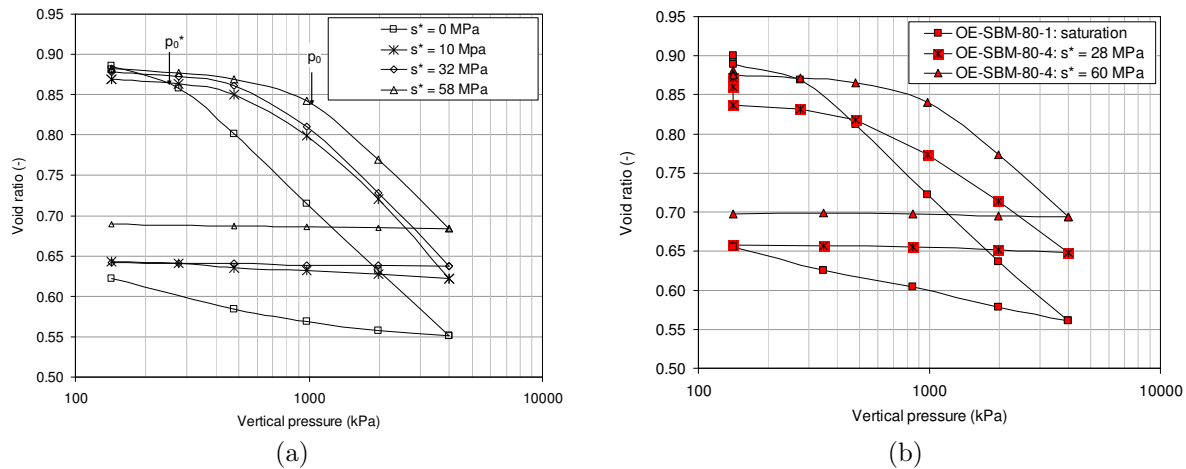
Figure 7.1: Void ratio vs. vertical pressure for different controlled suctions. (a) at $T = 20°C$ and (b) at $T = 80°C$

stiffness of the soil in a virgin state. Karube (1986); Josa et al. (1987) investigated stress-strain behaviour of compacted kaolin. The suction range investigated in these papers was smaller than 0.5 MPa. They reported that the slope of normal consolidated line ($\lambda(s)$) is suction-dependent and the value decreased with increasing suction. On the other hand, Wheeler and Sivakumar (1995); Wheeler et al. (2002) investigated stress-strain behaviour of the compacted Speswhite kaolin with the same range of suctions. They stated that the value $\lambda(s)$ increased with increasing suction. Regarding high plasticity soil, Lloret et al. (2003) studied highly compacted bentonite. They reported that the $\lambda(s)$ in a saturated condition ($s = 0$) was higher than $\lambda(s)$ in unsaturated conditions. But when controlled suction values were 4 MPa, $\lambda(s)$ did not depend on suction or the slope paths were relatively parallel. It is necessary to note that all the samples had a high initial suction and were subjected to the wetting process by controlled suction at the same confining pressure. During wetting process the total void ratio of the sample increased significantly.

The observed phenomenon can be interpreted by the interaction between the microstructure (intra-aggregate) and the macrostructure (inter-aggregate) for high plasticity soils (Gens and Alonso, 1992; Lloret et al., 2003; Agus et al., 2012). The macrostructure controlled mainly the stress-strain behaviour or major structure rearrangements, while the microstructure controlled the swelling and the osmotic suction relation. At high suction the mechanical behaviour was dominated by the relation of the swelling and the osmotic suction. At low suction mechanical behaviour was dominated by stress-strain relation; the increase of suction contributed only to the effective stress, which is determined by the threshold value of suction in (Agus et al., 2012). If the suction value is lower than

the threshold value (i.e. 100 kPa – 500 kPa depending on the clay content) the swelling pressure increment remains constant. The swelling pressure increment varies significantly at a suction range of 2 MPa to 100 MPa. In the suction-controlled test, the macropore was considered empty of water at low water content, and the water was stored in the micropore. The change of suction in this range did not induce the change of the water content in the macropore. Consequently, the change of controlled suction in this range did not effect the stiffness of the soil after pre-consolidation pressure. The increase or decrease in the stiffness of the soil in a virgin load state at low suction has been also discussed in (Wheeler et al., 2002). According to their paper, the normal compression lines $\lambda(s)$ could decrease with increasing suction $r < 1$ or increase with increasing suction $r > 1$ if a low suction was applied. It can be concluded that the slope of normal compression lines $\lambda(s)$ is not influenced significantly by the change of suction at a high suction value. At a low suction value $\lambda(s)$ is influenced by suction. The potential influence of suction is different for different types of soil. The slopes of normal consolidation line are influenced also by decreasing in soil void ratio Baille et al. (2010) in a higher loading pressure. However, this influence is relative small in this studied range of vertical loading pressure.

Regarding the mathematical model point of view, as described in the BBM the parameters p^c (Eq. 8.13) is defined as the value of $p_0 = p_0^*$ where the LC curve did not depend on suction. It could be observed that the soil stiffness under net stress ($\lambda(s)$) changed insignificantly as the suction changes, regardless of whether the p^c value was very large or very small. In this case, r value can be approximately equal to 1 in Eq. 2.42.

The unloading paths of unsaturated specimens are relatively parallel at different suction, which corroborates the BBM model. However, in the unloading path of the saturated specimen the void ratio increased significantly as compared with the void ratio of the unsaturated specimen. This result contradicts the BBM model, which assumes that the unloading paths at different suctions have the same slope, κ does not change with suction in pressure-void ratio plane. However, the unloading slope parameter, which is determined by reloading and unloading paths in a stress-specific volume plane, allows to change as the suction varies as in Eq. 7.1 in the thermo-elasto-plastic (BBM-TEP) model in CODE_BRIGHT. If α_i is negative, $\kappa_i(s)$ will increase when suction decreases and reach a peak when the suction equals zero.

$$\kappa_i(s) = \kappa_{io}(1 + \alpha_i s) \tag{7.1}$$

There are several methods to determine the pre-consolidation pressure, such as the method in Casagrande (1936); Silva (1970). The advantage of the Silva's method was discussed in

Clementino (2005)'s work. Herein Silva's method is used instead of Casagrande's method (Casagrande, 1936) to determine the pre-consolidation pressure. Alonso et al. (2005b)'s method could be used, which stipulates that the parallel line with the unloading line can be drawn from the initial pressure point and a tangent line can be drawn from the maximum loading point; the intersection between two lines is the pre-consolidation pressure (p_0^*). However, this method has been considered unfit to determine p_0^* for the saturated test, since the unloading paths are not always linear.

Tests on fully saturated soil were carried out, at 80°C. The results are presented in Fig. 7.1b for the stress-strain relationship at different controlled suctions. Fig. 7.2(a) shows the relationship between stress and the void ratio in the saturated condition and at 20°C and 80°C. From the figure one can see that there is no significant effect of temperature on the stress-strain relationship. The significant difference can be clearly seen in stress-strain behaviour at the unloading path.

Fig. 7.2(b) shows the relationship between stress and the void ratio at an applied suction of 60 MPa at both 20°C and 80°C. There is also no significant difference between the stress-strain relationship at 80°C and at 20°C for high suction value.

Testing saturated soil at 80°C is simple to perform. The suction of 60 MPa was the initial suction of the soil before it was compacted. Little time is required to control the suction at this suction value. Therefore it is easy and stable to conduct the two tests at 20°C and 80°C. However, it takes a substantial amount of time to change suction from the initial suction value to 10 MPa and 32 MPa suction.

The suction of the specimens and solutions before and after the tests were measured using the chilled-mirror method. When applying a suction of 60 MPa, the measured suction in the soil and in the solution before and after the test are nearly the same as the target value. However, the test with the target suction of 10 MPa was not successful, because the soil suction measured after the test are higher than its target value. The reduction in the water level in the solution bottle. Consequently, the suction of the soil specimen measured by the chilled mirror method was 32 MPa, which was not equivalent to the targeted suction (10 MPa). The stress- void ratio relation of this test is also presented in Fig. 7.1(b).

From the volume of the supplied water and from validating it with saturated hydraulic conductivity, one can get the result that water flowed through the sample from the bottom to the top for about 48 hours. The swelling phenomenon still occurred afterwards (Fig. 7.3). This phenomenon can be explained as follows: when macropores were saturated, the micropores were still taking water due to osmotic suction and swelling. During

the macropore saturation process, the soil volume decreased, after which it continued swelling due to the micropore taking water in; therefore the soil volume increased. This process is similar to the two peak swelling phenomenon in constant volume swelling tests. The non-monotonic swelling and collapsing phenomenon has frequently been interpreted (Pusch, 1982; Baille et al., 2010; Villar and Lloret, 2008; Schanz et al., 2010b). The soil volume decrease is due to the loss of shear strength at aggregate level due to a decrease in suction which caused a collapse in macrostructure level; a further increase in swelling pressure was attributed due to the redistribution of clay particles to a more homogenous and dispersed state (Pusch, 1982). Tripathy et al. (2004); Schanz and Tripathy (2009) interpreted the swelling phenomenon based on the diffuse double-layer theory; the collapse is based on the explanation that osmotic pressure in the inter-aggregate pores is insufficient to maintain the distance between the clay aggregates, which results in a collapse of the larger voids to compensate the equilibrium of the osmotic pressure .

The two peak swelling phenomenon (Fig. 7.3) can be interpreted as follows. There are two phenomena which occur on the micropore and macropore scales. In macropore structure, the matric suction potential (including capillary force and hydration force) is dominant. In micropore structure, the osmotic suction potential is dominant. The first phenomenon, the swelling phenomenon, can be explained by the diffuse double-layer theory with the exchange of cations in micropore structures among inter-layers and/or inter-particles. The decrease in suction induces swelling or an increase in soil stiffness. The second phenomenon, the collapsing phenomenon, occurs due to the decrease in matric suction (e.g. capillary pressure) which decreases the cohesion in the inter-aggregate pore. The reduction in cohesion induces the reduction of shear strength and the collapsing phenomenon occurs. The difference is controlled from the process in Agus et al. (2012) for multi-step suction, where the suction equilibrium is reached during each step of controlled suction, in which the two processes in micropore and macropore occur simultaneously during the hydration process. The wetting process occurs quickly before micropore can absorb water fully to its capacity. Whenever the swelling pressure path reaches the shear strength reduction pressure path, the collapse phenomenon will occur. The compaction process causes the macropore to decrease, thus increasing the matric suction (e.g. capillary pressure). In this test, the soil volume initially decreased then subsequently increased when the microstructure continued to absorb water (Fig. 7.3).

The model parameters of the BBM model for the sand-bentonite mixture are derived based on the oedometer test. The method of parameter derivation follows the guideline from Alonso et al. (1990). The determined parameters are presented in Table 7.1. The
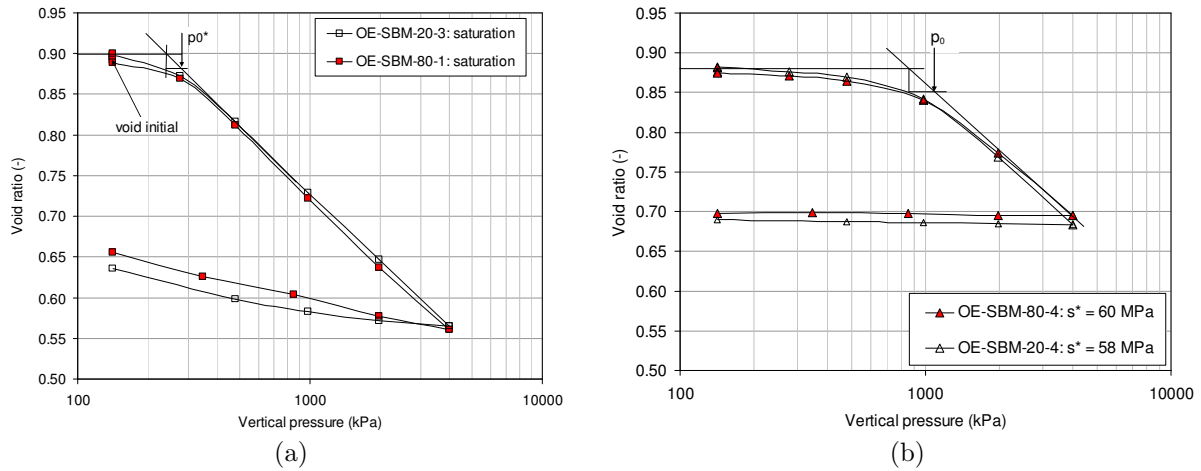
Figure 7.2: Void ratio versus vertical pressure at different temperatures. (a) at saturated condition and (b) at the same suction
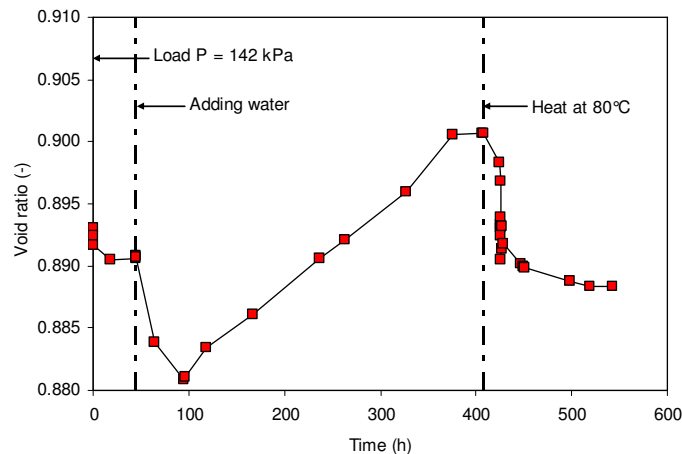
Figure 7.3: The evolution of void ratio during the hydration and heating process

elastic expansion of the soil skeleton due to temperature is determined based on the tests on saturated samples. The difference in soil volume before and after the temperature change is attributed to the magnitude of the parameter of thermal expansion: α_0.

7.2.2 Results of SWRC unconfined tests

The relation between suction and water content or degree of water saturation has also been studied by unconfined tests. The experimental procedure is presented in Chapter 5. The SWRC is presented in Fig. 7.4a and Fig. 7.4b. The relation between water content and suction obtained in this study is presented together with the SWRC unconfined test

Table 7.1: Derivation of parameters for the BBM model

	SBM4	SBM5	SBM7	SBM3
Suction (kPa)	58000	32000	10000	0
p_0 (kPa)	1020	730	650	280
$\kappa(s)$	0.001	0.002	0.007	0.02
$\lambda(s)$	0.115	0.115	0.019	0.115
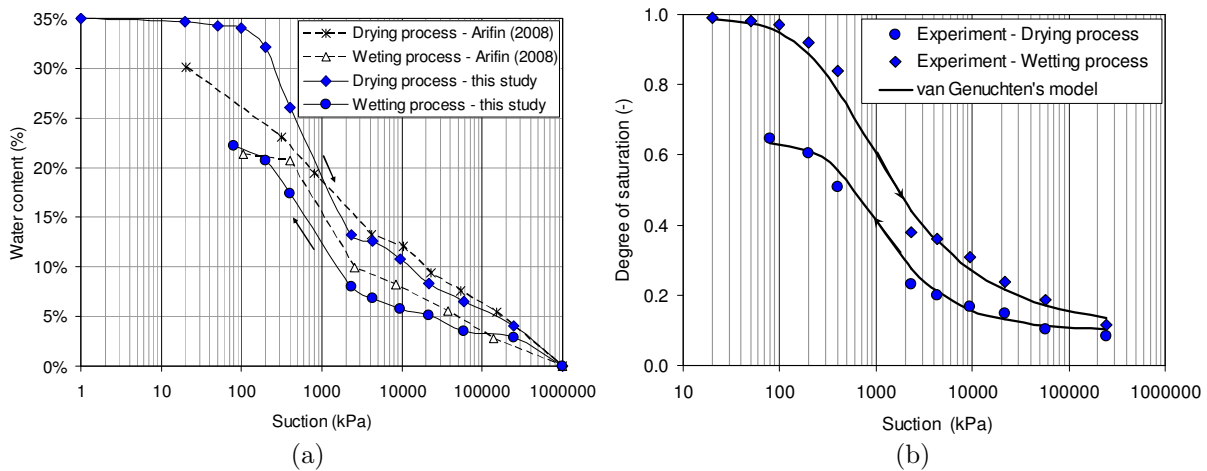
Figure 7.4: Soil water retention curve: (a) water content versus suction and (b) degree of saturation versus suction

results from Arifin (2008) for comparison. The initial dry density in Arifin (2008) was 1.6 Mg/cm^3. This initial water content originates from wet of optimum point using the standard proctor method of compaction for the drying curve. The result in Fig. 7.4a and Fig. 7.4b shows that the relation of suction and water content exhibits the same developing trend. The water content in this study is generally lower than the water content results obtained in Arifin's test. This can be explained by the initial dry density of this study being smaller (1.4 Mg/cm^3) as compared with the dry density of Arifin's specimen (1.6 Mg/cm^3).

The van Genuchten model (van Genuchten, 1980) presented in Eq. 8.21 was used to simulate the relation between suction and degree of saturation based on the experimental results. The model parameters were obtained by fitting the model with the experimental results. The parameters for the van Genuchten model are presented in Table 7.2. With the parameters in Table 7.2 the model was drawn in Fig. 7.4b by fitting method.

Table 7.2: Summary of parameters for van Genuchten model

Process	P_0	λ	S_{ls}	S_{lr}
Unit	(kPa)	(-)	(-)	(-)
Drying curve	346.2	0.33	1.0	0.1
Wetting curve	609.5	0.446	0.64	0.1

7.3 Results of the thermo-hydro-mechanical column tests

7.3.1 Validation tests

Each component of the column testing device such as TDR sensors, load cells, thermocouples, heaters, and coolers has been calibrated and its operation capability was validated before column assemblage. However, the functionality of the column device also had to be verified and validated after all the instrumentation parts operated together. In addition, the column cell was designed with several holes along its lateral wall as well as openings on the top and bottom of the cell. This required several O-rings to be placed on the hole interfaces. Therefore, the waterproof of the column needed to be verified with the variation of temperature in a range according to the test type, i.e. from 20°C to 80°C.

In order to verify the waterproofing of the instrumented column device, an initially fully saturated sample was used along with a soil with material properties that do not change significantly with variations in temperature. The aim is to have the same thermal conductivity along the sample and during the heating test, therefore allowing verification of the accuracy of the thermocouple devices and the heaters. Saturated fine sand was selected as a material for the validation test. Preparing the fully saturated sample occurs as follows. The top part of the column cell was opened and the cylindrical cell body was filled with de-aired water. Afterwards, dry sand was slowly pluviated into the water and at the same time the appropriate volume of water was taken out such that the inserted sand was always under the water. When the height of the sand column reached 30 cm, the top part of the column was installed. The water line in the bottom was connected with the burette to guarantee that the sand sample remained fully saturated during the test. The initial characteristics of the sand specimen in this test are presented in Table 7.4 where the test label is THM-S. The test programme is given in Table 7.3. Fig. 7.5 presents the temperature measured by the thermocouples along the column height.

The validation test showed that the column device provides a waterproof housing because no water leakage was observed. It also revealed a possible heat loss as the maximum

Table 7.3: THM-S test programme

Phase	1	2	3	4	5	6	7	8
Top T controlled (°C)	20	80	80	80	80	20	Free	Free
Bottom T controlled (°C)	80	Free	20	80	20	80	80	Free
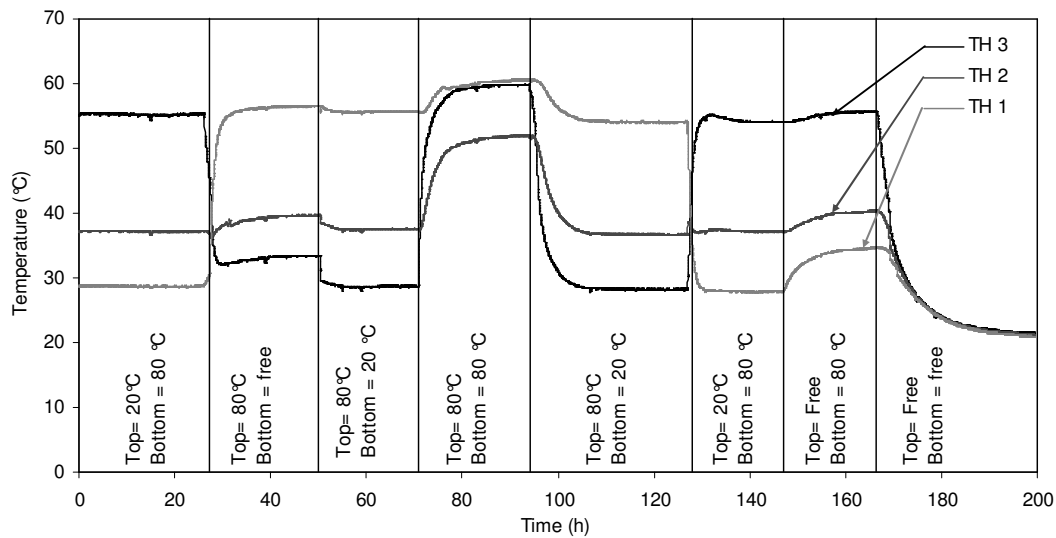
Figure 7.5: Temperature variation during the heating test

temperature achieved during phase 4 was 75% of the maximum and minimum prescribed for the heater temperature. The later conclusion was supported by the fact that there was no special isolation to completely prevent the heat loss.

7.3.2 Experiments on the sand bentonite mixture

7.3.2.1 Hydration test under constant temperature (HM-test)

The mixture of sand and Calcigel bentonite (SBM) was selected as a material for the main tests. The pre-determined initial density of the mixture is 1.4 g/cm^3. The preparation of the samples followed the procedure given hereafter. First, the sand and the clay were mixed and water was added to the mixture. The samples were placed into an air-tight container for more than two weeks in order to attain equilibrium. The initial conditions for the soil specimens are presented in Table 7.4 and they differ slightly from test to test. The initial water content was determined based on the oven drying method. The initial soil suction presented in Table 7.4 was measured in the chilled mirror device. The soil

Table 7.4: Initial soil sample conditions

Test name	mixture ratio (%)	Initial void ratio (-)	Intial dry density (g/cm^3)	Initial w/c (%)	Initial saturation (%)	Initial total suction (kPa)
THM-S	100S	0.71	1.55	26.5	98.9	0
HM-SBM	50B/50S	0.93	1.40	9.0	23.8	20200
THM-SBM	50B/50S	0.92	1.41	9.7	25.5	13930

samples were compacted into three separate parts and these parts were placed orderly into the cell body. The samples were 150 mm in diameter and 300 mm in height. During each test, after installing the TDR probes and the RH chambers, the specimen was kept in the same condition for six days in order to obtain equilibrium.

The first test performed on a sand-bentonite mixture (SBM) sample was a test at a constant temperature of 20°C. It is called the HM-SBM, where HM indicates that the test is conducted under coupled hydro-mechanical conditions. This test was conducted at room temperature controlled by an air conditioner. During the test the average temperature measured by the three thermocouples installed in the sample was 20.5($\pm$0.5°C) and the measured room temperature 21($\pm$1°C) on average. The soil specimen was hydrated from the bottom with de-aired and de-ionised water. The water was supplied using a burette and the water pressure was approximately 15 kPa. During this test there was no temperature control on the top or the bottom of the specimen. The distribution of the water content was monitored by means of the TDR devices, and the results are presented in Fig. 7.6(a). The evolution of the water content along the sample height shows that the water content initially reached the steady state at the lowest measurement point located 50 mm above the bottom of the sample (TDR 3). Next the water content equilibrium was reached at the middle of the sample (150 mm above the bottom of the sample - TDR 2) and last was taken at the highest measurement point located 50 mm below the top of the sample (TDR 1). The suction was determined based on the readings of the RH sensors, which also changed values during the experiment Fig. 7.6(b). Suction dropped from the initially measured value of approximately 20 MPa to zero when the soil reached saturation. The relative humidity was recorded by hand; therefore the results are discrete points.

When injecting water into the SBM sample, two competing phenomena begin to occur due to the interaction between microstructure and macrostructure of the soil. Mostly the

water is adsorbed within the microstructure owing to the exchange cation capacity of the diffuse double layer and according to the DDL theory (Gouy, 1910) and its modification (Tripathy et al., 2004). The absorbed water in the micropores causes an expansion of the microstructure within the confined system of the testing device and swelling pressure is induced. On the other hand, the volumetric expansion of the microstructure reduces the volume of the macropores, thereby reducing the available pore space for water and vapour flow.

The total axial stress measured by the load cells is presented in Fig. 7.7(a). The stress at the bottom of the sample includes swelling stress in addition to the weight of the top and bottom plugs and the weight of the soil sample. The stress on the top of the sample includes a load of about 0.1 kN applied prior to the test which is meant to ensure contact between the sample and the loading sensor. The maximum axial stress increment measured as compared to the initial state is 45 kPa. Agus and Schanz (2008) performed a series of swelling tests in isochoric cells for the same type of soil but at higher density (> 1.5 Mg/m^3). The swelling pressure reported in their work is 100±50 kPa on average. Taking into account that the swelling pressure increases with increasing soil density, the results in Agus and Schanz (2008) may be considered in agreement with the measured order of the swelling stress in the column device.

The value of swelling pressure of the SBM soil considered here is relatively small because of the sufficiently high initial density and clay content, as discussed in Tripathy et al. (2004) based on the interpretation of the diffuse doubled theory. To complete the information about this test, the water intake is shown in Fig. 7.7(b)

7.3.2.2 The test combining thermal and suction gradients (THM test)

The second sand-bentonite mixture test was conducted imposing both temperature and hydraulic boundary conditions on the top and bottom of the sample and it is called THM-SBM, where THM indicates it is a coupled thermo-hydro-mechanical test. The test consists of two phases. In the first phase (*phase 1*), the sample was heated from the bottom and cooled from the top until controlled stable values were reached: 20°C on the top of the sample and 80°C on the bottom of the sample. In the second phase (*phase 2*), water was supplied to the sample from the top of the sample under a pressure of 5 kPa. The temperature of the supplied water was 20°C. Temperature of the supplied water was controlled with an accuracy of ±0.01°C in the thermostat. But the water temperature may change when water intrudes the top cooling plate. Therefore, the temperature of

Table 7.5: Boundary conditions of THM-SBM test

		Thermal boundary		Water supplied boundary	
	Time (h)	top (°C)	bottom (°C)	top (kPa)	bottom (kPa)
Phase 1	$0 \rightarrow 2450$	20	80	-	-
Phase 2	$2450 \rightarrow 2560$	20	80	5.0	-

the cooling water was set and controlled at 16°C and the heater on the top of the sample was controlled to heat the sample to 21°C. Thus the thermocouple of the heater was used to monitor and guarantee that temperature near the top of the sample face was stable during the test. The temperature on the bottom of the specimen was kept at 80°C, whereas the temperature on the top face of the sample was maintained at 20°C during the entire process of sample hydration. The transient evolution of the temperature during THM-SBM test is presented in Fig. 7.8(a). The temperature values measured at the end of the heating phase at 50 mm below the top of the sample (TH 1), in the middle of the sample (TH 2) and at 50 mm above the bottom of the sample (TH 3) are 21.7°C, 28.3°C and 44°C, respectively Fig. 7.8(b). The water content measured by TDR 1, TDR 2 and TDR 3 is 6.5%, 9.2%, and 14%, respectively. The temperature had changed quickly along the sample and within 10 hours it reached the steady state. A slight reduction in temperature after the steady state was due to varied thermal conductivity induced by the variation in water content. When the soil was heated, vapour diffusion was initiated. The water vapour moved from high-temperature to low-temperature places. Because the soil thermal conductivity depends on water content (Olivella et al., 1996a), the slow change in water content induces a change of thermal conductivity of soil sample. Consequently the temperature measured along the sample also changed.

The evolution of water content measured by TDR probes during the heating phase of the test (*phase 2*) is presented in Fig. 7.10(a). The water content measured by the TDR probe installed near the bottom of the sample (TDR 3) increased rapidly to 10%. Afterwards it slowly decreased to 6.5%, whereas water content measured by TDR 2 in the middle of the sample increased for a relatively long period of time and decreased afterwards. The water content measured near the top of the sample had increased continuously up to 14%, after which it reached its steady state. Such behaviour reflects the results of (Gatabin and Billaud (2005), pp.34) where they heated the soil sample up to 130°C.

The measured suction varied similarly to the water content. The soil suction measured by the RH sensor near the soil sample increased significantly, whereas the suction measured

50 mm below the top of the sample slightly decreased. The evolution of suction in *phase 2* agrees qualitatively with the result reported in Bag (2011). The quantitative difference may be attributed to the fact that in Bag (2011) the RH sensors were located closer to the heater, and there was controlled temperature only on one side of the sample, which may cause the vapour diffusion process to occur faster.

The axial stress values measured by the load cells are presented in Fig. 7.10(b). The stress measured at the top load cell increased slowly and reached maximum value in about 600 hours. Afterwards the stress started to decrease. The stress measured at bottom load cell after calibrating the temperature showed that the bottom pressure did not change significantly during the heating phase of the test. An explanation may be that when the heating was being processed the bottom part of the sample near the heater endured shrinkage due to the diffusion of water vapour. However, the top part of the sample, which is closer to the cooler, swelled due to condensation of water vapour, thereby increasing the water content. At the end of *phase 1* the vertical stress measured at the bottom of the load cell was equal to the vertical stress measured at the top of the load cell.

For *phase 2* of the THM-SBM test, the water content measured during wetting process from the top is presented in Fig. 7.11(a). The water content increased until the soil specimen reached maximum saturation (suction reached zero value). Water content measured by TDR probes located near the top (TDR 1) and in the middle (TDR 2) of the sample decreased after they had reached the maximum water content. This may be explained by the change in the TDR waveguide environment during the hydration phase of the test.

The suction determined using the measured RH decreased together with the increase in water content. The decrease in suction measured near the bottom of the sample (RH 3) was more prominent, whereas the suction change in the middle (RH 2) and near the top of the sample (RH 1) was insignificant Fig. 7.11(b). When analysing these results it has to be noted that relative humidity measurement is not accurate at high relative humidity or low suction Beddoe et al. (2010).

When supplying water of 20°C from the top of the cell the values of the temperature measured by the thermocouples located in the middle (TH 2) and in near the bottom of the sample (TH 3) decreased for a short time at the beginning of *phase 2*. This may be explained because the water temperature was lower as compared with the sample temperature, and the system tried to attain thermal equilibrium Fig. 7.12(a). This decrease in sample temperature was later compensated by the heater. It can be seen that when the system reached the steady state, the temperature of the saturated specimen was higher than the temperature of specimen in its unsaturated condition. This corroborates the the-

ory that the thermal conductivity of saturated soil is higher than the thermal conductivity of partial saturated soil Olivella et al. (1996a).

The evolution of the axial stress measured by the load cells in *phase 2* is presented in Fig. 7.12(b). The increase of the stress measured at the top load cell was induced by the development of a swelling pressure and a load applied prior to *phase 2* of 0.2 kN to ensure the sample contact and the load sensor. The vertical stress measured at the bottom of the load cell was higher than the stress recorded at the top of the load cell. Pusch (1980b); Villar and Lloret (2004); Agus (2005) reported results for swelling pressure measured at different temperatures where the swelling pressure decreased with increasing temperature. Here, the maximum stress achieved at the end of *phase 2* during the THM-SB test is comparable to the maximum vertical stress during the HM-SBM test. Furthermore the difference may be attributed to load cell precision. However, the decrease in swelling pressure with increasing temperature contradicts the diffuse double layer theory (Yong et al., 1962; Tripathy et al., 2004).

Figure 7.13 presents the relationship between suction and water content obtained using data from different tests on SBM material. The results of the suction and water content relationship in confined conditions are placed with the results of the element tests for the soil water retention curve.

The unconfined SWRC (UC-SWRC) test compared to the column tests in Fig. 7.13 was performed under unconfined conditions using the axis translation technique and the vapour equilibrium technique. The dry density in all tests is approximately the same, 1.4 Mg/m^3. It has to be pointed out that during the HM and THM tests some parts of the sample may have undergone volume expansion, whereas the volume of some other parts may have decreased in order to preserve the volume increase of the whole specimen. Therefore not all sensor readings during the column tests represent the SWRC under confined conditions. The relationship between water content and suction determined based on the readings of the sensors near the top of the sample is the same for HM and THM tests because the temperature was identical during both tests and only wetting was realised. Furthermore, a comparison has been made of only the results of sensors pair TDR 1–RH 1 and the SWRC determined by means of a UC test. The difference in the SWRC obtained using the data from the column tests and UC-SWRC test is due to the difference in the initial soil state, namely, the presence of different soil microstructures. The samples for the column tests were prepared via compaction at low water content, thereby inducing clay particle flocculation, whereas for the UC-SWRC test the samples were compacted at high water content obtaining more oriented (parallel) clay platelet structure. Because
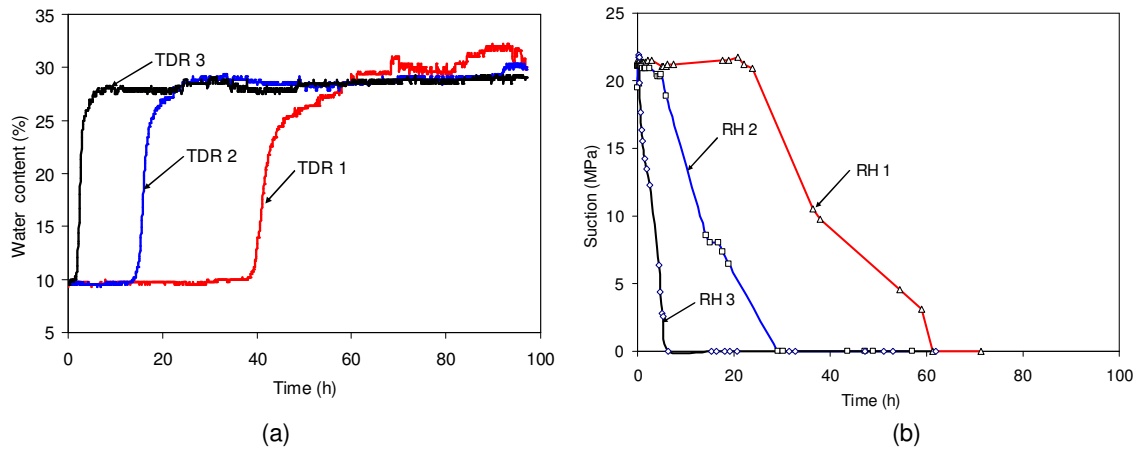
Figure 7.6: HM-SBM test: (a) evolution of water content. (b) evolution of suction.
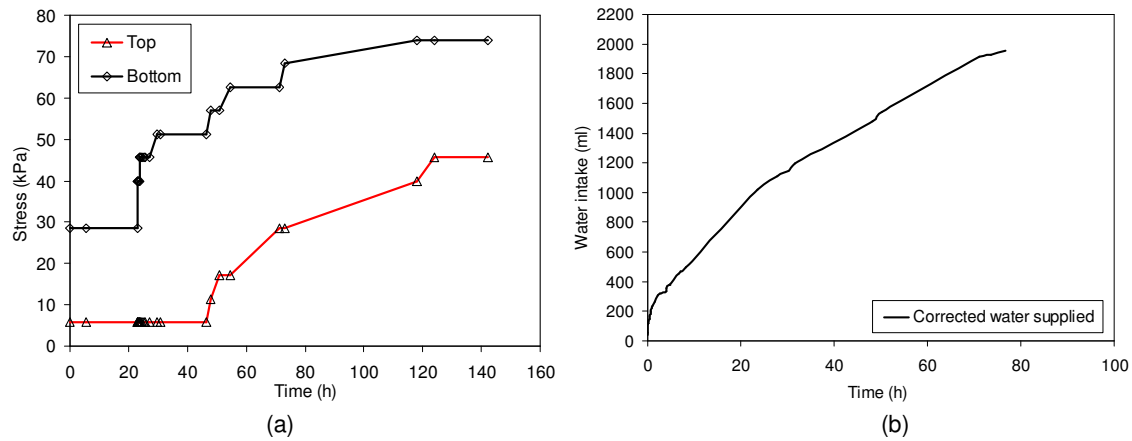
Figure 7.7: HM-SBM test: (a) evolution of axial stress, (b) water intake with time.

of the flocculation, the soil samples used in the column tests could retain more water at a given suction as compared with the sample used in the UC-SWRC test, as illustrated in Fig. 7.13. It is also noted that water was sucked up by capillary pressure during the UC-SWRC test with a pressure plate device. Some macropores could not be filled under capillary pressure in this test due to the snap-off effect of water in variety of pore sizes (Fredlund and Rahardjo, 1993). On the other hand, water was injected with positive water pressure (15 kPa) into the THM column. Therefore the soil specimen in the THM column attained more water than in the UC-SWRC test.
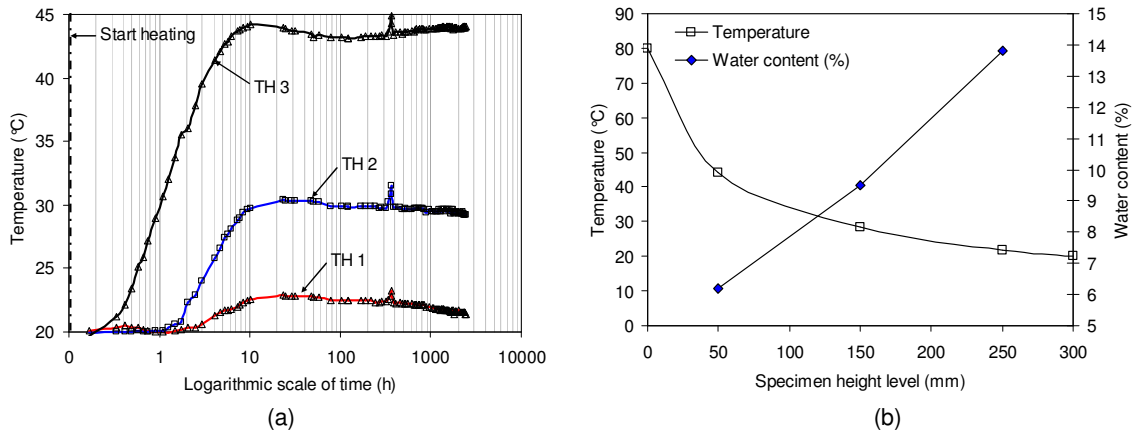
Figure 7.8: THM-SBM test, phase 1: (a) evolution of temperature, (b) temperature and water content along the column at the end of heating phase.
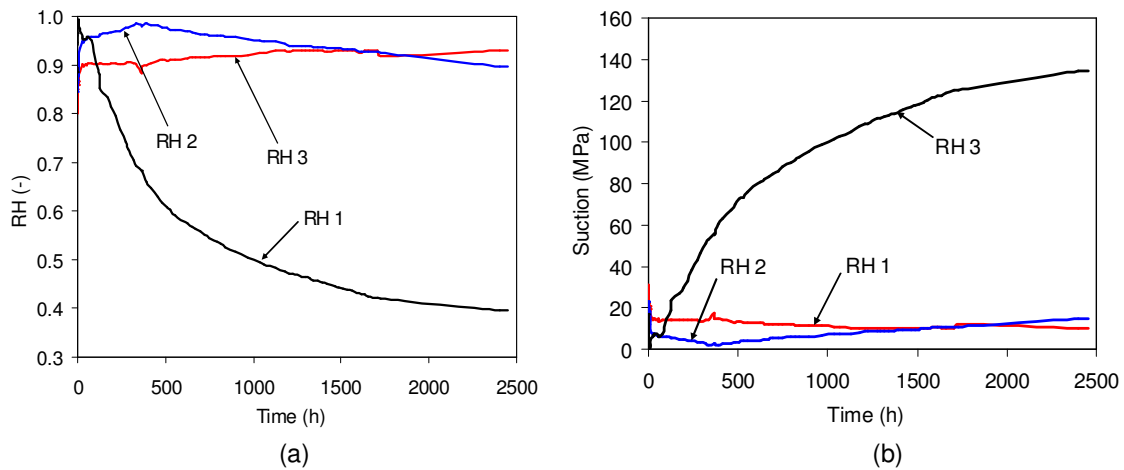
Figure 7.9: THM-SBM test, phase 1: (a) evolution of RH. (b) evolution of suction.

7.3.3 Effect of thermal gradients on on hydraulic conductivity of the sand-bentonite mixture

The effect of temperature on hydraulic conductivity has been considered by several researchers. Pusch (1980a) observed an increase in the coefficient of permeability in Darcy's law of bentonite MX-80 and Ca-bentonite (Erbslöh) when changed temperature from 20°C to 70°C at low hydraulic gradients. The effect of temperature was modelled based on statistical methods as in Eq. 7.2.

$$k \propto \frac{f(T)}{t + t_0} \tag{7.2}$$
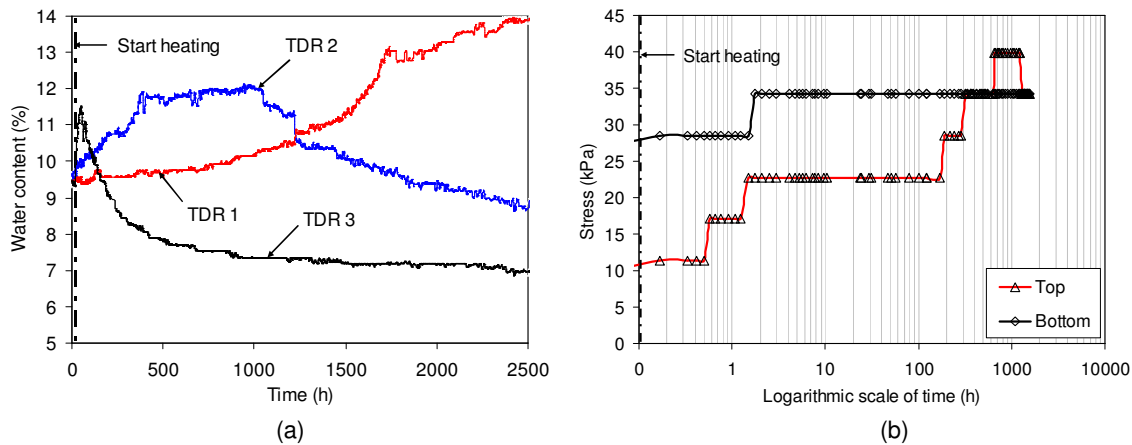
Figure 7.10: THM–SBM test, phase 1: (a) evolution of water content, (b) evolution of axial stress at top of the sample and bottom after calibration of the load cell with temperature.

where k is the coefficient of permeability (e.g. m/s), $f(T)$ is the function of temperature, and it is assumed that $f(T) = T^n$, $\forall\, n > 1$, t and t_0 are time measurement.

Cho et al. (1999) studied the hydraulic conductivity of Ca-bentonite from Kyungju, Korea. They found that hydraulic conductivity increases from 2.2×10^{-12} (m/s) at 20°C to 5.4×10^{-12} (m/s) at 80°C on average at a soil density of 1.4 Mg/m^3. If the soil density is 1.8 Mg/m^3, it increases from $4,5 \times 10^{-14}$ (m/s) at 20°C to 1.6×10^{-13} (m/s) at 80°C. Meanwhile, Delage et al. (2009) reported that intrinsic permeability insignificantly changed for the temperature at range from 20°C to 90 °C. They observed that the intrinsic permeability of Boom clay changes in the range from 6.0×10^{-19} to 7.0×10^{-19} m^2. The result of Ye et al. (2012) about the effect of temperature on intrinsic permeability agreed with the result of Delage et al. (2009).

When referring to HLW storage facility as designed, the canister is located inside the buffer and produces radiation heat. The temperature increases the closer the canister is. The temperature gradient not only changes the physicochemical property of the bentonite but also induces diffusion of water. It may affect the process of hydraulic conduction. Therefore, the effect of thermal gradients on hydraulic conductivity must be understood. These researchers have considered isothermal condition in their element tests. However, the effects of thermal gradient on permeability were not investigated.

The tests to determine the coefficient of permeability for Darcy's law were carried out after completing phase 2 of THM-SBM tests. Three types of tests were conducted on the same soil sample: (1) a test at 20°C, (2) a test after heating the soil from the bottom and
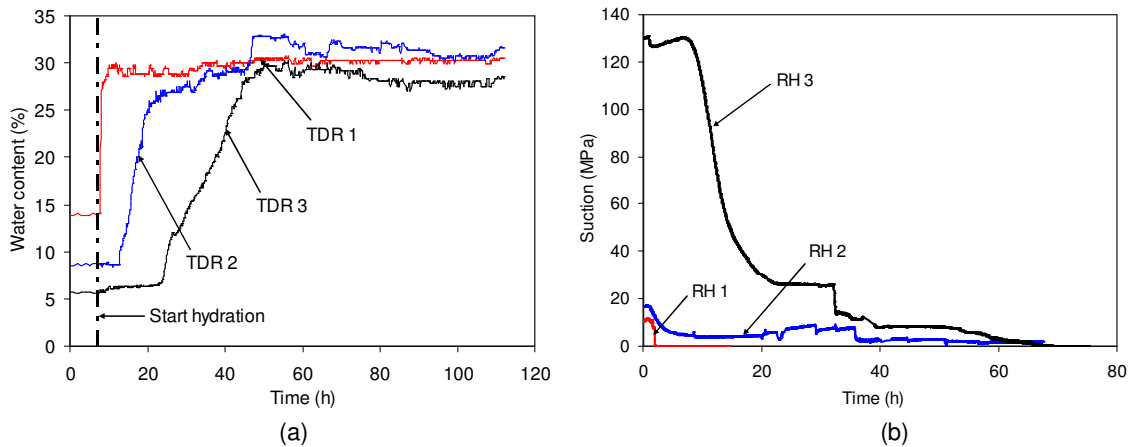
Figure 7.11: THM–SBM test, phase 2: (a) evolution of water content, (b) evolution of suction.
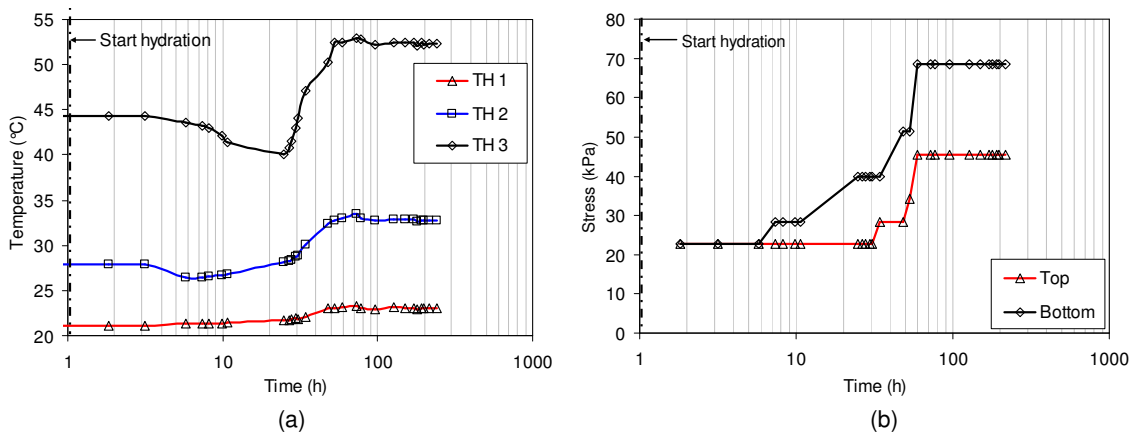
Figure 7.12: THM-SBM test, phase 2: (a) evolution of temperature, (b) evolution of axial stress.

supplying water from the top, and (3) a test after heating the soil from the bottom and supplying water from the bottom. The coefficient of conductivity is calculated based on the ASTM_D2434-68 (2000) §8. The results in the coefficient of conductivity are given in the Fig. 7.14.

According to Pusch (1980a) the temperature affects the hydraulic conductivity of soil in two ways: the increase in temperature induces a decrease in the dynamic viscosity of water and an increase in the creep rate, which also increases permeability. The dynamic viscosity of water is 0.890 mPa.s at 20°C and 0.378 mPa.s at 75°C (Lide, 2005). The change in hydraulic conductivity may be expressed by the Eq. 7.3 (Cho et al., 1999;
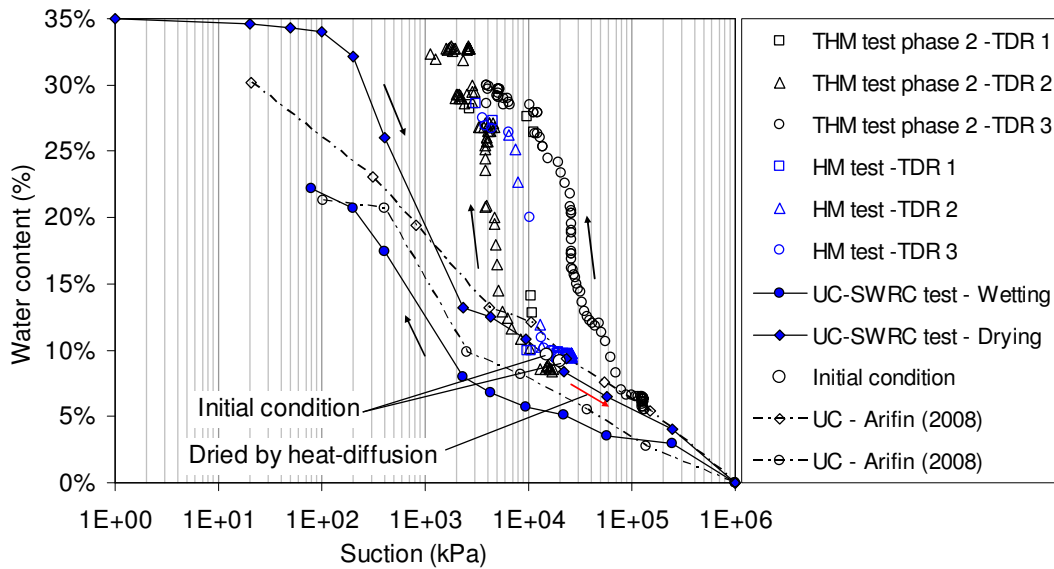
Figure 7.13: Relationship between suction and water content measured by confined (this study) and unconfined method

Delage et al., 2009).

$$k(T) = \frac{K \gamma_w(T)}{\mu(T)} \tag{7.3}$$

where K is the intrinsic permeability (e.g. m^2), $\mu(T)$ is the dynamic viscosity as a function of temperature and $\gamma_w(T)$ is the density of water also as a function of temperature. According to Lide (2005) $\gamma_w(20°C) = 0.99821$ g/cm^3 and $\gamma_w(80°C) = 0.97182$ g/cm^3. The decrease in density in this range of temperature is insignificant. Following Eq. 7.3, there are two processes inducing two contradictory behaviors of hydraulic conductivity with temperature; the dynamic viscosity decreases with an increase temperature inducing an increase in the coefficient of permeability. Meanwhile, the density of water decreases with an increase in temperature inducing a decrease in the coefficient of conductivity.

According to Fig. 7.14, the measured coefficient of conductivity increases when the hydraulic gradient and the thermal gradient have the same sign. A decrease in the coefficient of conductivity occurs when the hydraulic gradient and the thermal gradient have the opposite sign. However, the magnitude of the change in the hydraulic conductivity as it relates to temperature is insignificant.
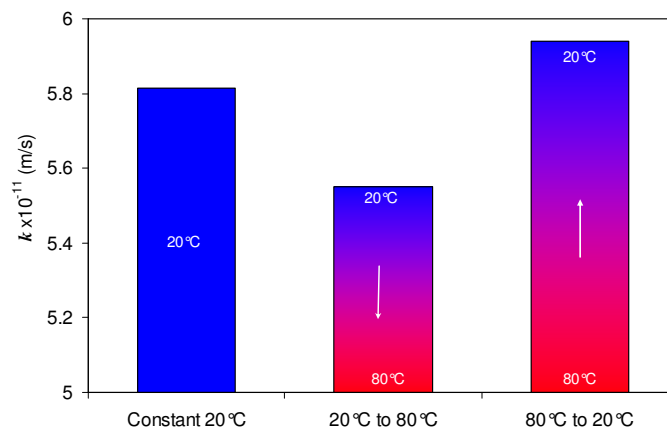
Figure 7.14: THM–SBM test: Coefficient of conductivity measured at different gradients
of temperature

7.3.4 Conclusion

A new column testing device was proposed and demonstrated reasonable results for moderately expansive sand-bentonite mixtures in laboratory investigations of coupled thermo-hydro-mechanical behaviour of expansive soils in conditions close to those used in nuclear waste buffers. The column device was designed to apply temperature and hydraulic loading from the top and the bottom of the sample, thus allowing thermal and suction gradients to be applied. The device was equipped with water content, temperature and relative humidity sensors at three different sections along the specimen. The water content and temperature sensors were specially fitted to minimise sample disturbance. Special attention was paid to calibrating the sensors, taking into account the influence of temperature. From the experimental results, there is a distinct advantage when measuring swelling stress simultaneously at the top and the bottom of the sample as it may differ under certain conditions. The tests also demonstrate the ability of the THM-testing device to provide rich data for understanding the coupled THM-process and the involved physical phenomena during the heating/cooling process while wetting expansive soils. Relevant physical phenomena include vapour diffusion, water convection and thermal transport within the complex pore system comprised of micropores and macropores. The column device described here gives insight into the transient nature of the suction-temperature-water content relationship for a sand-bentonite mixture, revealing that the true equilibrium state for suction and water content is significantly delayed. This depends on the magnitude of the total suction gradient between different levels of pores and the dynamics of the processes that take place due to interactions at different pore scales.

8 Numerical simulations and discussion

8.1 Theoretical framework for THM modelling

In this section, it is presented the thermo-hydromechanical model of expansive soil behaviour which is a part of the CODE BRIGHT (DIT-UPC, 2009) constitutive law library. The equations involved in the THM problem can be categorized into four main groups: balance equations, constitutive equations, equilibrium restrictions and definition constraints. Equations for mass balance were established following the compositional approach (Olivella et al., 1994). That is, the mass balance is performed for water, air and mineral species instead of using solid, liquid and gas phases. The equation for balance of energy is established for the medium as a whole. The equation of momentum balance for the porous medium is reduced to that of stress equilibrium (Olivella et al., 1996a). The theoretical framework used for fully coupled THM numerical simulations is presented hereafter.

8.1.1 Balance equations

Mass balance of water: Water is present in the liquid and gas phases. The total mass balance of water is expressed as follows.

$$\frac{\partial}{\partial t}\left(\theta_l^w S_l \phi + \theta_g^w S_g \phi\right) + \nabla \cdot \left(\boldsymbol{j}_l^w + \boldsymbol{j}_g^w\right) = f^w \tag{8.1}$$

where, f^w is an external supply of water, θ_l^w and θ_g^w are the volumetric mass of water in the liquid and gas phases, respectively. $\boldsymbol{j}_l^w$ is the mass flux of water in liquid phase, $\boldsymbol{j}_g^w$ is a flux of water in gas phase as the moisture.

Momentum balance for the medium: The momentum balance reduces to the equilibrium of stresses if the inertial terms are neglected.

$$\nabla \cdot \boldsymbol{\sigma} + \boldsymbol{b} = \boldsymbol{0} \tag{8.2}$$

where, $\boldsymbol{\sigma}$ is the stress tensor and $\boldsymbol{b}$ is the vector of body forces.

Internal energy balance for the medium: The equation for the internal energy balance for the porous medium is established taking into account the internal energy in each phase (E_s, E_l, E_g).

$$\frac{\partial}{\partial t}\left(E_s\rho_s\left(1-\phi\right)+E_l\rho_l S_l\phi+E_g\rho_g S_g\phi\right)+\nabla\cdot\left(\boldsymbol{i}_c+\boldsymbol{j}_{Es}+\boldsymbol{j}_{El}+\boldsymbol{j}_{Eg}\right)=f^Q \quad (8.3)$$

where, $\boldsymbol{i}_c$ is the energy flux due to conduction through the porous medium, the fluxes $\boldsymbol{j}_{Es}$, $\boldsymbol{j}_{El}$ and $\boldsymbol{j}_{Eg}$ are advective fluxes of energy caused by mass motions and f^Q is an internal/external energy supply, ρ_s is the density of solid, ρ_l is the density of liquid, and ρ_g is the density of gas.

8.1.2 Constitutive equations of the coupled thermo-elasto-plastic model

Based on the research of Baldi et al. (1988); Hueckel and Borsetto (1990); Hueckel and Pellegrini (1992) pioneered for saturated soil with temperature effects and Alonso et al. (1990) for unsaturated soil, Gens (1995) drew the constitutive model under the thermo-elasto-plastic theory for unsaturated soil (BBM-TEP). The (BBM-TEP) model is adopted for mechanical stress-strain behaviour in CODE_BRIGHT. It is assumed that the strain increment is a sum of the increment of the elastic strain $\boldsymbol{\varepsilon}^e$ and plastic strain $\boldsymbol{\varepsilon}^p$). It is presented incrementally as follows:

$$d\boldsymbol{\varepsilon}=d\boldsymbol{\varepsilon}^e+d\boldsymbol{\varepsilon}^p \quad (8.4)$$

Following the two stress variable concept in unsaturated soil mechanics, the elastic part of the strain increment is taken to be a sum of the increments of suction induced $\boldsymbol{\varepsilon}^{s-e}$, net stress induced $\boldsymbol{\varepsilon}^{\sigma-e}$ strains and the strain increment due to temperature change $d\boldsymbol{\varepsilon}^{T-e}$. The decomposition of the strain increment for the elastic strain increment reads:

$$d\boldsymbol{\varepsilon}^e=d\boldsymbol{\varepsilon}^{\sigma-e}+d\boldsymbol{\varepsilon}^{s-e}+d\boldsymbol{\varepsilon}^{T-e} \quad (8.5)$$

The nonlinear elastic law for the volumetric strain induced by the net stress is expressed in Eq. 8.6.

$$d\boldsymbol{\varepsilon}_v^{\sigma-e}=\frac{\kappa_i(s)}{1+e}\frac{dp'}{p'} \quad \text{and} \quad p'=p-\max(P_g,P_l) \quad (8.6)$$

$$\kappa_i(s) = \begin{cases} \kappa_{io} \left(1 + \alpha_i \, s\right) & \text{if } 1 + \alpha_i \, s \geq 0.001 \\ 0.001 \, k_{io} & \text{if } 1 + \alpha_i \, s < 0.001 \end{cases} \tag{8.7}$$

where p is the total mean stress, and p' is the generalised effective stress. In CODE_BRIGHT it is defined by $p' = p - \max(P_g, P_l)$. This means p' is a net mean stress in the unsaturated state or an effective stress in the saturated state, and P_g and P_l are gas pressure and liquid pressure, e is the void ratio and κ_{io} and α_i are model parameters.

Suction and temperature induce only volumetric strains with constitutive equations given as follows:

$$d\boldsymbol{\varepsilon}_v^{s-e} = \frac{\kappa_s(p', s)}{1 + e} \frac{ds}{s + p_{at}} \quad ; \quad d\boldsymbol{\varepsilon}_v^{T-e} = \alpha_o \, dT \tag{8.8}$$

with

$$\kappa_s(p', s) = \kappa_{so} \kappa_{sp} \, \exp\left(\alpha_{ss} \, s\right) \tag{8.9}$$

and

$$\kappa_{sp} = \begin{cases} 1 + \alpha_{sp} \ln\left(\frac{10^{-20}}{p_{ref}}\right) & \text{if } p' \leq 10^{-20} \\ 0 & \text{if } p' \geq p_{ref} \exp\left(\frac{-1}{\alpha_{sp}}\right) \\ 1 + \alpha_{sp} \ln\left(\frac{p'}{p_{ref}}\right) & \text{elsewhere} \end{cases} \tag{8.10}$$

The parameters involved are: α_o for the thermal expansion coefficient; κ_{so} is the elastic stiffness parameter when changing suction at zero net stress; p_{at} is the atmospheric pressure; and α_{ss} and α_{sp} are model parameters. The elastic slopes κ_i and κ_s may be considered independent of temperature in the case of moderate temperature gradients.

The volumetric elastic strain is the sum of volumetric strain induced by mechanical stress and volumetric strain induced by suction, plus non-linear elastic expansion/shrinkage due to temperature as follows:

$$d\varepsilon_v^e = \frac{k_i(s)}{1 + e} \frac{dp'}{p'} + \frac{k_s(p', s)}{1 + e} \frac{ds}{s + p_{at}} + (\alpha_o + 2\alpha_2 \Delta T) dT \tag{8.11}$$

where α_2 is parameter for the thermal elastic strain.

The yield surface in BBM model is given in the deviatoric plane $q - p$ via the following equation:

$$F = q^2 - M^2 \left(p' + p_s\right) \left(p_o - p'\right) = 0 \tag{8.12}$$

where $q = \sqrt{\frac{3}{2}\boldsymbol{\sigma}^D : \boldsymbol{\sigma}^D}$, with deviatoric stress defined as $\boldsymbol{\sigma}^D = \boldsymbol{\sigma}' - \frac{1}{3}\boldsymbol{\sigma}' : \boldsymbol{I}$. The pre-consolidation pressure p_o depends on suction, and according to Alonso et al. (1990) it is defined as:

$$p_o = p^c \left(\frac{p_o^*(T)}{p^c}\right)^{\frac{\lambda(0)-\kappa_{io}}{\lambda(s)-\kappa_{io}}} \tag{8.13}$$

where p^c is a reference pressure, $\lambda(0)$ is the plastic stiffness parameters for changes in effective stress in a saturated state, $p_o^*(T)$ is the pre-consolidation pressure in a saturated state. $p_o^*(T)$ is defined as a nonlinear function of temperature according to Hueckel and Pellegrini (1992) and adopted in Gens (1995) as follows:

$$p_o^*(T) = p_o^* + 2(\alpha_1\Delta T + \alpha_3\Delta T|\Delta T|) \quad \text{and} \quad \Delta T = T - T_{ref} \tag{8.14}$$

where α_1 and α_3 are model parameters, and T_{ref} is reference temperature. According to Hueckel and Pellegrini (1992), an increase in temperature induces a decrease in the pre-consolidation pressure. The stiffness parameter for changes in the mean net stress at a given suction is defined by:

$$\lambda(s) = \lambda(0)\left[(1-r)\exp(-\beta s) + r\right] \tag{8.15}$$

where r and β are model parameters.

The tensile strength equation is adopted from Gens (1995) in Eq. 2.45. The tensile strength p_s follows a linear relationship with suction and is a nonlinear function of temperature:

$$p_s = p_{s0} + k\,s\exp(-\rho\Delta T) \tag{8.16}$$

where k is the parameter that takes into account the increase in tensile strength due to suction, p_{s0} is tensile strength in a saturated state, ρ is a parameter that takes into account the decrease in tensile strength due to a temperature increase.

Isotropic hardening depends on the plastic volumetric strains as follows:

$$\mathrm{d}p_o^* = \frac{1+e}{\lambda(0)-\kappa_{io}}\,p_o^*\,\mathrm{d}\varepsilon_v^p \tag{8.17}$$

8.1.3 Constitutive equations of the hydraulic model

Advective flow of the water phase is described by the generalised Darcy's law:

$$\boldsymbol{q}_l = -\frac{\boldsymbol{k}k_{rl}}{\mu_l}\left(\nabla p_l - \rho_l\boldsymbol{g}\right) \tag{8.18}$$
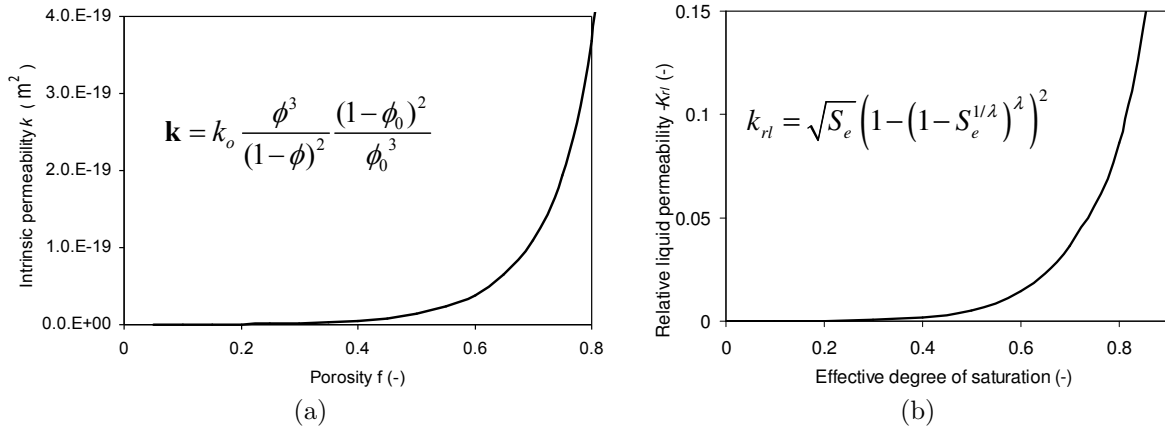
Figure 8.1: Illustration of permeability model. (a) Intrinsic permeability vs. porosity and (b) Relative permeability model vs. effective degree of saturation.

where μ_l is the dynamic viscosity of the pore liquid, $\boldsymbol{g}$ is the gravity acceleration, ρ_l is the liquid density. The tensor of intrinsic permeability $\boldsymbol{k}$ usually depends on porosity according to the Kozeny's model:

$$\boldsymbol{k} = \boldsymbol{k}_o \frac{\phi^3}{(1-\phi)^2} \frac{(1-\phi_o)^2}{\phi_o^3} \tag{8.19}$$

where ϕ is the porosity, ϕ_o is the reference porosity, $\boldsymbol{k}_o$ is the intrinsic permeability for a matrix with porosity ϕ_o. The relative permeability k_{rl}, is derived from Mualem-van Genuchten closed form model, van Genuchten (1980):

$$k_{rl} = \sqrt{S_e}\left(1 - \left(1 - S_e^{1/\lambda}\right)^\lambda\right)^2 \tag{8.20}$$

where λ is a shape parameter for the retention curve and S_e is defined as:

$$S_e = \frac{S_l - S_{rl}}{S_{ls} - S_{rl}} = \left(1 + \left(\frac{p_g - p_l}{P}\right)^{\frac{1}{1-\lambda}}\right)^{-\lambda} \quad \text{and} \quad P = P_0\left(\frac{\sigma_T}{\sigma_{T0}}\right) \tag{8.21}$$

where S_l, S_{ls} and S_{rl} are the current, the maximum and the residual liquid degree of saturation, respectively; P_0 is a model parameter; σ_T is the surface tension of liquid; and σ_T0 is the surface tension of liquid in which P_0 was measured. According to Olivella (1995) σ_T is calculated by empirical relation as in Eq. 8.22.

$$\sigma_T = 0.03059 \exp\left(\frac{252.93}{273.15 + T}\right) \tag{8.22}$$
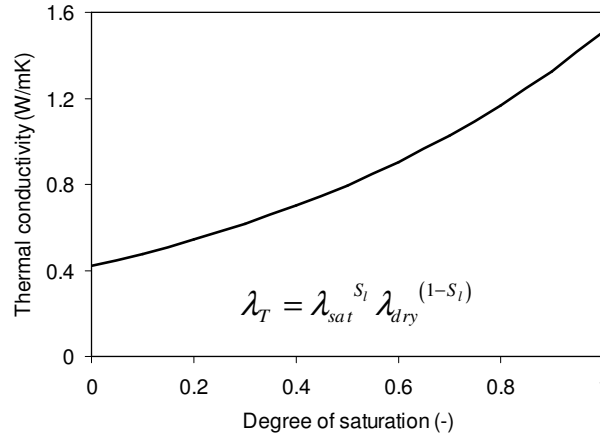
Figure 8.2: A relation of thermal conductivity with degree of saturation

Molecular diffusion of vapour in air: Fick's law is adopted to define the diffusive flux of water in gas phase $\boldsymbol{i}_g^w$:

$$\boldsymbol{i}_g^w = - \left(\phi \rho_g \, S_g \, D_m \boldsymbol{I} \right) \nabla \omega_g^w \tag{8.23}$$

where ρ_g is the vapour density, ω_g^w is the mass fraction of the water in the gas phase, $\boldsymbol{I}$ is the identity matrix and D_m is the diffusion coefficient of vapour in m^2/s is defined by:

$$D_m = \tau D \frac{(273.15 + T)^n}{P_g} \tag{8.24}$$

where τ is the tortuosity, D is the molecular diffusion coefficient at temperature 273.15K, and n is a coefficient.

8.1.4 Constitutive equations for the heat conduction

Fourier's law was adopted for the heat conduction flux, $\boldsymbol{i}_c$:

$$\boldsymbol{i}_c = -\lambda_T \nabla T \quad \text{where} \quad \lambda_T = \lambda_{sat}^{S_l} \lambda_{dry}^{(1-S_l)} \tag{8.25}$$

where λ_T is the soil thermal conductivity, λ_{sat} and λ_{dry} are soil thermal conductivity in the saturated and dry state, respectively. The relation of thermal conductivity and degree of saturation of the sand-bentonite mixture is presented in Fig. 8.2.

8.2 A model for predicting hysteretic unsaturated flow including air entrapment

In this section a new model reproducing the hysteresis of the soil water retention curve is introduced. The model takes air entrapment and variation of the air entry value during the drainage and the imbibition. The model is implemented in a finite element code, a CODE_BRIGHT. The model is applied to simulate the drainage and imbibition column tests for sand material. The new model is compared with the other soil-water retention models to illustrate the influence of soil water retention curve on modelling water and gas flow.

8.2.1 Introduction

The most important relation to describe unsaturated soil behaviour is the soil water retention curve (SWRC). The importance of the SWRC is not only in giving insight into the soil water interaction but in providing a tool to estimate hydraulic and mechanical characteristics of unsaturated soils. Therefore the SWRC model has to explain the experimental results with a sufficient accuracy in order to expect realistic prediction of the water flow behaviour in the unsaturated zone, making possible to assess the water uptake from plants, the course of pollutants and contamination and also the balance of water resources in the water cycle or the soil shear strength (Fredlund et al., 1996; Vanapalli et al., 1996; Lu et al., 2012), that is subsequently used in stability analysis.

Several two-phase flow experiments are available for determining hydraulic properties of unsaturated soil. Experiments are performed either under steady-state or transient flow conditions. Experimental results obtained under transient state conditions are presented and used for numerical simulation in the present investigation. Transient state tests were performed by Topp et al. (1967), Wildenschild et al. (1997), Schultze et al. (1999). Commonly, these types of tests are performed in a conventional column apparatus. The conventional column apparatus is equipped with sensors for measuring the capillary pressure-saturation relationship while draining and wetting the soil sample.

In many studies only pore water pressure measurements (Chapius et al., 2007) are performed along the column; therefore an inverse procedure has to be used to determine unsaturated soil parameters. Nützmann et al. (1998) used a column apparatus to determine the hydraulic properties of porous media, where water content and pore pressure were measured. However, the locations of pore pressure measurements and the water

content measurements were not at the same depth; therefore the SWRC could not be obtained directly. Experiments in a column apparatus were also performed by Yang et al. (2004a) and Yang et al. (2004b), where the pore water pressure and also the water content were measured pairwise in several depths. However, the effect of hysteresis was not investigated because the test programme did not include applying several drainage and imbibition cycles.

Parallel to experimental observations, several model concepts and formulations have been developed for the approximation of the hysteresis loop in SWRC. In general, models used to predict hysteretic SWRC can be classified into two categories (Pham et al., 2005): physically based models (e.g. domain models) and empirical models. Physical principle models based on the domain theory have been introduced by several authors, e.g. by Everett (1954); Topp (1971a,b); Mualem (1974), Beliaev and Hassanizadeh (2001); Mualem and Beriozkin (2009); Maqsoud et al. (2012). Other authors used empirical models to describe the hysteretic SWRC, (Scott et al., 1983; Kool and Parker, 1987; Feng and Fredlund, 1999; Kawai et al., 2000; Li, 2005; Stoimenova et al., 2006; Canone et al., 2008). These models employ regression analysis to fit the experimental data. However, the parameters in the model function, as a rule, have no physical meaning. Empirical hysteresis concepts have also been developed to account for non-wetting phase trapping resulting from drainage and imbibition cycles and have been verified with SWRC data measured in the laboratory (Parker and Lenhard, 1987; Tan, 1990; Gerhard and Kueper, 2003).

Recently, with the advance in computer power, numerical simulations have been increasingly employed to predict unsaturated flow in porous media. In problems that involve alternating drainage and imbibition paths, a significant issue related to the hysteresis in the soil water relationship is the trapping of air in the pore system that cannot be removed through the water imbibition process. Stauffer and Dracos (1986) has shown the significance of SWRC hysteresis by using experimental and numerical methods. The experiments and simulations were carried out for one draining and wetting cycle in their study. Numerical studies have also been conducted on unsaturated flow including hysteresis and air trapping effects (Rubin, 1967), Pickens and Gillham (1980), Stauffer (1995), while unsaturated flow under successive alternating of drainage and imbibition has been investigated in (Jaynes, 1992). Stauffer and Kinzelbach (2001) carried out an experiment and a numerical simulation for cyclic wetting and drainage processes in a dimensional flow case. The numerical simulation using the finite element method which employed the Mualem (1984) model was also performed. A non-wetting phase trapping along drainage and imbibition cycles has been pointed out in several experimental reports (Parker and

Lenhard, 1987), Tan (1990), Gerhard and Kueper (2003). However, the reduction in the maximum degree of saturation due to air entrapped in soil structures was not analysed in terms of numerical modelling and simulation of the experimental evidence.

The aim of this study is to allocate the appropriate SWRC model based on experimental observation that will yield to a reliable prediction of hysteretic unsaturated flow. Hysteresis and phase trapping effects have been thoroughly investigated by means of experiments as well as numerical modelling approaches.

Therefore in the section experimental results are presented which were obtained from a series of sand column tests to establish the soil water relationship. Several drainage and imbibition cycles according to the water level variation were experimentally and numerically simulated. This way the phenomena of hysteresis and occluded air were investigated quantitatively in order to be considered in SWRC modelling. During the testing procedure capillary pressure as well as water content were monitored by means of a tensiometer and TDR sensors. The measured data allowed the capillary pressure and water content development vs. time to be monitored during drainage and imbibition cycles and capillary pressure and water content to be linked directly to the soil water relationship.

For the numerical simulation of the tests presented here, three different approaches to model the SWRC were used (Sect. 8.3.3). The first approach accounts for the hysteresis loop in SWRC realised in first drying and main wetting soil water retention curve and ignores the phenomenon of occluded air. The scanning curves are modelled as parallel lines. Within the second approach the reduction in maximum saturation due to occluded air is considered in addition to the hysteresis loop. In the third approach, a new model is introduced taking into account the presence of occluded air and the variation in the air-entry value in the course of the wetting-drying cycles. The presented comparative study shows how predictions can be improved by employing conceptually simple, empirical hysteresis concepts in the numerical model and consequently to what extent one can expect accurate predictions of hysteretic two-phase flow. Finally, closing remarks related to the beneficial combination of the experimental and numerical modelling approaches used in this work are given in Sect. 8.3.4.

8.2.2 Theoretical framework for modelling two-phase flow

The equations that govern the two-phase flow can be categorised into four groups: mass and energy balance equations, equilibrium relationships, constitutive equations and

boundary constraints. According to experimental observations the sand column may be considered as non-deformable; therefore the equilibrium of mechanical forces is not considered. The temperature fluctuations during the test are small and the process is isothermal. Therefore the independent variables (unknowns) in that case are liquid pressure P_l and gas pressure P_g. Equations for mass and energy balance are established in CODE_BRIGHT following the compositional approach presented in Olivella et al. (1994). A detailed derivation of the governing equations is given there. The following is a brief description of some of the relationships in order to elucidate the importance of the SWRC.

Mass balance of water and air

Mass balance equations for water ($\alpha = w$) and air ($\alpha = a$) in the liquid phase and in the gas phase are written as:

$$\frac{\partial}{\partial t}\left(\theta_l^\alpha S_l \phi + \theta_g^\alpha (1 - S_l)\phi\right) + \nabla \cdot \left(\boldsymbol{j}_l^\alpha + \boldsymbol{j}_g^\alpha\right) = f^\alpha \tag{8.26}$$

where S_l is the degree of saturation in the liquid phase, ϕ is porosity, θ_l^α and θ_g^α are the mass of water or air per unit volume of liquid or gas phases, $\boldsymbol{j}_l^\alpha$ and $\boldsymbol{j}_g^\alpha$ are total fluxes of water or air, and f^α denotes the external supply of water or air. The dependent variables have to be related to the unknowns, P_l and P_g. This explains the importance of the SWRC as the degree of saturation S_l is expressed in terms of liquid pressure and gas pressure via the SWRC equation.

Boundary condition

The boundary conditions for balance equations are incorporated by means of simple addition of nodal flow rates. For instance mass flow rate of water in phase α ($\alpha = l, \; g$) is written as:

$$j_\alpha^w = (\omega_\alpha^w)^0 j_\alpha^0 + (\omega_\alpha^w)^0 \gamma_\alpha (P_\alpha^0 - P_\alpha) + \beta_\alpha \left[(\rho_\alpha \omega_\alpha^w)^0 - (\rho_\alpha \omega_\alpha^w)\right] \tag{8.27}$$

where the superscript $(...)^0$ stands for the prescribed values, ω_α^w is the mass fraction of water in phase α, ρ_α is the density of phase α and P_α is the pressure in phase α. j_α^0 is a prescribed mass flow for phase α, γ_α is a parameter that allows a boundary condition of the Cauchy type and β_α is a parameter to allow boundary conditions with the prescribed mass fraction of water in phase α at the boundary. In particular cases, where only flow rate is applied, γ_α and β_α are defined equal to zero.

Constitutive equations:

The advective flow of the water phase is described by the generalised Darcy's law and the equation for the liquid advective flux $\boldsymbol{q}_l$ reads:

$$\boldsymbol{q}_l = -\frac{\boldsymbol{k} k_{rl}}{\mu_l}\left(\nabla P_l - \rho_l \boldsymbol{g}\right) \tag{8.28}$$

where μ_l is the dynamic viscosity of the pore liquid, $\boldsymbol{g}$ is the gravity acceleration vector, ρ_l is the liquid density, $\boldsymbol{k}$ is a tensor of intrinsic permeability and k_{rl} is the liquid relative permeability.

The relative permeability k_{rl}, is derived from the Mualem–van Genuchten closed form model (van Genuchten (1980)):

$$k_{rl} = \sqrt{S_e} \left[1 - \left(1 - S_e^{1/\lambda} \right)^\lambda \right]^2 \tag{8.29}$$

where λ is a SWRC shape parameter and S_e is the effective degree of saturation defined as:

$$S_e = \frac{S_l - S_{lr}}{S_{ls} - S_{lr}} \tag{8.30}$$

where S_l is defined as degree of saturation, S_{ls} and S_{lr} are the maximum and the residual liquid degree of saturation respectively. In the closed form of the Mualem–van Genuchten SWRC model, S_e is related to the capillary pressure $\psi = P_g - P_l$ as follows:

$$S_e = f\left(\psi, \lambda, P_0\right) = \left[1 + \left(\frac{\psi}{P_0} \right)^{\frac{1}{1-\lambda}} \right]^{-\lambda} \tag{8.31}$$

where P_0 is a model parameter which represents the air entry value in soil drying path.

8.2.3 Modelling of the hysteresis in the soil–water retention response

In this section, three empirical models of hysteresis loop in SWRC are introduced in order to reproduce the hysteresis phenomenon along the drainage-imbibition cycle. The first model represents the hysteresis by means of two equations, one valid along the first drying path and another for the main wetting path. The scanning curves are modelled as linear lines connecting transition points between first drainage (drying) SWRC and the main imbibition (wetting) SWRC, (section 8.2.3.1). The second model considers the reduction of the maximum degree of saturation due to occluded air appearance in the course of the first drying path and thus an equation for the main drying curve is introduced. The third model is an enhancement of the second model by the variation of air entry and air expulsion values during imbibition-drainage cycles, (section 8.2.3.2). These three SWRC models will be employed in order to numerically simulate the two–phase flow experiment explained above. The numerical simulations carried out following these three different approaches to modelling SWRC are described in detail in section 8.3.2.

8.2.3.1 Hysteresis function representing the SWRC using scanning lines

Coming back to Eq. 8.31, the original two-parameter van Genuchten model of SWRC can not reproduce the hysteresis loops during soil wetting–drying cycles. For simulation of the hysteresis in the soil water relationship, the SWRC is defined through introducing equations for the first (or also for the main) drainage curve and for the main imbibition curve using the same functional form as in Eq. 8.31 but with different shape parameters, i.e. λ_d and $P_{0,d}$ for the first (or main) drainage curve and λ_i and $P_{0,i}$ for the main imbibition curve. The transition paths from main drainage curve to main imbibition curve (scanning or transition curves) are defined in this model as linear lines. The SWRC varies within residual liquid saturation, S_{lr} and maximum liquid saturation, S_{ls}. In other words, S_{lr} and S_{ls} determine the minimum and maximum degree of saturation possible to be reached during drainage and imbibition processes. The schematic representation of the first model is shown in Fig. 8.3(a). In the second model, a new parameter, a_{oc}, is introduced to account for the amount of the entrapped air during the first drainage path and the reduction of the maximum degree of saturation to $S_{oc} = S_{ls} - a_{oc}$. As soon as the degree of saturation drops below S_{oc}(see Fig. 8.3(b))it will not excess this value again. By defining the effective saturation accordingly, this model will become equivalent to the previous one in the effective saturation–capillary pressure plane, Fig. 8.3(a). The equation for the effective degree of saturation now reads:

$$S_e = \frac{S_l - S_{lr}}{S_{ls} - S_{lr} - \langle S_{oc} - S_l \rangle a_{oc} / (S_{oc} - S_l)} \tag{8.32}$$

where $\langle F \rangle = 0$ if $F < 0$ and $\langle F \rangle = F$ elsewhere. However, it has to be pointed out that along the first draining path S_e is defined by the Eq.8.30 and Eq.8.32 is launched when hydraulic loading deviates from the first drying path.

The scanning curves are defined as linear lines with a constant absolute value of the effective saturation increment from the initial state at main drainage or imbibition curve to the end value at main imbibition or drainage curve, respectively, and denoted by dS_e. The particular transition line is determined by the value of the capillary pressure at which the transition loading path starts. In case hydraulic loading changes its direction when soil state belongs to the main (or first) drainage curve it means that the transition position in capillary pressure–effective saturation plane to define the scanning curve is the pair $\psi_d, f(\psi_d, \lambda_d, P_{0,d})$ or $\psi_d, S_{e,d}$ as point 4 shown in Fig. 8.3(a). The maximum effective degree of saturation achieved by following this scanning path is $S_{e,i} = f(\psi_d, \lambda_d, P_{0,d}) + dS_e$. Similarly when saturated state transits from imbibing state to draining state, transition
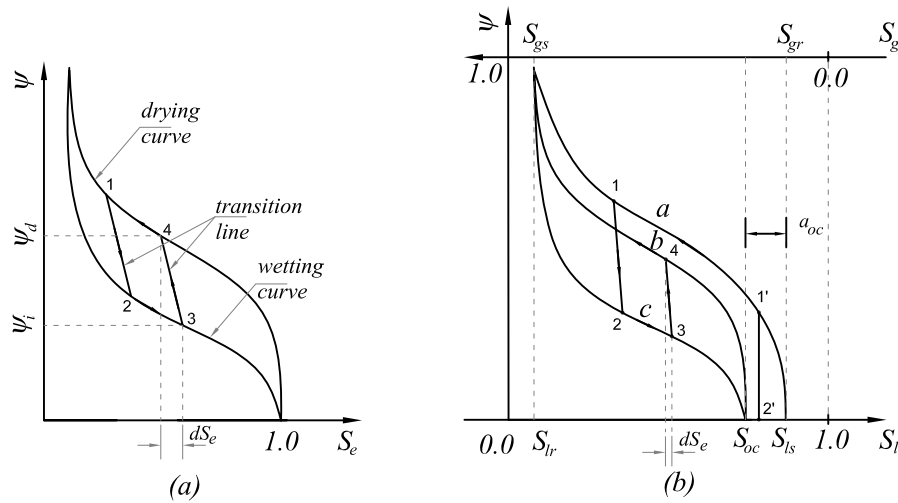
Figure 8.3: Scanning curve with occluded air in primary curve

point is defined by the pair $\psi_i, f\left(\psi_i, \lambda_i, P_{0,i}\right)$ or $\psi_i, S_{e,i}$. The equation of the SWRC at transition state reads as follows:

$$
S_e = \begin{cases} \dfrac{\psi_i - \psi}{\psi_d - \psi_i}\, dS_e + S_{e,i} & \text{for} \quad \text{imbibition} \to \text{drainage} \\[2mm] \dfrac{\psi_d - \psi}{\psi_d - \psi_i}\, dS_e + S_{e,d} & \text{for} \quad \text{drainage} \to \text{imbibition} \end{cases} \tag{8.33}
$$

The main drainage curve and main imbibition curve meet each other when capillary pressure ψ is either equal to zero or tends to infinity. Fig. 8.3 illustrates the mathematical algorithm in a loop of drainage-imbibition cycles. If at the initial state the liquid saturation S_l is less than S_{oc} the drainage and imbibition paths only go along curves b and c, respectively and the transient path follow e.g. line 3–4, see Fig. 8.3(b). If at the initial state S_l is in between S_{oc} and S_{ls}, there are two possibilities: (i) the soil state is at first drainage path and for drainage process, the drainage goes along curve a until e.g. point 1, the scanning curve is in between points 1 and 2 and the main wetting and secondary drainage cycle will follow the path $2 \to 3 \to 4$; (ii) for imbibition process, the imbibition path follows a scanning line up to capillary pressure equal to zero (line 1'-2') in Fig. 8.3(b). The relation between the gas phase saturation and the liquid phase saturation always obeys the following relation: $S_l + S_g = 1$.

8.2.3.2 The hysteresis soil water retention function with variation in air-entry and air-expulsion values

The model described in this section is developed within the third modelling approach for the simulation of the drainage-imbibition hysteresis loops. The experimental results of the drainage-imbibition test reveal that the air-entry and the air-expulsion values are dependent on the current position in the capillary pressure-effective saturation plane. This phenomenon has also been observed and modelled in previous works Mualem (1974, 1976); Kool and Parker (1987); Li (2005); Beliaev and Hassanizadeh (2001); Mualem and Beriozkin (2009). However, the previously proposed hysteresis functions do not take into account the air entrapment during the first drainage cycle. This thesis proposes a model that is able to reproduce both a reduction in the maximum saturation due to air occlusion and the variation in the air entry and the air expulsion during drainage-wetting cycles. The SWRC parameter that represents the air entry or the air expulsion values is modified to depend on the development of the drainage-imbibition process. The proposed equations read:

$$P_{0,i}^{j} = P_{0,i} + \left(S_{e,d}^{j} \right)^{n} \left(P_{0,d} - P_{0,i} \right) \tag{8.34}$$

$$P_{0,d}^{j} = P_{0,d} + \left(1 - \left(S_{e,i}^{j} \right)^{n} \right) \left(P_{0,d} - P_{0,i} \right) \tag{8.35}$$

where n is a model parameter which determines the magnitude of air-entry and expulsion values variation at the transition from drainage to imbibition and $S_{e,d}^{j}$ and $S_{e,i}^{j}$ are the effective saturation at transient positions of the jth drainage-imbibition loop. Their definition is given by the same relation as for the main drainage and imbibition curves but with modified parameters $P_{0,d}$ and $P_{0,i}$ in order to incorporate the secondary imbibition-drainage curves. The third approach to model the hysteresis loops in SWRC is schematically given in Fig. 8.4.

8.3 Numerical simulations of two-phase flow

8.3.1 Description of the experiment

As introduced above, the experimental part consists of a transient two phase flow column test where the water flow process is monitored along series of drainage and imbibition cycles. The column testing device used for determining the soil water retention relationship, the methods applied, and the testing procedure and experimental results are discussed in
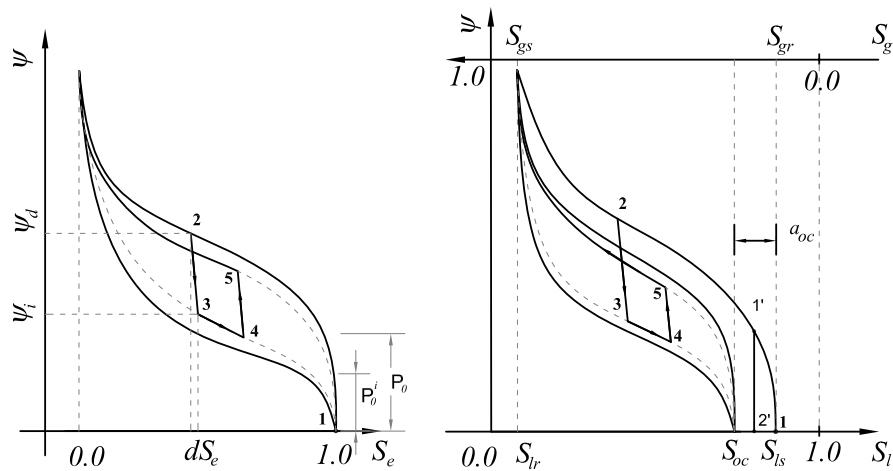
Figure 8.4: Schematic representation of the third approach for modelling hysteresis in SWRC.
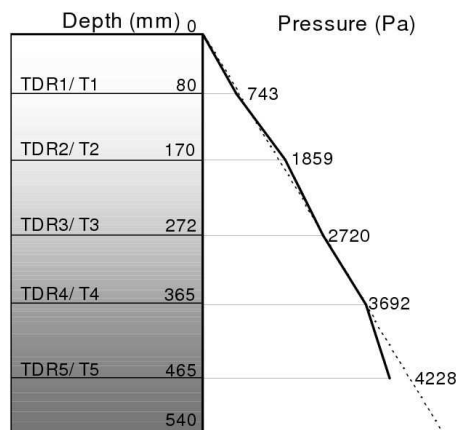
Figure 8.5: Initial conditions in the transient two-phase flow test.

detail in a paper by Lins et al. (2009). The tensiometers are used to measure the positive and negative pore water pressure. TDR sensors are used to measure volumetric water content. The change in total volume of the column was insignificant during the process of experiment (Lins et al., 2009). Therefore, the degree of saturation is linear in relation to the volumetric water content.

The material used in the column tests is Hostun Sand [Flavigny et al. (1990)] from France. Hostun Sand is a poorly graded medium-grained sand, and according to USCS classification the sand is described as SP sand (ASTM D422-63).

The initial condition in each of the tests is the complete water saturation of the specimen. At the start of the test when the sand specimen is fully water saturated, the tensiometers measure positive pore-water pressure. The measured pore water pressure increases with
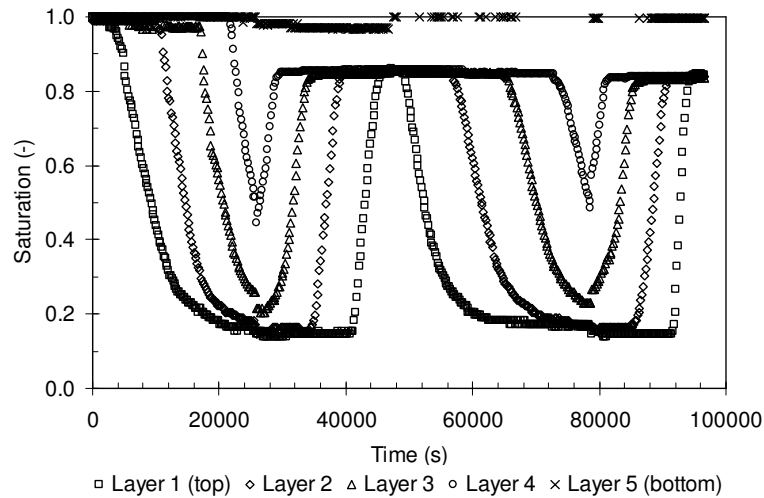
Figure 8.6: Experimental results of the first and second drainage and imbibition cycles –
           TDR measurements.

depth and almost exactly recovers the gravimetric pressure Fig. 8.5. The measured degree
of saturation at the start of the tests is equal or very close to 1 at each observation depth.

The water saturation obtained by means of the TDR sensors is plotted versus time in
Fig. 8.6. Accordingly, the tensiometer measurements versus time are given in Fig. 8.7.
The results from the first drainage, the first imbibition and the second drainage and second
imbibition cycles are shown in these figures. The initial condition with regard to water
saturation and pore pressure in the first drainage path is a completely water saturated
specimen with a water table located at the top of the specimen. As explained in Fig. 8.5
the TDR sensor TDR 1 and the tensiometer T 1 are located at the top of the column and
the sensor pair TDR 5 and T 5 is located at the bottom of the column.

When draining the sand specimen (first drainage path and also second drainage path), the
tensiometer sensors measured decreasing positive pore-water pressures at the beginning
of the process which reached negative values at the end of the process. The measured
negative pore-water pressures at the end of each drainage path showed lower values at
the top of the specimen compared with the values at the bottom of the specimen. Conse-
quently, the capillary pressure is higher at the top of the specimen than at the bottom of
the specimen. During drainage the saturation initially decreases on the top layer of the
specimen and finally on the bottom layer of the specimen.

At the beginning of the imbibition paths (first imbibition path and second imbibition
path) the tensiometer T 1 measures lower negative pore-water pressure than tensiome-
ter T 5, referring to a higher capillary pressure at the top of the sand specimen. The
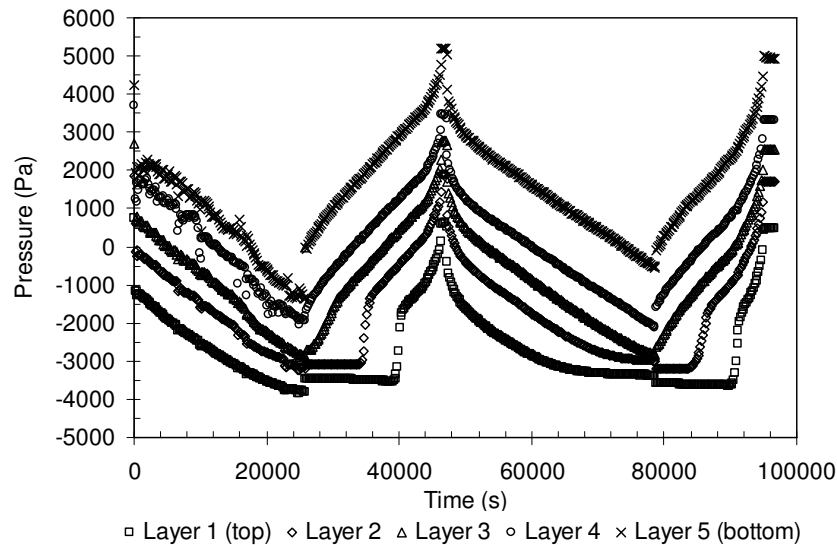
Figure 8.7: Experimental results of the first and second drainage and imbibition cycles – tensiometer measurements.

saturation at the top of the specimen is lower than the saturation at the bottom of the specimen. During imbibition paths (first imbibition path and second imbibition path) the saturation is increasing corresponding to a decreasing capillary pressure. Saturated conditions are reached when the tensiometers measure positive pore-water pressure. During the imbibition path the saturation increases first at the bottom of the specimen and then at the top of the specimen.

However, after the first imbibition path the calculated based on the TDR sensor readings and observing the column volume change showed that the fully saturated condition is not recovered. This may be due to occlusion of air that cannot be removed from the soil via imbibition. Only the TDR 5 sensor at the bottom of the specimen measured a saturation of $S_l = 1$. The reason for this is the observation that the portion of the specimen where TDR 5 is located remains saturated during the entire testing procedure no matter whether draining or imbibition is taking place and occluded air bubbles cannot form.

The tensiometer together with the TDR probe measurements enable a direct determination of the relationship between negative pore water pressure (capillary pressure) and water saturation. The readings of the tensiometers plotted against the corresponding TDR probe readings are given in Fig. 8.8 and 8.9. The measured data along the first drainage and imbibition cycle recorded at different depths are presented in Fig. 8.8. In this plot the regression fit for the two-parameter van Genuchten model is included (van Genuchten, 1980). The regression parameters are used as input data for the numerical

Figure 8.8: Experimental results linked to the first drainage and imbibition cycle – TDR
        sensors and tensiometer measurements.

simulations presented subsequently (see Sect. 3). The main drainage and scanning im-
bibition paths obtained at the different depths are presented in Fig. 8.9. As explained
above, TDR 5 and T 5 are located in the saturated zone; therefore the SWRC relationship
is plotted only for sensor pairs from TDR 1-T 1 to TDR 4-T 4.

The air-entry value, ψ_{aev}, is approximately 1500 [Pa]. After reaching this value, the sat-
uration in the sand specimen decreases rapidly. The transition zone is between 1500 [Pa]
and 2900 [Pa]. The residual zone starts at a relatively low capillary pressure in the
drainage cycle. The wetting paths result in different scanning curves, depending on the
starting point for the imbibition on the main drainage curve.

Due to the effect of air phase trapping, the water saturation in imbibition cycles reaches
a maximum value of $S_l = 0.84$. Different placement depths for the sensors resulted
in different initial capillary pressures and saturation, respectively, during the successive
imbibition cycles.

The two-parameter model proposed by van Genuchten (see Eq. 8.31) was used to interpret
the experimental data. The parameters for the drainage part of the SWRC are given in
Table 8.1. These values were used as input parameters for the later discussed numerical
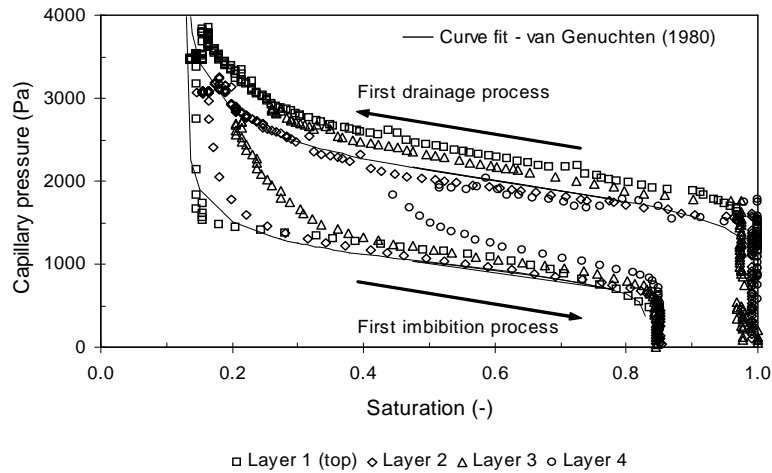simulations.
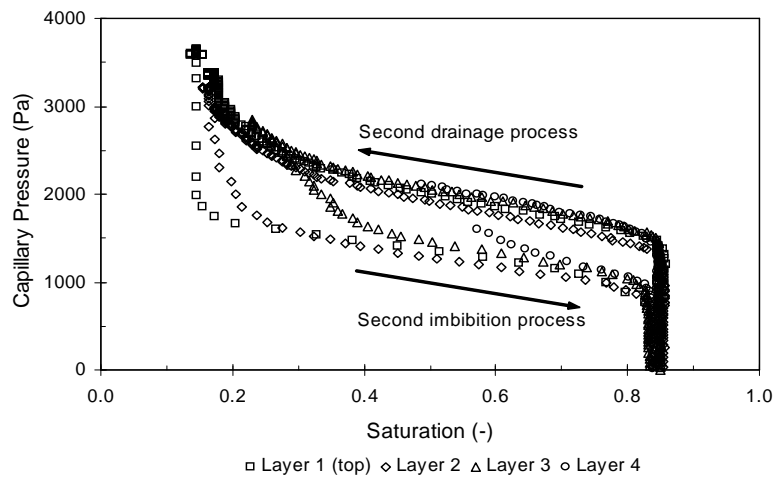
Figure 8.9: Experimental results linked to the second drainage and imbibition cycle – TDR sensors and tensiometer measurements.

Table 8.1: Parameter set for the SWRC

van Genuchten's SWRC parameter	S_{ls}	S_{lr}	P_0	λ
First drainage path	1.00	0.12	0.0006	0.846

8.3.2 Numerical simulations of sand column test

The soil water hysteresis models presented here are implemented into the finite element (FE) programme CODE_BRIGHT, which has been used to simulate the performed sand column tests. The FE-model with its geometry and discretisation is presented in Fig. 8.10(a,b). The positions of nodes are defined concurrently with the TDR sensors and tensiometers locations along the sand column height to guarantee data for comparison with the experimental measurements. Nodes 60, 48, 36, 22, and 8 are concurrent positions with the locations of the TDR and tensiometer pairs enumerated from 1 to 5 (i.e. layer 1 to 5) instrumented within the sand column.

In the first hydraulic loading phase, the first drainage phase, the degree of saturation started from 1.0 and dropped to a minimum of 0.12. The second loading phase, the first imbibition phase, the degree of saturation started from 0.12 and increased to maximum 0.84. Therefore the water retention capacity of the sand column decreased after the first drainage phase. However, the water supply might have exceeded the water storage capacity of the sand. When the material was saturated and the water supply continued, the water pressure increased rapidly due to water incompressibility. In regard to the numeri-
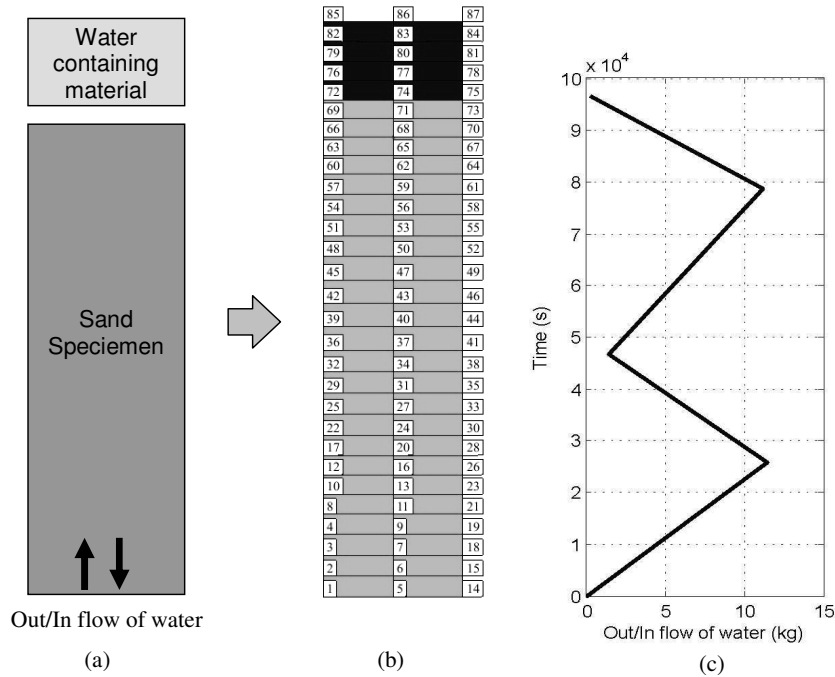
Figure 8.10: (a) Material scheme, (b) Geometry and discretisation, (c) Water in/out flow
            boundary conditions.

cal simulation this may cause the Newton-Raphson integration procedure non converging.
In order to avoid such a situation a water containing material (WCM) is placed above
the sand column, Fig. 8.10(a). When the sand is fully saturated, the water can move
to the WCM container and thus preventing a rapid and unrealistic increase in the water
pressure. The SWRC for the WCM is taken also to obey the van Genuchten type law
with a very small P_0 as compared with the parameter P_0 of sand. This way the existence
of the WCM in the numerical model will not influence the imbibition-drainage process in
sand material. For the drainage path first the degree of saturation of the WCM material
is reaching its residual value and after that a decrease of degree of saturation of sand
starts. In the imbibition phase after the degree of saturation of sand reaches its maxi-
mum then the degree of saturation of WCM starts to increase, see Fig. 8.11. The relative
permeability of WCM is constant and ($k_{rl} = 1$). The parameters of WCM material are
given in Table 8.3. No hysteresis and air entrapping phenomena are taken into account
for WCM.

The total height of the sand column is 540 mm, the width is 150 mm. Water can be
supplied and drained from the bottom boundary of the sand column. The prescribed
liquid flux values in course of the applied hydraulic loading are presented in Fig. 8.10(c).
Concerning the initial conditions, the porosity of sand is $\phi = 0.471$, and the porosity of
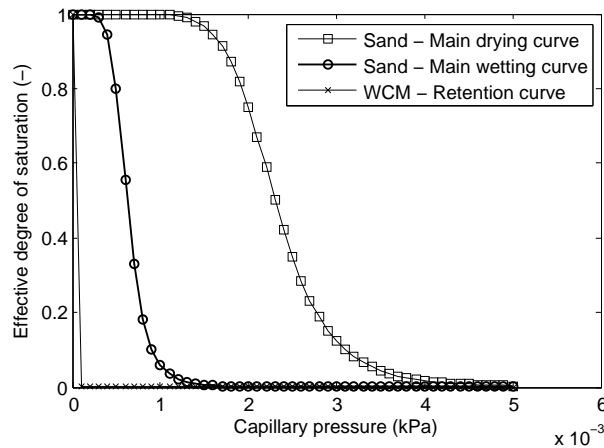
Figure 8.11: Retention curve for sand and WCM based on van Genuchten model.

Table 8.2: Column bottom boundary conditions

Load phase	1	2	3	4
q_l (kg/s)	-6.32E-03	5.85E-03	-3.70E-03	6.75E-03
Time period (s)	25740	20880	32040	18000

the WCM equals 0.98. In the numerical simulation gas pressure is considered to have the absolute value of atmospheric pressure, thus initial gas pressure in both materials (sand and WCM) is P_g=100 kPa. To get the saturated state for the sand, the capillary pressure $\psi = P_g - P_l$ at the sand column top is equal to zero or absolute pressure P_l=100 kPa. The liquid pressure at the bottom boundary is prescribed to be equal to the gravimetric pore water pressure, that is P_l=5400 Pa at the bottom of the sample.

The air in the numerical model is allowed to flow out from the top of the sand by applying gas pressure to the top boundary of sand material equal to the atmospheric pressure. After the liquid pressure in the sand material reaches equilibrium, the first step of in/out flow is started. The volume of water going in/out of the specimen with time is controlled to be the same as in the experiment. There are four phases of drainage and imbibition considered for numerical simulation. The volume of water and time for each phase are presented in Table 8.2. The parameters for sand are given in Table 8.3.

Previously three different models were introduced to explain soil water retention behaviour. The numerical simulation aims to verify the underlying theoretical assumptions against the experimental observations and to discuss the possibilities for reliable prediction by means of the three different modelling approaches. This not only attempts to compare the agreement between model prediction and experimental results but also

Table 8.3: Material parameters

	$P_{0,d}$	λ_d	S_{lr}	S_{ls}	$P_{0,i}$	dS_e	λ_i	$\boldsymbol{k}$	ϕ_0	n
Unit	(MPa)	(-)	(-)	(-)	(MPa)	(-)	(-)	(m^2)	(-)	(-)
Sand	2.3E-03	0.875	0.12	1.0	6.0E-04	0.04	0.846	2.8E-11	0.47	0.25
WCM	5.0E-05	0.9	0.00	1.0	-	-	-	2.8E-07	0.98	-

assesses the mutual effect of the SWRC shape to the flow process.

8.3.3 Results and discussion

The numerically and experimentally obtained results for time-dependent water saturation, time-dependent water pressure, and capillary pressure-degree of saturation curves are presented for comparisons in this part.

8.3.3.1 Comparison of the predictions using the first SWRC modelling approach with the experimental results

The comparison of experimental and numerical SWRC results are given in Fig. 8.12, where capillary pressure is plotted against saturation. Using the first model no occluded air was taken into account. The simulated saturation always reached the value 1.0 after each drainage-imbition loop because occluded air was not considered in this model. However, there was a similarity between the experimental and computational curves and the disagreement in saturation values is evident from Fig 8.13. Whenever the transit point is a small or large degree of saturation, the imbition line and drainage line are the same, called main imbition and drainage lines; therefore the water pressure in the imbition phase tends to be lower than measured data, Fig. 8.14 layer 1 and layer 2.

8.3.3.2 Comparison of the predictions using second model with the experimental results

The influence of occluded air was taken into account using the second model by means of the parameter a_{oc}. The initial water saturation measured in the experiment and in the numerical simulations was equal to 1.0. The introduction of the parameter a_{oc} resulted in a reduced degree of saturation during the numerical simulation, which occurred identically in the experiment. After the first drainage-imbition cycle the maximum saturation in
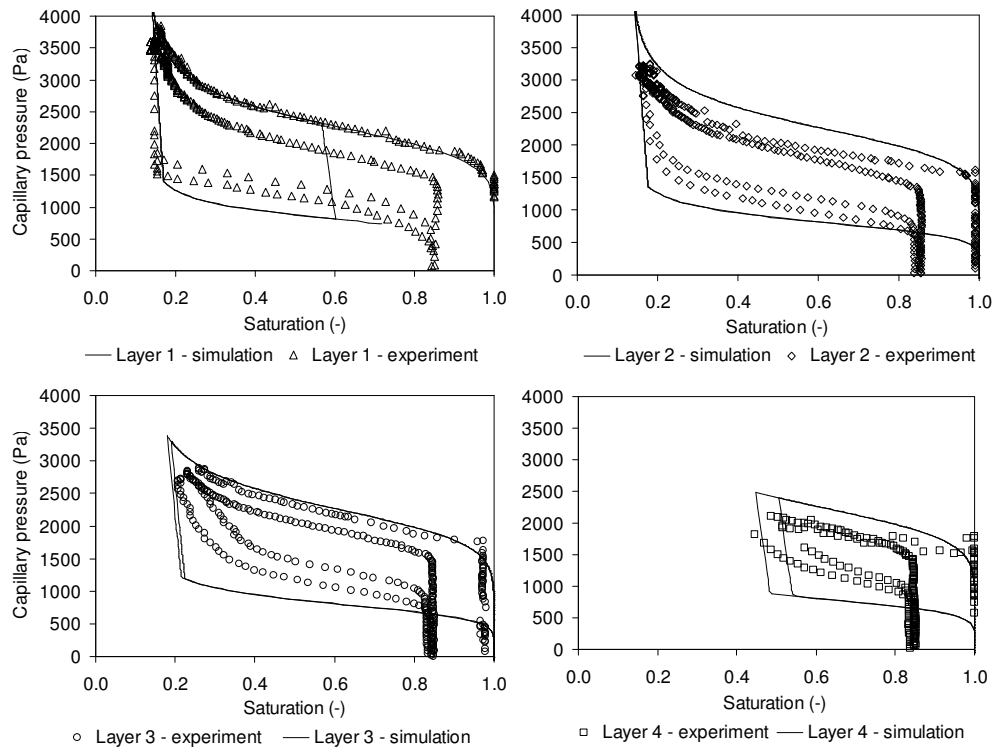
Figure 8.12: Experiment versus numerical simulation: first model-capillary pressure and saturation relationship.

the numerical simulation reached 0.84. The corresponding results are plotted in Fig. 8.15 and it can be seen that the experimental and model predictions are in a good agreement. Consequently, water saturation with time evolution in simulation is in a good agreement with the measured values Fig. 8.16. However, the numerically obtained curves are the same independent of the advancement of the drainage-imbibition process, which differs from the measured data. The measured data showed a change in the imbibition-drainage curves due to the change of points of loading transition. On the other hand, the simulated liquid pressure evolution with time shows better agreement with measured values, Fig. 8.17.

The occluded air parameter also influences the distribution of water content in porous media. The volume of water supplied to the soil sample was prescribed the same in both simulations employing the first and the second models. The maximum degree of saturation in the first model is 1.0 while it is 0.84 in the second model; therefore the water storage capacity in second model is smaller than the first model. Consequently, the degree of saturation when using the second model reaches a saturated state faster than in the simulation employing the first model. This fact may explain why the degree of
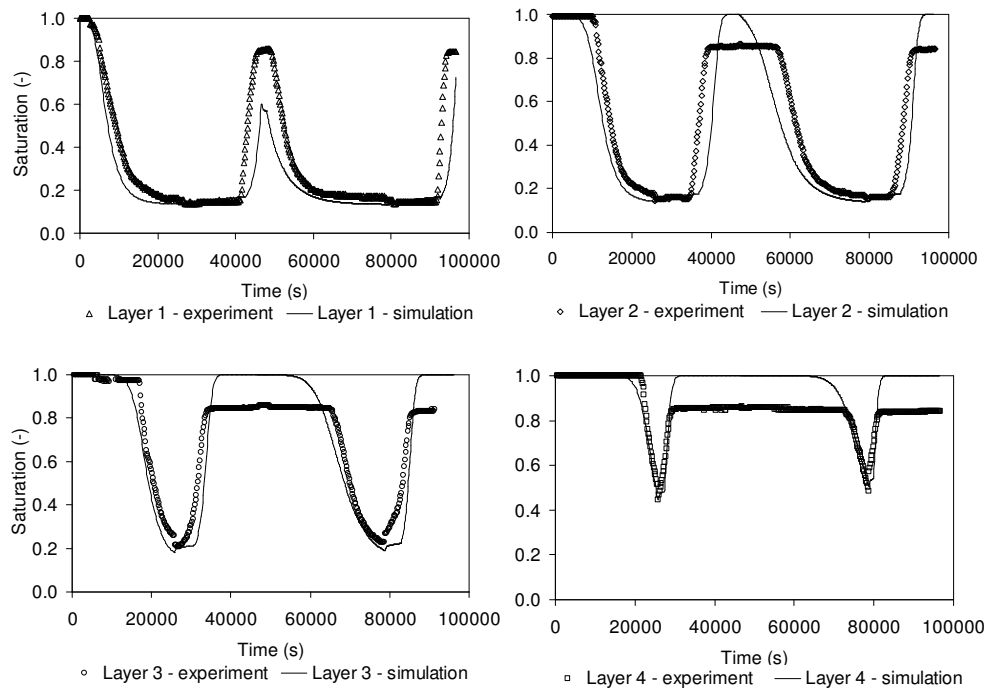
Figure 8.13: Experiment versus numerical simulation: first model-degree of saturation.

saturation in layer 1 in second loading phase for the first model (Fig. 8.13) is smaller than the one observed experimentally. Whereas the maximum degree of saturation in layer 1 in the second loading phase for the second model is in a good agreement with the one from the experiment (Fig. 8.16).

8.3.3.3 Comparing predictions using the third SWRC model against the experimental results

Because the occluded air is considered using parameter a_{oc} in the model developed within the third model to describe SWRC hysteresis, the maximum liquid saturation also reaches the value of 0.84 after the first draining-imbibition cycle. Consequently, liquid saturation time evolution obtained in the numerical simulation is in better agreement with the measured data (Fig. 8.19) as compared with the predictions of the model based on the first model (Fig. 8.13). Regarding SWRC, when hydraulic loading starts from an ultimate soil state such as a fully saturated or a fully dry state, the imbibition and drainage curves in the numerical model remain the same as the main imbibition and drainage curves in the experiment. But if the starting point of the loading transition is not at an ultimate state, the soil water retention curves are located in between the main imbibition and the main drainage curves. The shape evolution of the imbibition curves is not evident when reading
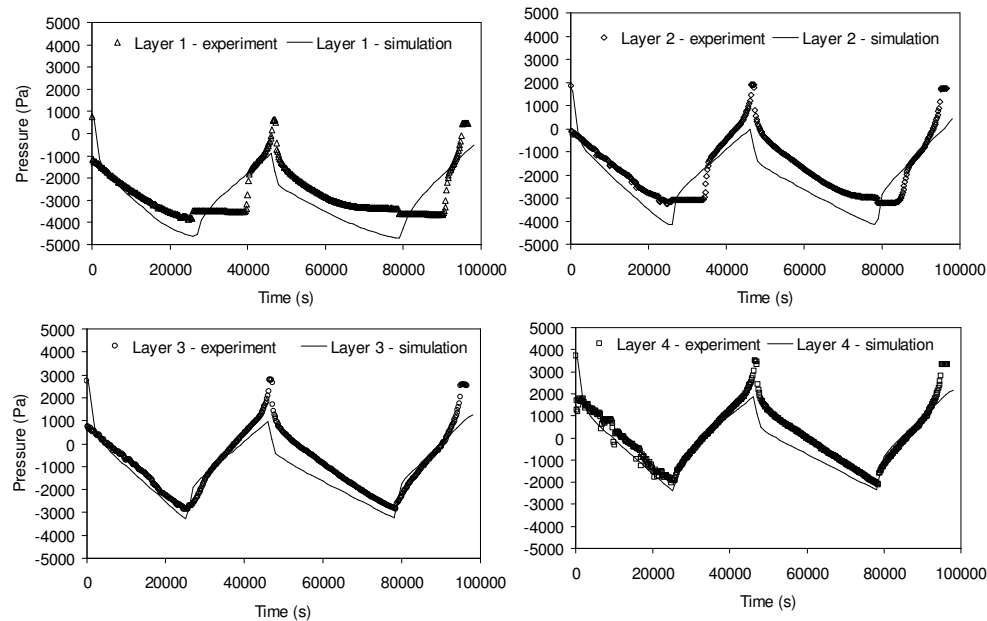
Figure 8.14: Experiment versus numerical simulation: first model-liquid pressure.

the TDR 1 sensor, i.e. in layer 1 (Fig. 8.18) because the transition points onto the two imbibition-drainage loops are close to each other. In the other observation points (layers 2, 3, 4) the difference in imbibition curves is more visible because of the more significant difference in transition points as compared with the saturated values. It can be concluded that the SWRC modelling predictions significantly improved as compared with the first and second modelling approaches. Consequently, water saturation and liquid pressure evolution with time are in better agreement with the measured values.

8.3.4 Conclusion

This section presents an experimental and numerical investigation of the hysteresis and air entrapment phenomena due to drying-wetting cycles in sand. A column testing device equipped with TDR and tensiometer sensors along the column height were used to assess the water content and capillary pressure redistribution during the imbibition and drainage loading paths. The experimental data reveal the presence of hysteresis in the water retention curve and a reduction in the maximum degree of saturation after the first drying path, which may be attributed to the occluded air that cannot be removed from the soil during the wetting procedure conducted in the experiment.

Numerical simulation of the experimental procedure is further presented in this part in order to establish a functional expression of the water retention curve valid along the whole
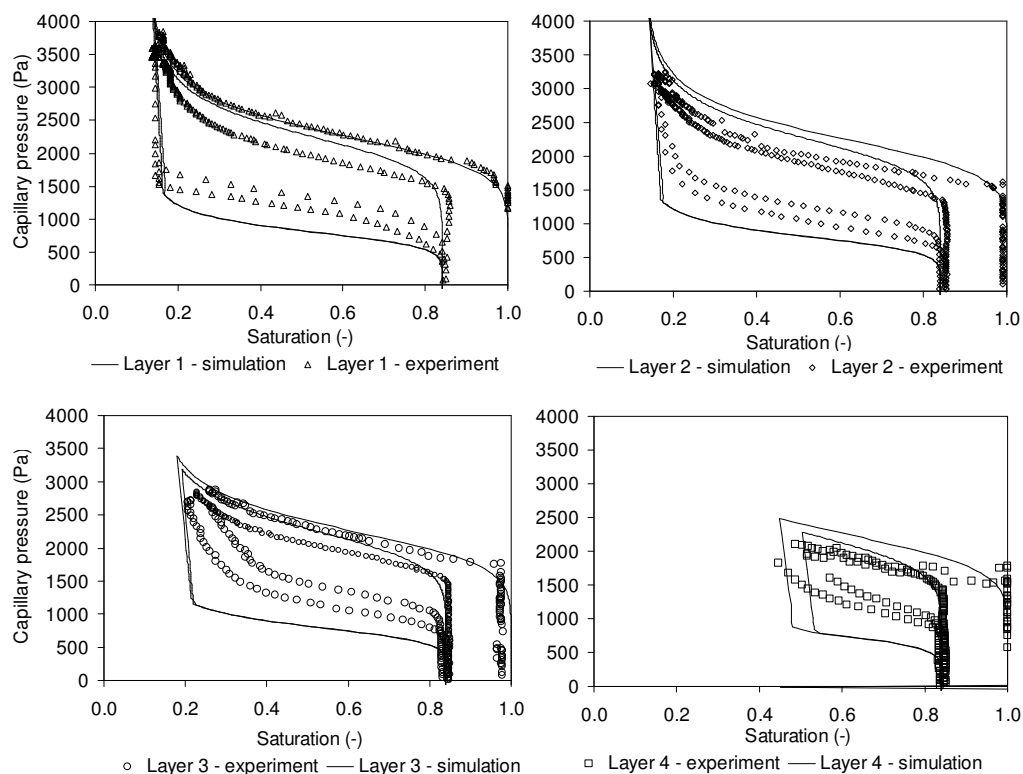
Figure 8.15: Experiment versus numerical simulation: second model - capillary pressure and saturation.

loading path including the first drying and the subsequent imbibition and desiccation paths. This procedure aims to discuss the possibility for reliable predictions using three different approaches for modelling the water retention curve. The numerical simulations incorporate information on the SWRC derived directly from the transient column test. The test simulation and the experimental results were compared in terms of saturation versus time as well as water pressure versus time for the entire sequence of alternating drainage and imbibition loading paths.

In the first modelling approach solely the hysteresis in the water retention curve is considered and the reduction in the maximum degree of saturation is neglected. The scanning curves are taken to be lines connecting the beginning and the end of the hydraulic loading in between first drying and main wetting and drying curves. The second approach to model the water retention curve assesses hysteresis and scanning paths similarly to the first modelling approach but considers the reduction in the maximum degree of saturation after the first drying path. The third water retention model was introduced to better explain the experimental data as compared with the first and second water retention models. This modelling approach introduces a new water retention model taking into
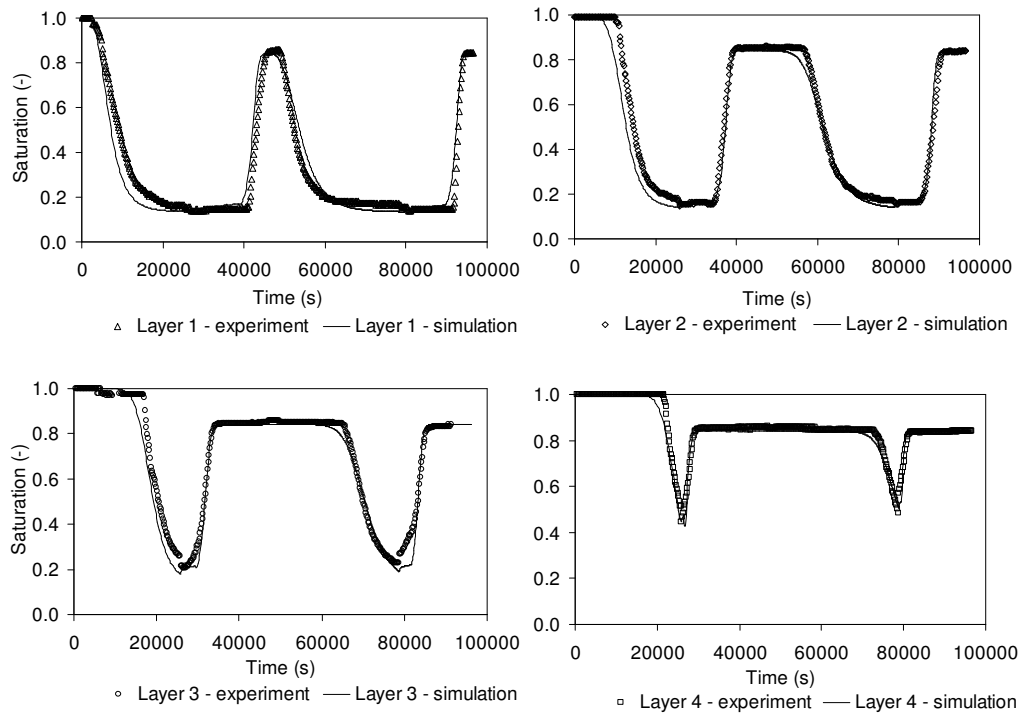
Figure 8.16: Experiment versus numerical simulation: second model - degree of saturation.

account the reduction in the maximum degree of saturation after the first drying path and the variation in the air-entry and air repulsion values with hydraulic loading cycles (section 8.2.3.2). The results derived from the numerical simulation of the column test based in the third model show the best agreement with the measured data (i.e. SWRC, saturation versus time and water pressure versus time results).

In conclusion, the comparison between numerical simulation and the experimental results indicates the need to consider water retention hysteresis and especially the importance of effect of occluded air on the maximum degree of saturation. Since the air-entry and air-repulsion values change depending on the transition point along the loading path, where hydraulic loading process is changing its direction, taking into account the variation in these values significantly improves the agreement between the model and the experimental data.
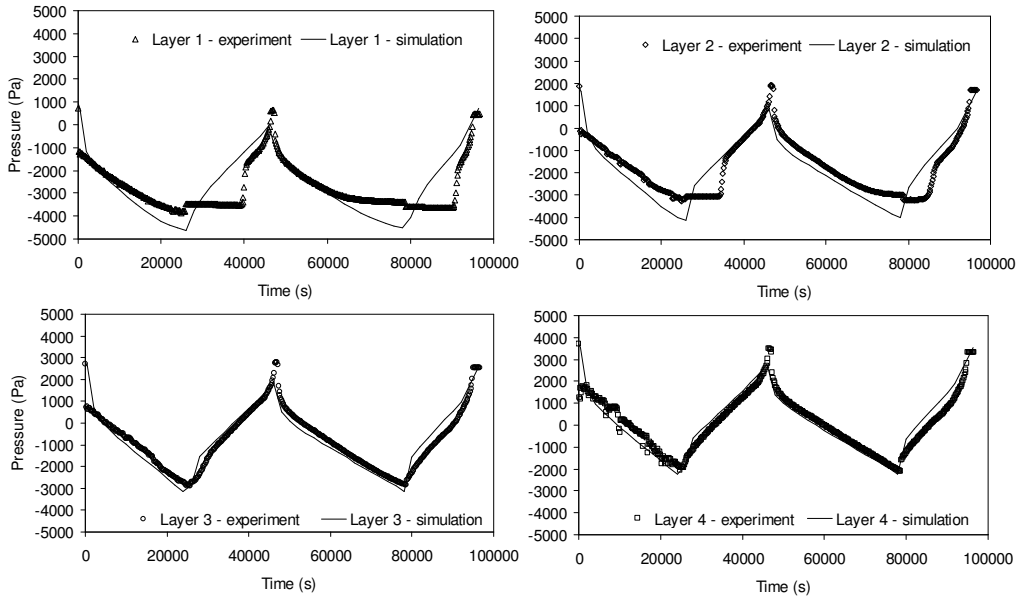
Figure 8.17: Experiment versus numerical simulation: second model - liquid pressure.
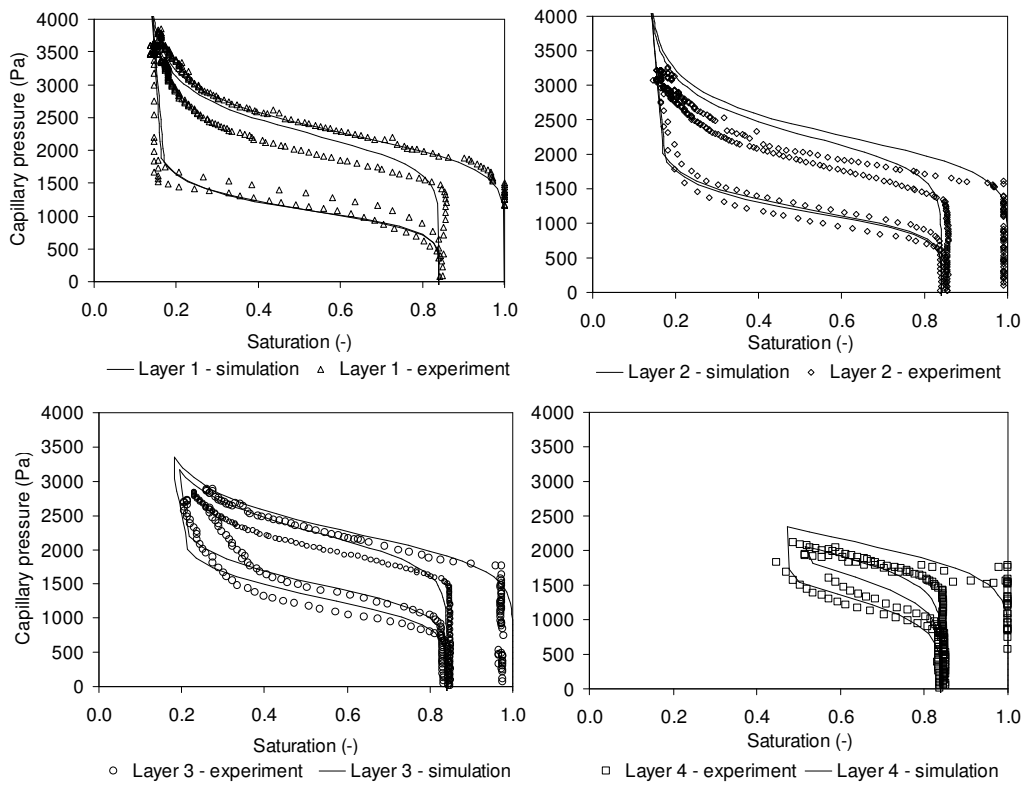
Figure 8.18: Experiment versus numerical simulation: third model - capillary pressure and saturation.
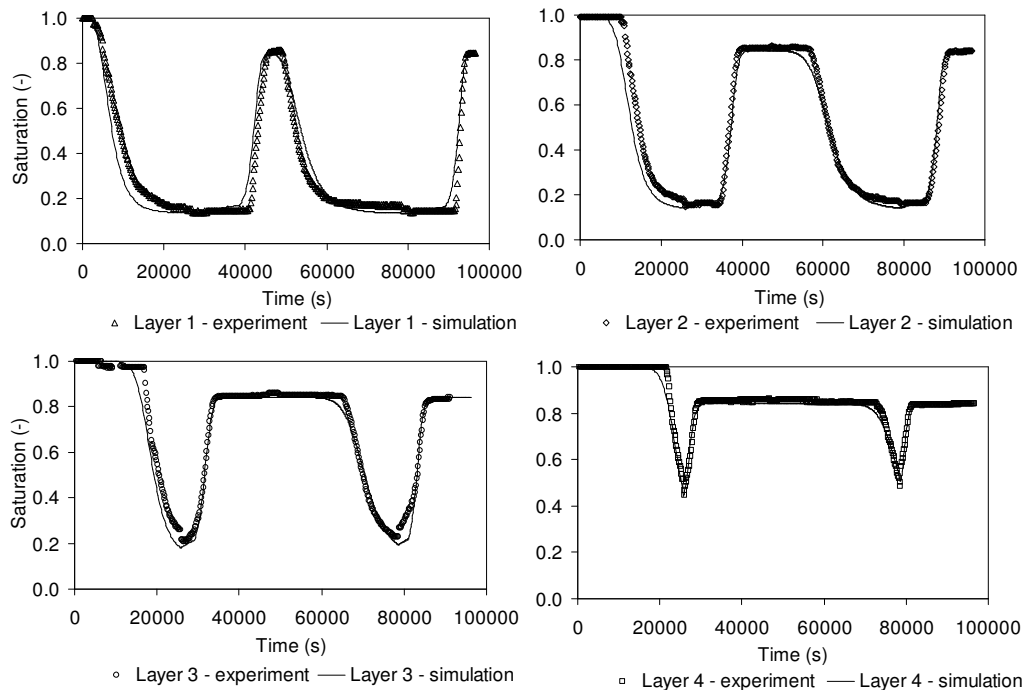
Figure 8.19: Experiment versus numerical simulation: third model - degree of saturation.

8.4 Numerical simulation using coupled THM analysis for THM column-type tests

The numerical simulations of the THM column-type tests are presented in this section, which attempts to reproduce the experimental processes. These processes is a boundary value problem with material models, initial conditions, and boundary conditions. Therefore, the material parameters, initial conditions, and boundary conditions are presented in this section. Based on the understanding of coupled THM behaviour, this behaviour will be mimicked using a numerical simulation close to the real behaviour of the soil. The aim of the numerical simulation in this section is to qualitatively analyse the process of stress-strain development, heat transfer, and water flow. The results of numerical simulation are used as initial information for the back analysis in the next section, in which the results of the numerical simulation are analysed quantitatively in comparison with the experimental results.
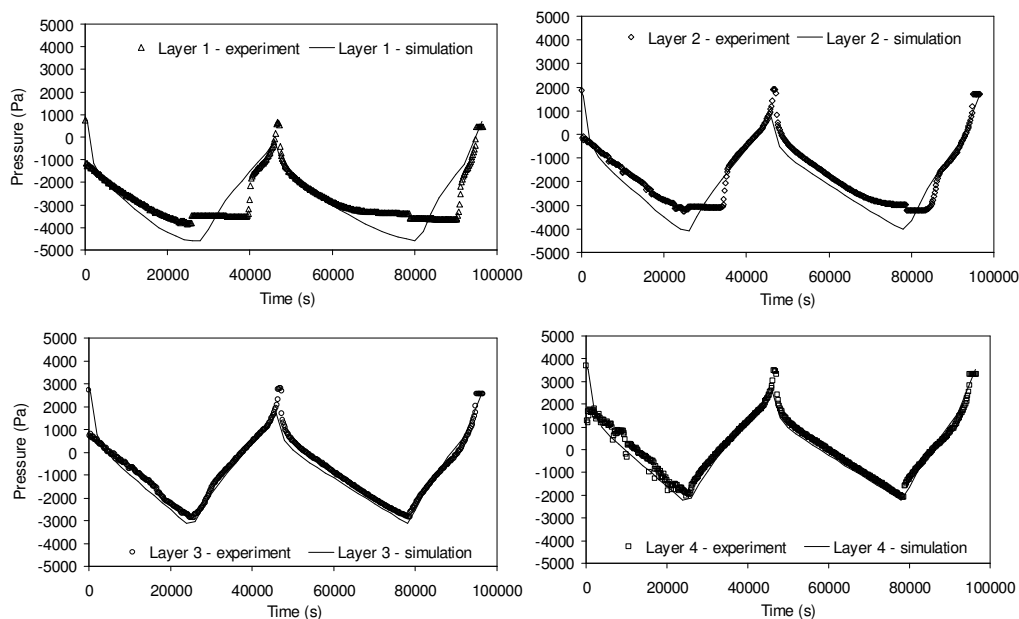
Figure 8.20: Experiment versus numerical simulation: third model - liquid pressure.

8.4.1 Initial parameters for coupled THM analysis

Mechanical parameters of the sand bentonite mixture:
Three materials are simulated in the FE-model: sand-bentonite materials, TPFE material, and steel 316L. Thermal conductivity of TPFE is 0.23 W/(m.K) at 0-100°C, and the thermal conductivity of the 316L steel (wall) is 16.2 W/(m.K) at 0-100°C (product data sheet).

The steel and PTFE are simulated by using linear elasticity models for mechanical behaviour. The elastic modulus of steel and PTFE is 1.93E+5 MPa and 700 MPa, respectively (product data sheet). No hydraulic flux is taken into account for these two materials.

For the sand-bentonite mixture material, several mechanical parameters were derived from the oedometer tests: α_{io}, α_{so}, $\lambda(0)$, p^c, p_o^*. The other parameters are assumed based on Agus (2005). The hydraulic parameters are derived from permeability tests in THM column. BBM-TEP model parameters for unsaturated soils are presented in Table 8.4 and Table 8.5.

Thermal parameters of the sand bentonite mixture:
The thermal parameters could be derived from thermal conductivity data in the THM column for the thermal stationary at a degree of saturation of 25.8% and 88%, where the degree of saturation is considered the same in the whole sample and assuming the

Table 8.4: TEP elastic parameters

κ_{io}	κ_{so}	K_{min}	ν	α_{ss}	α_i	α_{sp}	p^{ref}
(-)	(-)	(MPa)	(-)	(-)	(-)	(-)	(MPa)
0.01	0.0184	10	0.27	0	-0.01	0.3	0.126

Table 8.5: TEP plastic parameters

$\lambda(0)$	r	β	ρ	k	p^c	M	α	p_0^*	e_0
(-)	(-)	(MPa^{-1})	$°C^{-1}$	(-)	(MPa)	(-)	(-)	(MPa)	(-)
0.115	0.98	0.01	0.2	7.32E-03	0.01	1.12	0.426	0.28	0.88

heat transfer by diffusion is very small in the SBM as compared with heat transfer by conductivity. The heating test based on optimised energy to reach 80°C. However, the flux of heat varied with the thermal conductivity of the soil samples. The flux of heat was not measured during the test; thus the thermal conductivity could not be calculated that way. The thermal conductivity can be obtained by heat equation in un-stationary, where temperature is a function of time. Solving heat equations with time at very beginning of heating phase, assuming the heat transfers in one dimension, means the whole sample has the same thermal conductivity, and the heat transfer by diffusion is very small as compared with heat transfer by conductivity, the thermal conductivity at current (9.1%) water content λ_w is obtained by 0.4 (Wm^{-1}K^{-1}).

The basic parameters for temperature evolution and distribution is the thermal conductivity λ_s, which depends on liquid saturation. Gens et al. (1998) and Sánchez et al. (2004); Tang et al. (2008) determined parameters for different types of pure bentonite. Considering thermal conductivity derived directly from the test and the parameters in the literatures, the parameters used in this study are presented in Table 8.6. The thermal parameters related to the stress-strain behaviour of material are taken from Hueckel and Pellegrini (1992).

Table 8.6: Thermal parameters of the sand-bentonite mixture

λ_{sat}	λ_{dry}	α_o	α_1	α_3	T_{ref}
(Wm^{-1}K^{-1})	(Wm^{-1}K^{-1})	(°C^{-1})	(MPa °C^{-1})	(MPa °C^{-2})	(°C)
0.7	1.3	1.0E-05	9.0E-03	-4.7E-03	20

Hydraulic parameters of sand bentonite mixture:

Retention curve: Soil water retention curve is obtained based on the results of experiments reported in determining the SWRC. The water retention curve is expressed via the two well-known parameters of the van Genuchten model. The parameters were obtained via regression analysis and are shown in Table 8.7. However, the soil SWRC has been determined in the free swelling condition. SWRC in this case is simulated in the confined conditions. Therefore the soil parameter for SWRC can be substantially changed. Therefore, the parameters for SWRC are chosen from both tests: free swelling test and initial/final conditions of column tests. The maximum degree of saturation is determined by the constant volume test with oedometers during the hydration. The maximum water content of the soil sample in the wetting path after saturated is 30.6% corresponding to the degree of saturation of 88%.

Intrinsic and relative permeability: Intrinsic permeability is calculated by Kozeny's model based on experimental results from saturated hydraulic conductivity test in the THM column at 20°C. The detailed analysis of hydraulic conductivity is presented in section 7.3.3. Parameters for this model are presented in Table 8.7.

Molecular diffusion of vapour: The molecular diffusion of vapour in air is governed by the Fick's law. The diffusion coefficient is with dimension (m^2/s);

Table 8.7: Hydraulic parameters of the sand-bentonite mixture

P_0 (MPa)	λ (-)	k_o (m^2)	σ_{T0} (N/m)	ϕ_o (-)	S_{rl} (-)	S_{ls} (-)	D (m^2s^{-1})	τ (-)	n (-)
0.61	0.446	8.78E-16	0.072	0.481	0.11	0.88	5.6E-7	0.8	2.3

Phase properties:

The properties of two phase are considered in numerical simulation: a liquid phase and solid phase. The phase property of solid is taken from experimental data of Agus and Schanz (2005). The water property is taken from Lide (2005). The phase properties are presented in Table 8.8 and Table 8.9.

8.4.2 Numerical simulation of the hydro-mechanical test

Geometry and discretisation: The model was built on the X-Y plane Fig. 8.21(a). The problem was solved as an axis-symmetric problem with an axis of symmetry along

Table 8.8: Solid phase properties

C_s	874	J kg^{-1} K^{-1}	Solid phase specific heat
ρ	2700	kg m^{-3}	Solid phase density
α_s	1.20E-05	°C $^{-1}$	Linear thermal expansion coefficient for grains
T_0	20	°C	Reference temperature for thermal expansion

Table 8.9: Liquid phase properties

ρ_{lo}	1000	kg m^{-3}	Reference density
β	4.50E-04	MPa^{-1}	Compressibility
α_l	-3.40E-4	°C $^{-1}$	Volumetric thermal expansion coefficient
C_w	4184	J kg^{-1} K^{-1}	Liquid phase specific heat
μ_l	2.1E-12	MPa s	Water viscosity (default value)

AD, Y axis-symmetry. At the top and the bottom of the model flux boundary condition was applied; therefore, the discretisation there is finer. Discretisation is done in such way to have the coordinates of the measurement points coincide with FE-point coordinates at the beginning of the simulation. The elements were discretised manually in order to get the distances from points 8, 7 and 6 to the top of the model to be 50mm, 150mm and 250mm, respectively Fig. 8.21(b). Points 8, 7 and 6 correspond to the position of the water content and temperature sensors in the sample Fig. 8.21(b). Point 1 is located on the bottom of the sample and it was chosen to collect data corresponding to the load cell measurements. The primary variables used for the HM test simulation are the displacement variable (u), liquid pressure (P_l), and temperature (T).

Boundary conditions are as follows: no displacements in the Y-direction on boundary lines 1 or 2 was setup, corresponding to the bottom and top of the specimen respectively Fig. 8.21(c). No displacements in either the X or Y-direction on the boundary lines 7, 8, 9 and 10 and the symmetry condition was a line drawn from points 1 to 4. Water pressure of $P_l = 15$ kPa was applied on line AB corresponding to the bottom of the specimen. The primary unknowns to be solved are displacement vector (u), liquid pressure (P_l) and temperature (T). The temperature of the specimen and water supplied in the HM test was simulated initially at a constant 20°C.

Initial conditions were taken from the experimental measurements. The initial conditions are presented in Table 8.10. Total time corresponding with the experimental period was 100 hours.
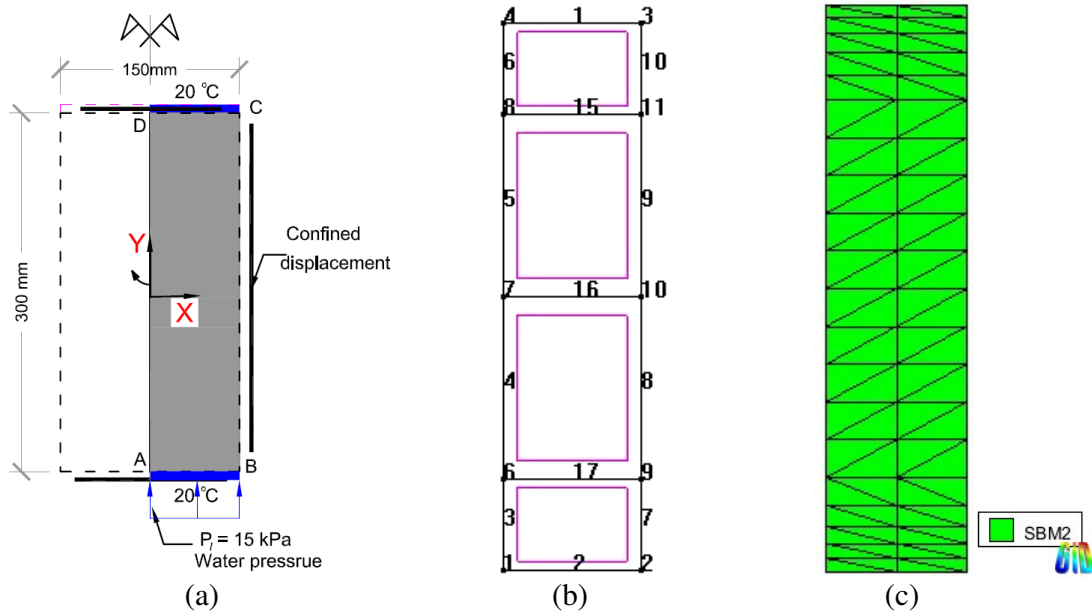
Figure 8.21: Description of the numerical simulation geometry: (a) Identification of boundary value model, (b) Clusters and points analysis (points 4,6,7 and 8 are point analysis), (c) Discretisation.

Table 8.10: Initial condition for the HM test

	Porosity	Suction	Temperature
Unit	(-)	(MPa)	(°C)
Value	0.485	21.4	20

8.4.3 Numerical simulation of the thermo-hydro-mechanical test

Geometry and discretisation: The geometrical model was also built on the X-Y plane Fig. 8.22(a). The problem was solved as an axis-symmetric problem with an axis-symmetry of the Y axis. At the top and the bottom of the model, where the flux boundary condition was applied, the discretisation there is finer Fig. 8.22(c). Points 6, 7 and 8 correspond to the position of the water content and temperature sensors in the sample Fig. 8.22(b). Points 1 and 4 are located on the bottom and the top of the sample and they were chosen to collect data corresponding to the load cell measurements. The primary variables used for the THM test simulation are the same with the simulation for the HM test (u, P_l, and T).

Stress-strain boundary condition: The test is a constant volume test; therefore line

Table 8.11: Initial conditions for THM test

Unit	Porosity (-)	Suction (MPa)	Temperature (°C)
Value	0.481	19.5	20

Table 8.12: Thermal boundary conditions for THM test

Line number	1	2	11	16	17	18	19	12
Temperature (°C)								
Phase 1 (2450 h)	20	80	36.5	35	32	26	24	20
Phase 2 (250 h)	20	80	37.2	36.4	33.3	28.6	24	20

numbers 1 and 2 are constrained in the Y direction, and line numbers 11, 12, 16, 17, 18 and 19 are constrained in the X direction Fig. 8.22(a). The stress-strain boundary condition is applied for all intervals.

Phase one: The specimen was heated at the bottom, and the temperature measured along the outer wall of the column increased to the steady state described in Table 8.12 within 20 hours and remained constant during the first phase. In order to simulate this process, the numerical simulation was divided into two intervals. In the first interval, thermal boundary conditions allowed the temperature to gradually increase from 20°C to the value in Table 8.12. In the second interval, the thermal boundary conditions were given constantly as in Table 8.12. The first interval occurred after 20 hours, the second interval occurred after 2450 hours.

Phase two: Water was supplied with a pressure of 5 kPa on the top, and the boundary temperature measured is presented in Table 8.12. The measured temperature along the outer steel wall changed when the soil was saturated due to the change in the thermal conductivity of the soil. Therefore in phase two, there are two intervals. In the first interval, the outer wall boundary temperature increased during the hydration test after 60 hours to the value described in Table 8.12 for the second phase. In the second interval, the outer temperature remained constant until the end of the testing process.

The initial conditions were taken from experimental measurement. The initial conditions are presented in Table 8.11. The total length of the numerical simulation is 2560 hours, which is similar to the total time required for experimental process.
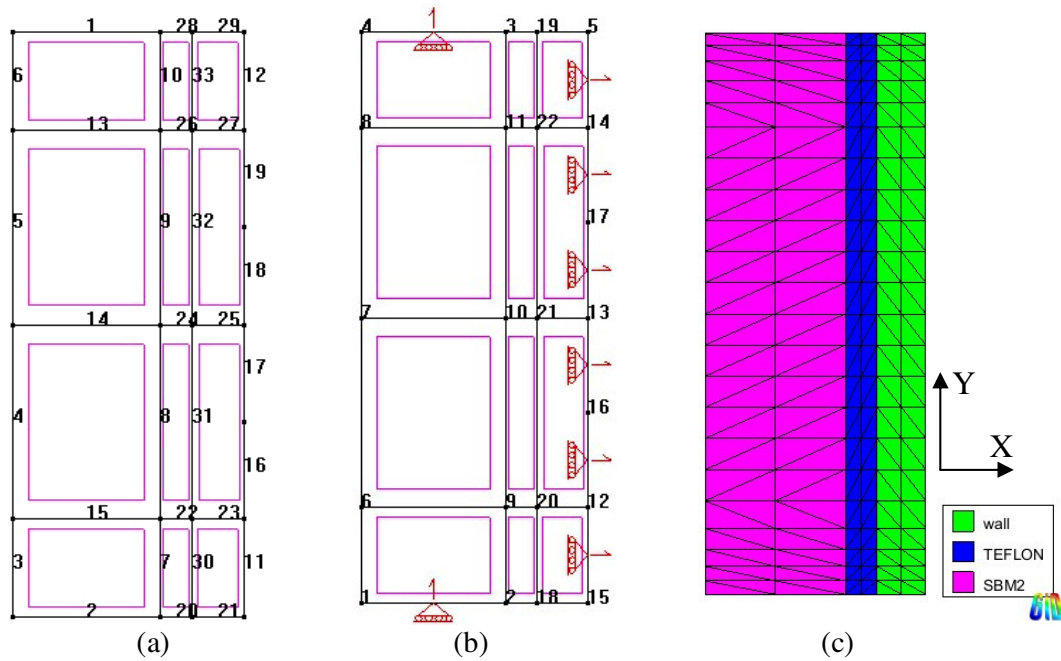
Figure 8.22: Description of the numerical simulation geometry: (a) Geometry and elements, (b) Stress-strain boundary condtions, and (c) Materials.

8.4.4 Results of the numerical simulation with initial parameters

With the supplied water from the bottom during the HM test, the water permeating through porous media obeys a generalised Darcy's law as in Eq. 8.18. The primary variable for hydraulic behavior is liquid pressure (P_l). The suction (s) is calculated by $s = P_g - P_l$. The relation between suction and degree of saturation as in the van Genuchten model (Eq. 8.21) was used for hydraulic flow law in an unsaturated state. The degree of saturation observed along the geometry at points 8, 7 and 6 corresponded to the TDR measurement: TDR 1, TDR 2, TDR 3, respectively increased one by one (Fig. 8.23(a)). Together with the increasing degree of saturation, the suction decreased at the points corresponding to measurement RH 1, RH 2, and RH 3 (Fig. 8.23(b)).

For the stress-strain relationship, the coupled thermo-elasto-plastic model (Eq. 8.4 to 8.11) is used to simulate such behaviour. The vertical stress (S_{yy}) increased as the degree of saturation increased. The vertical stress measured by the load cell at the bottom is total stress, including weight of the soil sample, plus the weight of the two load cells and the weight of the water volume injected into the soil sample. The stress calculated by FEM method is the net stress in unsaturated conditions and the effective stress in saturated conditions. In order to compare the experimental result and numerical simulated result, the calculated total stress is a sum of the net stress and positive water pressure Fig. 8.24(a).

The stress at the bottom increased faster than stress at the top due to the hydration at the bottom. The maximum vertical pressure at the bottom is higher than the maximum stress at the top because the pressure at the bottom includes soil weight and the water injected during the test.

The result of calculated temperature can be seen in Fig. 8.24(b) and was constant during the hydration process. The conduction of temperature in the porous medial was controlled by Eq. 8.25 and Eq. 8.23.

Using the same mathematical frameworks, the results of numerical simulation for the THM test are presented in Fig. 8.25 and Fig. 8.26. The numerical simulation includes two phases: the first phase is a heating phase, and the second phase is a hydration phase. In the heating phase the degree of saturation on the bottom part of the specimen decreased slightly; however, the suction simultaneously increased at the same location. The degree of saturation and suction at points 7 and 8 changed insignificantly during the first phase. In the second phase, the degree of saturation rapidly developed to a maximum saturated condition and suction quickly reached zero Fig. 8.25(a) and Fig. 8.26(b).

When the specimen was heated, the stress at bottom (point 4) decreased due to the shrinkage phenomenon with a decrease in suction Fig. 8.26(a). The temperature increased and this was distributed based on the distance from the point to the heater (Fig. 8.26(b)). In the hydration phase, the pressure on the bottom part increased more than the pressure at the top. The temperature decreased temporarily because the cold water induced a reduction in the temperature in the specimen. Then the temperature observed at points 6, 7 and 8 increased to the steady state due to saturated thermal conductivity (λ_{sat}) which was higher than thermal conductivity of dry soil (λ_{dry}).

In summary, the numerical simulation results show the agreement with the theoretical frameworks for unsaturated soil. They also agree qualitatively with the experimental results. The quantitative agreement with the experimental results may be carried out by performing calibrating the input parameters. The calibration of the parameters is presented in the next section, known as a back analysis approach.
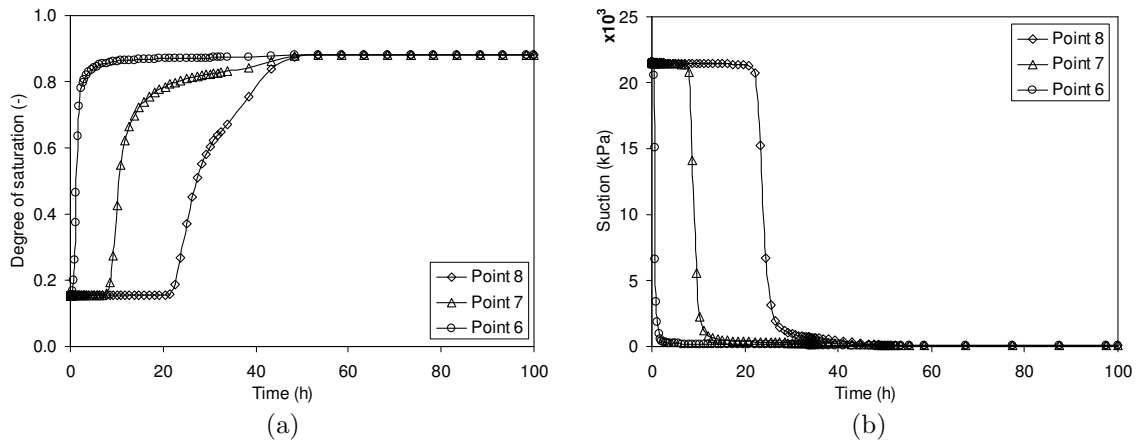
Figure 8.23: Result of the HM test simulation with initial parameters (a) Degree of saturation versus time and (b) Suction versus time.
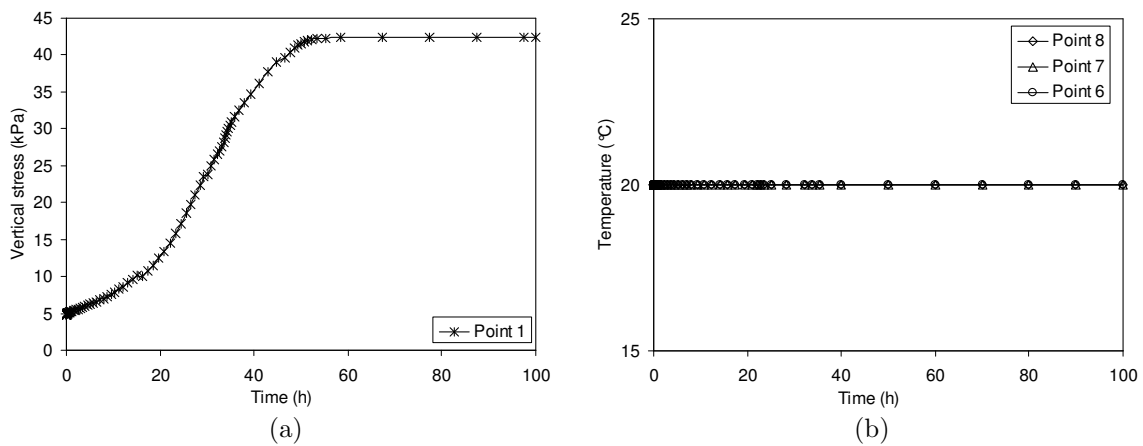
Figure 8.24: Result of the HM test simulation with initial parameters (a) Vertical stress versus time and (b) Temperature versus time.
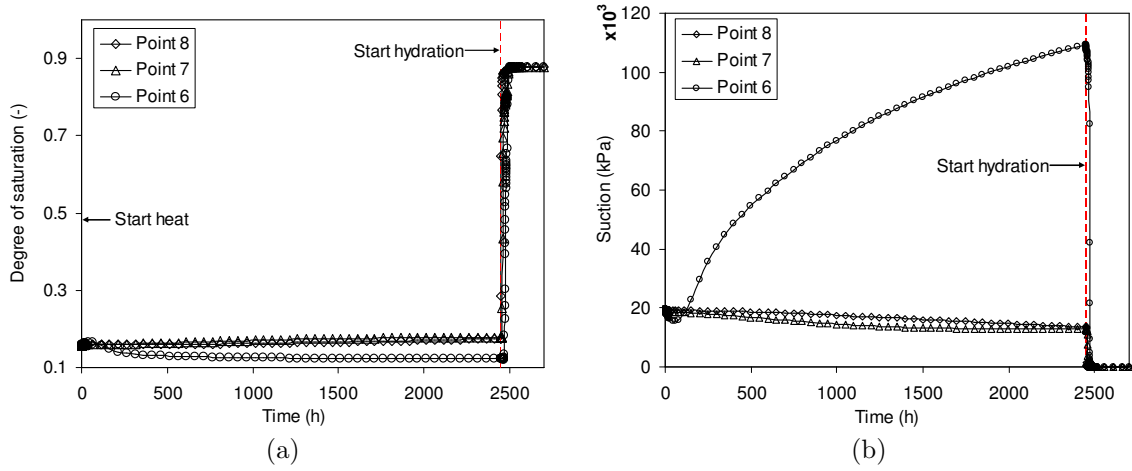
Figure 8.25: Result of the THM test simulation with initial parameters (a) Degree of saturation versus time and (b) Suction versus time.
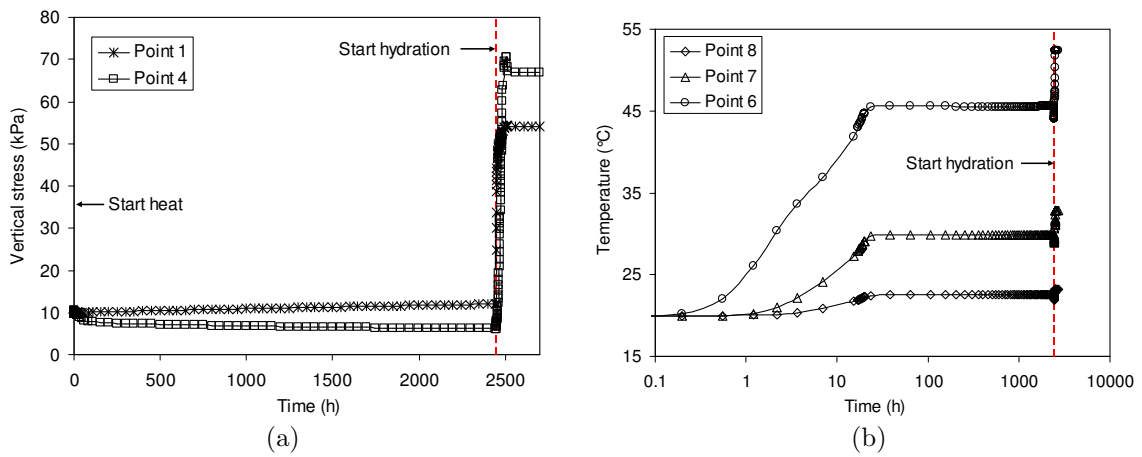
Figure 8.26: Result of the THM test simulation with initial parameters (a) Vertical stress versus time and (b) Temperature versus time.

8.4.5 Conclusion

This part introduces a numerical simulation for two experimental processes in the THM column-type test: a hydro-mechanical (HM) test and a thermo-hydro-mechanical (THM) test. The coupled thermo-hydro-mechanical analysis in finite element software was used to simulate these two tests. The primary results show that coupled THM analysis is competent in fully reproducing the stress-strain behaviour, vapour transport, and temperature conduction occurring in the soil sample as well as how these factors interact. The simulations were performed based on some parameters derived directly from the experiment. The other parameters were adopted from the materials which have similar properties to this studied material. Therefore the results may not reflect the sample behaviour quantitatively. The parameters must be re-estimated via back analysis to assess their accuracy. This procedure is demonstrated in the next chapter.

9 Identifying model parameters via back analysis approach

9.1 Formulation of the back analysis problem

9.1.1 Introduction

Back analysis in geotechnical engineering includes several aspects: uncertainty and sensitivity analysis, optimisation algorithms, and reliability analysis for identified parameters, see section 3. The optimisation algorithms are meant to minimise the error function, which describes the difference between model prediction and measurement data in the hope of: (i) decreasing the error function values to a minimum, (ii) identifying parameters which are representative for the characteristics of the studied soil material, when the value of error function is minimal.

In fact, for non-linear model there may exist some sets of parameters that provide the same values of the error function. This indicates that the optimisation problem may not have unique solution. Therefore, a reliability analysis needs to be performed to assess the accuracy of optimisation problem solutions. The gradient of the error function reacts differently to the variation of the model parameters. In other words, some parameters may vary substantially while the error function remains almost constant. Consequently, some parameters may not be identified reliably even when the error function reaches its minimum. For instance, when identifying soil hydraulic parameters several parameters cannot be estimated using inverse analysis because of the low sensitivity or high correlation between the parameters. To avoid this situation, a strategy selecting the meaningful parameters for identification has been introduced in Schanz et al. (2008, 2011b), where the authors employed model sensitivity analysis to select the most sensitive parameters for the optimisation process. The parameters exhibiting low influence on the model response should be excluded from the optimisation process in order to reduce the uncertainty in
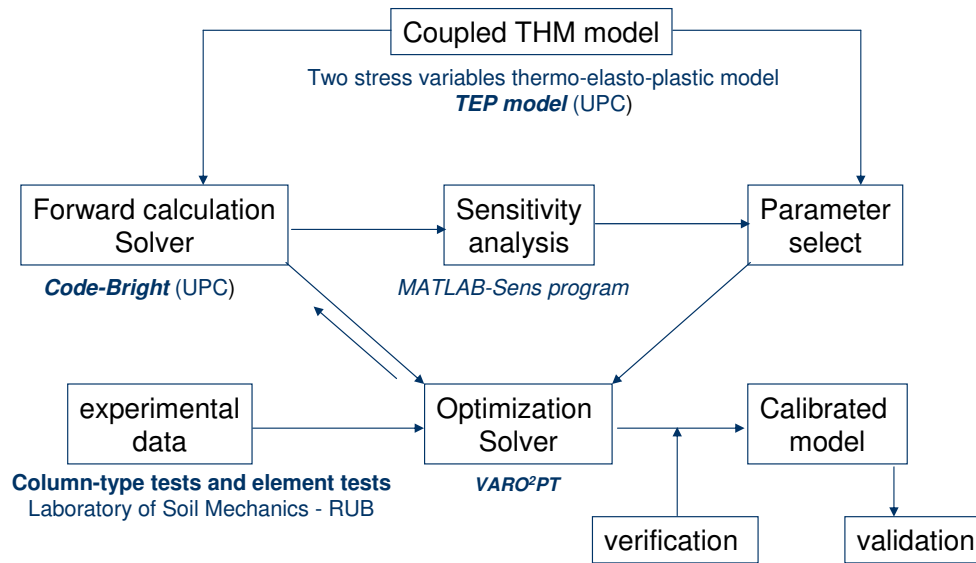
Figure 9.1: A concept of back analysis, according to Schanz (2009)

the identified parameters. The concept introduced in these papers is summarised in the flowchart given in Fig. 9.1.

The aim of the back analysis procedure depicted in Fig. 9.1 is to identify the model parameters based on experimental data, numerical simulations, model validation and verification of the performed optimisation procedure. Firstly, one has to select an appropriate constitutive model and build numerical models. Secondly, the forward calculation has to be performed by solving numerically the posed initial and boundary value problem. Then a sensitivity analysis has to be carried out to select the most sensitive parameters for the optimisation process. Thirdly, the optimisation algorithm has to be applied employing the experimental data, the numerical solution, and the selected parameters for identification. The minimal value of the objective function gives the parameter values that provide a model response most close to the experimental observation. The solution of the optimisation problem needs to be subsequently verified.

In the frame of back analysis of geotechnical problems, local sensitivity analysis is popularly used and examples may be found in (Hill, 1998; Zhang et al., 2003; Schanz et al., 2008; Knabe et al., 2013). However, with regard to coupled THM analysis it has to be acknowledged that this is a complicated problem involving high nonlinearity and the model may be sensitive to a parameter at a particular local value of parameter's set but may not be sensitive at the other local value of parameters' set. The "initial guess" for the model parameters used for sensitivity analysis may not be the set of optimal (true) parameters. Therefore, the result of the sensitivity analysis using the initial suggested set

of parameters may not truly reflect the model sensitivity to the parameters and this may introduce difficulties when solving the optimization problem. In this study, an appropriate global sensitivity method is used employing a variance-based method, which allows all parameters to vary simultaneously in their design space.

Next, it is important to point out that even applying Maximum Likelihood method (Ledesma et al., 1996b) or Bayesian method (Honjo et al., 1994b) can not overcome the lack of prior information about the parameters. On the other side, some researchers proposed that the confidence in the identified parameters can be accessed based on sensitivity analysis (Ledesma et al., 1996a; Knabe et al., 2013). However, parameter sensitivity depends on the type of model responses analysed and the type of the boundary value problems. One parameter may be sensitive to a typical model response but not sensitive to other types of responses. Therefore, estimating the confidence in identified parameters based on sensitivity analyisis is questionable and hardly applicable for the multi-response analysis carried in this case study. Moreover, the confidence intervals may not be reliably determined based on only one optimization test because the optimization problem is mostly to not possessing unique solution.

If the boundary conditions do not activate the constitutive property characterised by the particular parameter, the parameter will not play any role in the current analysis. Secondly, for the multi-response problem, the sensitivity of the responses is not sufficient to select parameters for optimization. In order to overcome these difficulties in the present study it is proposed an innovative back analysis strategy employing a stochastic approach.

The back analysis strategy used here is illustrated in Fig. 9.2. According to this strategy, a coupled THM problem is formulated and solved numerically and a solution of the forward problem is found this way, (see section 8.1). The CODE_BRIGHT code, a finite element tool, is used in order to solve the forward problem. The numerical solution is compared with measured data by means of an objective function, which is minimised by the optimisation solver. Running the optimisation solver is called an optimisation test. The reliability of the identified parameters is assessed via their confidence intervals, and the multi-replication (test-retest) technique is adopted to estimate the probability distribution of the obtained optimal parameters. The optimisation test is replicated N_p times to get N_p sets of optimal parameters. Particle Swarm Optimisation (PSO) (Kennedy and Eberhart, 1995) is used to solve the optimization problem. The difference between the optimisation tests consists in the randomly selected initial values for the PSO execution. When the number of replication times n_p is equal to N_p, the obtained sets of parameters are processed applying the probability distribution theory. In addition, the relationship
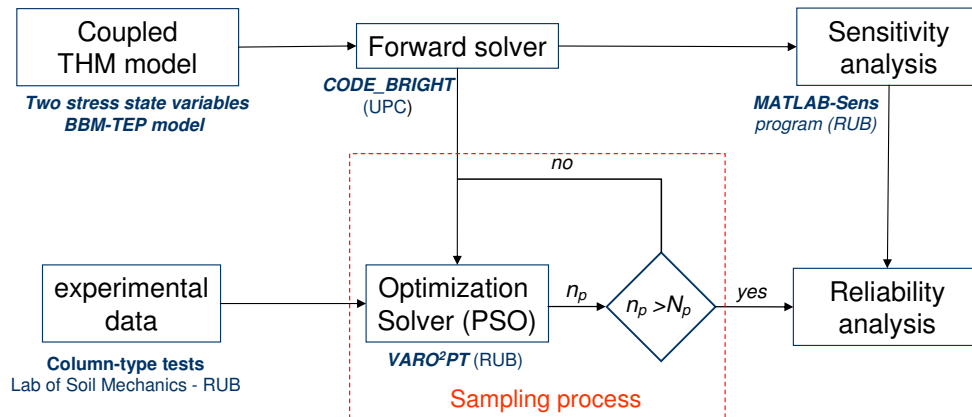
Figure 9.2: Back analysis strategy for this study

Table 9.1: Constitutive relations in coupled THM analysis

Variables	Constitutive equation	Notation
Liquid and gas advective flux	Darcy's law	q_l, q_g
Vapour and air non-advective fluxes	Fick's law	i_g^w, i_l^a
Conductive heat flux	Fourier's law	i_c
Liquid phase degree of saturation	Retention curve	S_l, S_g
Stress tensor	Mechanical constitutive model	σ

between model sensitivity to the parameters and the reliability of the identified parameters is investigated.

9.1.2 Formulation of the back analysis problem

The solution of the coupled thermo-hydro-mechanical problems was performed via the finite element method. The constitutive relations are summarised in Table 9.1. The BBM-TEP model was used to reproduce the stress-strain behaviour of the soil under non-isothermal conditions. Generalised Darcy's law is used to describe the unsaturated as well as the saturated flow of moisture/water in the porous medium. The two-parameter van Genuchten model is selected for the soil water retention relationship. Fick's law is used to describe vapour transfer by diffusion. These relationships are presented in section 8.

The parameters involved in the considered fully coupled THM analysis are classified in groups of parameters related to stress-strain behaviour, hydraulic transfer, and temperature change. The classification of the parameters helps to clarify the influence of each

group of parameters on different types of response. The input parameter vector $\boldsymbol{x}$ is composed of:

- Parameters involved in modelling net stress driven processes ($d\boldsymbol{\sigma} \neq 0$):

$$\{\mathcal{M}\} = \{k_{io}, \alpha_i, p_{ref}, \lambda(0), r, \beta, k, p_{s0}, p^c, M, \alpha, e_o, p_o^*\}$$

- Parameters involved in modelling suction driven processes ($ds \neq 0$):

$$\{\mathcal{H}\} = \{P_0, \lambda, \phi_0, k_o, k_{s0}, \alpha_{ss}, \alpha_{sp}\}$$

- Parameters involved in modelling temperature driven processes ($dT \neq 0$):

$$\{\mathcal{T}\} = \{\tau, D, \lambda_{sat}, \lambda_{dry}, \alpha_0, \alpha_1, \alpha_3, \rho\}$$

- Total 28 parameters summarised in the vector:

$$\{\boldsymbol{x}\} = \{\mathcal{H}, \mathcal{T}, \mathcal{M}\}$$

The model response within coupled THM analysis provided by CODE_BRIGHT is defined by several output variables, including: total stress, effective stress, water pressure, degree of saturation, displacement, suction and temperature. Here we consider THM model response that is consistent with the measurement data obtained from the tests performed by means of the column-type device. Therefore the vector of model response $\boldsymbol{y}$ was composed as follows:

$$\boldsymbol{y} = \{S_l(t), \sigma_{yy}(t), T(t), s(t)\}$$

where $S_l(t)$ is the degree of saturation over time t, $\sigma_{yy}(t)$ is the vertical stress over time, and $T(t)$ is the temperature over time, and $s(t)$ is suction over time. All these response variables were printed out at locations where the measurements were carried out during the experiment. Within the back analysis the model parameters are the unknown variables and hereafter we will use the term "input factors" for the considered in the analysis parameters. The relationship between model response and the input factors is given in Eq. 9.1. Given two domains $\mathbb{X}$ and $\mathbb{Y}$, where the vector of input factors is $\boldsymbol{x} \in \mathbb{X}$ and the vector of model response is $\boldsymbol{y} \in \mathbb{Y}$, the THM model maps $\mathbb{X}$ to $\mathbb{Y}$ according to the mapping rule:

$$y_k = f_k(\boldsymbol{x}) \tag{9.1}$$

The analysis that assesses how variation in each element of $\boldsymbol{x}$ affects the model response y_k ($k = 1, 2, 3, 4$) is called sensitivity analysis. The algorithms which vary the input parameters $\boldsymbol{x}$ in order to compare the output data of model response with the measured data and to find the minimum of a prescribed measure of the misfit are called optimisation algorithms (algorithms to solve the optimisation problem).

9.2 Sensitivity analysis

9.2.1 Introduction of SA in this study

The purpose of sensitivity analysis (SA) in this study is to determine the most influential parameters in THM boundary value problems. More general, the SA is defined as *a computation of the effect of changes in input values or assumptions (including boundaries and model functional form) on the outputs* (Morgan and Henrion, 1990). An essentially influential parameter of the model is called a sensitive parameter. From the result of the sensitivity analysis, one may select the most influential parameters to perform optimisation or assess the confidence interval of the identified parameters. The methods in sensitivity analysis may be classified as local sensitivity analysis (LSA) and global sensitivity analysis (GSA). This section will present both GSA and LSA as well as how they were implemented in MATLAB code.

9.2.1.1 Local sensitivity analysis

LSA addresses sensitivity relative to point estimates of parameter values. Local methods usually involve taking the partial derivative of the output with respect to an input factor.

The LSA was carried out herein by deviating 1% of the value for each parameter from its center value. A vector $\boldsymbol{x}$ allows only one element to be changed at one time in each calculation while keeping others fixed. This method is called one-at-a-time (OAT) procedure (Saltelli et al., 2008). The experimental design is understood herein as the design of input parameter values to investigate the corresponding model output response. The partial derivative of the output with respect to the particular component of the vector of input factors $\boldsymbol{x}$ is used to measure the local sensitivity. The OAT procedure is easy to perform and it is suitable for linear models where the input factors participate in a linear way in the model description. However, for non-linear models, the sensitivity measured via OAT technique may depend on the step size for the numerical calculation of the partial derivatives.

OAT method is technically easy to implement. However, it has to be underlined that the result of the LSA only measure the influence of a given parameter at the nominal value and do not give information about the sensitivity along the entire parameter design space. The numerical calculation of the partial derivatives is based on the expansion of the function representing the model response in a Taylor's series at the center point. The

corresponding equation reads:

$$y_k = f_k(\boldsymbol{x}) = \sum_{n=0}^{\infty} \frac{f_k^{(n)}(\boldsymbol{x}_0)}{n!}(x_i - x_{i0})^n \tag{9.2}$$

where $f_k^{(n)}$ denotes the nth derivative of f_k.

From Eq. 9.2 when considering the linearisation, the high order derivatives of f_k are not considered and the series is truncated to the first order derivatives.

$$f_k(\boldsymbol{x}) \approx f_k(\boldsymbol{x}_0) + \frac{\partial f_k(\boldsymbol{x})}{\partial x_i}(x_i - x_{i0}) \tag{9.3}$$

The Eq. 9.3 can be rewritten as Eq. 9.4. The equation presents the conventional sensitivity index S_{ik} (Ledesma et al., 1996b; Saltelli et al., 2004):

$$S_{ik} = \frac{\partial y_k}{\partial x_i} \approx \frac{f_k(\boldsymbol{x}) - f_k(\boldsymbol{x}_0)}{x_i - x_{i0}} \tag{9.4}$$

The first two terms in the Taylor's series represent the slope of the function f_k at the value x_{i0} and is a linearisation of f_k at the vicinity of x_{i0}. The S_{ik} only represents model sensitivity in vicinity of value x_{i0} and because of that is called local sensitivity index.

The application of the sensitivity analysis to a model whose response is found as a numerical solution via finite element method of a boundary value problem, may possess two possible types of error related to the finite difference algorithm used to calculate the partial derivatives: truncation error and condition error (Iott et al., 1985). The difference between the exact value and the computed value of a function is the truncation error. The truncation error increases with increasing the step size for computing the approximated value. Condition errors are associated with numerical noise and are caused by a loss in numerical precision (e.g. a round-off value, convergence criteria). Condition errors in finite difference method generally increase with decreasing step sizes (Iott et al., 1985). When $x_i \to x_{i0}$ then $f_k(x_i) \to f_k(x_{i0})$ the truncation error disappears while the effect of the condition error in numerical calculation is dominant when calculating S_{ik} (Iott et al., 1985).

Some researchers attempted to reduce the effect of the dimension scale of the input factors in the sensitivity index (Hill, 1998; Zhang et al., 2003). They multiplied S_{ik} with the input factor x_i. This study presents the local sensitivity analysis adopting the procedure proposed by (Zhang et al., 2003; Schanz et al., 2011b).

9.2.1.2 Global sensitivity analysis

This section provides the consideration of the different GSA and the selection of the suitable analysis method for the THM problem. GSA examines sensitivity with regard to the entire parameter domain. The advantage is that GSA copes with the sensitivity analysis for non-linear models. The main drawback of the GSA is its relatively high computation cost. According to Saltelli et al. (2008), the computation costs and the disadvantage of each GSA method applied to the considered here coupled THM model can be determined as it is presented in Table 9.2.

Table 9.2: Summary on GSA methods

GSA method	Sampling number		Disadvatage
	General case	THM case	
Elementary effect	$r(I+1)$	4*21 = 84	Difficult to implement
Scatterplots	$N = 1000$	1000	Difficult to compare two factors having nearly the same influence
Variance-based	$N(I+2)$	22000	High cost
Random Balance Designs	$N = 1000$	1000	Can only determine first order sensitivity indices
Monte Carlo filter	500-1000	500-1000	Low successful rate, low accuracy

where I here is the number of parameters, N is the number of samplings, r is the number of elements (4-10).

Selection of the method for GSA:
Choosing the GSA method is based on the guidelines given by Saltelli et al. (2008) in section 6.5 of their book. The choice depends on the cost and the method feasibility when implementing in the MATLAB code.

The numerical simulation of a THM column test costs 10 minutes execution of the forward calculation (numerical experiment). One sensitivity analysis may take 4 days to complete 1000 samples. Random Balance Designs (RBD) is a variance-based method to calculate the first order sensitivity indices. The method requests relatively low computation costs. The pros and cons for RBD method are:

Advantage: The cost is only 1000 samples, easy numerical experiment design and its easy implementation in MATLAB code.

Disadvantage: it provides only the first order or main sensitivity indices.

In summary, two methods of sensitivity analysis regarding LSA and GSA are selected for comparison in this thesis: LSA via partial derivative method and the variance-based GSA using RBD method.

9.2.2 Description of the LSA approach

The LSA presented in this section uses the partial derivatives to measure the sensitivity and the analysis follows the procedure presented in Schanz et al. (2011b).

The notations used hereafter are: $\boldsymbol{x}$ is the vector of input factors and $\boldsymbol{y}$ is the vector of model response (e.g. degree of saturation) for the selected points, m is the label of the observation point in the experiment ($m = 1, 2, ..., M$), k is is the label of the specific model response considered in the analysis($k = 1, 2, ..., K$) and t is the time step ($t = 1, 2, ..., T$). It is to note that the dimension of the response vector is ($T \times M \times K$).

By utilising the OAT procedure, using the nominal value $\boldsymbol{x}_0$ which does not change during the analysis. It is calculated the LSA measures for each of the considered model responses. In order to complete the LSA there have to be executed I (I is the total number of the model parameters due to LSA) forward calculations. The influence of the step size in determining the approximation to the partial derivatives is evaluated by varying the step size from $\pm 1\%$ to $\pm 10\%$ of the nominal value of the corresponding parameter. The OAT procedure is similar to the method in Schanz et al. (2008) and Schanz et al. (2011b) and it uses the measures defined by Eq. 9.6 and Eq. 9.7. The LSA analysis is implemented in MATLAB code, see section 9.2.4.

1- Determining scaled sensitivity (SS): this is the scaled sensitivity of the $ktm - th$ model response to the $i - th$ input factor

$$SS_{ik}^{tm} = \frac{\Delta y_k^{tm}}{\Delta x_i} x_i \tag{9.5}$$

where y_k^{tm} is the model response k at time t at the selected observation point m.

2- Determining composite scaled sensitivity (CSS): CSS is introduced to combine the effects along the time and with the observation point position. The equation to calculate it reads:

$$CSS_{ik} = \sqrt{\frac{1}{TM} \sum_{t=1}^{T} \sum_{m=1}^{M} \left[SS_{ik}^{tm} \right]^2} \tag{9.6}$$

3- Determining the local sensitivity index γ: The local sensitivity index γ_{ik} is used as a normalisation of CSS_{ik} in the range from zero to one.

$$\gamma_{ik} = \frac{CSS_{ik}}{\max(CSS_{ik})} \tag{9.7}$$

9.2.3 Global sensitivity analysis: a Random Balance Designs

General description of the SA and sensitivity indices:
Suppose we have a generic model defined as, Saltelli et al. (2008)

$$y = f\left(x_1, x_2, ..., x_I\right) \tag{9.8}$$

$E_{x \sim i}\left(y|x_i\right)$ is the expected y value considering the variation of all values $x \neq x_i$. $V(y)$ is the variance in y considering the variance of all factors of x. The conditional variance $V_{x_i}\left(E_{x \sim i}\left(y|x_i\right)\right)$ is called the first order effect of x_i on y. Then the first order of sensitivity indices is defined by:

$$S_i = \frac{V_{x_i}\left(E_{x \sim i}\left(y|x_i\right)\right)}{V\left(y\right)} \tag{9.9}$$

Random Balance Designs:
Tarantola et al. (2006) proposed random balance designs (RBD) by modifying the Fourier Amplitude Sensitivity Test (FAST) for GSA analysis. The method is a variance-based method for GSA. Cukier et al. (1978) developed a classical FAST method based on selecting N design points of vector $\boldsymbol{x} = (x_1, x_2, ..., x_I)$ over an input factor space. The design of $\boldsymbol{x}$ is to explore each factor with a different (integer) frequency $(\omega_1, \omega_2, ..., \omega_I)$. A complex algorithm is used to set the frequencies such that they are free of interference up to a given order L. The computational model is run at each design point and the Fourier spectrum is calculated on the model output at specific frequencies $\{\omega, 2\omega, ..., L\omega\}$ in order to estimate the sensitivity index of each input factor x_i. The design parametric curve used in classic FAST is defined as:

$$x_i(s_j) = G_i(\sin \omega_i s_j) \quad \forall i = 1, 2, ..., I \quad \text{and} \quad \forall j = 1, 2, ..., N \tag{9.10}$$

where function G_i is chosen according to the desired PDF of x_i, s_j is the parametric variable varying in $(-\pi, +\pi)$ which is sampled over its range using N points, and ω_i is the frequency.

The RBD method allows S_i to be calculated by N designed points over the input space. They explore the input space using the same frequency ω to avoid the use of the complex

algorithms. Then, the output is reordered such that the number of design points increase with respect to factor x_i. The Fourier spectrum is calculated on the model output at the frequency ω and its higher harmonics $\{\omega, 2\omega, ..., L\omega\}$ and yield the estimation of the sensitivity indices S_i. Eq. 9.12 provides a random permutation of input factor x_i.

$$x_i(s_{ij}) = G_i(\sin \omega s_{ij}) \quad \forall i = 1, 2, ..., I \quad \text{and} \quad \forall j = 1, 2, ..., N \tag{9.11}$$

where $(s_{i1}, s_{i2}, ..., s_{iN},)$ denote the ith random permutation of N points.

The model is evaluated N times over the vector sample, which has a size of N:

$$y(s_{ij}) = f\left(x_i(s_{1j}), x_i(s_{2j}), ..., x_i(s_{Ij})\right) \quad \forall j = 1, 2, ..., N \tag{9.12}$$

The values of model output $y(s_{ij})$ are then re-ordered as $y^R(s_{ij})$ corresponding to the values of $x_i(s_{ij})$ ranked in increasing order. By doing so, the harmonic content of x_i propagates through function f to $y^R(s_j)$. The sensitivity of y to $\boldsymbol{x}$ is determined by harmonic content of y^R, which is quantified by its Fourier's spectrum as in Eq. 9.13. The sensitivity of y is evaluated at $\omega = 1$ and its higher harmonics ($\omega = 2, 3, 4, 5, 6$).

$$F_i(\omega) = \left|\frac{1}{\pi} \sum_{j=1}^{N} y^R(s_{ij}) \exp\left(-\mathrm{i}\omega s_{ij}\right)\right|^2 \tag{9.13}$$

and in discrete cases the index

$$\hat{V}_i = \mathrm{Var}[E(y|x_i)] = \sum_{l=1}^{L} F_i(\omega)|_{w=l} = \sum_{l=1}^{L} F_i(l) \tag{9.14}$$

is an estimate of the main effect V_i of input factor x_i on the model y. The procedure is repeated for all input factors, whereby the same set of model outputs is simply reordered according to $x_i(s_{ij})$ and the Eq. 9.13 and 9.14 are used to estimate V_i, with $i = 2, ..., I$. The MATLAB code is also provided in Saltelli et al. (2008) so that MATLAB can compute a generic sensitivity index according to the RBD method.

Arrangement of input parameters for the RBD:

As above description, RBD allows one y value to be calculated based on one set of input factors $\boldsymbol{x}$. In THM numerical simulations one set of parameters $\boldsymbol{x}$ can produce a series of output y_k^t that is time dependent. Some parameters affect the output model over a short period of time while others have a long-term effect.

The variation in the output value y can be estimated and compared with respect to the measurement results. Therefore, analysed points are selected at the same points of TDR

Table 9.3: Parameters: initial values and search intervals

	κ_{i0}	κ_{s0}	α_{ss}	α_i	α_{sp}	α_0	λ_0	r	β	M
Ini.	0.010	0.018	0.000	-0.010	0.300	1.0E-05	0.115	0.980	0.010	1.120
LB	0.005	0.010	-0.200	-0.030	-0.100	8.0E-06	0.050	0.300	0.005	0.90
UB	0.020	0.030	0.000	-0.003	0.500	4.0E-05	0.150	0.980	1.000	1.40

	p^c	p_0^*	P_0	λ	$\boldsymbol{k}_0$	D	τ	n	λ_{dry}	λ_{sat}
Ini.	0.010	0.280	0.610	0.446	5.9E-16	5.6E-09	0.8	2.3	0.700	1.300
LB	0.008	0.100	0.300	0.350	1.0E-16	5.6E-10	0.5	2.0	0.400	1.100
UB	0.080	0.800	1.500	0.650	9.0E-16	5.6E-08	1.0	2.5	0.900	1.500

measurements: points 6, 7 and 8 and to these point the points 1 and 4 at the top and bottom of the geometrical model depicted in (Fig. 8.22) are added, ending with total of five observation points to be used in the GSA.

Obtaining the output y_k

In order to present indices S_i versus time for each time step t one S_i will be calculated. The vector y_k^t - the output of model response with respect to time (t), is an average over all the selected points.

$$y_k^t = \frac{1}{M} \sum_{m=1}^{M} y_k^{tm} \tag{9.15}$$

For one set of parameters input, one can get an output y_k^t as a matrix with columns of degree of saturation, stress and temperature and rows their values at time steps. From y_k^t we can calculate S_{ik}.

Based on the constitutive equations employed in the selected THM model, a set of parameters including 20 parameters is considered for sensitivity analysis. A range of parameters value, i.e. (upper bound (UB) and lower bound (LB), is defined and the design domain is the same as for the optimization problem within the back analysis. The parameters and bounds values are presented in Table 9.3.

9.2.4 Sensitivity analysis implementation in MATLAB

A computing program developed by the author in MATLAB allows parameter values to be modified in the input files of the FEM program (CODE_BRIGHT), executing the

FEM program to read the input files and to release the output files, and finally reading the output files with elements and time steps to perform the sensitivity analysis. For sensitivity analysis, one has to prepare a data file to define parameters and a time step for interpolation. One has to determine the pre-set for the time step because the time step in the output is not the same for each FEM execution time. It should be noted that CODE_BRIGHT allows users to preset time steps for one interval; however, the program may reduce the time step size automatically if the solution of the boundary value problem does not satisfy the convergence criteria.

The algorithm for the sensitivity analysis is presented in Fig. 9.3. The input factor values in this case can vary based on the experimental design (i.e. OAT design or a permutation random design). The values of the input factors are designed and introduced to the FEM model via input files. The computing program extracts the relevant data after each forward calculation to do SA based on the sensitivity functions: local derivative based functions and global variance-based functions. The result is drawn in a graph and saved in data files. For further development, the program can use the extracted data to compare with the experiment data and to optimise the input factors.

Numerical simulations of the THM column tests are used for doing sensitivity analysis. Two tests are numerically simulated: the HM test and the THM test. Firstly, the HM observation test points were selected. The positions of the selected points herein correspond to the geometric points where the measurements took place. The model response consists in the degree of saturation and the vertical stress component. In case of the numerical simulation of the THM test, the vector of the model response is $\boldsymbol{y} = \{S_l(t), \sigma_{yy}(t), T(t)\}$ as presented in section 9.1.2.

9.2.5 Validation of the RBD implementation in MATLAB

The function for calculating the first order sensitivity (S_i) implemented in MATLAB code needs to be validated. In this section the calculation of S_i is validated for two generic models. The first generic model is defined by the function:

$$y = f(x_1, x_2) = 4x_1^2 + 3x_2 \quad \forall x_1, x_2 \in U[-1/2, 1/2] \tag{9.16}$$

The sensitivity index for this function can be obtained directly by using the analytical method Tarantola (2010). The analytical solution reads:

$$S_1 = \frac{\text{Var}[f_1(x_1)]}{V} = \frac{0.08}{0.838} = 0.106 \quad \text{and} \quad S_2 = \frac{\text{Var}[f_1(x_1)]}{V} = \frac{0.75}{0.838} = 0.894 \tag{9.17}$$
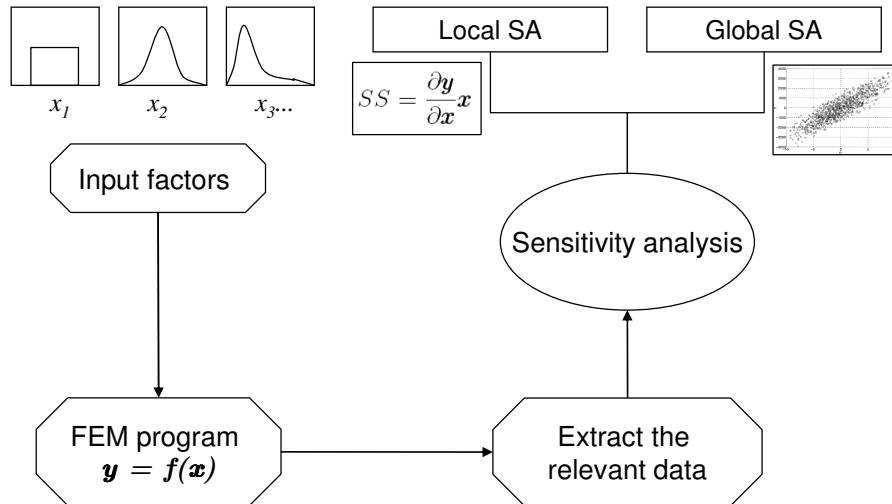
Figure 9.3: An algorithm for the sensitivity analysis program associated with FEM
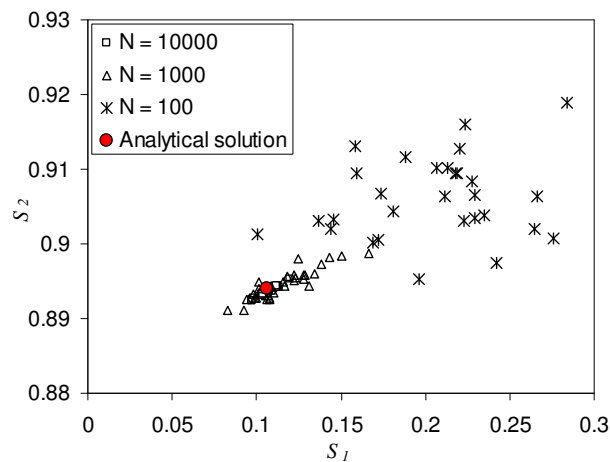

Figure 9.4: Validation of RBD sensitivity function in MATLAB

Numerical solutions using MATLAB code are obtained from different sizes of the sample N = 100, 1000, 10000, respectively. The calculation is replicated 30 times for each sample size. The numerical solutions is presented in Fig. 9.4. It is clear that the higher the number of samples, the more accurate is the solution. If only 10 samples are considered, the average of S_1 and S_2 are 97% and 1%, respectively deviated from exact solution. For 10000 samples the deviation reduces significantly to only 0.5% (S_1) and 0.05% (S_2).

The second function used for validation is the Sobol's function (Sobol', 1990), which is defined as:

$$f(x_i) = \prod_{i=1}^{k} g_i(x_i) \tag{9.18}$$

where k is the number of input factors and $g_i(x_i)$ is given by

$$g_i(x_i) = \frac{|4x_i - 2| + a_i}{1 + a_i} \quad \text{for} \quad 0 \leq x_i \leq 1 \text{ and } a_i \geq 0 \tag{9.19}$$

The function is widely used as a benchmark function for sensitivity analysis because it is a strongly non-linear and non-monotonic function. The values of the a_i determine the range of variation in each g_i.

From Eq. 9.19, it can be seen that a_i is a parameter to determine the relative importance of the variable x_i. If $a_i = 0$ the corresponding input factor x_i plays a very important role in g_i function. If $a_i = 9$, it is not important. If $a_i = 99$, x_i plays a non-significant role in g_i function. The analytical solution is presented in Tarantola et al. (2006) as:

$$V_i = \frac{1}{3(1 + a_i)^2} \quad \text{and} \quad V = \prod_{i=1}^{k} (V_i + 1) - 1 \tag{9.20}$$

Tarantola et al. (2006) are using for a_i the values {0, 1, 4.51, 9, 99, 99, 99, 99}. The results obtained with MATLAB are presented in Table 9.4. From the table it is clear that the RBD method is a very reliable method to estimate influential factors but it overestimates the sensitivity of the insignificant factors.

In summary, the RDB implemented in MATLAB code calculates global sensitivity indices correctly. The method can be combined with FEM code to analyse the sensitivity of the THM simulation of the column tests.

Table 9.4: Validation of the RDB in MATLAB using Sobol's function Sobol' (1990)

	S_1	S_2	S_3	S_4	S_5	S_6	S_7	S_8
Anal. Sol.	0.716	0.179	0.0024	0.0072	7.16E-05	7.16E-05	7.16E-05	7.16E-05
N=10000	0.712	0.175	0.0240	0.0073	1.94E-03	1.16E-03	1.25E-03	9.62E-04
N=1000	0.720	0.182	0.0464	0.0230	9.36E-03	8.39E-03	2.62E-03	1.04E-02
N=100	0.756	0.288	0.1783	0.1819	1.54E-01	8.14E-02	1.28E-01	1.16E-01

9.2.6 Sensitivity analysis: results and discussion

9.2.6.1 Local SA

The sensitivity analysis was applied to the HM test and THM test simulations. The parameter variations were from $\pm 1\%$ to $\pm 10\%$ of the corresponding nominal value in this

analysis. It can be easily seen that the parameters P_0, λ, and $\boldsymbol{k}_0$ have most influence on the degree of saturation for the HM test, Fig. 9.5. The parameters κ_{s0}, P_0, α_{sp}, $\boldsymbol{k}_0$, and λ were found to be the most influential parameters for the evolution of vertical stress. However, γ changed according to different step sizes in the finite difference approximation of the partial derivatives. The λ parameter decreased its influence on the variation of the degree of saturation, whereas the $\boldsymbol{k}_0$ parameter increased its influence on the same type of model response (Fig. 9.5). We have also different results when using positive or negative Δx_i. For instance, γ for the parameter λ with regard to the vertical stress is higher for negative Δx_i.

The results of sensitivity analysis using as model response the liquid saturation in the numerical THM test simulations are shown in Fig. 9.6 and 9.9. The THM test simulation included two phases: the heating phase and the hydration phase. Using local sensitivity analysis, the parameters P_0, λ, $\boldsymbol{k}_0$, and n were the most important parameters regarding the evolution of the degree of saturation. Utilising the same method, the parameters α_{sp}, $\boldsymbol{k}_0$, and κ_{s0} were important to the evolution of the vertical stress. Parameters λ_{sat}, P_0, λ, and λ_{dry} definitely play the most important role in the evolution of temperature.

The sensitivity of parameters was found to be time-dependent. The variation with time of the parameter sensitivity with respect to degree of saturation and stress is illustrated in (Fig. 9.7 and 9.8). In Fig. 9.7, one can see that the local sensitivity index γ increases in the first half of hydration phase and decreases in the second haft of this phase for the HM test simulation. The sensitive parameters concerning the development in the degree of saturation were in the hydraulic parameter group (P_0, λ, $\boldsymbol{k}_0$). When analysing the stress (Fig. 9.8), it was found that the hydraulic parameter group affects the stress development as well. However, the effect took place before entering the saturated state; therefore, the effect was greatly reduced when soil models were fully saturated. However, the importance of the mechanical parameters (κ_{so} and α_{sp}) increased monotonically during the hydration process and remained constant after the saturated state was reached. Therefore, the sensitivity of the parameters is not only time-dependent but also depends on the boundary conditions and the initial state.

Fig. 9.9, 9.10, and 9.11 present the local sensitivity index γ related to time for THM test simulations. The sensitivity of parameters are changed from the heating phase to the hydration phase. For instance, the parameter λ_{sat} which is high sensitive to the evolution of temperature in the first phase, became less important in the second phase of the simulation, (Fig. 9.11). Contrary, the parameter P_0, which is not sensitive to the
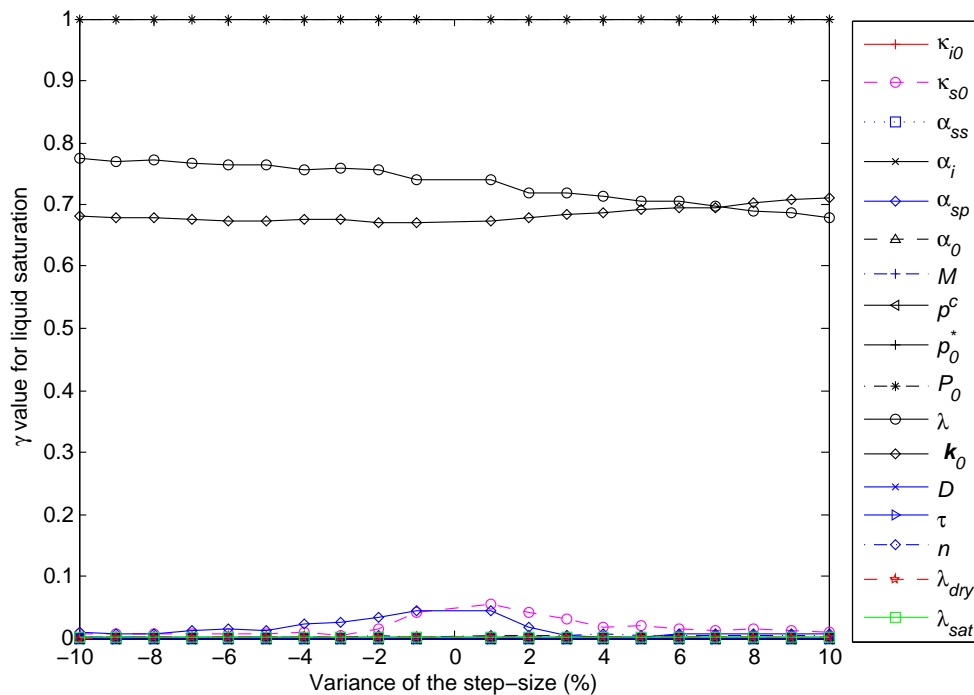
Figure 9.5: LSA for the liquid saturation in the HM test simulation.

evolution of temperature in the first phase, played an important role during the second phase.

As introduced in section 9.2.1 local sensitivity analysis based on the derivative method may be considered as based on linearisation of the input parameter $\boldsymbol{y}$ at the nominal point. The LSA result can be a good argument in small-range parameter variation or in linear models. For large-range parameter variations and for non-linear models, the accuracy of the results is not guaranteed.

In summary, the result of the LSA can vary depending on time analysis, the step size for calculating the partial derivatives, boundary conditions, and the location of the set of input parameters in input parameter space. For the small-range value of the input parameters, the result of LSA may be accepted as useful, but for the large-range values of the input factors, the result may not be adequate. These drawbacks of LSA invoke the usage of GSA as a more informative sensitivity method.

9.2.6.2 Global SA
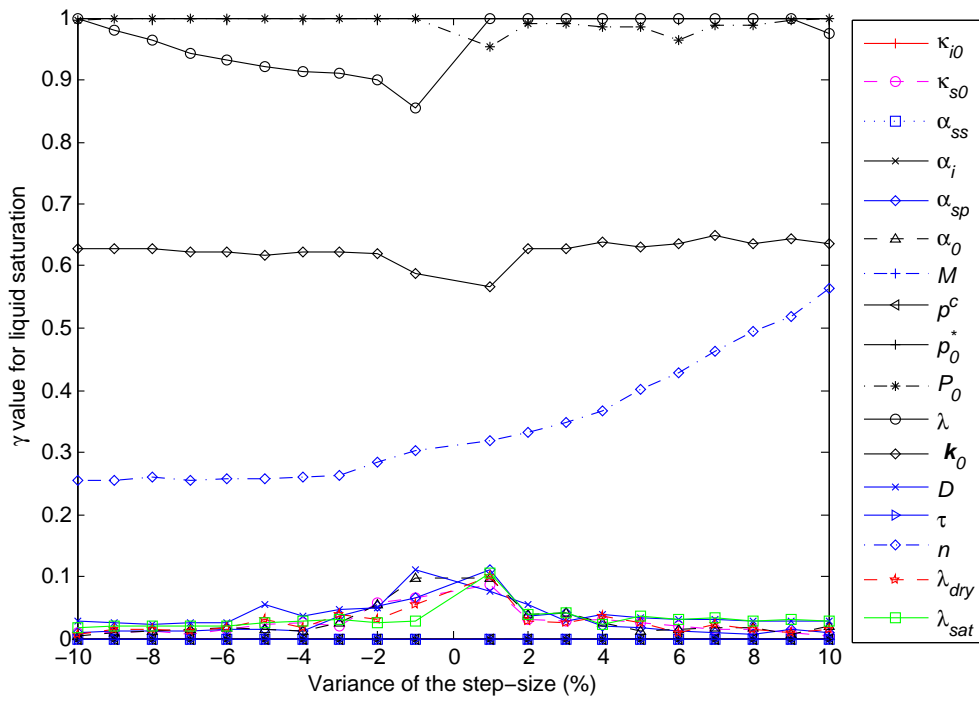
Scatterplots for sensitivity analysis:

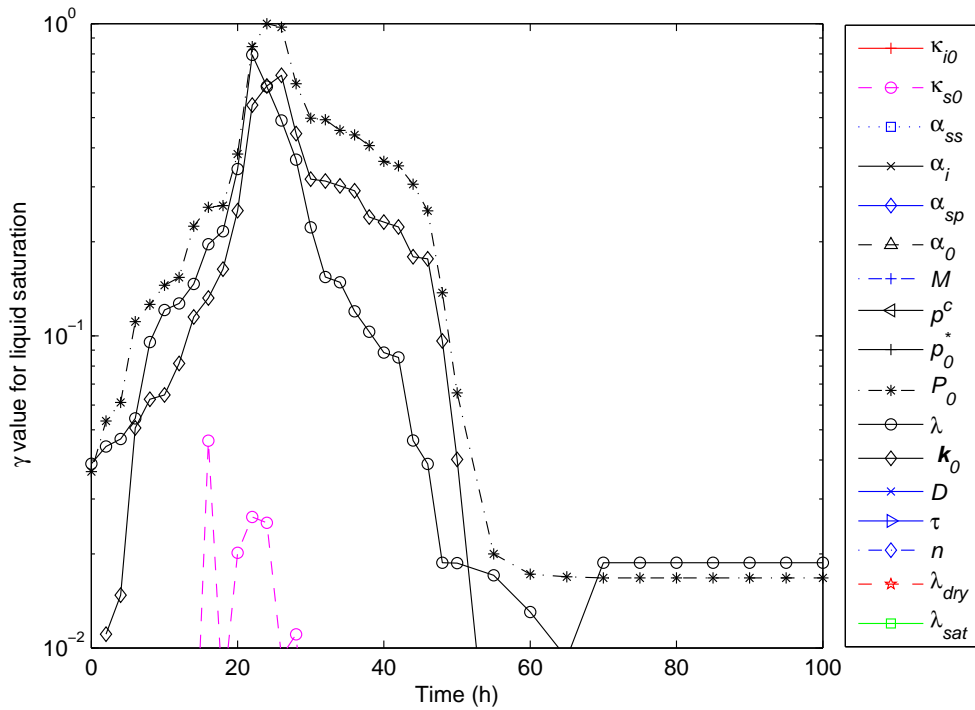Figure 9.6: LSA for liquid saturation using THM test simulation.

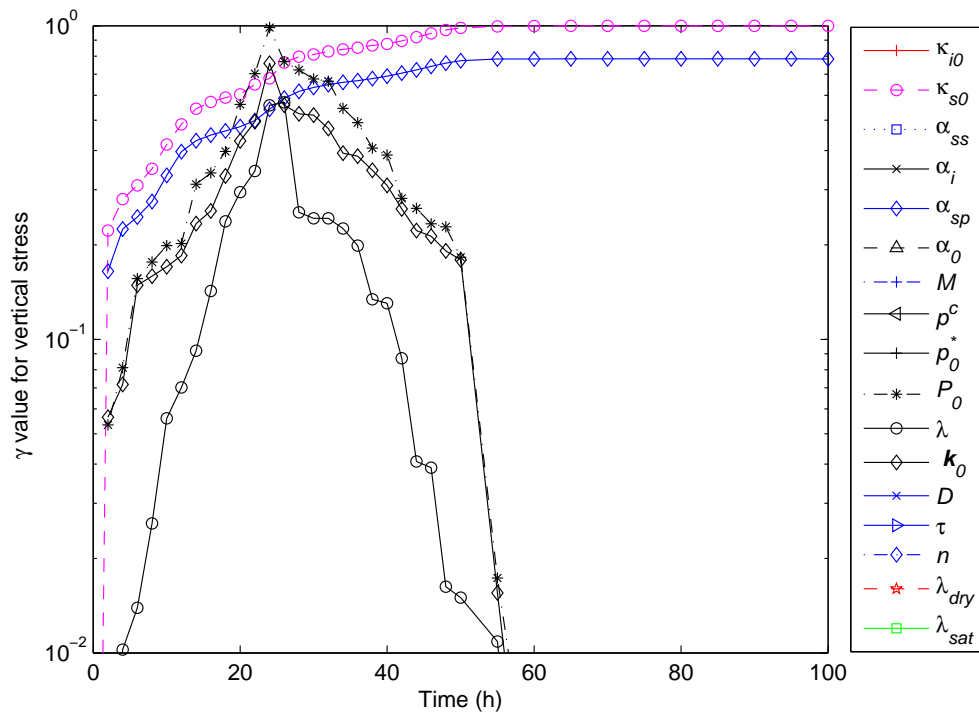Figure 9.7: LSA for liquid saturation using HM test simulation.

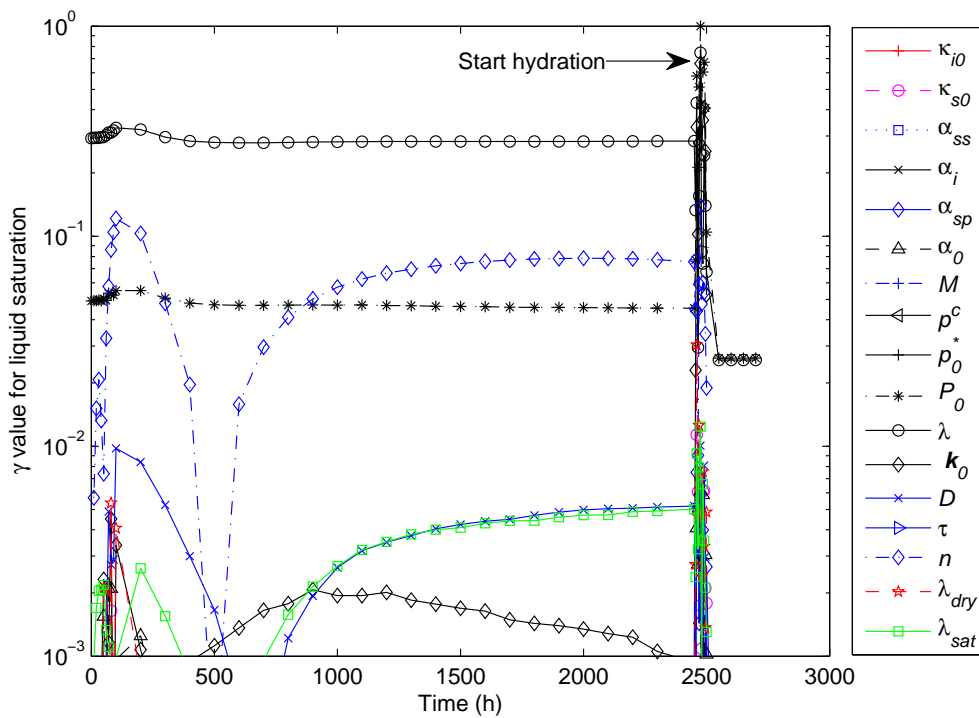Figure 9.8: LSA for vertical stress using HM test simulation.

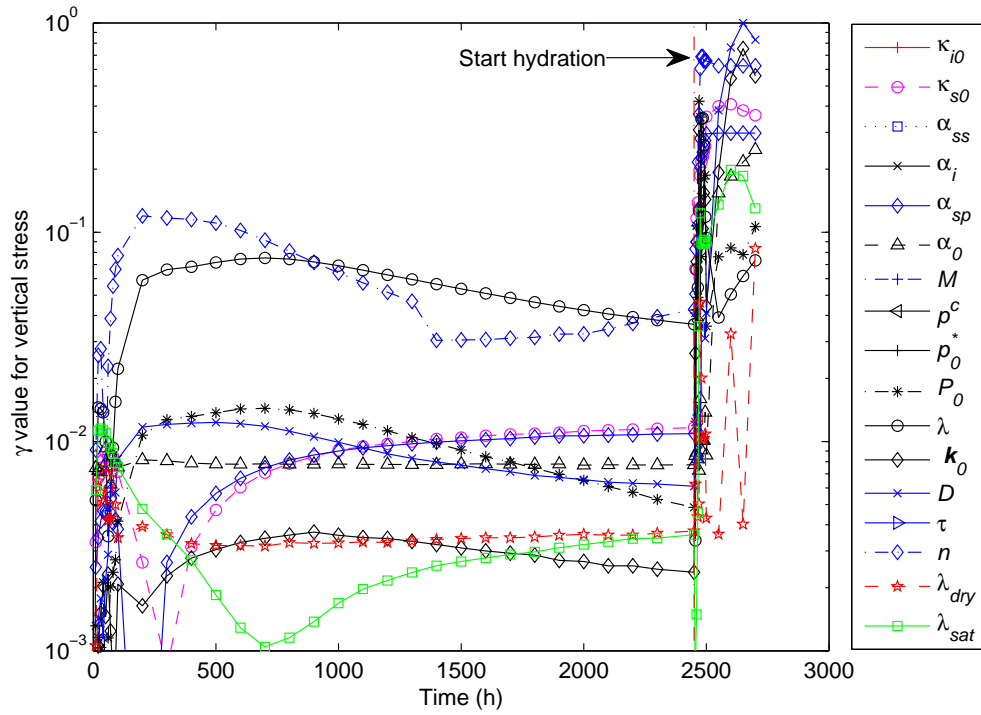Figure 9.9: LSA for liquid saturation using THM test simulation - time history.

Figure 9.10: LSA for vertical stress using THM test simulation - time history.
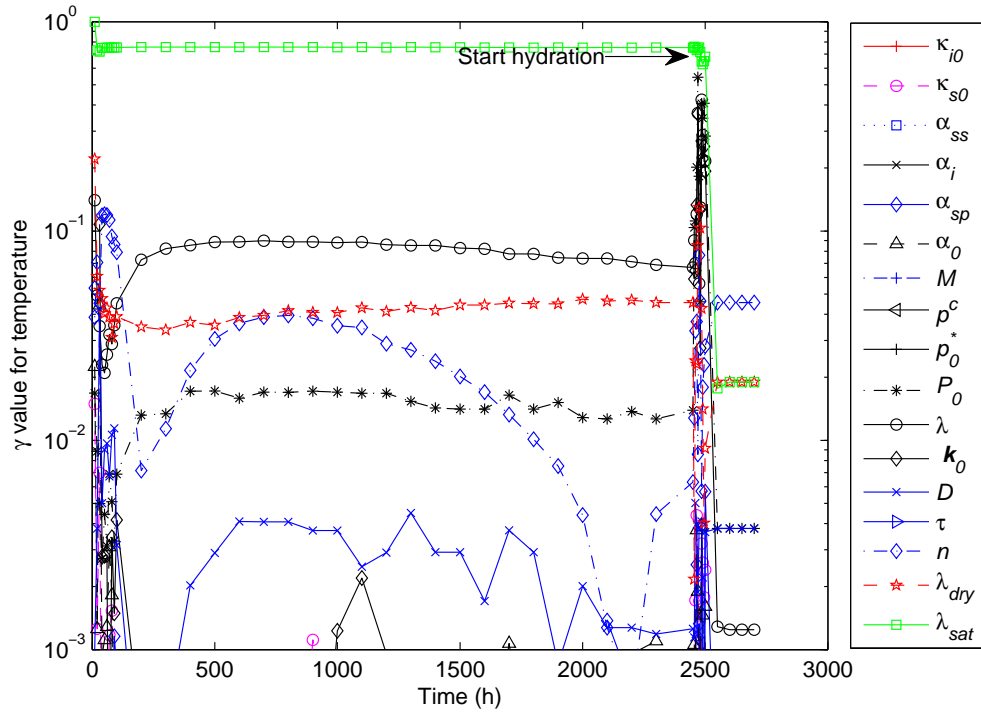

Figure 9.11: LSA for temperature distribution using THM test simulation - time history.

A scatterplot is a graphing technique to classify the influence of parameters on a mathematical model. Generally a scatterplot analysis is performed based on the random input parameters (e.g. the Monte Carlo experiment, random permutation) (Saltelli et al., 2008).

The RBD method arranges the input factors as random permutations. From the input factors or model parameters, the model responses are obtained. The influence of the factors can be roughly estimated using a scatterplot. The scatterplot results in Fig. 9.12 were obtained by analysing the variation in the degree of saturation and employing the THM test simulation. The parameter λ for the retention curve changed within its value range(0.35-0.65) and strongly influenced the degree of saturation during the time analysis. The parameter P_0 also significantly influenced the results but less than the parameter λ. The two parameters α_{sp} and M influenced the model response insignificantly in terms of the degree of saturation. The influence of λ was more than the influence of P_0 and P_0 influenced the model more than α_{sp} and M, but it is relatively difficult to judge which of the two parameters α_{sp} and M was more influential.

In general, most of the sensitivity analysis tools developed by practitioners aim to preserve the rich information provided by scatter plots in a condensed format (Saltelli et al., 2008). The challenge of the sensitivity analysis with many input factors is how to rank the factors fast and automatically without having to look at several different scatterplots. While compact sensitivity measures can be defined for sets, the sensitivities of sets cannot be visualised via simple two-dimensional scatterplots. Another problem occurs when models contain many independent or dependent outputs and the output is time-dependent and the boundary-value-dependent, thus ranking parameters becomes challenging in that case. Therefore, more effective tool is necessary to rank the influence of parameters. Such method is random balance designs. The method was introduced in section 9.2.3. In the next part, the result of sensitivity analysis is discussed after ranking the influence of parameters on the model output.

Result of the RBD method:
The results of sensitivity analysis using the RBD method for the HM test are presented in Fig. 9.13 and 9.14. Parameters P_0, $\boldsymbol{k}_0$, and λ definitely played the most important role in the evolution of the degree of saturation. Parameters α_{sp}, $\boldsymbol{k}_0$, and p_0^* definitely played the most important role in the evolution of the stress. However, the effect of each factor during the hydration process was different. For instance, while the sample was in an unsaturated state, the $\boldsymbol{k}_0$ parameter played an important role, but its role decreased after the soil had been saturated. On the contrary, the role of pre-consolidation pressure p_0^* in the initial state was small; however, it increased after the soil had reached a saturated
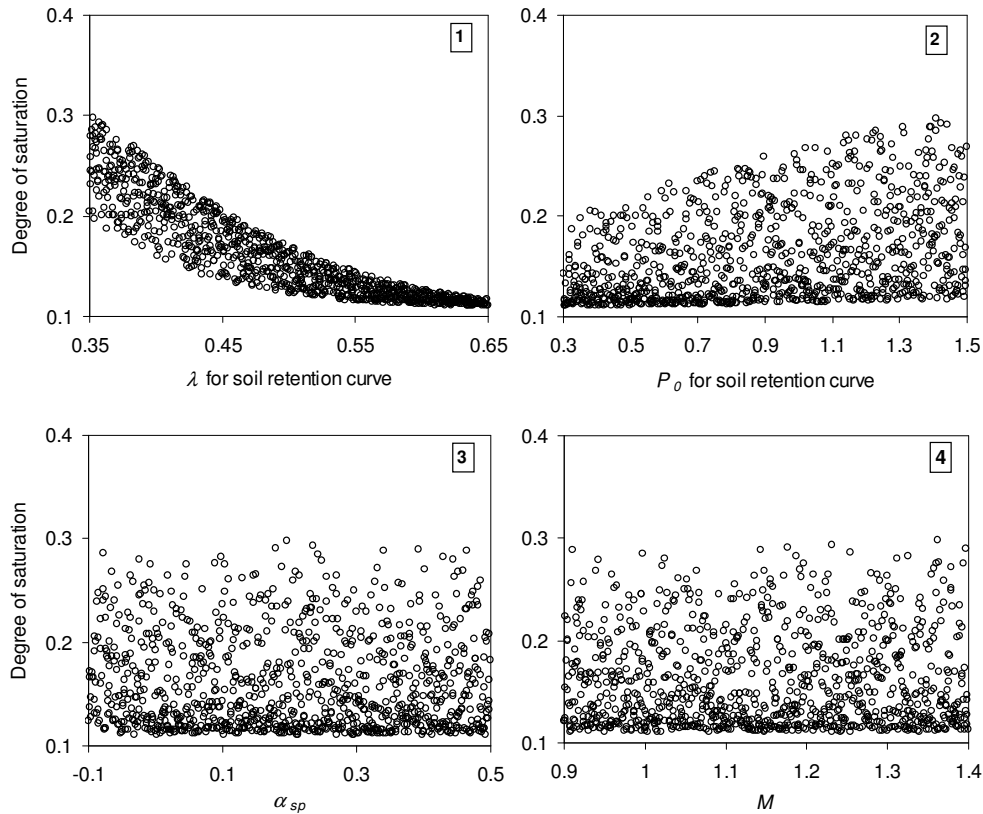
Figure 9.12: Sensitivity analysis using scatterplots: The degree of saturation considering the change in parameters in their feasible ranges.

state, when the swelling pressure reached the pre-consolidation pressure. The total sum of sensitivity indices is equal to one ($\sum S_{Ti} = 1$) (Sobol', 1990). If sum of the first order indices is closer to one ($\sum S_i \rightarrow 1$), it can be said that the higher order of sensitivity does not play an important role in the global sensitivity analysis. Herein Fig. 9.13 the average sums of first order sensitivity indices are 0.905 and 0.821 for analysing liquid saturation and stress, respectively. It means that the first order sensitivity index can be a good indicator for ordering the sensitivity of the input parameters.

The results of sensitivity analysis using the RBD method for the THM test are presented in Fig. 9.15, 9.16, and 9.17. The results are presented for many time steps along two phases: the heating phase and the hydration phase. According to Fig. 9.15 the λ, P_0, and D parameters played an important role in the degree of saturation during the first phase. The role of λ decreased significantly in the second phase, in contrast to the α_{sp} parameter, whose role increased in terms of the development of liquid saturation.

For the development of the stress, the α_{sp} parameter played a insignificant role in the first phase; however, its effect becomes significantly higher as compared with the other

parameters Fig. 9.16. The parameters, α_{sp} and λ, were the important factors in the first phase; nevertheless their role decreased significantly in the second phase. Whereas parameters λ_{sat} and λ_{dry} played moderate role in the first phase, their roles increased significantly in the second phase Fig. 9.17. The GSA method was repeated three times for the HM test and two times for the THM test, and the sensitivity of parameters remained qualitatively stable when applying the test-retest method.

With the average sensitivity analysis indices over time are presented in Fig. 9.18 and Fig. 9.19. The column height in these figures presents the sum of the average of the sensitivity indices for different responses (e.g. liquid saturation, stress, and temperature). In general, factors α_{sp}, P_0, $\boldsymbol{k}_0$ and λ played an important role in the HM test simulation, and factors λ, P_0, n, α_{sp}, and $\boldsymbol{k}_0$ played an important role in the THM test simulation.

Selecting the range of input parameters to analyse also plays an important role in the results of the GSA method. Analysing in wide range of values for the input factors may yield different results as compared to the results obtained for a narrow range for the input factors. The range of parameter variation should be feasible. For this study, the selected range of the input parameters is based on the prior information about sand-bentonite mixture. The range of the values for the input parameters is the same for both the GSA and the optimisation problem.

In summary, sensitivity analysis using RBD method allows the sensitivity of the model parameters to be estimated for their entire domain. It also indicates how to rank the input factors fast and automatically without having to analyse several different scatterplots. The method allows the user to estimate the model parameters for different periods of time. It is shown that the GSA is a robust method for conducting sensitivity analysis. However, the method is associated with relatively high high computation costs.

9.2.6.3 Local sensitivity versus global sensitivity analysis

The general advantages and disadvantages of the local and global sensitivity analyses are discussed in general in section (section 9.2.1). This part only concentrates on analysing sensitivity for numerical simulation of HM and THM tests.

For the HM test simulation, both LSA and GSA showed results that are time - dependent, and the sensitivity indices varied more substantially when considering the hydration phase of the simulations. After passing the hydration phase, the sensitivity indices showed more stable behaviour Fig. 9.8 and 9.14. The most sensitive parameters in both LSA and GSA were identified to be P_0, $\boldsymbol{k}_0$, and λ for the evolution of the degree of saturation. It indicates
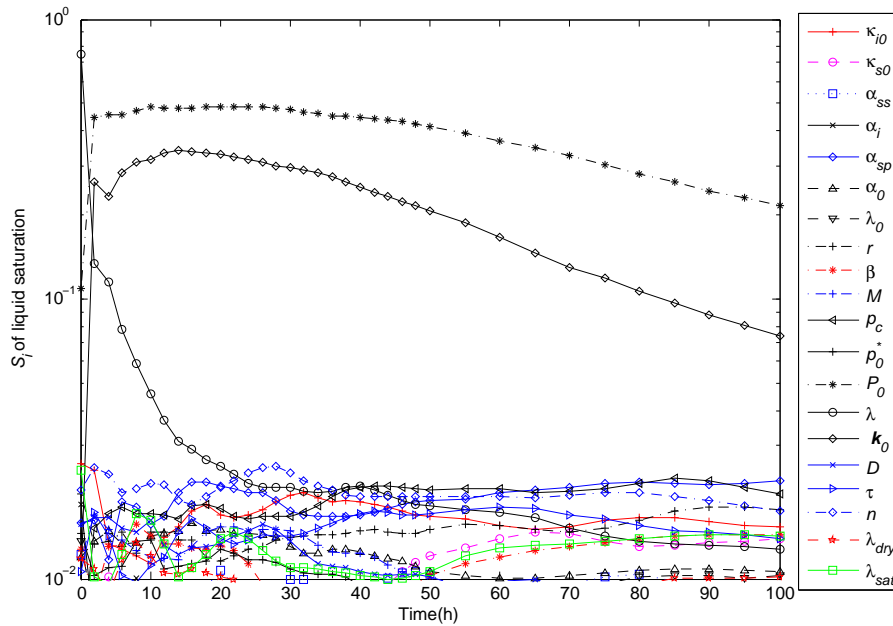
Figure 9.13: GSA (RBD) for liquid saturation using HM test simulation - time history.

that the relation between parameter and model output is a low curvature function in the parameters' domain. However, the most influent parameters for stress analysed by LSA were κ_{s0}, α_{ss}, P_0, $\boldsymbol{k}_0$, and λ, whereas by GSA were α_{sp}, $\boldsymbol{k}_0$, p_0^*, and κ_{s0} Fig. 9.14.

It should be noted that the pre-consolidation pressure p_0^* is a non-sensitive parameter according to LSA, but it is a sensitive parameter according to GSA. It can be interpreted as follow. p_0^* plays a role as activated parameters for the plastic equations. If p_0^* is larger than swelling pressure the soil behaves as elastic behaviour, and p_0^* does not play any role in the analysis. If p_0^* is smaller than swelling pressure the soil behaves as plastic behaviour, and p_0^* plays a role in the analysis. In our case, the norminal value analysed by LSA located in the elastic zone, therefore, p_0^* does not play a role according to the LSA. However, in GSA analysis, p_0^* varies in both elastic zone and plastic zone. Consequently, p_0^* is a sensitive parameter according to GSA.

For the numerical THM test simulations, the sensitivity of parameters depends on the types of boundary conditions in both the LSA and the GSA method (Fig. 9.9 and Fig. 9.15). While analysing liquid saturation by using LSA, parameters n and $\boldsymbol{k}_0$ played an important role in the first phase. Whereas by using GSA, parameters λ, P_0 played an important role in the first phase.

It can be seen from Eq. 8.21 and Eq. 8.25 that n and λ are parameters of non-linear functions in relation with temperature. It is an explanation that parameters n and λ were
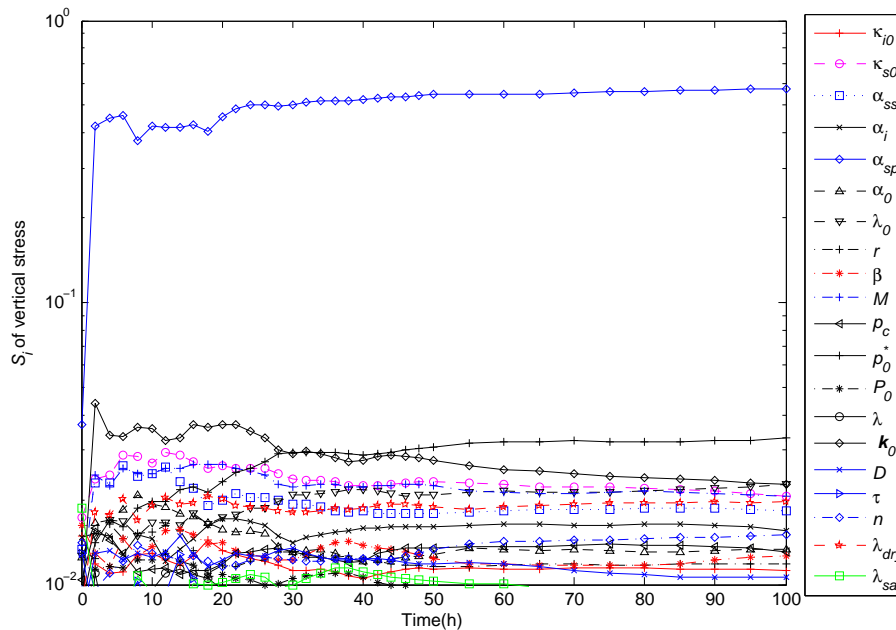
Figure 9.14: GSA (RBD) for vertical stress using HM test simulation - time history.

the most sensitive when using GSA to analyse the evolution of temperature (Fig. 9.17), while they did not play the most important role when using LSA to analyse this type of response.

In summary, the sensitivity analysis using LSA indicates the same value as GSA when the numerical model function is relatively linear with the input parameters. When function is highly non-linear, the results analysed by LSA differ from those by GSA.

9.3 Optimisation problem

9.3.1 Selection of optimisation algorithms

It has been known that all optimisation methods have their limitations. HEEDS (2008) may be a good guideline for selecting the optimisation method. According to HEEDS (2008), some optimisation methods work effectively only when it is possible to accurately compute solution gradients with respect to the variables. Some methods work only for continuous or discrete variables (but not both), or for a relatively small number of variables. And some methods require a relatively large number of design evaluations to be performed in order to find an optimal solution. In order to choose the best method for the given problem, one must first understand the type of design space that is being searched.
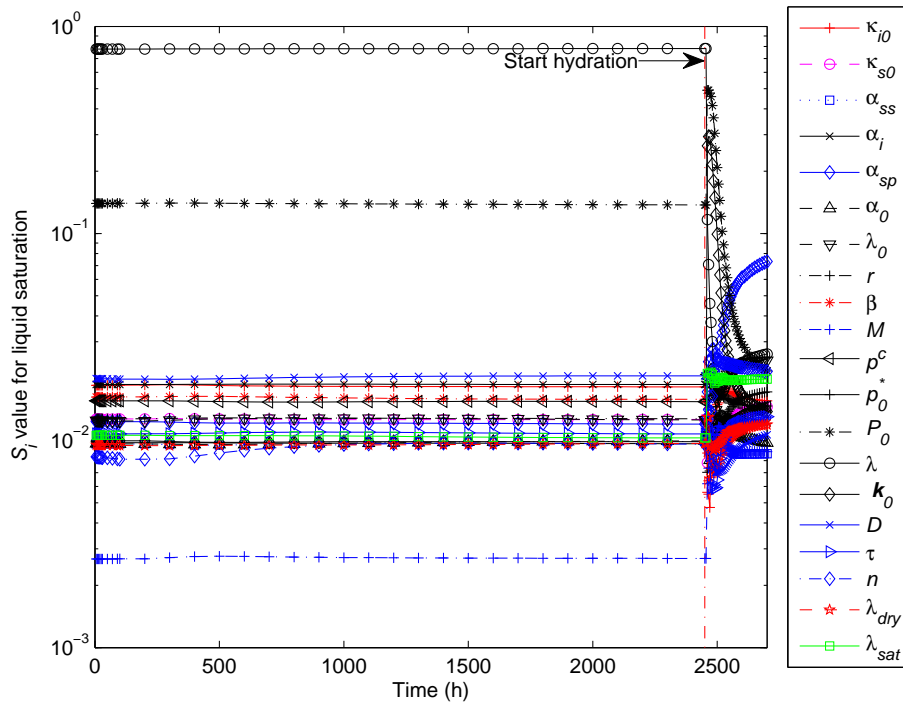
Figure 9.15: GSA (RBD) for liquid saturation using THM test simulation - time history.

A design space can be characterised primarily in terms of its smoothness (e.g., smooth, rugged, or discontinuous) and modality (e.g., unimodal or multimodal). In a smooth design space, it is possible to calculate design sensitivity gradients. Solution gradients cannot be computed directly in rugged or discontinuous design spaces. In a multimodal design space the design landscape may have many peaks and valleys for instance in THM simulations they include the degree of saturation, stress, and temperature. However, a unimodal design space has only one minimum and maximum. Other characteristics of a design space may also play a role in the effectiveness of the given search algorithm, such as the functional order of the solution and the interactions among the design variables.

As introduced in section 3.3, one way to overcome the limitations of optimisation method is a hybrid or combined method for the optimisation algorithm. For instance, the algorithm GODLIKE (Oldenhuis and Vandekerckhove, 2009) was designed which attempts to generalise and to improve the robustness of the four metaheuristic optimisation algorithms such as: genetic algorithms, particle swarm optimisation, differential evolution and adaptive simulated annealing. Next the algorithm can generalise the optimisation process to solve both single-objective and multi-objective optimisation problems.

In general the optimisation methods can be classified in the following groups as in section 3.3.2: sampling-based stochastic methods, gradient-based methods, direct search
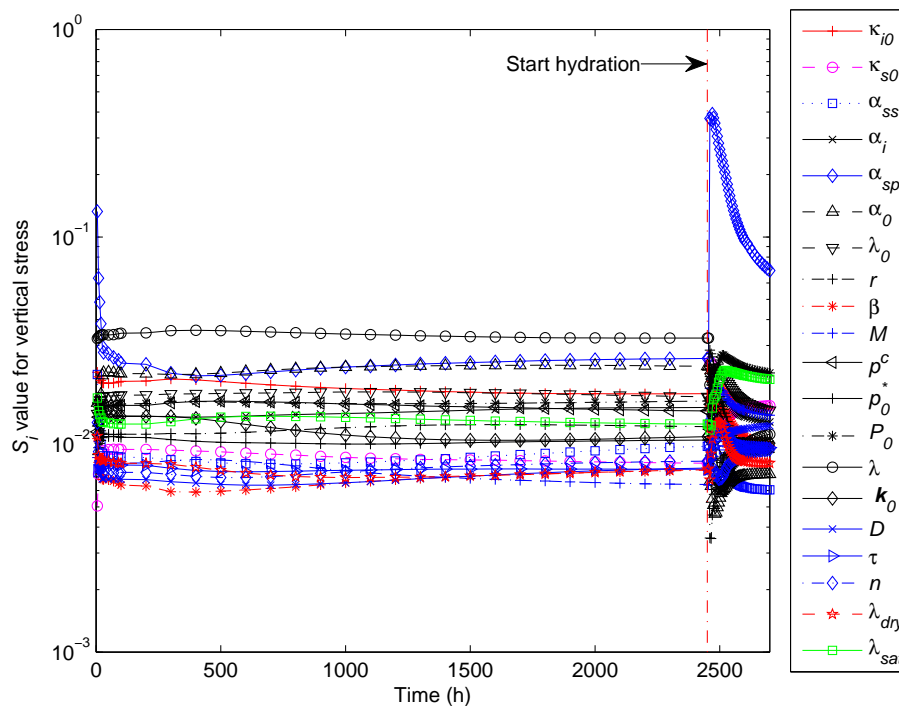
Figure 9.16: GSA (RBD) for vertical stress using THM test simulation - time history.

(or derivation free) methods and population-based methods. Among these groups, a population-based method provides a more global and intelligent search; however, it is relatively expensive. It is suitable for non-linear models. Therefore, the PSO (Kennedy and Eberhart, 1995) is selected as an optimisation method which considers the non-linearity of the numerical THM test simulation and the independence from the initial method estimates.

Particle swarm optimisation was initially introduced by Kennedy, Eberhart and Shi (Kennedy and Eberhart, 1995; Shi and Eberhart, 1998) and was first intended to simulate social behaviour, as a stylised representation of the movement of organisms in a flock of birds or a school of fish. The algorithm was simplified, and it was adapted to perform optimisation.

A basic variant of the PSO algorithm works by having a population (called a swarm) of candidate solutions (called particles). These particles are moved around in the search space according to several simple formulas. The movements of the particles are guided by their own best known position in the search space as well as the entire swarm's best known position. When improved positions are discovered, they will guide the movements of the swarm. The process is repeated and by doing so, it is hoped that a satisfactory solution will eventually be discovered, but this is not guaranteed.
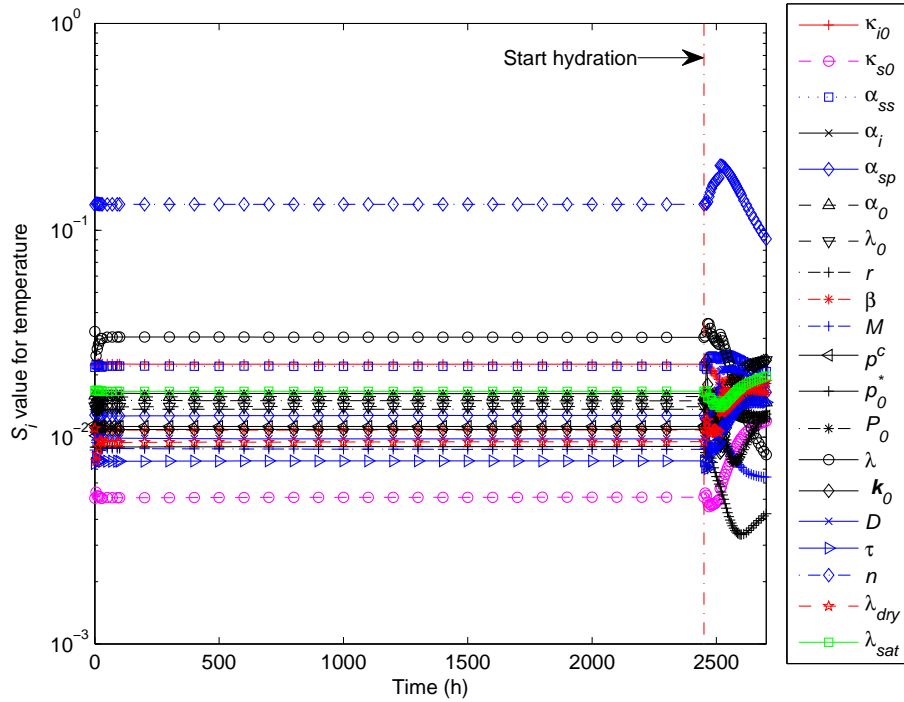
Figure 9.17: GSA (RBD) for temperature using THM test simulation - time history.

The algorithm is presented basically as follows:

- Considering function g: $\mathbb{X} \to \mathbb{Y}$ is an objective function which must be minimised.

- To define n is the size of the swarm, the initial position of input factor $x_i \in \mathbb{X}$ and a velocity $v_i \in \mathbb{X}$ with $i = 1, 2, ..., n$.

- The velocity is calculated as:

$$v_i(k + 1) = \Phi(k)v_i(k) + c_1 r_1(p_k^i - x_i(k)) + c_2 r_2(p_k^g - x_i(k)) \qquad (9.21)$$

and the position of particle is:

$$x_i(k + 1) = x_i(k) + v_i(k + 1) \qquad (9.22)$$

where p_k^i is called the actual best position of an individual particle, p_k^g is the best position of all particles in the swarm, c_1 and c_2 are considered cognitive and social parameters, r_1 and r_2 are random numbers between 0 and 1, Φ is the inertia function, i is the particle index and i is the discrete time index.

For implementing the PSO in the code, the algorithm contains the following steps.

1. Initialise:

    a) Set constants k_{max}, c_1, c_2
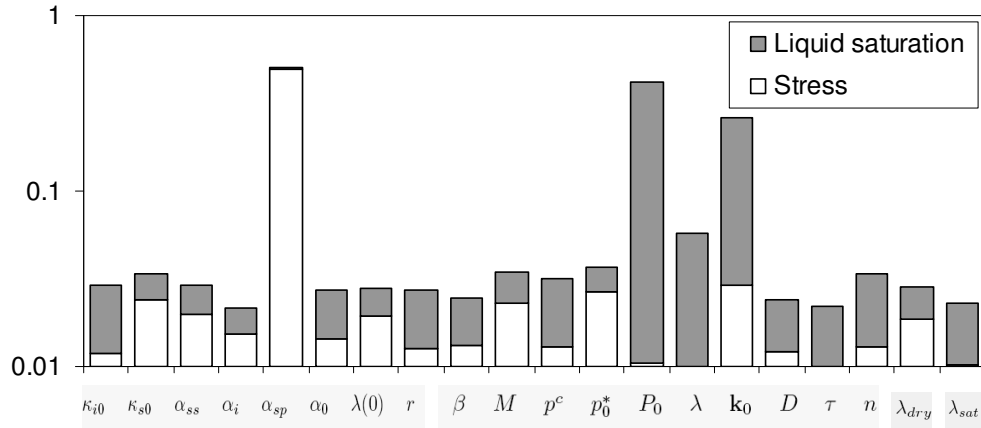
Figure 9.18: HM test: Average of sensitivity indices S_i over time.
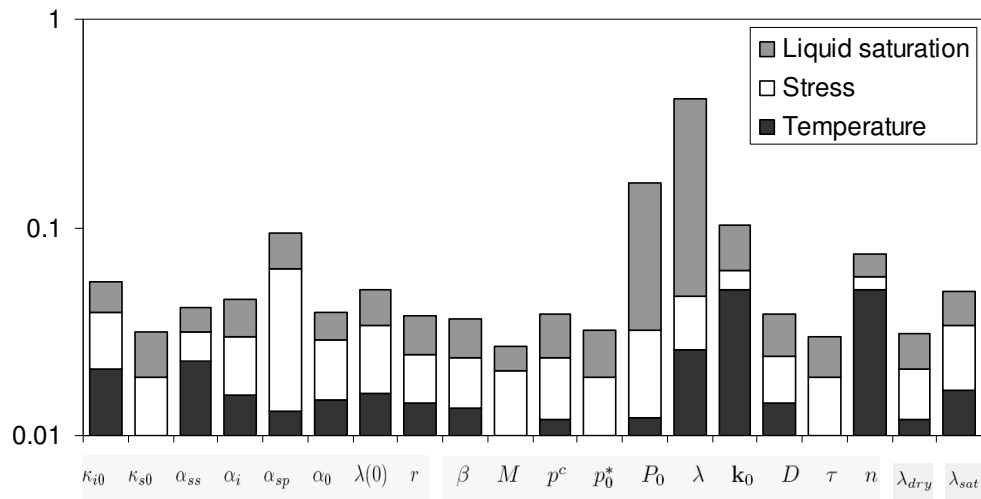
Figure 9.19: THM test: Average of sensitivity indices S_i over time.

  b) Random initialise particle position $\boldsymbol{x}_0^i \in D[\boldsymbol{x}^{min}, \boldsymbol{x}^{max}]$ for $i = 1, 2, ..., n$

  c) Random initialise particle velocities $0 \leq v_0^i \leq v_0^{max}$ for $i = 1, 2, ..., n$

  d) Set $k = 1$

2. Optimise:

  a) Evaluate function value g_k^i using design space coordinates x_k^i.

  b) If $g_k^i \leq g_{best}^i$ then $g_{best}^i = g_k^i$, $p_k^i = x_k^i$

  c) If $g_k^i \leq g_{best}^g$ then $g_{best}^g = g_k^i$, $p_k^g = x_k^i$

  d) If stop criteria is satisfied then go to 3.

  e) Update all particle velocities v_k^i for $i = 1, 2, ..., n$

    f) Update all particle positions x_k^i for $i = 1, 2, ..., n$

    g) $k = k + 1$.

    h) Go to 2(a).

3. Terminate the program: solution $G = g_{best}^g$

The algorithm for particle swarm optimisation is implemented in VARO^{2}PT (Zimmerer, 2010). The objective function can be created by combining a serial- and multi-measurement procedure.

9.3.2 Defining the objective function

As introduced in section 3.3, the objective function must be defined in order to conduct optimisation. The objective function G is a "norm" of the difference between measured data and numerical simulation output. If $y_k^{tm,meas}$ is a value observed from a experiment and $y_k^{tm,calc}$ is a value obtained by numerical calculation with a vector of model parameters $\boldsymbol{x} = \{x_1, x_2, ..., x_I\}$, the difference between a point of measured data and numerical simulation data is defined by

$$g_k^{tm}(\boldsymbol{x}) = y_k^{tm,meas} - y_k^{tm,calc}(\boldsymbol{x}) \tag{9.23}$$

The main objective function can be defined as a mean of quadratic difference as follows:

$$G_{MQ}(\boldsymbol{x}) = \frac{1}{M \times T} \sum_{t=1}^{T} \sum_{m=1}^{M} (g_k^{tm})^2(\boldsymbol{x}) \omega_k^{tm} \tag{9.24}$$

where a number $t = 1, 2, ..., T$ is a number of measured data according to time, a number $m = 1, 2, ..., M$ is selected points for observation, ω_k^{tm} is a weighting factor for each measurement. The value of ω_k^{tm} depends on the importance of the measured points and the reliability of the measured points as well as calculation points. In the case of multi-dimensional output, the data need to be normalised. The normalisation of the quadratic function $(g_k^{tm})^2$ with the quadratic value mean of the measurements is $\frac{1}{M \times T} \sum_{t=1}^{T} \sum_{m=1}^{M} (y_k^{tm,meas})^2$. Therefore the objective function is expressed as:

$$G_k^{MAE}(\boldsymbol{x}) = \sqrt{\frac{\sum_{t=1}^{T} \sum_{m=1}^{M} (g_k^{tm})^2(\boldsymbol{x})}{\sum_{t=1}^{T} \sum_{m=1}^{M} (y_k^{tm,meas})^2} \omega_k^{tm}} \tag{9.25}$$

The consideration of multi-measurement, such as multi-measured locations and serial measurements, leads to flowing equations:

$$G_{total}(\boldsymbol{x}) = \frac{1}{K} \sum_{k=1}^{K} G_k^{MAE}(\boldsymbol{x}) \omega_k \tag{9.26}$$

where ω_k is a weighting factor for each serial measurement and ω_k allows the influence between different serial measurements to be regulated. The value of weighting factors is given in the next sections. In this study, the objective functions are generated for the optimisations of the numerical HM test and THM test simulations. They are created based on Eq. 9.25 and Eq. 9.26 in this section.

Objective functions for HM test optimisation:
The measurements used for objective functions are: the degree of saturation (measured at TDR 1, TDR 2, and TDR 3 position), suction (measured at RH 1, RH 2, and RH 3 position) and the vertical pressure (measured on the top load cell). The weighting factor is also applied to generate the objective function. As discussed in previous section the measurement of liquid saturation using the TDR method is more robust than measuring RH humidity. Therefore all the values of liquid saturation ω_k receive a value of 1.5, the ω_k values for suction and vertical stress receive a value of 1.0. The values of water content and suction at the beginning and at the end of a test are measured directly by the oven method and the chilled mirror method. The two measurement methods have high reliability; therefore the initial weighting factors and those at the end of the test are higher than the other points. The ω_{tm} for three measurement points of liquid saturation and suction at the beginning and at the end of the test receive a value of 5.0. The weighting factors (ω_{tm}) of the other measurement points all receive a value of 1.0.

Objective functions for THM test optimisation:
In this optimisation, the objective function is generated based on the measurements as defined in the HM test and additional values of temperature (measured at the top, middle, and bottom). The weighting factors ω_k of the suction measurements receive a value of 0.5, the ω_k of the other types of measurement receive a value of 1.0. The value ω_{tm} for of three measurement points of liquid saturation and suction at the beginning and end of the test receive a value of 5.0. The weighting factors of the other measurement points receive a value of 1.0.

9.3.3 Validation of the optimisation tool convergence

The Particle Swarm Optimisation tool is effective in minimising the objective function. The PSO proved its good performance when applied to define the convergence of the objective function in terms of analytical expressions mathematical models. However, for mathematical models defined via PDE, whose solution depends on the particular boundary value problem, validating the optimisation tool against the particular boundary conditions
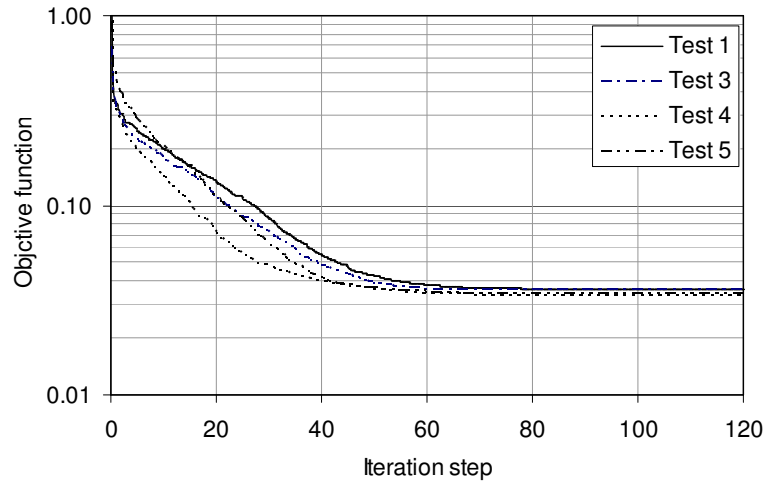
Figure 9.20: Performance of the objective function with advancing the iteration steps.

must be done. Four optimisation tests of the hydration test have been simulated for statistical assessment. The value of the objective function decreases quickly from the first iteration to the 60th PSO iteration. There is a saturation in the change of the objective function value after the 60th iteration step and it became almost constant after 80th iterations. Fig. 9.20. It is confirmed that the solution of the optimisation problem is likely to converge in up to 120 iterations. That is why we selected 120 iterations in the PSO as a stop criterion for the particle population of 10 individuals.

9.4 Confidence interval of the optimised parameters

9.4.1 Methodology

While validating the convergence of the optimisation method, several optimisation tests were performed for the same objective function with the same iteration steps. The algorithm used for optimisation is the PSO method. The initial parameter values of the swarm were randomly selected in the search space for one optimisation test. Different optimisation tests were performed, and different sets of parameters were obtained. Some of the obtained parameters vary widely across the different tests, even g_{best}^g converges to identical values. It may be due to non-unique solutions, and it is supposed that the boundary value problem is non-sensitive for several parameters; therefore they can wander in their space without affecting a change in the objective function. The distribution of parameters needs to be quantified and estimated to determine the reliability of the obtained

parameters. In this section, an innovative approach is proposed to identify parameters for the coupled THM numerical analysis based on the stochastic method. Each HM test and THM test optimisation is repeated 12 times, called multi-replication testing technique. The confidence interval is calculated based on the sets of the parameters obtained by the optimisations.

In order to compare the variation in the parameters, the parameter x_i is normalised from $0 - 1$. The normalised value is x_i^{norm} is

$$x_i^{norm} = \frac{x_i - x_i^{min}}{x_i^{max} - x_i^{min}} \tag{9.27}$$

where x_i^{min} and x_i^{max} are the lower and upper boundaries of the x_i. Assuming that the estimated parameters varies in their domain and the number of the samples is sufficiently large, normal distribution is used to estimate the parameter distribution. Considering normal distribution, a standard deviation value is calculated as Eq. 9.28.

$$\sigma_i^{sd} = \sqrt{\frac{1}{N_p - 1} \sum_{n_p=1}^{N_p} (x_{i,n_p}^{norm} - \mu_i^{norm})^2} \tag{9.28}$$

where μ_i^{norm} is the arithmetic mean value of normalised parameters, n_p is the label of the samples $(n_p = 1, 2, ..., N_p)$. Considering x_i^{norm} is the continuous value, the PDF function is written as follows.

$$f(x_i^{norm}) = \frac{1}{\sigma_i^{sd}\sqrt{2\pi}} \exp\left[-\frac{(x_i^{norm} - \mu_i^{norm})^2}{2(\sigma_i^{sd})^2}\right] \tag{9.29}$$

The PDF function of Student's t-distribution is expressed as:

$$f(x_i^{norm}) = \frac{\Gamma\left(\frac{\nu+1}{2}\right)}{\sqrt{\nu\pi}\,\Gamma\left(\frac{\nu}{2}\right)} \left[1 + \frac{(x_i^{norm})^2}{\nu}\right]^{-\frac{\nu+1}{2}} \tag{9.30}$$

where $\nu = N_p - 1$ is the degree of freedom, N_p is a sample size $(N_p = 24)$, and Γ is the gamma function.

When considering the distribution to be normal distribution, the 68-95-99.7 rule can be used to estimate the confidence interval. The confidence interval can be selected as $\mu_i - 2s_i \leq x_i \leq \mu_i + 2s_i$ as it is illustrated in the Fig. 9.21(a) (Montgomery and Runger, 2002) where s_i is the standard deviation of parameter values.

When a number of sampling values is small, the Student's t-distribution is recommended to be used to estimate confidence intervals (Papoulis, 1991; Hill, 1998). When the number
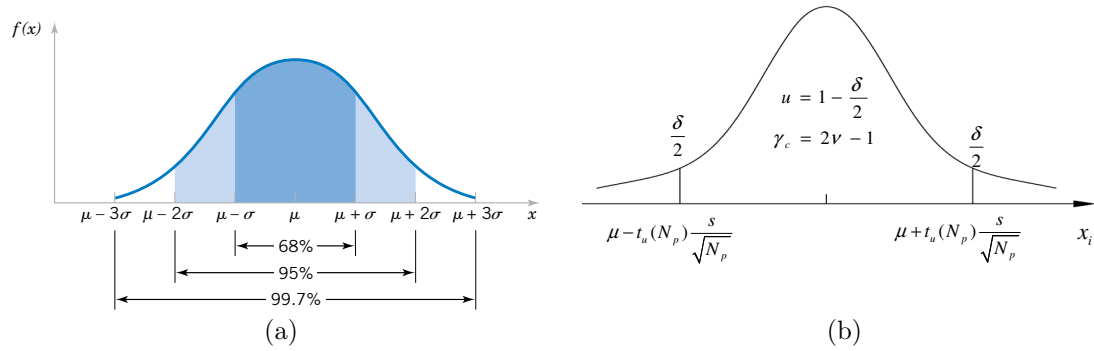
Figure 9.21: Confidence intervals: (a) empirical rule for normal distribution, (b) Student's
t-distribution, Papoulis (1991).

of samples is smaller than 30, assuming an unbiased estimate of s_i, the confident interval
is estimated by:

$$\mu_i - t_u(N_p)\frac{s_i}{\sqrt{N_p}} \leq x_i \leq \mu_i + t_u(N_p)\frac{s_i}{\sqrt{N_p}} \tag{9.31}$$

where μ_i is the mean value of parameter, $t_u(N_p)$ is Student's t-distribution percentile
dependent on a percentile of x_i and N_p, $t_u(N_p)$ is listed in Table 9-2 of Papoulis (1991).
The confidence interval with Student's t-distribution is presented in Fig.9.21(b), where γ_c
is the confidence coefficient, δ is the confidence level.

9.4.2 Results and discussion

An input factor is estimated based on 24 samples obtained from 24 optimisation tests.
The frequency observation of each parameter is presented in a histogram (Fig. 9.23).
The parameters are normalised in the range of $0 - 1$ in their intervals as formulated in
Eq. 9.27. It is clear that highly sensitive parameters have their frequency of appearance
in a small range of values (i.e. P_0, λ, $\boldsymbol{k}_0$). Less sensitive parameters have their frequency
of appearance in a larger range of values (i.e. λ_{sat}, D, n), and the other non-sensitive
parameters have their frequency of appearance in all of their intervals.

Fig. 9.23 also shows that the sensitive parameter has its distribution close to the shape of
normal distribution (i.e. P_0, λ, $\boldsymbol{k}_0$, λ_{sat}, D, n). Therefore the confidence intervals of these
parameters may be considered reliable. The other non-sensitive parameters demonstrate
unclear distribution. Therefore, the confidence interval concept of these parameters can
not be applied to those parameters whose distribution deviates from the normal distribu-
tion. Figure 9.23 shows that the parameters related to plastic behaviour such as ($\lambda(0)$, β,

Table 9.5: Confidence intervals of the optimised parameters

	P_0	λ	$\mathbf{k}_0$	λ_{sat}	D	n
Mean	1.51	0.339	2.03E-16	1.33	3.35E-08	0.79
CI_L	1.45	0.328	1.55E-16	1.28	2.75E-08	0.73
CI_U	1.58	0.349	2.50E-16	1.38	3.95E-08	0.86

r) do not show to be densely distributed around one particular value. Although the elastic parameter (e.g. κ_{s0}) falls more densely around one value, the shape of their probability distribution as far from the normal one. It is expected that if the search interval range is larger on the left-hand side, the histogram of κ_{s0} appears closer to normal distribution.

The Student's t-distribution is suitable to estimate the confidence interval, because the input factor values are less than 30. The probability density function (PDF) shown in the Student's t-distribution of the parameters is presented in Fig. 9.22. Comparing the PDF graph with parameter sensitivity indicates that the more highly sensitive the parameter is, the more densely distributed the parameter is around the mean value. The parameters k_o, λ, and P_0 in the retention curve are the most influential in the hydration test simulation; the density distribution shows higher probability to the arithmetic mean values.

The confidence intervals are estimated considering typical confidence coefficients ($\gamma_c = 0.95$), which means that x_i locates in this interval with probability 0.95. Table 9.5 presents the mean value, the upper confidence bound (CI_U) and the lower confidence bound (CI_L) calculated as Eq. 9.31. The result in Fig. 9.22 shows that in general the parameters, which are highly sensitive (e.g. $\mathbf{k}_0$, λ, P_0), have a higher probability. In contrast, the low sensitivity parameters (e.g. λ_{sat}, D, n) have lower probability.

Based on the above presented analysis it can be suggested that the following issues should be considered when identifying soil model parameters via back analysis:

- The general THM analysis contains a large set of input parameters because of considering many physical processes which possibly occur in the unsaturated media under mechanical, hydraulic and thermal loads. The model sensitivity with respect to a given model parameter depends on the boundary conditions and the extent of the influence of the physical process whose mathematical description includes this parameter. Therefore, the boundary value problems must be strongly coupled with the targeted parameters for identifying. For instance, one cannot determine thermal parameters based on isothermal boundary value problems.
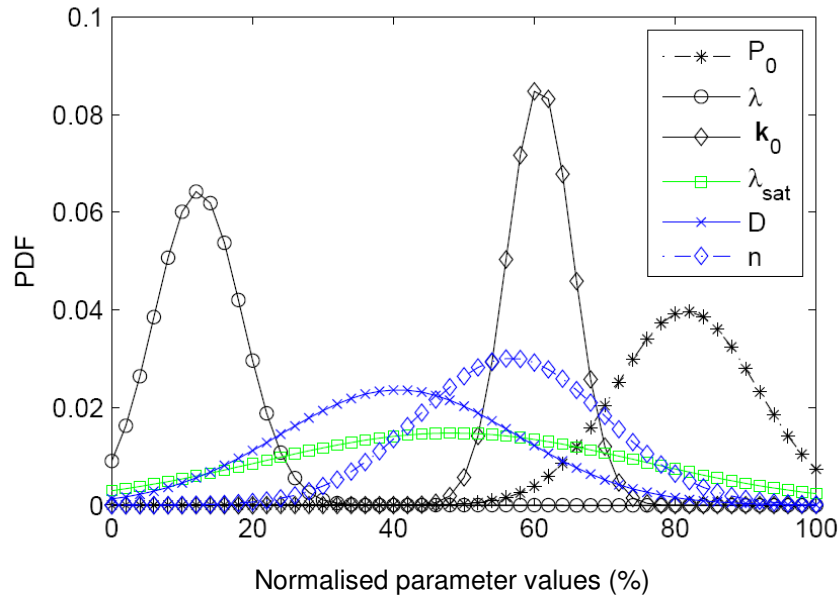
Figure 9.22: Probability density function of the selected parameters

- The parameter sensitivity determines the confidence in the parameters obtained by the optimisation method. However, ranking the general sensitivity of a parameter should be carried out with the awareness that parameter influences differently on the different types of the response in multi-response models.

- With current approach, there are two methods to improve possibly the reliability of the identified parameters. The first method, a nowadays popular method, is to increase a number of the laboratory tests with different boundary conditions. The second method, as discussed in this thesis, is to increase the number of optimization sampling. However, it is not guaranteed the latter method can improve significantly the solution due to uncertainties in some measured data and in the imposed boundary conditions.

- The proposed back analysis approach may be considered expensive because it requires large number of optimization tests to construct the parameter distributions.

9.5 Assessing the goodness of fit

Based on the confidence interval analysis, the mean values for optimised parameters was used as identified parameters for numerical simulation of the HM test and THM test. The quality of the model parameters were assessed via the goodness of fit between the

experimental measurement data and the output data from the numerical simulation. Two methods were adopted to assess the goodness of fit: graphical analysis and residual analysis.

The graphical analysis can present the differences between output simulated values and measured values. Graphical analysis demonstrates where these differences come from in great detail as well as which physical phenomenon induces the differences and whether the differences come from the measurement uncertainties or a shortcoming of the model. From this analysis, a new or modified model can be proposed to improve the performance numerical simulations of particular materials and boundary value problems. Moreover, one may also find the uncertainty of the measured data or measurement method in order to find the solution and alleviate the experimental uncertainty.

In order to assess the quality of the identified parameters qualitatively, one must bring an assessment index into comparison. The graphical analysis has a disadvantage on its scale dependence and its color effect. Residual analysis is proposed to provide a good comparison based on the coefficients and figures to compensate for these disadvantages.

9.5.1 Graphical method

In this part, the numerical simulation data and measurement data are plotted in the same graphs to visualise the difference between two types of data. The graphs are divided into two groups: the data fitted before back analysis and data fitted after the back analysis process. These groups show that the back analysis process has allowed the model output to fit better with measured data in general.

In total seven curves need to be fitted in the optimisation of the HM test including the degree of saturation versus time (3 curves), the top measured load cell (1 curve) and suction versus time (3 curves). Fig. 9.24 presents the results of numerical simulation before and after optimisation of the HM test simulation. The obtained results of simulation correspond to observations during experiment. In Fig. 9.24(b) after optimisation, while the numerical simulation at the bottom (TDR 3) has a good agreement with the measurement, the numerical simulation at the top has a difference at the time when the degree of saturation started increasing. The numerical simulation of the swelling pressure fits quite well with the experimental results. However, the development of suction in numerical simulation results does not fit with the experimental results. It is also noted that when the degree of saturation in measured, three TDRs are saturated, and there is uncertainty

in measured water content. The uncertainty of the measured results is discussed in detail in experiment section.

In the process of optimisation for the THM test, 10 curves are used to perform optimisation including suction versus time (3 curves), the degree of saturation versus time (3 curves), temperature versus time (3 curves), and the top measured load cell (one curve). Fig. 9.25 presents the results of numerical simulation before and after optimisation of the THM test simulation. The obtained results of simulation correspond to the places of observation in experiment. Fig. 9.25(b) shows a good agreement between numerical simulation results and measured results. Fig. 9.25(d) shows a good agreement between numerical simulation results and measured results in the second phase, but in the first phase the result do not fit. It is supposed that the measurement of the small swelling pressure of the load cell has low accuracy.

The temperature between numerical simulation and experimental results fits relatively well. When the soil was heated from the bottom, the temperature increased rapidly to the maximum; afterwards it reduced slightly to the steady state because of the decrease of thermal conductivity (λ) with the degree of saturation. When water was supplied, the temperature decreased at the beginning then increased to the steady state. The interpretation of this phenomenon is presented the experimental section. The reduction in temperature at the beginning of the second phase was reproduced numerically by the balance equation of energy with phase properties and specific heat parameters.

Fig. 9.25(e) and Fig. 9.25(f) visualise the evolution of suction versus time. The agreement is quite good for the high suction measured at the bottom (RH 3); however, the disagreement in suction value can be seen at a low suction measured values and simulated values.

9.5.2 Method of residuals

The quantile-quantile (Q-Q) plots of measurement normalised data against normalised prediction data are used to assess the goodness of fit. The normalization of the data is performed as follows:

$$y_k^{tm,norm} = \frac{y_k^{tm}}{[\max(y^t)]_k^m} \tag{9.32}$$

where y_k^{tm} is a model response k or measurement data at observation point m and time t, $[\max(y^t)]_k^m$ is the maximum value of y_k at observation point m. The coefficient of

determination is calculated as follows.

$$SS_k^{tot} = \sum_{tm} (y_k^{tm} - \bar{y}_k)^2 \tag{9.33}$$

$$SS_k^{err} = \sum_{tm} (y_k^{tm,meas} - y_k^{tm,cal})^2 \tag{9.34}$$

$$R_k^2 = 1 - \frac{SS_k^{err}}{SS_k^{tot}} \tag{9.35}$$

where R_k^2 is the coefficient of determination, SS_k^{err} is the sum of the squared residuals, SS_k^{tot} is the total sum of squares, y_k^{tm} is the measured data ($meas$) or output of numerical calculation (cal) data at time (t) and measurement point (m), $\bar{y}_k$ is mean value of y_k^{tm}.

To analyse the HM test, the Q-Q plots for measurement normalised data against simulation normalised data are presented in Fig. 9.26. The figure illustrates three types of data which were considered in the optimisation: the evolution of the degree of saturation, the evolution of vertical stress measured at the top of the THM column, and the evolution of suction. Good agreement can be seen from Fig. 9.26(a) between numerical simulation and measurements at the location of TDR 1. Good agreement occurs at low water content and high water content; however, the agreement worsen with the increase of the water content. The numerical simulation of stress development posseses quite good agreement with the measured values (Fig. 9.26(b)). The agreement measured via the coefficient of determination R^2 is high for these types of observation. However, the agreement between measured values and simulated values is low for the evolution of suction (Fig. 9.26(c)). The R^2 value is quite high because there are many points at the initial state and the saturated state where measured values and simulated values are equal.

In general, the coupled THM analysis can predict the development of the degree of saturation and the development of vertical stress derived from HM test in the isothermal condition quite well. But the analysis shows that the suction values obtained from simulation do not fit the measurement values. This result may be a deficiency of the mathematical model or due to uncertainty in the suction measurements method, which will be discussed in the next section.

To analyse the THM test, the Q-Q plots for normalised measurement data against simulation data are presented in Fig. 9.27. The figure illustrates for four types of data which were considered in the optimisation: the evolution of degree of saturation, the evolution of vertical stress measured at the top of the THM column, the evolution of suction and the evolution of temperature. There is a high agreement between the measured value and simulated value at the low degree and high degree of saturation but a lower agreement during an increase in the degree of saturation (Fig. 9.27(a)). It can be seen from

Fig. 9.27(a) that there is a good agreement between measured values and simulated values of the degree of saturation at locations of the TDR 3.

The simulated values and measured values do not highly fit in the development of vertical stress with a low R^2 value (Fig. 9.27(b)). There is good agreement between measured values of suction and calculated values of suction at the RH 3 location where the variation of suction is high during the THM test (Fig. 9.27(c)). However, the agreement is not good at the RH 1 and RH 2 locations where the measured suction values are low. For temperature development, Fig. 9.27(c) illustrates the agreement between measured values and simulated values of suction.

In general, the coupled THM analysis can predict the following quite well: the development of the degree of saturation, the development of temperature, and the development of suction at RH 3 derived from the THM test in non-isothermal conditions. But analysis shows that the suction values at RH 1 and RH 2 obtained from simulations do not fit the measurement values. Moreover, the prediction of stress development in numerical simulations do not fit the measurements well.

9.5.3 Discussion and outlook

Regarding the development of degree of saturation in the THM column as illustrated in Fig. 9.25(f), the curve shape between numerical simulation and measurement at location TDR 1 and TDR 2 does not fit well during the increase in the degree of saturation. It may derive from using Darcy's law for the low permeability material. The hydraulic conductivity of the buffer materials (e.g. bentonite, the sand-bentonite mixture) have been investigated in the research of Pusch (1980a); Pusch et al. (2011). Determining the hydraulic conductivity of swelling clays is, in fact, far from straightforward Pusch et al. (2011) because of the following reasons:

- *Gas bubbles* can affect the infiltration; thus bubbles occupy wider voids and channels resulting in the hindrance of the through-flow of water.

- Water can migrate by *diffusion*, provided that there is a driving force, which can be a gradient in hydration potential, as manifested by differences in water content on the microstructural scale.

- The stability of *micro-structure* through erosion and particle transport.

- Generation of *electrical potentials* will tend to counteract flow by penetrating water and yield too low a hydraulic conductivity.

Cui et al. (2008) discussed that the Darcy's law is commonly used in coarse-grained natural soils, but it should be used with care for low-permeability clay when the large pores are clogged by a small clay particles. The non-linearity of hydraulic conductivity was interpreted as follows: the activation energy of pore liquid is much higher in fine-grained soils than in coarse-grained soils.

Modifying Darcy's law is recommended to determine hydraulic permeability for swelling clay. The relative permeability equation may be modified to better reproduce the penetration of water into clayey soil. Other methods to determine hydraulic permeability can be found in Fredlund et al. (1994a).

From residual analysis for variation of suction in both HM tests and THM tests, the suction simulated values on the bottom did not fit the measured value well, except for the suction values observed at location RH 3 in the THM test. It is also noted that RH 3 in the THM test measured very high suction value (Fig. 9.25f). At low suction value, the RH-sensors measured values did not fit the simulated value. It confirms another time that the relative humidity sensors measure high suction values more effectively than low suction value.

The other uncertainty in the measurement may stem from the measurement conditions, namely the hysteresis in suction measurements via relative humidity device: one can see in Fig. 9.24(b) and Fig. 9.24(f) the whole soil sample reached a saturated state at 60 hours, but the suction remained 5 MPa to 10 MPa. The value is too high as compared with air entry value of the sand-bentonite mixture (0.8-1.5 MPa). The hysteresis in the relative permeability measurement can be explained by the following: (1) the water flow in the center was higher than water at the side (Arifin, 2008), (2) water chamber area was large and (3) the water vapor required more time to fill the chamber in order to attain equilibrium relative humidity in the chamber and in the soil sample. If the flow of water was slow, there would have sufficient time to obtain vapour equilibrium between the chamber and the soil sample.

There is also another assumption that the model itself is not appropriate to reproduce the relation between the degree of saturation and suction. The van Genuchten model did not fit data for sand-bentonite mixture well in the transient vapour transfer conditions. There has been a plethora of research on the efficiency of the van Genuchten model in regard to its application for active clay soil. The results may be improved by using the SWR model proposed by Fredlund and Xing (1994) for clayey soil, considering pore-size distribution with the correction factor $C(s)$.

For the THM test, when the soil was heated from the bottom, the temperature increased rapidly to the maximum, after which it decreased slightly to a steady state because of the decrease in thermal conductivity (λ) with the degree of saturation. When water was supplied, the temperature decreased at very beginning and then increased to the steady state. The interpretation of this phenomenon is presented in the experimental section. The reduction in temperature was to guarantee the thermal equilibrium when cold water was supplied into the column. The decrease in temperature was later compensated by the heater. All of these phenomena are taken into account in the mathematical simulation. The reduction in temperature at the beginning of the second phase was reproduced by the balance equation of energy (Eq. 8.3), with phase properties and the specific heat parameter. The temperature measured after the hydration phase was higher in the heating phase when it was in the steady state. Therefore, thermal conductivity in a saturated state (λ_{sat}) is higher than in a dry state (λ_{dry}).

In summary, the advantage and disadvantage of the model as well as the uncertainty of measurements are discussed in this subsection. Back analysis enables the accuracy of the numerical models as well as the measurement methods to be demonstrated. Consequently, the new or modified methods may be proposed to improve the performance of the experiments and numerical simulation in the future.
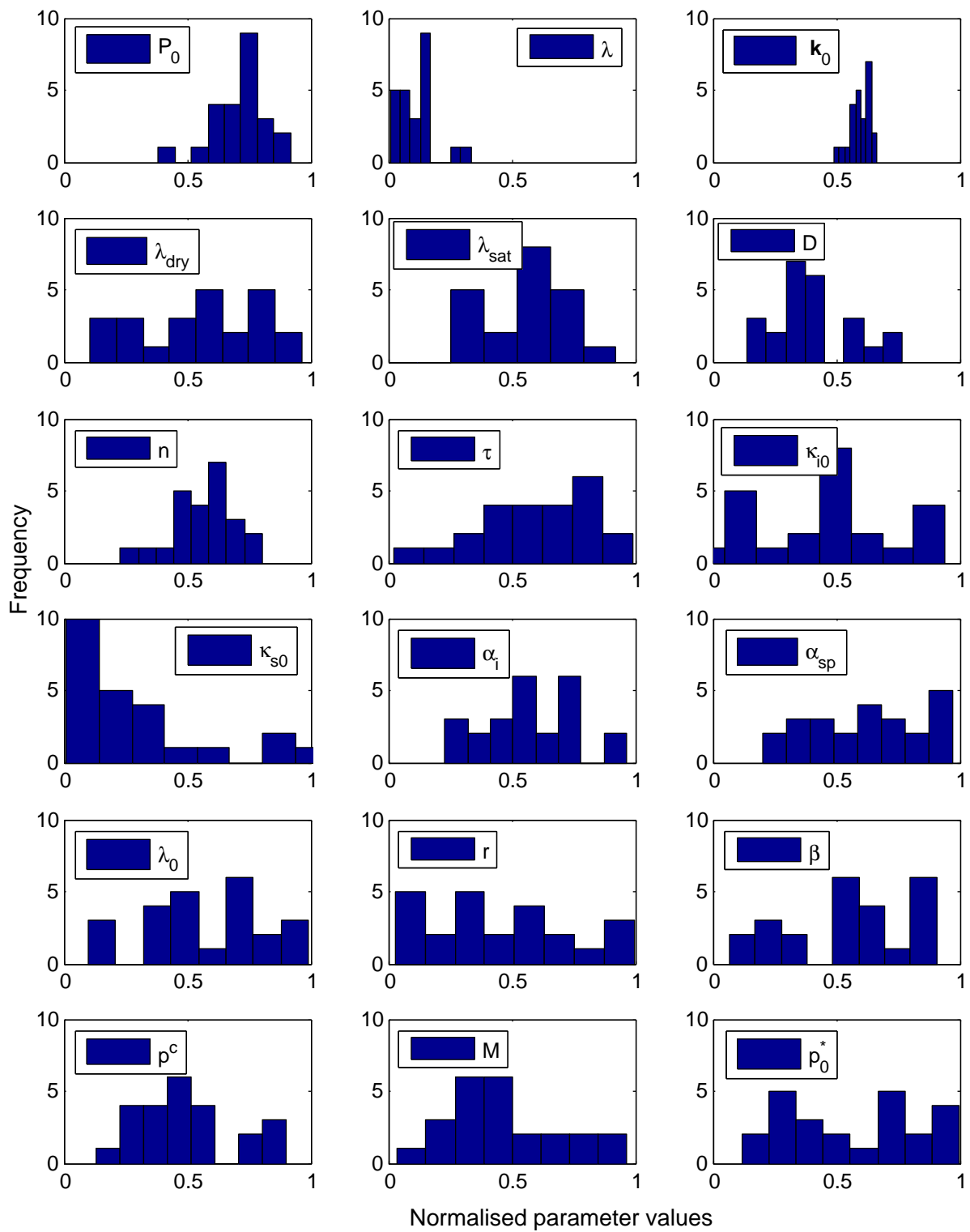
Figure 9.23: Histograms of the parameters obtained by the test-retest procedure
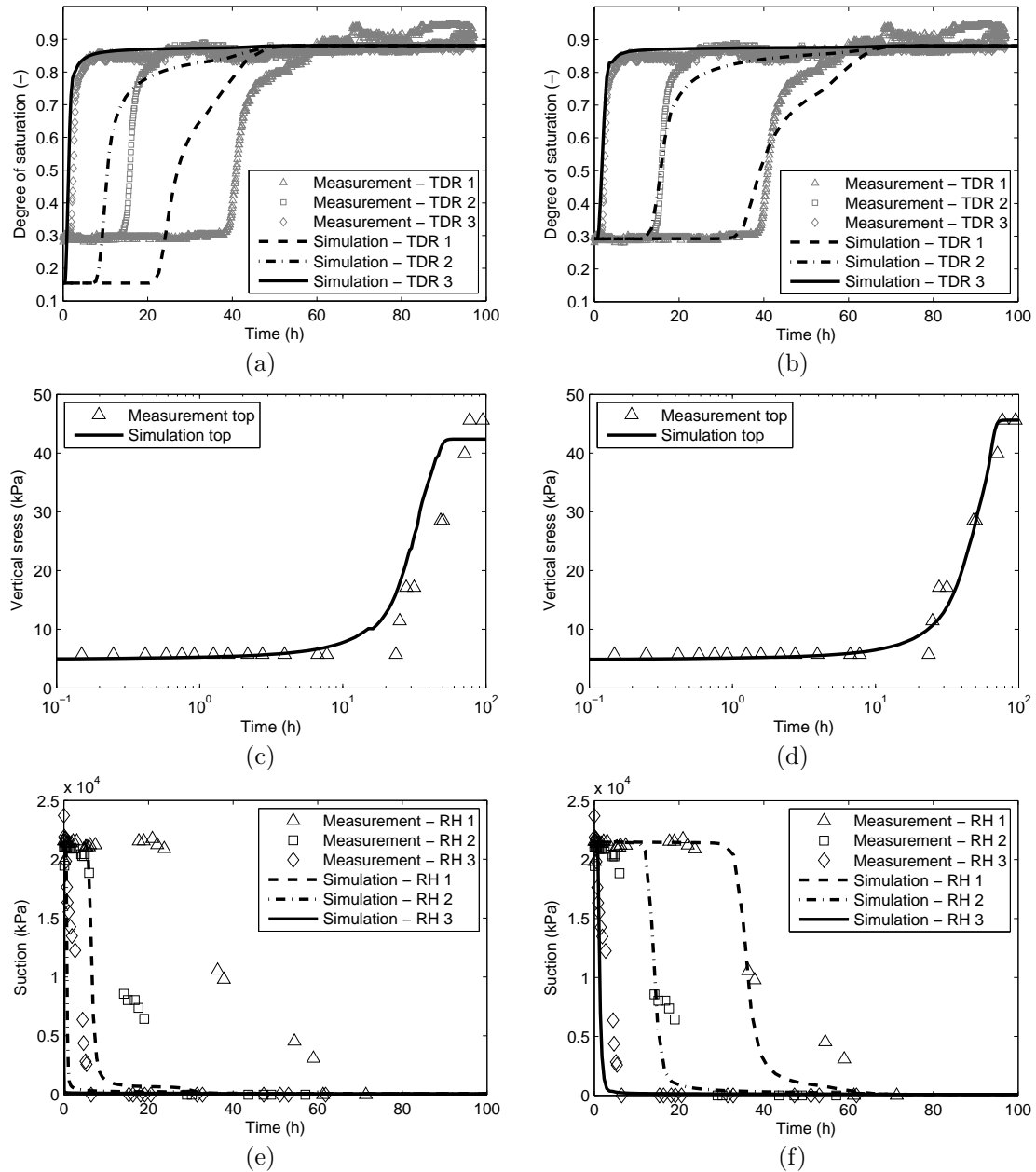
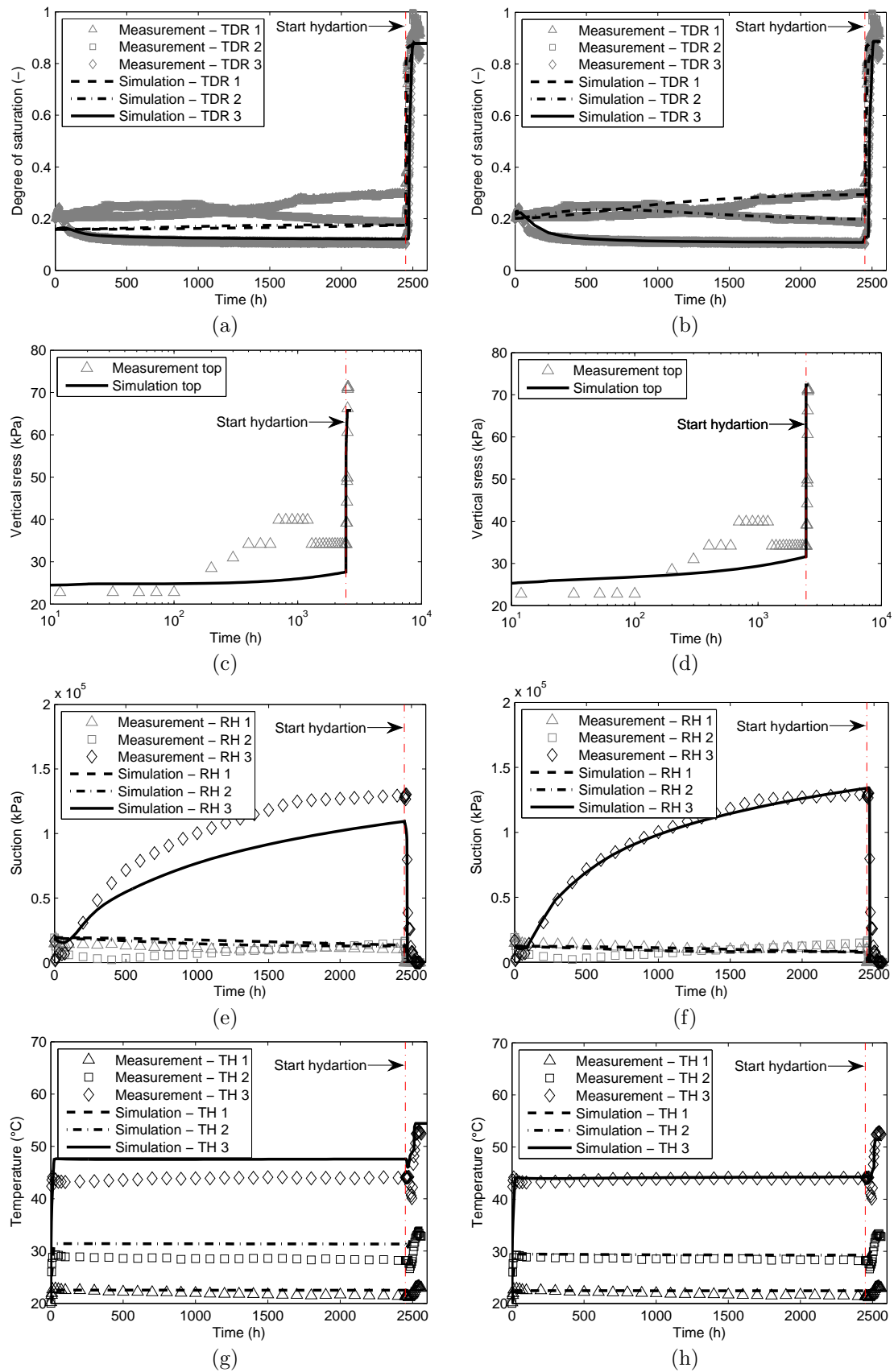Figure 9.24: The curve fitting before and after optimisation of HM test.

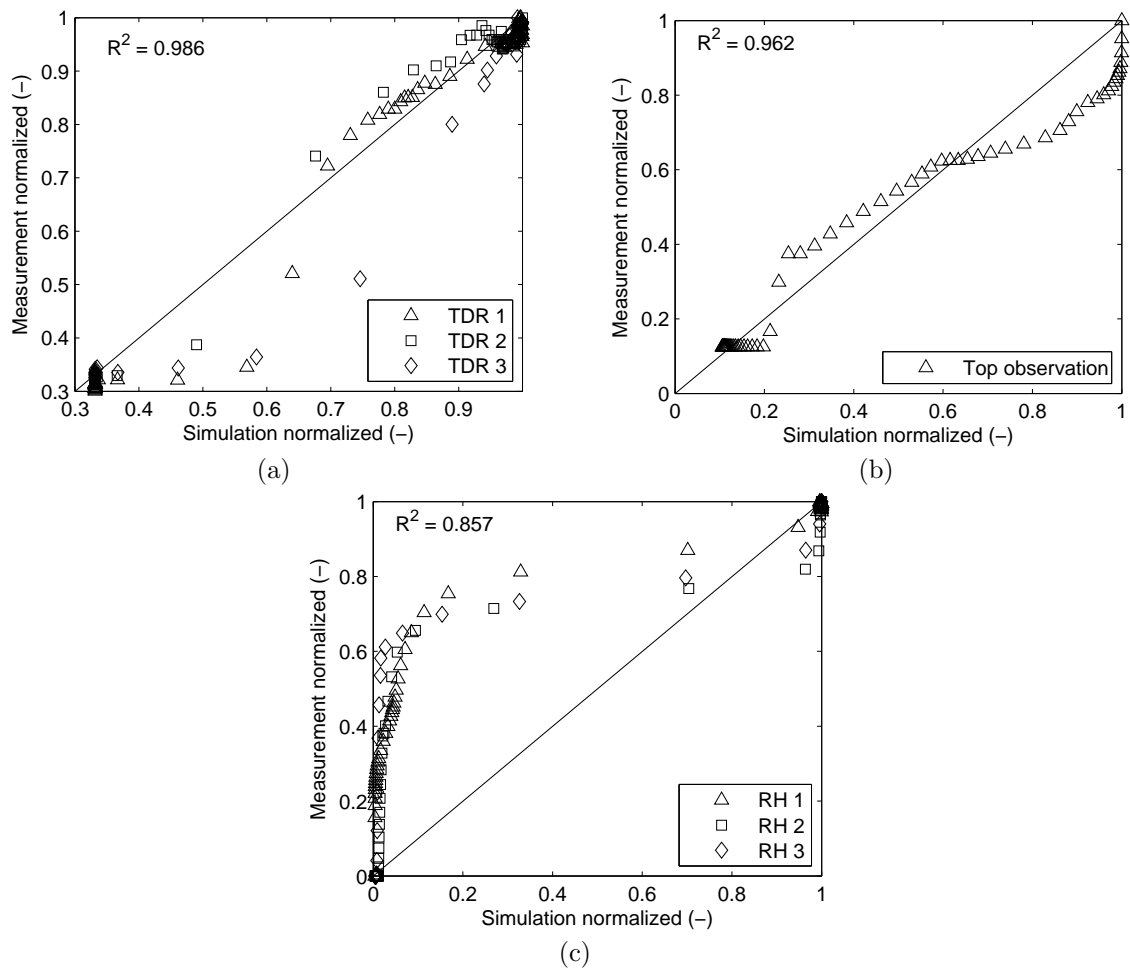Figure 9.25: The curve fitting before and after optimisation of THM test.

Figure 9.26: HM test - normalised measurement versus simulation results after back analysis: (a) Degree of saturation. (b) Stress. (c) Suction.
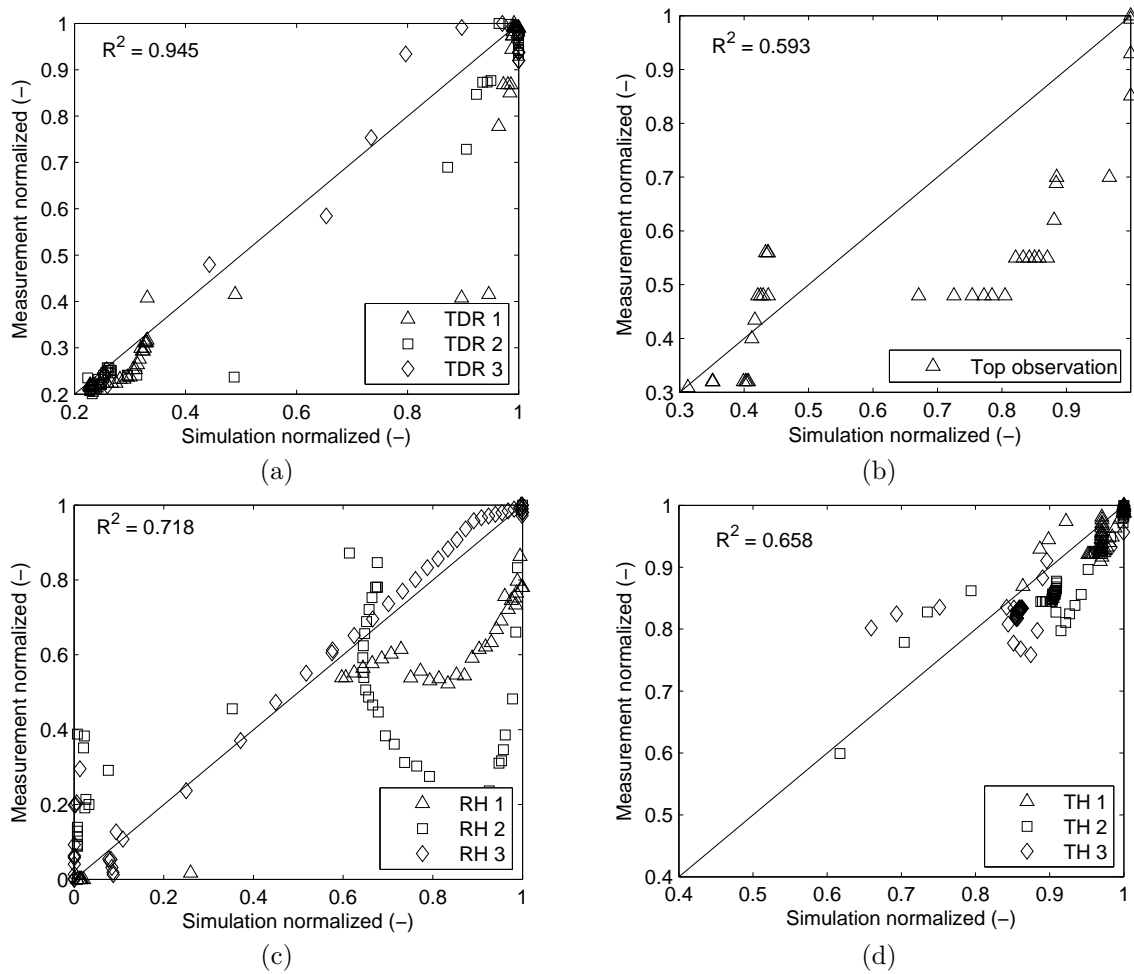
Figure 9.27: THM test - normalised measurement versus simulation results after back analysis: (a) Degree of saturation. (b) Stress. (c) Suction. (d) Temperature.

10 Conclusions and outlook

10.1 Conclusions

The research performed within this doctoral work deals with coupled THM-phenomena that are relevant to nuclear waste engineered barriers. It was done in terms of experiments, numerical simulations and back analyses. A new column-type device for the laboratory investigation of the coupled thermo-hydro-mechanical behaviour of expansive soils was used and shown to provide reasonable data for the behavior of sand-bentonite mixtures in conditions close to those existing in nuclear waste buffers. The column device is designed to apply temperature and hydraulic loading from top and bottom of the sample and thus it allows thermal and suction gradients to be exerted. The device is equipped with water content, temperature and relative humidity sensors at three different sections along the specimen height. The water content and temperature sensors were designed in the way to minimise sample disturbance. A special focus was placed on calibrating the sensors while taking into account the influence of high temperature. The advantage of measuring the swelling pressure simultaneously along the top and the bottom of the sample was made evident. It was also demontrated the ability of the THM column-type device to provide rich data to understand the phenomena taking place in expansive soils during heating-cooling and wetting processes. It can be concluded that the new column-type device is a promising tool for investigating the coupled thermo-hydro-mechanical behaviour of soils in laboratory conditions.

From the experiments with the column-type device, several physical phenomena were revealed and discussed. The transient SWRC measured in the column-type device was found different from that determined using conventional tests under the conditions of equilibrium water flow. This can be explained by the re-arrangement of the fabric platelets (parallelisation or flocculation) during the compaction and hydration phases and by the different boundary conditions in each test. In addition, hydraulic conductivity of the SBM was found to be affected by thermal gradients. However, the magnitude of the change

in hydraulic conductivity with temperature changes appeared to be small and may be neglected.

Next, it is analysed the effects of temperature on the determination of soil water content by means of the time domain reflectometry method. For this purpose, the dielectric constant of soil specimens with known water content was measured at different temperatures ranging from 20 to 80°C. The soil types used in the present study are fine sand, sand-bentonite mixture and sandy loam. For each soil type, the dielectric constant of at least three specimens which had identical dry density but varying initial water content were measured at temperatures ranging from 20 to 80°C. The results obtained agree with previous studies showing that there are two competing phenomena while measuring soil water content using TDR sensors: *(i)* the soil bulk dielectric constant increases with increasing temperature due to the release of bound water from solid soil particles and *(ii)* soil bulk dielectric constant decreases with increasing temperature due to the temperature effect of free water molecules. Moreover, an equilibrium water content exists at which both competing phenomena compensate each other. However, no equilibrium water content was found for the sand-bentonite mixture, and the dielectric constant increased monotonically with temperature for the whole water content range. This can be explained by the significant clay content and the relatively high specific surface area.

For the purposes of this study, a high pressure oedometer device was modified to allow performing tests at different temperatures. Using the modified high pressure oedometer a series of tests under non-isothermal conditions (20°C and 80°C) were carried out. The result of these tests shows that the stress-strain behaviour of the sand-bentonite mixture is not significantly influenced by temperature. It is confirmed that the slope of the normal consolidation line is independent of temperature as modelled by Cui et al. (2000). Furthermore, the NCL slope is independent of suction when soil sample is loaded at a high suction value.

The experimental data reveal in the common case the presence of hysteresis in the water retention curve and a reduction in the maximum degree of saturation after the first drying path, which may be attributed to the occluded air that cannot be removed from the soil during the wetting procedure. A numerical simulation of cyclic hydration tests was performed and the results are discussed in this thesis. The main aim of the numerical simulations was to establish a functional expression for the relation between water content and suction that is valid along the whole loading path including the initial drying and the subsequent imbibition and desiccation paths. Three numerical modelling approaches to soil-water retention relationships were considered and compared. The aim is to study the

possibility of reliable predictions using three different approaches to model the water retention curve. The numerical simulations incorporate the information based on the SWRC derived directly from the transient infiltration column test. The numerical simulation and the experimental results are compared in terms of saturation versus time as well as water pressure versus time for the entire sequence of alternating drainage and imbibition loading paths. The comparison between the numerical simulation and the experimental results shows the need to consider water retention hysteresis and particularly the importance of incorporating the effect of occluded air on the maximum degree of saturation in the water retention model. Taking into account the variation in air-entry and air-repulsion values allows the agreement between the model and the experimental data to be significantly improved.

The next contribution of this study consists of application of back analysis to identify the THM-model parameters. The proposed here approach includes: (i) sensitivity analysis , (ii) selection of optimisation algorithms, (iii) selection of a set of parameters to be optimised and a setup of the parameters' constraints, and (iv) assessment of the reliability and accuracy of the model and the identified parameters. The comparison of local sensitivity analysis with global sensitivity analysis and the assessment of the effect of the model response with the variation in parameters were also performed in addition to the investigation of the confidence in the identified via back analysis model parameters. The advantages and disadvantages of local and global sensitivity analysis are discussed in the context of the nonlinearity of the considered problem and the demand of computational resources

The next conclusion that may be drawn related to perform back analysis and the solution of the optimization problem is that we can not guarantee the uniqueness of the optimal set of parameters. Next, the considered boundary value problem is most likely non-sensitive to some of the model parameters; therefore they can wander in their space without affecting a change in the objective function. A stochastic approach is proposed to identify parameters via confidence interval analysis. The proposed approach enables to improve the results in non-unique solution and uncertainty problems when using the optimisation method. Utilising this approach, the distribution of parameters was quantified and estimated to determine the reliability of the optimised parameters. The quality of the identified parameters was further assessed via residual analysis. Back analysis also indicates that RH measurements at low suction values have a low accuracy. It can be concluded that coupled THM analysis can predict the development of the degree of saturation,temperature, and suction quite well.

10.2 Outlook

Based on the results and discussion in this thesis, there are some remarkable points, which can be further investigated in future.

- In the process of developing the THM column device, it was found that there is a need of a device that is able to measure wider range of suction, e.g. from 10kPa to 100 MPa. It is challenging to develop such a device for the future studies.

- The results obtained within this doctoral work indicate that the high plasticity soil has some special characteristics that significantly affect the hydraulic conductivity. Related to this it is necessary to carefully verify the appropriateness and the applicability of the Darcy's law for determination of the water flow in case of high plasticity soils.

- Osmotic suction plays a very important role in clayey soil. Changing temperatures also significantly affect osmotic suction. The effect of temperature on osmotic suction needs to be investigated further and a modified SWRC model which takes temperature into account needs to be developed.

Bibliography

Abuel-Naga, H. M., Bergado, D. T., Bouazza, A., Pender, M., 2009. Thermomechanical model for saturated clays. Géotechnique 59 (3), 273–278.

Abuel-Naga, H. M., Bergado, D. T., Bouazza, A., Ramana, G. V., 2007. Volume change behaviour of saturated clays under drained heating conditions: experimental results and constitutive modeling. Canadian Geotechnical Journal 44 (8), 942–956.

AECL, 1994. Atomic energy of canada limited (AECL). Tech. rep., Official Website. www.aecl.ca.

Agus, S., Arifin, Y., Tripathy, S., Schanz, T., 2012. Swelling pressure–suction relationship of heavily compacted bentonite–sand mixtures. Acta Geotechnica, 1–11.

Agus, S. S., 2005. An experimental study on hydro-mechanical characteristics of compacted bentonite-sand mixtures. Ph.D. thesis, Bauhaus-University Weimar.

Agus, S. S., Schanz, T., 2005. Comparison of four methods for measuring total suction. Vadose Zone Journal 4 (4), 1087–1095.

Agus, S. S., Schanz, T., 2008. A method for predicting swelling pressure of compacted bentonites. Acta Geotechnica 3, 125–137.

Aitchison, G. D., 1960. Relationships of moisture stress and effective stress functions in unsaturated soils. In: Proc. Conf. pore pressure. Butterworths. London:. pp. 47–52.

Aitchison, G. D., Donald, I. B., 1956. Effective stresses in unsaturated soils. In: Proc. 2nd Aust. N.Z. Conf. Soil Mech. pp. 192–199.

Akaike, H., 1974. A new look at the statistical model identification. I.E.E.E. Trans. Auto. Control AC 19, 716–739.

Akaike, H., 1978. A Bayesian analysis of the minimum AIC procedure. Annals of the Institute of Statistical Mathematics 30, 9–14, 10.1007/BF02480194.

Akaike, H., 1981. Likelihood of a model and information criteria. Journal of Econometrics 16, 3–14.

Al-Badran, Y., May 2011. Volumetric yielding behavior of unsaturated fine-grained soils. Ph.D. thesis, Faculty of Civil and Environmental Engineering, Ruhr-Universität Bochum.

Alonso, E., Alcoverro, F., et al., 2005a. The FEBEX benchmark test: case definition and comparison of modelling approaches. International Journal of Rock Mechanics and Mining Sciences 42 (5–6), 611–638.

Alonso, E., Alcoverro, J., 2005. The FEBEX benchmark test: case definition and comparison of different modelling approaches. In: Stephanson, O. (Ed.), Coupled THMC Processes in Geo-Systems - Fundamentals, Modelling, Experiments and Applications. Vol. 2. Elsevier, pp. 95 – 111.

Alonso, E., Gens, A., Josa, A., 1990. A constitutive model for partially saturated soils. Géotechnique 40 (3), 405–430.

Alonso, E. E., Gens, A., High, D. W., 1987. Special problem soils: General report. In: Proc. 9th European Conf. Soil Mech. Fdn Englng, Dublin. No. 1087–1146.

Alonso, E. E., Romero, E., Hoffmann, C., Garcia-Escuder, E., 2005b. Expansive bentonite-sand mixtures in cyclic controlled-suction drying and wetting. Engineering Geology 81, 213–226.

Alonso, E. E., Vaunat, J., Gens, A., 1999. Modelling the mechanical behaviour of expansive clays. Engineering Geology 54, 173–183.

Andres, T. H., Hajas, W., 1993. Using iterated fractional factorial design to screen parameters in sensitivity analysis of a probabilistic risk assessment model. In: Conference in Computing in Nuclear Safety. Karlsruhe.

Arai, K., Ohta, H., Yasui, T., 1983. Simple optimization techniques for evaluating deformation moduli from field observations. Soils and Foundations 23 (1), 107–113.

Arifin, Y. F., 2008. Thermo-hydro-mechanical behavior of compacted bentonite-sand mixtures: an experimental study. Ph.D. thesis, Bauhaus-University Weimar.

Arifin, Y. F., Schanz, T., 2009. Osmotic suction of highly plastic clays. Acta Geotechnica 4, 177–191.

Asaoka, A., 1978. Observational procedure of settlement prediction. Soils and Foundations 18 (4), 87–100.

Asaoka, A., Matsuo, M., 1980. An inverse problem approach to settlement prediction. Soils and Foundations 20 (4), 53–66.

Asaoka, A., Matsuo, M., 1984. An inverse problem approach to the prediction of multi-dimensional consolidation behavior. Soils and Foundations 24 (1), 49–62.

Ascough II, J., Green, T., Ma, L., Ahjua, L., 2005. Key criteria and selection of sensitivity analysis methods applied to natural resource models. In: Zerger, A., Argent, R. M. (Eds.), International Congress on Modelling and Simulation: Advances and Applications for Management and Decision Making. Melbourne University, Vic, pp. 2463–2469.

ASTM-D2435, 1996. Standard test methods for one-dimensional consolidation properties of soils using incremental loading.

ASTM_D2434-68, 2000. Standard test method for permeability of granular soils (constant head).

Bachmann, J., Horton, R., Grant, S., Ploeg, R., 2002. Temperature dependence of water retention curves for wettable and water-repellent soils. Soil Sci. Soc. Am. J. 66, 44–52.

Bäck, T., 1996. Evolutionary Algorithms in Theory and Practice: Evolution Strategies, Evolutionary Programming, Genetic Algorithms. Oxford University Press US.

Bäck, T., Hammel, U., jun 1994. Evolution strategies applied to perturbed objective functions. In: Proceedings of the First IEEE Conference on Evolutionary Computation. IEEE World Congress on Computational Intelligence. Vol. 1. IEEE Press, pp. 40–45.

Bag, R., 2011. Coupled thermo-hydro-mechanical-chemical behaviour of MX80 bentonite in geotechnical applications. Ph.D. thesis, Cardiff University.

Baille, W., Tripathy, S., Schanz, T., 2010. Swelling pressures and one-dimensional compressibility behaviour of bentonite at large pressures. Applied Clay Science 48 (3), 324–333.

Baldi, G., 1987. Coupling of thermo-plastic and hydraulic effects in a clay repository: Near field analysis. In: Coupled Processes Associated with Nuclear Waste Repositories, Chin-Fu Tsang, Eds. No. 564–580. Academic Press, Orlando, Fla.

Baldi, G., Hueckel, T., Pellegrini, R., 1988. Thermal volume changes of mineral-water system in low-porosity clay soils. Can. Geotech. J. 25 (4), 807–825.

Bear, J., Corapcioglu, M. Y., 1981. A mathematical model for consolidation in a thermoelastic aquifer due to hot water injection or pumping. Water Resources Research 17 (3), 723–736.

Beddoe, R. A., Take, W. A., Rowe, R. K., 2010. Development of suction measurement techniques to quantify the water retention behaviour of GCLs. Geosynthetics International 17 (5), 301–312.

Beliaev, A., Hassanizadeh, S., 2001. A theoretical model of hysteresis and dynamic effects in the capillary relation for two–phase flow in porous media. Transport in Porous Media 43, 487–510.

Bettonvil, B., Kleijnen, J. P., 1997. Searching for important factors in simulation models with many factors: Sequential bifurcation. European Journal of Operational Research 96 (1), 180 – 194.

Bishop, A., 1959. The principle of effective stress. Tecnisk Ukeblad 39, 859–863.

Bishop, A., Blight, G., 1963. Some aspects of effective stress in saturated and partly saturated soils. Géotechnique 13, 177–197.

Bishop, A. W., 1972. Shear strength parameters for undisturbed and remoulded soils specimens. In: Parry, R. H. G. (Ed.), Stress-strain behaviour of soils. London: Foulis., pp. 3–58.

Bishop, A. W., Alpan, I., Blight, G. E., Donald, I. B., 1960. Factors controlling the strength of partly saturated cohesive soils. In: Proc. Am. Sot. Ciu. Engrs Research Conj: Shear Strength of Cohesive Soils, Boulder. No. 1027–1042.

Bolzon, G., Schrefler, B. A., Zienkiewicz, O. C., 1996. Elastoplastic soil constitutive generalized to partially saturated states. Géotechnique 46 (2), 279–289.

Booker, J. R., Savvidou, C., 1985. Consolidation around a point heat source. Int. J. for Numerical and Analytical Methods in Geomechanics 9 (2), 173–184.

Bosman, P. A. N., Thierens, D., 2002. Multi-objective optimization with diversity preserving mixture-based iterated density estimation evolutionary algorithms. International Journal Approximate Reasoning 31 (3), 259–289.

Bossart, P., Nussbaum, C. (Eds.), 2007. Mont Terrri Project – Heater Experiment, engineered Barrier Emplacment and Ventilation experiment. Swiss Geological Survey.

Burger, A., Recordon, E., Bovet, D., Cotton, L., Saugy, B., 1985. Thermique des nappes souterraines. Presses polytechniques romandes, 253p.

Burland, J., 1965a. The yielding and dilation of clay, correspondence. Géotechnique 15, 211–214.

Burland, J. B., 1965b. Some aspects of the mechanical behaviour of partly saturated soils. In: Aitchison, G. D. (Ed.), Moisture Equilibria and Moisture Changes in the Soils Beneath Covered Areas, Butterworth, Sydney, Australia. pp. 270–278.

Campanella, R. G., Mitchell, J. K., 1968. Influence of temperature variations on soil behavior. J. of the Soil Mechanics and Foundations Division 94 (3), 709–734.

Campolongo, F., Cariboni, J., Saltelli, A., 2007. An effective screening design for sensitivity analysis of large models. Environmental Modelling and Software 22, 1509–1518.

Campolongo, F., Kleijnen, J., Andres, T., 2000. Screening methods in Sensitivity Analysis. Chapter 4 in Sensitivity Analysis. John Wiley and Sons.

Canone, D., Ferraris, S., Sander, G., Haverkamp, R., 2008. Interpretation of water retention field measurements in relation to hysteresis phenomena. Water Resources Research 44, W00D12. 14P.

Cardoso, R., Romero, E., Lima, A., Ferrari, A., 2007. A comparative study of soil suction measurement using two different high-range psychrometers. In: Schanz, T. (Ed.), Experimental Unsaturated Soil Mechanics. Bauhaus–University Weimar, Weimar, Germany.

Carrera, J., Neuman, S. P., 1986. Estimation of aquifer parameters under transient and steady conditions: 1, 2 & 3. Water Resources Research 22 (2), 199–242.

Carrera, J., Vázquez-Suné, E., Castillo, O., Sánchez-Vila, X., 2004. A methodology to compute mixing ratios with uncertain end-members. Water Resources Research 40 (W12101), 12101–1212.

Casagrande, 1936. The determination of preconsolidation load and its practical significance. Proc. Int. Conf. Soil Mech. Foun. Eng., 22–26 June 1936 3, 60–64.

Cawlfield, J., 2000. Reliability Algorithms (FORM and SORM). Chapter 7 in Mathematical and Statistical Methods for Sensitivity Analysis of Model Output. John Wiley and Sons.

Chapius, R. P., Masse, I., Madinier, B., Aubertin, M., 2007. A drainage column test for determining unsaturated properties of coarse materials,. Geotechnical Testing Journal 30, 83 – 88.

Charlier, R., 1987. Approche unifiée de quelques problèmes non linéaires de mècanique des milieux continus par la méthode des éléments finis (grandes déformations des métaux et des sols, contact unilatéral de solides, conduction thermique et écoulements en milieu poreux). Ph.D. thesis, FSA - Département ArGEnCo, Université de Liège.

Charlier, R., Radu, J., 1997. Hydro-mechanical coupling and strain localisation. In: In: Final Proc. NAFEMS World Congress, NAFEMS, Glasgow (1997). pp. 299–310.

Chatfield, C., 1995. Problem solving: a statistician's guide. Chapman & Hall, ISBN: 0-412-60630-5.

Cherubini, C., 2000. Reliability evaluation of shallow foundation bearing capacity on c' and ϕ' soils. Canadian Geotechnical Journal 37 (1), 264–269.

Chiu, C. F., Ng, C. W. W., 2003. A state-dependent elasto-plastic model for saturated and unsaturated soils. Géotechnique 53 (9), 809–829.

Cho, W., Lee, J., Chun, K., 1999. The temperature effects on hydraulic conductivity of compacted bentonite. Applied Clay Science 14 (1–3), 47–58.

Christian, J. T., Ladd, C. C., Baecher, G. B., 1994. Reliability applied to slope stability analysis. Journal of Geotechnical & Geoenvironmental Engineering 120 (12), 2180–2207.

Cividini, A., Jurina, L., Gioda, G., 1981. Some aspects of 'characterization' problems in geomechanics. International Journal of Rock Mechanics and Mining Sciences 18 (6), 487 – 503.

Cividini, A., Maier, G., Nappi, A., 1983. Parameter estimation of a static geotechnical model using a Bayes' approach. International Journal of Rock Mechanics and Mining Sciences 20 (5), 215–226.

Clementino, R. V., 2005. Discussion of "An oedometer test study on the preconsolidation stress of glaciomarine clays". Canadian Geotechnical Journal 40, 857–872.

Coleman, J., 1962. Correspond: Stress strain relations for partly saturated soil. Géotechnique 12 (4), 348–350.

Collin, F., Li, X., Radu, J., Charlier, R., 2002. Thermo-hydro-mechanical coupling in clay barriers. Engineering Geology 64, 179–193.

Conn, A. R., Scheinberg, K., Toint, P. L., 1997. Recent progress in unconstrained nonlinear optimization without derivatives. Mathematical Programming 79, 397–414.

Cooley, R. L., 1982. Incorporation of prior information on parameters into nonlinear regression groundwater flow models. Water Resources Research 18 (4), 965–976.

Coope, I. D., Price, C. J., 2001. On the convergence of grid-based methods for unconstrained optimization. SIAM J. Optim. 11, 859.

Cuevas, J., Villar, M., Fernández, A., Gomez, P., Martín, P., 1997. Pore waters extracted from compacted bentonite subjected to simultaneous heating and hydration. Applied Geochemistry 12 (4), 473 – 481.

Cui, Y., Sultan, N., Delage, P., 2000. A thermomechanical model for clays. Can. Geotech. J. 37, 607–620.

Cui, Y., Tang, A., Loiseau, C., Delage, P., 2008. Determining the unsaturated hydraulic conductivity of a compacted sand-bentonite mixture under constant volume and free-swell conditions. Physics and Chemistry of the Earth 33 (1), 462–471.

Cui, Y., Tang, A., Qian, L., Ye, W., Chen, B., 2011. Thermal-mechanical behavior of compacted GMZ bentonite. Soils and Foundations 51 (6), 1065–1074.

Cui, Y. J., Delage, P., 1996. Yielding and plastic behaviour of an unsaturated compacted silt. Geotechnique 46 (2), 291–311.

Cukier, R. I., Fortuin, C. M., Shuler, K. E., Petschek, A. G., Schaibly, J. H., 1973. Study of the sensitivity of coupled reaction systems to uncertainties in rate coefficients. i theory. Journal of Chemical Physics 59 (8), 3873–3878.

Cukier, R. I., Levine, H. B., Shuler, K. E., 1978. Nonlinear sensitivity analysis of multi-parameter model systems. J. Computational Phys. 26 (1), 1–42.

Datcheva, M., Schanz, T., 2003. Anisotropic bounding surface plasticity with rotational hardening for unsaturated frictional materials. J. Phys. IV France 105, 305–312.

Davidon, W. C., 1991. Variable metric method for minimization. SIAM J. Optim. 1 (1), 1–17.

Delage, P., Sultan, N., Cui, Y.-J., 2000. On the thermal consolidation of boom clay. Canadian Geotechnical Journal 37 (2), 343–354.

Delage, P., Sultan, N., Cui, Y.-J., Li, X.-L., 2009. Permeability changes in boom clay with temperature. In: International Conference and Workshop "Impact of Thermo-Hydro-Mechanical-Chemical (THMC) processes on the safety of underground radioactive waste repositories", European Union, Luxembourg, 29 September - 1 October 2009.

Demars, K. R., Charles, R. D., 1982. Soil volume changes induced by temperature cycling. Can. Geotech. J. 19 (2), 188–194.

Derski, W., Kowalski, S. T., 1979. Equations of linear thermoconsolidation. Archives of Mech. 31 (3), 303–316.

Dimov, I., Georgieva, R., 2010. Monte carlo algorithms for evaluating sobol' sensitivity indices. Mathematics and Computers in Simulation 81 (3), 506 – 514.

DIN:18121-1, 1998. Baugrund und Grundwasser: Benenen und Beschreiben von Boden und Fels.

Dirksen, C., Dasberg, S., 1993. Improved Calibration of Time Domain Reflectometry Soil Water Content Measurements. Soil. Sci. Soc. Am. J. 57 (3), 660–667.

DIT-UPC, 2009. CODE_BRIGHT user's guide. Universitat Politècnica de Catalunya, Barcelona, Spain.

Donoso, Y., Fabregat, R., 2010. Multi-Objective Optimization in Computer Networks Using Metaheuristics. Taylor & Francis Group.

DOW, C. C., 2003. Calcium chloride handbook: A guide to properties, forms, storage and handling. Tech. rep., Dow Chemical Company, USA.

Edlefsen, N. E., Anderson, A. B., 1943. Thermodynamics of soil moisture. Hilgardia 15 (2), 31–298.

European-Commission, 2002. EC, 2000, European Commission's Communication on Extended Impact Assessment. Guidelines for implementing the directive are available at the Governance page of the EC. Commission of The European Communities, 05/06/2002 COM(2002) 276 final.

Everett, D., 1954. A general approach to hysteresis - part 3: a formal treatment of the independent domain model of hysteresis. Transactions of the Faraday Society 50, 1077–1096.

Everett, D. H., Smith, F. W., 1954. A general approach to hysteresis. part 2: Development of the domain theory. Trans. Faraday Soc. 50, 187–197.

Everett, D. H., Whitton, W. I., 1952. A general approach to hysteresis. Trans. Faraday Soc. 48, 749–757.

Evett, S. R., Tolk, J. A., Howell, T. A., 2005. Time domain reflectometry laboratory calibration in travel time, bulk electrical conductivity, and effective frequency. Vadose Zone J. 4, 1020–1029.

Fayer, M. J., 2000. UNSAT-H Version 3.0: Unsaturated Soil Water and Heat Flow Model: Theory, User Manual, and Examples. U.S. Department of Energy.

Feng, M., Fredlund, D. G., 23-24 October 1999. Hysteresis influence associated with thermal conductivity sensor measurements. In: Theory to the Practice of Unsaturated Soil Mechanics in Association withthe 52nd Canadian Geotechnical Conference and the Unsaturated Soil Group. Regina, Sask., pp. 651–657.

Fernández, A., Villar, M., Gómez-Espina, R., 2007. Geochemical behaviour of a bentonite barrier: Results up to 8 years of thermo-hydraulic treatment in the laboratory. In: International Meeting, September 17-18, 2007, Lille, France Clays in Natural & Engineered Barriers for Radioactive Waste Confinement.

Flavigny, E., Desrues, J., Palayer, B., 1990. Note technique: Le sable d'Hostun RF. Rev. Franc. Géotech. 53, 67–70.

François, B., Laloui, L., 2007. A stress-strain framework for modeling the behaviour of unsaturated soils under non-isothermal conditions. In Theoretical and numerical unsaturated soils mechanics, Springer Proceedings in Physics 113, 119–126.

François, B., Laloui, L., 2008. ACMEG-TS: A constitutive model for unsaturated soils under non-isothermal conditions. Int. J. Numer. Anal. Meth. Geomech. 32, 1955–1988.

Fredlund, D., 2000. The 1999 R.M. Hardy Lecture: the implementation of unsaturated soil mechanics into geotechnical engineering. Canadian Geotechnical Journal 37, 963–986.

Fredlund, D., Morgenstern, N., 1977. Stress state variables and unsaturated soil. Journal of Geotech Eng. Div. ASCE 103, 447–466.

Fredlund, D., Xing, A., 1994. Equation for the soil-water characteristic curve. Canadian Geotechnical Journal 31, 521–532.

Fredlund, D., Xing, A., Huang, S., 1994a. Predicting the permeability function for unsaturated soils using the soil-water characteristic curve. Canadian Geotechnical Journal 31 (4), 533–546.

Fredlund, D. G., Morgenstern, N. R., Widger, A., 1978. Shear strength of unsaturated soils. Can. Geotech. J. 15 (3), 313–321.

Fredlund, D. G., Rahardjo, H., 1993. Soil Mechanics for Unsaturated Soils. John Wiley & Sons, Inc.

Fredlund, D. G., Xing, A., Fredlund, M. D., Barbour, S. L., 1996. The relationship of the unsaturated soil shear strength to the soil-water characteristic curve. Can. Geotech. J. 33, 440–448.

Fredlund, D. G., Xing, A., Huang, S., 1994b. Predicting the permeability function for unsaturated soils using the soil-water characteristic curve. Can. Geotech. J. 31, 533–546.

Frey, H., Patil, R., 2002. Identification and review of sensitivity analysis methods. Risk Analysis 22 (3), 553–577.

Friedman, S. P., 1997. Statistical mixing model for the apparent dielectric constant of unsaturated porous media. Soil. Sci. Soc. Am. J. 61 (3), 742–745.

Fujimaki, H., Inoue, M., 2003. Reevaluation of the multistep outflow method for determining unsaturated hydraulic conductivity. Vadose Zone Journal 2, 409 – 415.

Gaber, N., Foley, G., Pascual, P., Stiber, N., Sunderland, E., Cope, B., Nold, A., Saleem, Z., 2009. Guidance on the Development, Evaluation, and Application of Regulatory Environmental Models. U.S. Environmental Protection Agency.

Gatabin, C., Billaud, P., 2005. Bentonite THM mock-up experiments: Sensors data report. Tech. rep., CEA, Rapport NT-DPC/SCCME 05-300-A. CEA, Paris.

Geet, M. V., Bastiaens, W., Volckaert, G., Weetjens, E., Sillen, X., Maes, N., Imbert, C., Billaud, P., Touzé, G., Filippi, M., Plas, F., Villar, M., García-Gutiérrez, M., Mingarro, M., Gens, A., Vallejan, B., 2009. RESEAL II: A large-scale in situ demonstration test for repository sealing in an argillaceous host rock –Phase II. Tech. rep.

Geiser, F., 1999. Comportement mécanique dún limon non saturé - Étude expérimentale et modélisation constitutive. Ph.D. thesis, PhD Thesis. Lausanne, EPFL.

Geiser, F., Laloui, L., Vulliet, L., 1997. Constititutive modelling of unsaturated sandy silt. Computer Methods and Advances in Geomechanics, Rotterdam, 899–907.

Gens, A., 1995. Constitutive laws. In: Gens, A., Jouanna, P., Schrefler, B. (Eds.), Modern issues in non-saturated soils. Springer-Verlag.

Gens, A., 1996. Constitutive modelling: application to compacted soil. In: Unsaturated soils, Vol. 3. Balkema, Rotterdam,. pp. 1179–1200.

Gens, A., 1 August 2003. The role of geotechnical engineering for nuclear energy utilisation. ECSMGE Special lecture.

Gens, A., Alonso, E. E., 1992. A framework for the behaviour of unsaturated expansive clays. Canadian Geotechnical Journal 29, 1013–1032.

Gens, A., Garcia-Molina, A. J., Olivella, S., Alonso, E. E., Huertas, F., 1998. Analysis of a full scale in situ test simulating repository conditions. Int. J. Numer. Anal. Meth. Geomech. 22, 515–548.

Gens, A., Olivella, S., 2001. THM phenomena in saturated and unsaturated porous media: Fundamentals and formulation. Revue Française de Gènie Civil 5 (6), 693–717.

Gens, A., Potts, D., 1988. Critical state models in computational geomechanics. Engineering Computations 5, 178–197.

Gens, A., Sanchez, M., Sheng, D., 2006. On constitutive modelling of unsaturated soils. Acta Geotechnica 1, 137–147, 10.1007/s11440-006-0013-9.

Gerhard, J., Kueper, B. H., 2003. Capillary pressure characteristics necessary for simulating DNAPL infiltration, redistribution and immobilization in saturated porous media. Water Resources Research 39 (8), 1212–1212.

Gilbert, R. B., Wright, S. G., Liedtke, E., 1998. Uncertainty in back analysis of slopes: Kettleman hills case history. Journal of Geotechnical & Geoenvironmental Engineering 124 (12), 1167–1177.

Gioda, G., Maier, G., 1980. Direct search solution of an inverse problem in elastoplasticity: Identification of cohesion, friction angle and in situ stress by pressure tunnel tests. International Journal for Numerical Methods in Engineering 15 (12), 1823–1848.

Gioda, G., Sakurai, S., 1987. Back analysis procedures for the interpretation of field measurements in geomechanics. Int. J. for Numerical and Analytical Methods in Geomechanics 11 (6), 555–583.

Glover, F., 1986. Future paths for integer programming and links to artificial intelligence. Computers & Operations Research 13 (5), 533–549.

Gouy, G., 1910. Electric charge on the surface of an electrolyte. Journal of Physics 4 (9), 457.

Grant, S., 2003. Extension of temperature effects model for capillary pressure saturation relations. Water Resources Research 39 (1), 1003–1003.

Grant, S., Salehzadeh, A., 1996. Calculations of temperature effects on wetting coefficients of porous solids and their capillary and wetting wrcs. Water Resources Research 32, 261–279.

Grifoll, J., Gastó, J. M., Cohen, Y., 2005. Non-isothermal soil water transport and evaporation. Advances in Water Resources 28 (11), 1254 – 1266.

Guntsch, M., Middendorf, M., 2001. Pheromone modification strategies for ant algorithms applied to dynamic tsp. In: Boers, E. J. W., Gottlieb, J., Lanzi, P. L., Smith, R. E., Cagnoni, S., Hart, E., Raidl, G. R., Tijink, H. (Eds.), Proceedings of the Evo Workshops on Applications of Evolutionary Computing. Springer, Berlin, Lake Como, Milan, Italy, pp. 213–222.

Hamada, M. S., Wilson, A., Reese, C. S., Martz, H., 2008. Bayesian Reliability. Springer New York.

Hamby, D. M., 1995. A comparison of sensitivity analysis techniques. Health Phys. 68 (2), 195—204.

HEEDS, 2008. How to select the right optimization method for your problem. Wp–1022, rev. 05.08, Red Cedar Technology, Multidisciplinary Design Optimization Software.

Helton, J. C., 1993. Uncertainty and sensitivity analysis techniques for use in performance assessment for radioactive waste disposal. Reliability Engineering and System Safety 42, 327–367.

Helton, J. C., Davis, F. J., 2000. Sampling Based Methods. Chapter 6 in Mathematical and Statistical Methods for Sensitivity Analysis of Model Output.

Hill, M., 1998. Methods and guidelines for effective model calibration. report 98-4005, U.S. Geological survey, water-resources investigations.

Hoang, T., 1998. Convex Analysis and Global Optimization (Nonconvex Optimization and Its Applications). Springer.

Homma, T., (1996), A. S., 1996. Importance measures in global sensitivity analysis of nonlinear models. Reliability Engineering and System Safety 52, 1–17.

Honjo, Y., 2010. Reliability analysis in geotechnical engineering: Procedure of reliability analysis. Tech. rep., Geotechnical Seminar in Munich, Germany.

Honjo, Y., Darmawan, P., 1991. Prediction of future subsidence with quantified uncertainty by an inverse analysis. In: Proc. 4th Int. Symp. on Land Subsidence. Houston, TX, USA, pp. 625–634.

Honjo, Y., K.L.T., C., Hara, T., Shirato, M., Suzuki, M., Kikuchi, Y., 2009. Code calibration in reliability based design level I verification format for geotechnical structures. In: Honjo, e. a. (Ed.), Geotechnical Risk and Safety. Taylor & Francis Group, London, pp. 435–452.

Honjo, Y., Wen-Tsung, L., Guha, S., 1994a. Inverse analysis of an embankment on soft clay by extended bayesian method. Int. J. for Numerical and Analytical Methods in Geomechanics 18 (10), 709–734.

Honjo, Y., Wen-Tsung, L., Sakajo, S., 1994b. Application of Akaike information criterion statistics to geotechnical inverse analysis: the extended Bayesian method. Structural Safety 14 (1-2), 5 – 29.

Hopmans, J., Dane, J., 1986. Temperature dependence of soil water retention curves. Soil Science Society of America Journal 50, 562–567.

Hornberger, G., Spear, R., 1981. An approach to the preliminary analysis of environmental systems. Journal of Environmental Management 7, 7–18.

Horst, R., Pardalos, P. M., Thoai, N. V., 2000. Introduction to global optimization. Springer Verlag.

Hueckel, T., Borsetto, M., 1990. Thermoplasticity of saturated soils and shales: Constitutive equations. Jnl. Geot. Eng. ASCE 116, 1765–1777.

Hueckel, T., Borsetto, M., Peano, A., 1987. Modelling of coupled thermo-elasto-plastic-hydraulic response of clays subjected to nuclear waste heat. In: Numerical Methods in Transient and Coupled Problems, W. Lewis et al. Eds. John Wiley and Sons, Chichester, United Kingdom, pp. 213–235.

Hueckel, T., Pellegrini, R., 1992. Thermo-plastic modelling of untrained failure of saturated clay due to heating. Soils and Foundations 31, 1–16.

Hvorslev, M. J., 1937. Über die Festigkeitseigenschaften Gestörter. In: Bindiger Böden. Copenhagen.

IAEA, 1992. Current practices foe the management and confinement of uranium mill tailings. Tech. Rep. 335, International Atomic Energy Agency Technical Report Series, Viena, Austria.

Iott, J., Haftka, R. T., Adelman, H. M., 1985. Selecting step sizes in sensitivity analysis by finite differences. Tech. rep., Langley Research Center, NASA-TM-86382.

ISO, 1986. ISO 8402 International Standard: Quality Vocabulary. International Organization for Standardization, Geneva, Switzerland.

Jacinto, A. C., 2010. Thermo-hydro-mechanical behaviour of expansive clays under high temperatures. Ph.D. thesis, Technical University of Catalonia, School of Civil Engineering.

Jaynes, D., 1992. Estimating hysteresis in the soil retention function. In: van Genuchten, M., Leij, F., Lund, L. (Eds.), Indirect methods for estimating the hydraulic properties of unsaturated soils. U.S. Salinity Lab, USDA, Riverside, CA.

Jennings, J. E., Burland, J. B., 1962. Limitations to the use of effective stresses in partly saturated soils. Géotechnique 12 (2), 125–144.

Jia, Y., Wileveau, Y., an G. Duveau, K. S., Shao, J. F., 2007. Thermo-hydro-mechanical modelling of an in situ heating experiment. Géotechnique 57 (10), 845–855.

Jing, L., Tsangs, C.-F., Stephansson, O., 1995. DECOVALEX - an international co-operative research project on mathematical models of coupled THM processes for safety analysis of radioactive waste repositories. Int. J. of Rock Mechanics and Mining Sciences 32 (5), 389–398.

JNC, 1999. Project to establish the scientific and technical basis for HLW disposal in Japan. project overview report. Tech. rep., Japan Nuclear Cycle Development Institute (JNC).

Jommi, C., 2000. Remarks on the constitutive modelling of unsaturated soils. In: Tarantino, A., Mancuso, C. (Eds.), Experimental Evidence and Theoretical Approaches in Unsaturated Soils., 139–153.

Josa, A., Alonso, E., Loret, A., Gens, A., 1987. Stress-strain behavior of partially saturated soils. In: Proc. 9th European Conf. Soil Mech. Fdn. Engineering. Vol. 2. pp. 561–564.

JRC, 2011. Course on sensitivity analysis. In: European Commission, Joint Research Centre, Ispra. Rome (2-3 May 2011).

Kalman, R. E., 1960. A new approach to linear filtering and prediction problems. ASME - Journal of Basic Engineering 82, 35–45.

Kanno, T., Fujita, T., Takeuchi, S., Ishikawa, H., Hara, K., Nakano, M., 1999. Coupled thermo-hydro-mechanical modelling of bentonite buffer material. International Journal for Numerical and Analytical Methods in Geomechanics 23 (12), 1281–1307.

Karnland, O., Sandén, T., Johannesson, L.-E., Eriksen, T. E., Jansson, M., Wold, S., Pedersen, K., Motamedi, M., Rosborg, B., 2000. Long term test of buffer material: Final report on the pilot parcels. Tech. rep., SKB project.

Karube, D., 1986. New concept of effective stress in unsaturated soil and its proving test. In: ASTM special technical publication – American Society for Testing and Materials. Vol. ST 977 of 539–552.

Kawai, K., Karube, D., Kato, S., 2000. The model of water retention curve considering effects of void ratio. In: Rahardjo, H., Toll, D., Leong, E. (Eds.), Proceedings of Asian Conference on Unsaturated Soils, Singapore. A.A. Balkema, Rotterdam, The Netherlands, pp. 329–334.

Kennedy, J., Eberhart, R., 1995. Particle swarm optimization. In: Proceedings of IEEE International Conference on Neural Networks. IV. pp. 1942–1948.

Khalili, N., Geiser, Blight, G. E., 2004. Effective stress in unsaturated soils: Review with new evidence. International Journal of Geomechanics 4 (2), 115–126.

Khalili, N., Loret, B., 2001. An elasto-plastic model for non-isothermal analysis of flow and deformation in unsaturated porous media: formulation. International Journal of Solids and Structures 38 (46-47), 8305 – 8330.

Klausner, Y., 1991. Fundamentals of continuum mechanics of soils. Springer-Verlag, New York.

Knabe, T., Datcheva, M., Lahmer, T., Cotecchia, F., Schanz, T., 2013. Identification of constitutive parameters of soil using an optimization strategy and statistical analysis. Computers and Geotechnics 49 (0), 143–157.

Kohgo, Y., Nakano, M., Miyazaki, T., 1993. Theoretical aspects of constitutive modelling for unsaturated soils. Soils and Foundations 33 (4), 49–63.

Kool, J. B., Parker, J. C., 1987. Development and evaluation of closed-form expressions for hysteretic soil hydraulic properties. Water Resources Research 23 (1), 105–114.

Laloui, L., 2001. Thermo-mechanical behaviour of soils. Revue Française de Génie civil 5 (6), 809–843.

Laloui, L., Cekerevac, C., 2008. Non-isothermal plasticity model for cyclic behaviour of soils. Int. J. Numer. Anal. Meth. Geomech. 32 (5), 437–460.

Laloui, L., Nuth, M., 2009. On the use of the generalised effective stress in the constitutive modelling of unsaturated soils. Computers and Geotechnics 36 (1–2), 20–23.

Ledesma, A., Gens, A., Alonso, E., 1991. Identification of parameters of nonlinear geotechnical model. In: Cairns, Balkema, B. B., Carter (Eds.), Proc. 7th Int. Conf. Computer Methods & Adv. Geomechanics. Balkema, Rotterdam, pp. 1005–1010.

Ledesma, A., Gens, A., Alonso, E. E., 1996a. Estimation of parameters in geotechnical backanalysis - I. maximum likelihood approach. Computers and Geotechnics 18 (1), 1 – 27.

Ledesma, A., Gens, A., Alonso, E. E., 1996b. Parameter and variance estimation in geotechnical back analysis using prior information. Int. J. for Numerical and Analytical Methods in Geomechanics 20, 119 – 141.

Ledieu, J., Ridder, P. D., Clerck, P. D., Dautrebande, S., 1986. A method of measuring soil moisture by time-domain reflectometry. Journal of Hydrology 88 (3-4), 319 – 328.

Lee, I.-M., Kim, D.-H., 1999. Parameter estimation using extended Bayesian method in tunnelling. Computers and Geotechnics 24 (2), 109 – 124.

Leong, E.-C., Tripathy, S., Rahardjo, H., 2003. Total suction measurement of unsaturated soils with a device using the chilled-mirror dew-point technique. Géotechnique 53 (2), 173–182, ISSN: 0016–8505.

Levasseur, S., Malecot, Y., Boulon, M., Flavigny, E., 2009. Statistical inverse analysis based on genetic algorithm and principal component analysis: Method and developments using synthetic data. Int. J. Numer. Anal. Meth. Geomech. 33 (12), 1485–1511.

Levenberg, K., 1944. A method for the solution of certain problems in least squares. Quart. Appl. Math. 2, 1964–1968.

Lewis, R. M., Torczon, V., 1996. Rank ordering and positive bases in pattern search algorithms. Tech. rep., Institute for Computer Applications in Science and Engineering, NASA Langley Research Center, Hampton, Virginia 23681-2199.

Li, X., 2005. Modelling of hysteresis response for arbitrary wetting/drying paths. Computers and Geotechnics 32 (2), 133 – 137.

Lide, D. R., 2005. CRC Handbook of Chemistry and Physics 85th. CRC Press, Inc. Boca Raton, FL.

Lim, P., Barbour, S., Fredlund, D., 1998. The influence of degree of saturation on the coefficient of aqueous diffusion. Canadian Geotechnical Journal 35, 811–872.

Lin, C., Tang, S., 2005. Development and calibration of a TDR extensometer for geotechnical monitoring. Geotechnical Testing Journal (ASTM) 28 (5), DOI: 10.1520/GTJ12188.

Lins, Y., 2009. Hydro-Mechanical properties of partially saturated sand. Ph.D. thesis, the Faculty of Civil Egineering, Ruhr-University Bochum.

Lins, Y., Schanz, T., Fredlund, D., 2009. Modified pressure plate apparatus and column testing device for measuring SWCC of sand. Geotechnical Testing Journal 32 (5), 450–464.

Liu, E. L., Xing, H. L., 2009. A double hardening thermo-mechanical constitutive model for overconsolidated clays. Acta Geotechnica 4, 1–6.

Liu, H.-H., Dane, J., 1993. Reconciliation between measured and theoretical temperature effects on soil water retention curves. Soil Science Society of America Journal 57, 1202–1207.

Lloret, A., Villar, M., Sanchez, M., Gens, A., Pintado, X., Alonso, E. E., 2003. Mechanical behaviour of heavily compacted bentonite under high suction changes. Géotechnique 53 (1), 27 – 40.

Loret, B., Khalili, N., 2002. An effective stress elastic-plastic model for unsaturated porous media. Mechanics of Materials 34 (2), 97 –116.

Lu, N., 2008. Is matric suction a stress variable? Journal of Geotechnical and Geoenvironmental Engineering 134 (7), 899–905.

Lu, N., Kaya, M., Collins, B., Godt, J., 2012. Hysteresis of unsaturated hydro-mechanical properties of a silty soil. Journal of Geotechnical and Geoenvironmental Engineering 2.

Lu, N., Likos, W. J., 2004. Unsaturated soil mechanics. John Wiley & Sons, Inc.

Mahnken, R., P., S., 2001. A finite element algorithm for parameter identification of material models for fluid saturated porous media. Int. J. for Numerical and Analytical Methods in Geomechanics 25 (5), 415–434.

Maier, G., Gioda, G., 1981. Optimization methods for parametric identification of geotechnical systems. In: Martins, J. B. (Ed.), In Numerical Methods in Geomechanics. Nato A.S.I. Series, Reidel, Boston, MA.

Manju, M., Schanz, T., Tripathy, S., 2008. A column device to study THM behaviour of expansive soils. In: The 12th International Conference of International Association for Computer Methods and Advances in Geomechanics (IACMAG), October 2008. Goa, India.

Maqsoud, A., Bussire, B., Aubertin, M., Mbonimpa, M., 2012. Predicting hysteresis of the water retention curve from basic properties of granular soils. Geotechnical and Geological Engineering 30, 1147–1159.

Martín, P., Barcala, J., Huertas, F., 2006. Large-scale and long-term coupled thermo-hydro-mechanic experiments with bentonite: the FEBEX mock-up test. Journal of Iberian Geology 32 (2), 259–282.

Mattsson, H., Klisinski, M., Axelsson, K., 2001. Optimization routine for identification of model parameters in soil plasticity. Int. J. for Numerical and Analytical Methods in Geomechanics 25 (5), 435–472.

Matyas, E., Radhakrishna, H., 1968. Volume change characteristics of partially saturated soils. Géotechnique 18, 432–448.

McKay, M., Beckman, R., Conover, W., 1979. A comparison of three methods for selecting values of input variables in the analysis of output from a computer code. Technometrics 21 (2), 239–245.

Meeker, W. Q., Escobar, L. A., 1998. Statistical Methods for Reliability Data. Hoboken, New Jersey: Wiley, iSBN 0471143286.

Metropolis, N., Ulam, S., 1949. The Monte Carlo Method. Journal of the American Statistical Association 44 (247), 335–341.

Michalewicz, Z., Fogel, D. B., 2004. How to Solve It: Modern Heuristics. Springer, second, revised and extended edition.

Mohamed, A., Yong, R., Kjartanson, B., 1992. Temperature and moisture distributions in a clay buffer material due to thermal gradients. In: MRS Proceedings. Vol. 294. pp. 417–425.

Mojid, M., Wyseure, G., Rose, D., 2003. Electrical conductivity problems associated with time-domain reflectometry (TDR) measurement in geotechnical engineering. Geotechnical and Geological Engineering 21, 243–258, 10.1023/A:1024910309208.

Montgomery, D. C., Runger, G. C., 2002. Applied Statistics and Probability for Engineers. John Wiley & Sons Inc.

Morgan, G., Henrion, M., 1990. The nature and sources of uncertainty. In: Uncertainty: A Guide to Dealing With Uncertainty in Quantitative Risk and Policy Analysis. Cambridge University Press, Cambridge, U.K.

Morris, M. D., 1991. Factorial sampling plans for preliminary computational experiments. Technometrics 33, 161–174.

Mualem, Y., 1974. A conceptual model of hysteresis. Water Resources Research 10, 514–520.

Mualem, Y., 1976. A new model for predicting the hydraulic conductivity of unsaturated porous media. Water Resources Research 12, 593–622.

Mualem, Y., 1984. A modified dependent-domain theory of hysteresis. Soil Sci. 137, 283–291.

Mualem, Y., Beriozkin, A., 2009. General scaling rules of the hysteretic water retention function based on Mualem's domain theory. European Journal of Soil Science 60 (4), 652–661.

Mualem, Y., Dagan, G., 1975. A dependent domain model of capillary hysteresis. Water Resources Research 11, 452–460.

Murajama, S., Shibata, T., 1966. Flow and stress relaxation of clays. In: IUTAM Symp. on Rheology and Soil Mechanics, J. Kravtchenko and M. Sirieys, Eds. No. 99–129. Springer-Verlag, Berlin, W. Germany.

Myers, R., Montgomery, D., 1995. Response Surface Methodology: Process and Product Optimization Using Designed Experiments. Wiley-Interscience, New York, NY.

Neldel, J. A., Mead, R., 1965. A simplex method for function minimisation. The Computer Journal 7, 308 – 313.

Neuman, S. P., 1973. Calibration of distributed parameter groundwater flow models viewed as a multiple-objective decision process under uncertainty. Water Resources Research 9, 1006–1021.

Neuman, S. P., Yakowitz, S., 1979. A statistical approach to the inverse problem of aquifer hydrology: 1. theory. Water Resources Research 15 (4), 845–860.

Nguyen-Tuan, L., Datcheva, M., Khan, M., Schanz, T., 2011. Numerical investigation and back analysis for high swelling pressure in constant volume test. In: Topping, B., Tsompanakis, Y. (Eds.), Proc. of the 13th Int. Conf. on Civil, Structural and Environmental Eng. Computing. Vol. No 96. Civil-Comp Press.

Nguyen-Tuan, L., Datcheva, M., Schanz, T., 2009. Numerical simulation and back analysis of coupled thermo-hydro-mechanical behavior of sand-bentonite mixture. In: Guerlebeck, K., Koenke, C. (Eds.), 18th Int. Conf. on the Appl. of Computer Sci. and Math. in Architecture and Civil Engineering. Weimar, Germany, p. paper 184, iSSN: 1611 - 4086.

Nguyen-Tuan, L., Lins, Y., Datcheva, M., Schanz, T., 2013. Modelling hysteresis and air entrapment phenomena – experimental and numerical investigation. Transport in Porous Media (submitted).

Nimmo, J., Miller, E., 1986. The temperature dependence of isothermal moisture vs potential characteristics of soils. Science Society of America Journal 50, 1105–1113.

Nova, R., Wood, D. M., 1979. A constitutive model for sand in triaxial compression. Int. J. for Numerical and Analytical Methods in Geomechanics 3, 255–278.

Nuth, M., Laloui, L., 2008. Effective Stress Concept in Unsaturated Soils :Clarification and Validation of an Unified Framework. Int. Journ. of Numerical and Analytical Methods in Geomechanics. 32, 771–801, sols.

Nützmann, G., Thiele, M., Maciejewski, S., Joswig, K., 1998. Inverse modelling techniques for determining hydraulic properties of coarse-textured porous media by transient out-flow method. Advances in Water Resources 22, 273 – 284.

Oka, Y., Wu, T. H., 1990. System reliability of slope stability. J. Geotech. Engineering 116 (8), 1185–1190.

Oldenhuis, R., Vandekerckhove, J., 2009. Global Optimum Determination by Linking and Interchanging Kindred Evaluators. Delft University of Technology.

Olivares, L., Damiano, E., Greco, R., Zeni, L.and Picarelli, L., Minardo, A., Guida, A., Bernini, R., 2009. An instrumented flume to investigate the mechanics of rainfall-induced landslides in unsaturated granular soils. Geotechnical Testing Journal 32 (2), DOI: 10.1520/GTJ101366.

Olivella, S., Carrera, J., Gens, A., Alonso, E., 1994. Non-isothermal multiphase flow of brine and gas through saline media. Transport in porous media 15, 271 – 293.

Olivella, S., Carrera, J., Gens, A., Alonso, E. E., 1996a. Porosity variations in saline media caused by temperature gradients coupled to multiphase flow and dissolution/precipitation. Transport in Porous Media 25 (1), 1–25.

Olivella, S., Gens, A., Carrera, J., Alonso, E. E., 1996b. Numerical formulation for a simulator (CODE_BRIGHT) for the coupled analysis of saline media. Engineering Computations 13, 87–112.

Olivella, S. P., 1995. Nonisothermal multiphase flow of brine and gas through saline media. Ph.D. thesis, Universitat Politècnica de Catalunya.

Papoulis, A., 1991. Probability, random variables, and stochastic processes, Chapter 9, number third Edition. McGraw-Hill Series in Electrical Engineering.

Parker, J. C., Lenhard, R. J., 1987. A model for hysteretic constitutive relations governing multiphase flow: 1. saturation-pressure relations. Water Resources Research 23 (12), 2187–2196.

Pepin, S., Livingston, N. J., Hook, W. R., 1995. Temperature-dependent measurement errors in time domain reflectometry determinations of soil water. Soil. Sci. Soc. Am. J. 59 (1), 38–43.

Pepin, S., Plamondon, A., Stein, J., 1992. Peat water content measurement using time domain reflectometry. Can. J. For. Res. 22, 534–540.

Persson, M., 1997. Soil solution electrical conductivity measurements under transient conditions using time domain reflectometry. Soil. Sci. Soc. Am. J. 61 (4), 997–1003.

Petersen, L. W., Jacobsen, O., Plauborg, F., Andersen, M., Rolston, D., 1995. The effects of temperature on the determination of soil water content by time-domain reflectometry. In: Soil Sci. Soc. of Ame. annual meeting. Oct. 29 to Nov- 03, 1995.

Pham, Q. H., Fredlund, D. G., Barbour, S. L., 2005. A study on the hysteresis models for soil–water characteristic curves. Canadian Geotechnical Journal 42 (6), 1548–1568.

Pichler, B., Lackner, R., Mang, H. A., 2003. Back analysis of model parameters in geotechnical engineering by means of soft computing. Int. J. for Num. Meth. in Eng. 57 (14), 1943–1978.

Pickens, J. F., Gillham, R., 1980. Finite element analysis of solute transport under hysteretic unsaturated flow conditions. Water Resources Research 16 (1), 1071 – 1078.

Pintado, X., Ledesma, A., Lloret, A., 2002. Back analysis of thermohydraulic bentonite properties from laboratory tests. Engineering Geology 64 (2-3), 91 – 115.

Pitzer, K., Peiper, J., Busey, R. H., 1984. Thermodynamic properties of aqueous sodium chloride solutions. Journal of Physical and Chemical Reference Data 13 (1), 1–102.

Powell, M. J. D., 1964. An efficient method for finding the minimum of a function of several variables without calculating derivatives. Computer Journal 7, 155–162.

Powell, M. J. D., 1998. Direct search algorithms for optimization calculations. Acta Numerica 7, 287–336.

Pusch, R., 1980a. Permeability of highly compacted bentonite. Tech. rep., SKB Technical Report 80-16, Swedish Nuclear Fuel and Waste Management.

Pusch, R., 1980b. Swelling pressure of highly compacted bentonite. Tech. rep., SKB Technical Report 80-13, Swedish Nuclear Fuel and Waste Management.

Pusch, R., 1982. Mineral-water interactions and their influence on the physical behaviour of highly compacted na bentonite. Canadian Geotechnical Journal 19, 381–387.

Pusch, R., Knutsson, S., Xiaodong, L., Prikryl, R., 2011. Numerical calculation of the rate and distribution of porewater flow in clay used for isolating hazardous waste. In: Topping, B. H. V., Tsompanakis, Y. (Eds.), Proceedings of the Thirteenth International Conference on Civil, Structural and Environmental Engineering Computing. Civil-Comp Press, Stirlingshire, United Kingdom, paper.

Pusch, R., Yong, R., 2003. Water saturation and retention of hydrophilic clay buffer-microstructural aspects. Appl. Clay Sci. 23, 61–68.

Puzrin, A., Houlsby, G., 2001. A thermomechanical framework for rate-independent dissipative materials with internal functions. International Journal of Plasticity 17 (8), 1147–1165.

Rayward-Smith, V. J., Osman, I. H., Reeves, C. R., Smith, G. D., 1996. Modern Heuristic Search Methods. Wiley.

Richards, B., 1966. The significance of moisture flow and equilibria in unsaturated soils. in relation to the design of engineering structures built on shallow foundation australia. In: Symp. on permeability and capillary, Amer. Test Materials, NJ. (1966).

Robinet, J.-C., Rahbaoui, A., Plas, F., Lebon, P., 1996. A constitutive thermomechanical model for saturated clays. Engineering Geology 41 (1-4), 145 – 169.

Robinson, D. A., Jones, S. B., Wraith, J. M., Or, D., Friedman, S. P., 2003. A review of advances in dielectric and electrical conductivity measurement in soils using time domain reflectometry. Vadose Zone J. 2 (4), 444–475.

Romero, E., Villar, M., Lloret, A., 2005. Thermo-hydro-mechanical behaviour of two heavily overconsolidated clays. Engineering Geology 81 (3), 255 – 268.

Romero Morales, E., 1999. Characterisation and thermo-hydro-mechanical behaviour of unsaturated boom clay: an experimental study. Ph.D. thesis, UPC, Barcelona.

Ronald, S., 1995. Preventing diversity loss in a routing genetic algorithm with hash tagging. Complexity International 2.

Roscoe, K., Burland, J., 1968. On the generalized stress-strain behaviour of wet clay. In: Heyman, J., F.A. Leckie (Eds.). Cambridge University Press, C. U. (Eds.), Engineering Plasticity. pp. pp. 535–609.

Roscoe, K. H., Schofield, A. N., Thrairajah, A., 1963. Yielding of clays in states wetter than critical. Géotechnique 13 (3), 211–240.

Roscoe, K. H., Schofield, A. N., Wroth, C. P., 1958. On the yielding of soils. Géotechnique 8 (1), 22–53.

Rosenquist, T., 1959. Physico-chemical properties of soils in soil-water system. J. Soil Mech. and Found. Engrg. Div. 85 (2), 31–53.

Roth, K., Schulin, R., Flühler, H., Attinger, W., 1990. Calibration of time domain reflectometry for water content measurement using a composite dielectric approach. Water Resources Research 26, 2267–2273.

Rubin, J., 1967. Numerical method for analyzing hysteresis-affected, post-infiltration redistribution of soil moisture. Soil Sci. Soc. Am. Proc. 31 (13 – 20).

Rutqvist, J., Bögesson, L., Chijimatsu, M., Nguyen, T., Jing, L., Noorishad, J., Tsang, C.-F., 2001. Coupled thermo-hydro-mechanical analysis of a heater test in fractured rock and bentonite at kamaishi mine–comparison of field results to predictions of four finite element codes. Int. J. of Rock Mechanics and Mining Sciences 38 (1), 129 – 142, decovalex II.

Sah, N., Sheorey, P., Upadhyaya, L., 1994. Maximum likelihood estimation of slope stability. International Journal of Rock Mechanics and Mining Sciences 31 (1), 47 – 53.

Sakurai, S., Takeuchi, K., 1983. Back analysis of measured displacements of tunnels. Rock Mechanics and Rock Engineering 16, 173–180.

Saltelli, A., Chan, K., Scott, M., 2000. Sensitivity Analysis. New York: John Wiley and Sons.

Saltelli, A., Ratto, M., Andres, T., Campolongo, F., Cariboni, J., Gatelli, D., Saisana, M., Tarantola, S., 2008. Global Sensitivity Analysis: The Primer. John Wiley & Sons.

Saltelli, A., S., T., Chan, K., 1999. A quantitative, model independent method for global sensitivity analysis of model output. Technometrics 41 (1), 39–56.

Saltelli, A., Tarantola, S., 2002. On the relative importance of input factors in mathematical models: Safety assessment for nuclear waste disposal. Journal of American Statistical Association 97 (459), 702–709.

Saltelli, A., Tarantola, S., Campolongo, F., Ratto, M., 2004. Sensitivity Analysis in Practice: A Guide to Assessing Scientific Models. Wiley.

Sánchez, M., Gens, A., Olivella, S., 2004. Thermo-hydro-mechanical modelling of low permeability media using a double-porosity formulation. Mecanica Computacional XXIII (7), 733 – 754.

Savvidou, C., Booker, J. R., 1989. Consolidation around a heat source buried deep in a porous thermoelastic medium with anisotropic flow properties. Int. J. for Numerical and Analytical Methods in Geomechanics 13, 75–90.

Schanz, T., 2009. Kalibrierung und simulation des halbtechnischen versuchs (HTV-1), validierung des modells. Tech. rep., Bauhaus Universität Weimar.

Schanz, T., Arifin, Y. F., Khan, M. I., Agus, S. S., 2010a. Time effects on total suction of bentonites. Soils and Foundations 50 (2), 195–202.

Schanz, T., Baille, W., Nguyen-Tuan, L., 2011a. Effects of temperature on measurements of soil water content with time domain reflectometry. ASTM - Geotechnical Testing Journal 34 (1), 01–08.

Schanz, T., Datcheva, M., Nguyen-Tuan, L., 2011b. Back analysis of a coupled thermo-hydro-mechanical model based on instrumented constant volume column test. In: IV Int. Conf. on Comp. Methods for Coupled Problems in Sci. and Eng., M. Papadrakakis, E. Onate and B. Schrefler (Eds), 20-22 June, 2011, Kos Island, Greece. pp. 76–89.

Schanz, T., Khan, M. I., Tripathy, S., 2010b. Swelling pressures and hydraulic conductivities of compacted bentonites: An experimental investigation. In: Proceeding of the International Conference on Geotechnical Engineering. Sohail Kibria, Hamid Masood Qureshi and Arooj Mahmood Rana (Eds.), Lahore, Pakistan. November 5-6, 2010. pp. 147–155.

Schanz, T., Nguyen-Tuan, L., Datcheva, M., 2013. A column experiment to study the thermo-hydro-mechanical behaviour of expansive soils. Rock Mechanics and Rock Engineering 46 (6), 1287–1301.

Schanz, T., Tripathy, S., 2009. Swelling pressure of a divalent-rich bentonite: Diffuse double-layer theory revisited. Water Resources Research 45, W00C12.

Schanz, T., Zimmerer, M., Datcheva, M., 2008. Identification of coupled hydro-mechanical parameters with application to engineered barrier systems. In: Toll et al. (Ed.), Unsaturated Soils: Advances in Geo-Engineering – 1st European Conference on Unsaturated Soils. Durham, UK, pp. 797–803.

Schultze, B., Ippisch, O., Huwe, B., Durner, W., 1999. Dynamic nonequilibrium during unsaturated water flow. In: Proc. of the Int. Workshop on Characterization and Measurement of the Hydraulic Properties of Unsaturated Porous Media.

Scott, P. S., Farquhar, G. J., Kouwen, N., 1983. Hysteretic effects on net infiltration. In: Advances in infiltration. ASAE St. Joseph, MI, Publ. 11, pp. 163–170.

Sheng, D., Fredlund, D., 2008. Elastoplastic modelling of unsaturated soils: an overview. In: Keynote Lecture, 12th Int. Conf. Int. Assoc. Computer Methods & Advances in Geomechanics (IACMAG), 1-6 October, 2008, Goa, India, Indian, Institute of Technology, Bombay. pp. 2084–2105.

Sherpa, 2006. The Sherpa Reference Manual. Harvard University.

Shi, Y., Eberhart, R., 1998. A modified particle swarm optimizer. In: Proceedings of IEEE International Conference on Evolutionary Computation. pp. 69–73.

Shoji, M., Ohta, H., Arai, K., Matsumoto, T., Takahashi, T., 1990. Two-dimensional consolidation back-analysis. Soils and Foundations 30 (2), 60–78.

Shoji, M., Ohta, H., Matsumoto, T., Morikawa, S., 1989. Safety control of embankment foundation based on elastic-plastic back analysis. Soils and Foundations 29 (2), 112–126.

Siddiqui, S., Drnevich, V., Deschamps, R., 2000. Time domain reflectometry development for use in geotechnical engineering. Geotechnical Testing Journal 23 (1), 9–20.

Silva, P., 1970. A new graphical construction for determination of the pre-consolidation stress of a soil sample. In: Proceeding of the 4th Brazilian Conference on Soil Mechanics and Foundation Engineering. Vol. 2. Rio de Janeiro, Brazil, pp. 225–232.

Skierucha, W., 2009. Temperature dependence of time domain reflectometry-measured soil dielectric permittivity. Journal of Plant Nutrition and Soil Science 172 (2), 186–193.

Sladen, J. A., D'Hollander, R. D., Krahn, J., 1985. The liquefaction of sands, a collapse surface approach. Canadian Geotechnical Journal 22 (4), 564–578.

Sobol', I. M., 1990. Sensitivity estimates for nonlinear mathematical models. Matematicheskoe Modelirovanie 2, 112–118, in Russian, translated in English in Sobol , I. (1993). Sensitivity analysis for non-linear mathematical models. Mathematical Modeling & Computational Experiment (Engl. Transl.), 1993, 1, 407-414.

Sobol', I. M., 2001. Global sensitivity indices for nonlinear mathematical models and their monte carlo estimates. Mathematics and Computers in Simulation 55 (1-3), 271 – 280.

Sposito, G., 1981. The thermodynamic of soil solution. Tech. rep., Oxford Clarendon Press, London.

St George, J., 1986. Back analysis of slope failures to determine probabilistic design parameters using a bayesian approach. In: Speciality Geomechanics Symposium: Interpretation of Field Testing for Design Parameters; Vol. 1 and 2. Barton, A.C.T.: Institution of Engineers, Australia, pp. 149–152.

Stauffer, F., 1995. Hysteretic storativity of periodic flow in phreatic aquifers. In: Gardiner, J. (Ed.), XXVI IAHR Congress London: The hydraulics of water resources and their development. Vol. 4.

Stauffer, F., Dracos, T., 1986. Experimental and numerical study of water and solute infiltration in layered porous media. Journal of Hydrology 84 (1), 9 – 34.

Stauffer, F., Kinzelbach, W., 2001. Cyclic hysteretic flow in porous medium column: model, experiment, and simulations. Journal of Hydrology 240, 264 – 275.

Stoimenova, E., Lins, Y., Datcheva, M., Schanz, T., 2006. Inverse modelling of soil hydraulic characteristic functions. In: Gürlebeck, K., Könke, C. (Eds.), 17th Int. Conf. on the Application of Com. Sci.and Math. in Architecture and Civil Engineering. Weimar, Germany, 12–14 July 2006.

Szeliga, D., Gawa, J., Pietrzyk, M., 2004. Parameters identification of material models based on the inverse analysis. Int. J. Appl. Math. Comput. Sci. 14 (4), 549–556.

Tan, T., 1990. Representation of hysteresis in capillary pressure for reservoir simulation models,. Canadian Journal of Petroleum Technology 29 (4), 84 – 8.

Tang, A.-M., Cui, Y.-J., 2005. Controlling suction by the vapour equilibrium technique at different temperatures and its application in determining the water retention properties of MX80 clay. Canadian Geotechnical Journal 42 (1), 287–296.

Tang, A.-M., Cui, Y.-J., 2009. Modelling the thermomechanical volume change behaviour of compacted expansive clays. Géotechnique 59 (3), 185–195.

Tang, A.-M., Cui, Y.-J., Le, T. T., 2008. A study on the thermal conductivity of compacted bentonites. Applied Clay Science 41, 181–189.

Tang, Y.-G., Kung, G. T.-C., 2009. Application of nonlinear optimization technique to back analyses of deep excavation. Computers and Geotechnics 36 (1-2), 276 – 290.

Tarantola, A., 1984. Inversion of seismic reflection data in the acoustic approximation. Geophysic 49, 1259–1266.

Tarantola, S., 2010. Random balance designs. In: Joint Research Centre of the European Commission, Summer School on Sensitivity Analysis Florence.

Tarantola, S., Gatelli, D., Mara, T., 2006. Random balance designs for the estimation of first order global sensitivity indices. Reliability Engineering & System Safety 91 (6), 717 – 727.

Terzaghi, K., 1923. Die berechnung der Durchlassigkeitsziffer des Tones aus dem Verlauf der hydrodynamischen Spannungserscheinungen. Sitz, Akademie de Wissenschaffen in Wien, part II A, vol. 132, Vienna, Austria, 125-138 132, 125–138.

Thomas, H., Leall, P., Chandler, N., Dixon, D., Mitchell, H., 2003. Water infiltration into a large-scale in-situ experiment in an underground research laboratory. Géotechnique 53 (2), 207–224.

Thomas, H. R., He, Y., 1995. Analysis of coupled heat, moisture and air transfer in a deformable unsaturated soil. Géotechnique 45 (4), 677–689.

Thomas, H. R., Siddiqua, S., Seetharam, S. C., 2009. Inclusion of higher-temperature effects in a soil behaviour model. Gétechnique 3, 279–282.

Todinov, M., 2005. Reliability and Risk Models: Setting Reliability Requirements. Wiley.

Topp, G., 1971a. Soil-water hysteresis: The domain theory extended to pore interaction conditions. Soil Science Society of America Proceedings 35, 219–22.

Topp, G. C., 1971b. Soil water hysteresis on silt loam and clay loam soils. Water Resources Research 7 (4), 914–920.

Topp, G. C., Davis, J. L., Annan, A. P., 1980. Electromagnetic determination of soil water content: Measurements in coaxial transmission lines. Water Resources Research 16, 574–582.

Topp, G. C., Klute, A., Peters, D. B., 1967. Comparison of water content-pressure head data obtained by equilibrium, steady-state and unsteady-state methods. Soil Sci. Soc. Am. Proc. 31, 312 – 314.

Tripathy, S., C., L. E., H., R., 2003. Total suction measurement of unsaturated soils with a device using the chilled-mirror dew-point technique. Géotechnique 53 (2), 173–182.

Tripathy, S., Sridharan, A., Schanz, T., 2004. Swelling pressures of compacted bentonites from diffuse double layer theory. Canadian Geotechnical Journal 41, 437–450.

Trochim, W. M., 2006. Types of reliability the research methods knowledge base.
URL `http://www.socialresearchmethods.net/kb/reltypes.php`

Turanyi, T., Rabitz, H., 2000. Local methods and their applications. Chapter 5 in Mathematical and Statistical Methods for Sensitivity Analysis of Model Output. John Wiley and Sons.

Vaessens, R. J. M., Aarts, E. H. L., Lenstra, J. K., 1992. A local search template. In: Proceedings of Parallel Problem Solving from Nature 2, PPSN II,. Brussels, Belgium, pp. 67–76.

Vaisala-Oyj, 2011. Vaisala User's Guide: Vaisala HUMICAP humidity and temperature transmitter series HMT330. P.O. box 26, FI-00421 Helsinki, Finland.

van Genuchten, M. T., 1980. A closed-form equation for predicting the hydraulic conductivity of unsaturated soils. Soil Sci. Soc. Am. J. 44, 892–898.

Vanapalli, S., Fredlund, D. G., Pufahl, D. E., Clifton, A. W., 1996. Model for the prediction of shear strength with respect to soil suction. Canadian Geotechnical Journal 33 (3), 379–392.

Verstricht, J., Neerdael, B., Meyendonck, P., Volckaert, G., 1994. Clay moisture measurements in radioactive waste disposal research. In: Proc. Symp. on TDR in environmental, infrastructure, and mining applications, Evanston, Ill., U.S. Bureau of Mines Spec. Publ. SP 19-94: 337-348.

Villar, M., December 9-12, 2002 2002. Effect of temperature on the hydro - mechanical behaviour of compacted bentonite. In: Clays in natural and engineered barriers for radioactive waste confinement, International Meeting, Reims, France.

Villar, M., Gómez-Espina, R., 2007. Retention curves of two bentonites at high temperature. In: Schanz, T. (Ed.), Experimental Unsaturated Soil Mechanics. pp. 267–274.

Villar, M., Gomez-Espina, R., Martin, P., 2006. Behaviour of MX-80 bentonite at unsaturated conditions and under thermo-hydraulic gradient. Band 1081, Informes técnicos Ciemat.

Villar, M., Lloret, A., 2004. Influence of temperature on the hydro–mechanical behaviour of a compacted bentonite. Applied Clay Science 26 (1–4), 337–350.

Villar, M. V., Lloret, A., 2008. Influence of dry density and water content on the swelling of a compacted bentonite. Applied Clay Science 39 (1-2), 38 – 49.

Weast, R., Astle, M., W.H. Beyer, E., 1986. CRC Handbook of Chemistry and Physics. CRC Press, Inc. Boca Raton, FL.

Weise, T., 2009. Global Optimization Algorithms - Theory and Application. http://www.it-weise.de/.

Welch, W. J., J.Buck, R., Sacks, J., Wynn, H. P., Mitchell, T. J., Morris, M. D., 1992. Screening, predicting, and computer experiments. Technometrics 34 (1), 15–47.

Whalley, W. R., 1993. Considerations on the use of time-domain reflectometry (TDR) for measuring soil water content. European Journal of Soil Science 44 (1), 1–9.

Wheeler, S., Gallipoli, D., Karstunen, M., 2002. Comments on use of the Barcelona Basic Model for unsaturated soils. Journal for Numerical and Analytical Methods in Geomechanics 26 (15), 561–1571.

Wheeler, S., Sivakumar, V., 1995. A elasto-plastic critical state framework for unsaturated soil. Géotechnique 45(1):35-53. 45 (1), 35–53.

Wheeler, S. J., Karube, D., 1996. Constitutive modelling: state of the art report. In: Unsaturated Soils (eds. Alonso & Delage). Balkema, Rotterdam. pp. 1179–1200.

Wheeler, S. J., Sharma, R. S., Buisson, M. S. R., 2003. Coupling of hydraulic hysteresis and stress-strain behaviour in unsaturated soils. Géotechnique 52 (1), 41–54.

Wildenschild, D., Jensen, K. H., Hollenbeck, K. J., Illangasekare, T. H., Znidarcic, D., Sonnenborg, T., Butts, M. B., 1997. A two-stage procedure for determining unsaturated hydraulic characteristics using a syringe pump and outflow observations. Soil Sci. Soc. Am. J. 61, 347 – 359.

Woersching, H., Becker, R., Schlaeger, S., Bieberstein, A., Kudella, P., 2006. Spatial-tdr moisture measurement in a large scale levee model made of loamy soil material. Proc. TDR 2006, Purdue University, West Lafayette, USA, Paper ID 33, 15 p.

Wolpert, D., Macready, W., 1997. No free lunch theorems for optimization. IEEE Transactions on Evolutionary Computation 1, 67–82.

Wolpert, D. H., Macready, W. G., 1995. No free lunch theorems for search. Technical report SFI-TR-95-02-010, The Santa Fe Institute, 1399 Hyde Park Rd., Santa Fe, NM, 87501, USA.

Wraith, J. M., Or, D., 1999. Temperature effects on soil bulk dielectric permittivity measured by time domain reflectometry: Experimental evidence and hypothesis development. Water Resources Research 35 (2), 361–369.

Wright, W., Yoder, R., Rainwater, N., Drumm, E., 2001. Calibration of five-segment time domain reflectometry probes for water content measurement in high density materials. Geotechnical Testing Journal 24 (2), 172–184.

Wu, W., Li, X., Charlier, R., Collin, F., 2004. A thermo-hydro-mechanical constitutive model and its numerical modelling for unsaturated soils. Computers and Geotechnics 31, 155–167.

Xie, M., Bauer, S., Kolditz, O., Nowak, T., Shao, H., 2006. Numerical simulation of reactive processes in an experiment with partially saturated bentonite. Journal of Contaminant Hydrology 83 (1–2), 122 – 147.

Yang, H., Rahardjo, H., Leong, E. C., Fredlund, D. G., 2004a. A study of infiltration on three sand capillary barriers. Can. Geotech. J. 41, 629 – 643.

Yang, H., Rahardjo, H., Wibawa, B., Leong, E. C., 2004b. A soil column apparatus for laboratory infiltration study. Geotechnical Testing Journal 27 (4), 347 – 355.

Ye, W. M., Wan, M., Chen, B., Chen, Y. G., Cui, Y. J., Wang, J., 2012. Temperature effects on the unsaturated permeability of the densely compacted GMZ01 bentonite under confined conditions. Engineering Geology 126, 1–7.

Yong, R., Taylor, L., Warkentin, B., 1962. Swelling pressures of sodium montmorillonite at depressed temperatures. In: Eleven National Conference on Clays and Clay minerals. Soil Mechanics Series 4.

Zhang, J., Tang, W. H., Zhang, L. M., 2010. Efficient probabilistic back-analysis of slope stability model parameters. Journal of Geotechnical and Geoenvironmental Engineering 136 (1), 99–109.

Zhang, Y., Gallipoli, D., Augarde, C., 2013. Parameter identification for elasto-plastic modelling of unsaturated soils from pressuremeter tests by parallel modified particle swarm optimization. Computers and Geotechnics 48 (0), 293–303.

Zhang, Z. F., Ward, A. L., Gee, G. W., 2003. Estimating soil hydraulic parameters of a field drainage experiment using inverse techniques. Vadose Zone J. 2 (2), 201–211.

Zhou, M., Li, Y., Xiang, Z., Swoboda, G., Cen, Z., 2007. A modified extended Bayesian method for parameter estimation. Tsinghua Science and Technology 12 (5), 546 – 553.

Zimmerer, M. M., 2010. VARO^{2}PT. User Manual.

Schriftenreihe des Lehrstuhls für Grundbau, Boden- und Felsmechanik der Ruhr-Universität Bochum

Herausgeber: H.L. Jessberger

1 (1979) **Hans Ludwig Jessberger**
Grundbau und Bodenmechanik an der Ruhr-Universität Bochum

2 (1978) **Joachim Klein**
Nichtlineares Kriechen von künstlich gefrorenem Emschermergel

3 (1979) **Heinz-Joachim Gödecke**
Die Dynamische Intensivverdichtung wenig wasserdurchlässiger Böden

4 (1979) **Poul V. Lade**
Three Dimensional Stress-Strain Behaviour and Modeling of Soils

5 (1979) **Roland Pusch**
Creep of soils

6 (1979) **Norbert Diekmann**
Zeitabhängiges, nichtlineares Spannungs-Verformungsverhalten von gefrorenem Schluff
unter triaxialer Belastung

7 (1979) **Rudolf Dörr**
Zeitabhängiges Setzungsverhalten von Gründungen in Schnee, Firn und Eis
der Antarktis am Beispiel der deutschen Georg-von-Neumayer- und Filchner-Station

8 (1984) **Ulrich Güttler**
Beurteilung des Steifigkeits- und Nachverdichtungsverhaltens von
ungebundenen Mineralstoffen

9 (1986) **Peter Jordan**
Einfluss der Belastungsfrequenz und der partiellen Entwässerungs-
möglichkeiten auf die Verflüssigung von Feinsand

10 (1986) **Eugen Makowski**
Modellierung der künstlichen Bodenvereisung im grundwasserdurchströmten
Untergrund mit der Methode der finiten Elemente

11 (1986) **Reinhard A. Beine**
Verdichtungswirkung der Fallmasse auf Lastausbreitung in nichtbindigem
Boden bei der Dynamischen Intensivverdichtung

12 (1986) **Wolfgang Ebel**
Einfluss des Spannungspfades auf das Spannungs-Verformungsverhalten
von gefrorenem Schluff im Hinblick auf die Berechnung von Gefrierschächten

13 (1987) **Uwe Stoffers**
Berechnungen und Zentrifugen-Modellversuche zur Verformungsabhängigkeit
der Ausbaubeanspruchung von Tunnelausbauten in Lockergestein

14 (1988) **Gerhard Thiel**
Steifigkeit und Dämpfung von wassergesättigtem Feinsand unter Erdbebenbelastung

Herausgeber: T. Schanz

Curriculum Vitae

Personal information

Name, given name	Nguyen-Tuan, Long
Nationality	Vietnamese
Date of birth	July 04, 1979
Birthplace	Hanoi, Vietnam

Working experience

04.2009 - Present	Chair of foundation, soil and rock mechanics
	Ruhr-Universität Bochum, Germany
	Position: Research assistant
	Assignment: Experiment, numerical simulation, and back analysis
12.2002 - 9.2006	Department of geotechnics and geology engineering
	Hanoi University of Mining and Geology
	Position: Teaching assistant
	Assignment: Foundation technique

Education

04.2009 - Present	Chair of foundation, soil and rock mechanics
	Ruhr-Universität Bochum, Germany
	For degree: Doctor of philosophy
	Topic: Thermo-hydro-mechanical behaviour of soils:
	experiments and back analysis.
09.2006- 12.2008	Faculty of civil engineering
	Bauhaus-Universität Weimar, Germany
	For degree: Master of Science
	Field: Natural Hazards Mitigation in Structural Engineering
09.1997 - 04.2002	Faculty of civil engineering
	Hanoi Architectural University, Vietnam
	For degree: Bachelor
	Field: Civil Engineering

Publications

1. Nguyen-Tuan, L., Viefhaus, H., Datcheva, M., Schanz, T., 2013b. Coupled thermo-hydro-mechanical modelling of crack development along fossil dinosaur's footprints in soft cohesive sediments. In: V Conference on Computational Methods for Coupled Problems in Science and Engineering, Ibiza, Spain (17-19 June, 2013). Vol. 5. pp. 67–79.

2. Schanz, T., Nguyen-Tuan, L., Datcheva, M., 2013. A column experiment to study the thermo-hydro-mechanical behaviour of expansive soils. Rock Mechanics and Rock Engineering, 46, 1287-1301.

3. Nguyen-Tuan, L., Lins, Y., Datcheva, M., Schanz, T., 2013a. Modelling hysteresis and air entrapment phenomena – experimental and numerical investigation. Transport in Porous Media (submitted).

4. Schanz, T., Nguyen-Tuan, L., Datcheva, M., 2012. Thermo-hydro mechanical column experiment to study expansive soil behaviour. In: Laloui, L., Ferrari, A. (Eds.), Advances in Multiphysical Testing of Soils and Shales Springer Series in Geomechanics and Geoengineering. Springer, pp. 125–130.

5. Nguyen-Tuan, L., Datcheva, M., Khan, M., Schanz, T., 2011. Numerical investigation and back analysis for high swelling pressure in constant volume test. In: Topping, B., Tsompanakis, Y. (Eds.), Proc. of the 13th Int. Conf. on Civil, Structural and Environmental Eng. Computing. Vol. No 96. Civil-Comp Press.

6. Schanz, T., Baille, W., Nguyen-Tuan, L., 2011a. Effects of temperature on measurements of soil water content with time domain reflectometry. ASTM - Geotechnical Testing Journal 34 (1), 01–08.

7. Schanz, T., Datcheva, M., Nguyen-Tuan, L., 2011b. Back analysis of a coupled thermo-hydro-mechanical model based on instrumented constant volume column test. In: IV Int. Conf. on Comp. Methods for Coupled Problems in Sci. and Eng., M. Papadrakakis, E. Onate and B. Schrefler (Eds), 20-22 June, 2011, Kos Island, Greece. pp. 76–89.

8. Nguyen-Tuan, L., Datcheva, M., Schanz., T., 2010a. Landslide hazard: A coupled hydro-mechanical analysis with variation of suction and soil stiffness during wetting process - ma river case study. In: Pham, H., Mai, T., Ohtsu, H., Dang, V., Nguyen, H. (Eds.), Proc. of the Int. Sym. Hanoi Geoengineering. Hanoi, Viet Nam, pp. 219–226.

9. Khan, M. I., Nguyen-Tuan, L., Schanz, T., November 5-6 2010. Experimental and numerical investigation of swelling pressure in compacted bentonite. In: Kibria, S., Qureshi, H. M., Rana, A. M. (Eds.), Proc. of the Int. Conf. on Geotechnical Engineering. Lahore, Pakistan, pp. 147–155.

10. Nguyen-Tuan, L., Datcheva, M., Schanz, T., 2010b. Landslide hazard: A coupled hydro-mechanical analysis with variation of suction and soil stiffness during wetting process - Ma river case study. Vietnam Geotechnical Journal (in English) 14 (2E), 42–51, iSSN-08068-279X.

11. Nguyen-Tuan, L., Datcheva, M., Schanz, T., 2009. Numerical simulation and back analysis of coupled thermo-hydro-mechanical behavior of sand-bentonite mixture. In: Guerlebeck, K., Koenke, C. (Eds.), 18th Int. Conf. on the Appl. of Computer Sci. and Math. in Architecture and Civil Engineering. Weimar, Germany, p. paper 184, iSSN: 1611 - 4086.

Eidesstattliche Erklärung

Hiermit erkläre ich an Eides Statt, dass ich die vorliegende Diplomarbeit selbstständig und ohne fremde Hilfe angefertigt, keine anderen als die angegebenen Quellen und Hilfsmittel benutzt und die den benutzten Quellen wörtlich oder inhaltlich entnommenen Stellen als solche kenntlich gemacht habe.

Bochum, Datum   Unterschrift

26.08.2013